Thermal Transport in Nanostructured Materials: Preparation, Characterization and Simulation

DISSERTATION

zur Erlangung des akademischen Grades einer Doktorin
der Naturwissenschaften (Dr. rer. nat.)

an der Fakultät für Biologie, Chemie und Geowissenschaften
der Universität Bayreuth

vorgelegt von

Alexandra Philipp
geboren in Münchberg

Bayreuth, 2022

Die vorliegende Arbeit wurde in der Zeit von November 2014 bis August 2018 in Bayreuth am Lehrstuhl Physikalische Chemie I unter Betreuung von Herrn Prof. Dr. Markus Retsch angefertigt.

Vollständiger Abdruck der von der Fakultät für Biologie, Chemie und Geowissenschaften der Universität Bayreuth genehmigten Dissertation zur Erlangung des akademischen Grades einer Doktorin der Naturwissenschaften (Dr. rer. nat.

Dissertation eingereicht am: 07.06.2022

Zulassung durch die Promotionskommission: 15.06.2022

Wissenschaftliches Kolloquium: 14.06.2023

Amtierender Dekan: Prof. Dr. Benedikt Westermann

Prüfungsausschuss:

Prof. Dr. Markus Retsch (Gutachter)

Prof. Dr. Georg Papastavrou (Gutachter)

Prof. Dr. Josef Breu (Vorsitz)

Prof. Dr. Seema Agarwal

Diese Dissertation wurde als kumulative Arbeit angefertigt und beinhaltet die folgenden Publikationen:

- Understanding Thermal Insulation in Porous, Particulate Materials.
  P. Ruckdeschel, **A. Philipp**, M. Retsch, *Advanced Functional Materials* **2017**, 27(38), 1702256.

- Low Thermal Conductivity through Dense Particle Packings with Optimum Disorder.
  F. A. Nutz‡, **A. Philipp**‡, B. A. F. Kopera, M. Dulle, M. Retsch, *Advanced Materials* **2018**, 30(14), 1704910.

- Thermal Transport in Binary Colloidal Glasses: Composition Dependence and Percolation Assessment.
  P. Ruckdeschel‡, **A. Philipp**‡, B. A. F. Kopera, F. Bitterlich, M. Dulle, N. W. Pech-May, M. Retsch, *Physical Review E* **2018**, 97(2), 022612.

- Direct Measurement of the In-Plane Thermal Diffusivity of Semitransparent Thin Films by Lock-In Thermography: An Extension of the Slopes Method.
  A. Philipp, N. W. Pech-May, B. A. F. Kopera, A. M. Lechner, S. Rosenfeldt, M. Retsch, *Analytical Chemistry* **2019**, 91(13), 8476-8483.

- The Accuracy of Laser Flash Analysis Explored by Finite Element Modeling and Numerical Fitting.
  A. Philipp, J. Eichinger, R. C. Aydin, A. Georgiadis, C. J. Cyron, M. Retsch, *Heat and Mass Transfer* **2020**, 56, 811-823.

- Tunable Thermoelastic Anisotropy in Hybrid Bragg Stacks with Extreme Polymer Confinement.
  Z. Wang, K. Rolle‡, T. Schilling‡, P. Hummel‡, **A. Philipp**‡, B. A. F. Kopera, A. M. Lechner, M. Retsch, J. Breu, G. Fytas, *Angewandte Chemie International Edition* **2020**, 59(3), 1286-1294.

- Anisotropic Thermal Transport in Spray-Coated Single-Phase Two-Dimensional Materials: Synthetic Clay vs. Graphene Oxide.
  A. Philipp‡, P. Hummel‡, T. Schilling, P. Feicht, S. Rosenfeldt, M. Ertl, M. Schöttle, A. M. Lechner, Z. Xu, C. Gao, J. Breu, M. Retsch, *ACS Applied Materials & Interfaces* **2020**, 12, 18785-18791.

‡ *These authors contributed equally to the work.*

Für meinen Sohn

Maximilian

Table of Contents

Summary

Nanostructured materials are of rising interest for thermal management applications. As a consequence, new nanomaterials are developed continuously. For their application, an exact knowledge of the thermal transport properties of these new materials is required. In addition, new characterization methods are needed due to the small dimensions of these materials. In my thesis, I present both a theoretical and an experimental approach for the characterization of thermal transport in nanostructured materials: the finite element method (FEM) and lock-in thermography (LIT). Thereby, I investigated nanoscale heat transport phenomena of two promising dielectric nanomaterials: porous colloidal assemblies and fully-dense Bragg stacks. Both are easily processable from aqueous dispersions. Furthermore, they possess highly controlled structural properties. The latter allowed me to study the governing structure-property relationships in great detail.

In the first part of my thesis, I used the FEM to analyze heat transfer through colloidal particle assemblies from a theoretical point of view. Thereby, I supported the experimental characterization conducted by the laser flash analysis (LFA), which was done by two colleagues. Prior to these studies, I proved that the LFA is robust against a variety of non-ideal experimental conditions, some of which occur in measuring colloidal assemblies. This confirmed that the thermal transport properties of this nanomaterial can be precisely measured by the LFA. Subsequently, I simulated the heat transport through a variety of colloidal particle assemblies made of silica hollow spheres, polystyrene particles, and mixtures of silica hollow spheres and latex particles. For a better understanding of the governing processes, we conducted the experiments and simulations under vacuum conditions. From these studies, we derived several parameters which are important for the fabrication of a highly insulating material. Firstly, the particle

geometry itself. The studies showed that colloidal crystals made of silica hollow spheres with very thin shells have the best thermal insulation properties compared to all the other tested colloidal crystals. Secondly, the interparticle bonding strength. My simulation confirmed that a reduction of the interparticle bonding strength leads to a significant decrease of the thermal conductivity of the particle assemblies. Thirdly, the order of the particle assembly. We discovered that disordered structures in general exhibit better thermal insulation properties than ordered structures. Furthermore, we found that by mixing two differently-sized polymer particles in an ideal size and mixing ratio, disordered structures with a significant lower thermal conductivity can be achieved. Beside thermal insulation, we investigated thermal percolation effects in particle colloidal assemblies. However, the mixing behavior of same-sized silica hollow spheres with polymer particles just follows the effective medium mixing model. Subsequently, I showed that a very large thermal conductivity ratio of the two particle types is required to actually achieve thermal percolation effects.

In the second part of my thesis, I set up the method lock-in thermography and established the data evaluation process. LIT allows the measurement of the in-plane thermal transport in thin, free-standing films and fibers. Supported by numerical simulations, I demonstrated that even optically semitransparent thin films can be evaluated using the well-known slopes method, although it was originally developed for opaque samples. This allowed me to determine the in-plane thermal conductivity of different optically semitransparent samples. In cooperation with a colleague, who used the photoacoustic method to characterize the cross-plane thermal conductivity, I investigated the anisotropic thermal conductivity of nanostructured, thin films. First, we compared the heat spreading properties of Bragg stacks consisting of highly ordered sodium fluorohectorite platelets to graphene oxide (GO). We found a high in-plane thermal conductivity (5.7 $Wm^{-1}K^{-1}$) in direction of the clay platelets and a low cross-plane thermal

conductivity (0.2 $Wm^{-1}K^{-1}$) perpendicular to the layers. This resulted in a promising high thermal conductivity anisotropy of ≈30 for the synthetic clays. This anisotropy ratio is significantly higher than the anisotropy ratio of the GO samples. Subsequently, we studied the anisotropic thermal transport properties of hybrid Bragg stacks made of alternating layers of sodium fluorohectorite and polyvinylpyrrolidone. I showed that, despite the extreme polymer confinement, the in-plane thermal conductivity follows a parallel mixing model and linearly increases with decreasing polymer content from 0.2 $Wm^{-1}K^{-1}$ to 5.7 $Wm^{-1}K^{-1}$. However, the introduction of polymer layers into the Bragg stack leads to a strong drop of the cross-plane thermal conductivity. Here, all hybrid samples independent of the polymer layer thickness have an ultralow value of 0.09 $Wm^{-1}K^{-1}$. This is due to the mixing of unlike materials and the associated introduction of a high number of hard-soft interfaces. In total, we found a maximum thermal conductivity anisotropy of 38 which is quite high for an optically transparent material.

In summary, this thesis showed that the FEM and LIT are two powerful techniques to investigate thermal transport in nanostructured materials. Furthermore, my studies demonstrate that tailored nanostructuring provides access to both highly insulating materials as well as materials with highly anisotropic thermal transport properties.

Zusammenfassung

Nanostrukturierte Materialien werden fortlaufend relevanter für Wärmemanagementanwendungen. Durch dieses steigende Interesse werden stetig neue Nanomaterialien entwickelt. Für die spätere Anwendung ist es dringend erforderlich, dass ihre Wärmetransporteigenschaften genau bekannt sind. Aufgrund der kleinen Dimensionen der nanostrukturierten Materialien werden außerdem neue Charakterisierungsmethoden benötigt. In meiner Doktorarbeit präsentiere ich einen theoretischen und einen experimentellen Ansatz, um Wärmetransport in nanostrukturierten Materialien zu analysieren: die Finite-Elemente-Methode (FEM) und die Lock-in Thermografie (LIT). Mithilfe dieser beiden Methoden habe ich nanoskalige Wärmeübertragungsphänomene in zwei vielversprechenden dielektrischen Nanomaterialien untersucht: poröse kolloidale Assemblierungen und dicht-gepackte Bragg-Stapel. Beide Materialien können sehr einfach aus einer wässrigen Dispersion verarbeitet werden. Außerdem besitzen sie sehr kontrollierte strukturelle Eigenschaften. Dies ermöglichte es mir, die vorherrschenden Struktur-Eigenschaft-Beziehungen detailliert zu studieren.

Im ersten Teil meiner Arbeit habe ich die FEM verwendet, um Wärmetransport in kolloidalen Partikelassemblierungen theoretisch zu analysieren. Dabei unterstützte ich die experimentelle Charakterisierung dieser Materialien, die von zwei Kollegen mithilfe der Laser-Flash-Analyse (LFA) durchgeführt wurde. Zunächst zeigte ich mittels der FEM, dass die LFA auch bei nicht optimalen Bedingungen, wie sie zum Beispiel beim Messen von kolloidalen Assemblierungen auftreten können, zuverlässige Messergebnisse erlaubt. Dieses Ergebnis bestätigte, dass die Wärmetransporteigenschaften dieses Nanomaterials sehr präzise mit der LFA gemessen werden können. Anschließend simulierte ich den Wärmetransport in einer Vielzahl an kolloidalen Partikelassemblierungen.

Diese bestanden aus Silikahohlkugeln, Polystyrolpartikel und aus Mischungen von Silikahohlkugeln mit Latexpartikeln. Um die vorherrschenden Prozesse besser verstehen zu können, haben wir die Experimente und Simulationen unter Vakuumbedingungen durchgeführt. Dadurch identifizierten wir einige Stellschrauben, mit denen ein hochisolierendes Material hergestellt werden kann. Hier zu nennen ist die Geometrie selbst. Die Studien zeigten, dass Kolloidkristalle bestehend aus Silikahohlkugeln mit sehr dünnen Schalen die besten Wärmeisolationseigenschaften im Vergleich zu allen anderen getesteten Kolloidkristallen haben. Ein weiterer Parameter ist die interpartikuläre Bindungsstärke. Meine Simulationen bestätigten, dass eine Reduktion der interpartikulären Bindungsstärke zu einer signifikanten Verringerung der Wärmeleitfähigkeit der Partikelassemblierung führt. Letztlich spielt die Ordnung der Partikelassemblierung eine große Rolle. Wir zeigten, dass ungeordnete Strukturen generell bessere Wärmeisolationseigenschaften als geordnete Strukturen besitzen. Außerdem fanden wir heraus, dass durch das Mischen von unterschiedlich großen Polymerpartikeln in einem idealen Größen- und Mischverhältnis ungeordnete Strukturen mit einer deutlich niedrigeren Wärmeleitfähigkeit erhalten werden können. Neben Wärmeisolations-eigenschaften haben wir auch Perkolationseffekte in kolloidalen Partikelassemblierungen untersucht. Das Mischverhalten von gleich großen Silikahohlkugeln und Polymerpartikeln folgte jedoch nur dem Effektiv-Medium-Mischmodell. Ich zeigte anschließend, dass ein sehr großes Wärmeleitfähigkeits-verhältnis der beiden Partikeltypen notwendig ist, um tatsächlich Wärmeperkolationseffekte zu erhalten.

Im zweiten Teil meiner Doktorarbeit baute ich die Lock-in Thermografie auf und etablierte den Datenauswerteprozess. LIT erlaubt die Messung des lateralen Wärmetransports in dünnen Filmen oder auch Fasern. Unterstützt von numerischen Simulationen zeigte ich, dass sogar dünne, optisch semitransparente

Filme mit der bekannten Slopes-Methode ausgewertet werden können, obwohl diese ursprünglich für opake Proben entwickelt wurde. In Zusammenarbeit mit einem Kollegen, der die photoakustische Methode zur Bestimmung der Wärmeleitfähigkeit senkrecht zur Ebene anwendete, untersuchte ich die anisotrope Wärmeleitfähigkeit von nanostrukturierten, dünnen Filmen. Wir verglichen zuerst die Wärmeverteilungseigenschaften von optisch semi-transparenten Bragg-Stapel bestehend aus hochgeordneten Natriumfluorhectorit-Plättchen mit denen von Graphenoxid (GO). Wir ermittelten eine hohe Wärmeleitfähigkeit in der Ebene (5.7 $Wm^{-1}K^{-1}$) in Richtung der Schichtsilikatplättchen und eine niedrige Wärmeleitfähigkeit senkrecht zur Ebene (0.2 $Wm^{-1}K^{-1}$). Dies resultierte in einer vielversprechend hohen Wärmeleitfähigkeitsanisotropie von ≈30 für die synthetischen Schichtsilikate. Dieses Anisotropieverhältnis ist deutlich höher als das der GO-Proben. Anschließend studierten wir die anisotropen Wärmetransporteigenschaften von hybriden Bragg-Stapel, die aus abwechselnden Schichten von Natriumfluorhectorit und Polyvinylpyrrolidon hergestellt wurden. Ich zeigte, dass trotz der extremen Polymereinengung die Wärmeleitfähigkeit in der Ebene einem parallelen Mischmodell folgt und linear mit zunehmenden Schichtsilikatanteil von 0.2 $Wm^{-1}K^{-1}$ auf 5.7 $Wm^{-1}K^{-1}$ zunimmt. Die Einführung von Polymerschichten in den Bragg-Stapel führt zu einem starken Abfall der Wärmeleitfähigkeit senkrecht zur Ebene. Alle Hybridproben zeigen unabhängig von der Polymerschichtdicke einen sehr niedrigen Wert von 0.09 $Wm^{-1}K^{-1}$. Dies kann auf das Mischen von ungleichen Materialien und der damit verbundenen Einführung einer hohen Anzahl an hart-weich Grenzflächen zurückgeführt werden. Insgesamt ermittelten wir eine maximale Wärmeleitfähigkeitsanisotropie von 38. Dieser Wert ist relativ hoch für ein optisch transparentes Material.

Zusammengefasst zeigt diese Arbeit, dass die FEM und LIT zwei leistungsstarke Methoden sind, um Wärmetransport in nanostrukturierten Materialien zu untersuchen. Außerdem belegen meine Studien, dass maßgeschneiderte Nanostrukturierung den Zugang zu hochisolierenden Materialien und zu Materialien mit hohen anisotropen Wärmetransporteigenschaften ermöglicht.

List of Publications

Peer-Reviewed Publications Included in this Thesis:

1. Understanding Thermal Insulation in Porous, Particulate Materials.
   P. Ruckdeschel, **A. Philipp**, M. Retsch, *Advanced Functional Materials* **2017**, 27(38), 1702256.

2. Low Thermal Conductivity through Dense Particle Packings with Optimum Disorder.
   F. A. Nutz, **A. Philipp**, B. A. F. Kopera, M. Dulle, M. Retsch, *Advanced Materials* **2018**, 30(14), 1704910.

3. Thermal Transport in Binary Colloidal Glasses: Composition Dependence and Percolation Assessment.
   P. Ruckdeschel, **A. Philipp**, B. A. F. Kopera, F. Bitterlich, M. Dulle, N. W. Pech-May, M. Retsch, *Physical Review E* **2018**, 97(2), 022612.

4. Direct Measurement of the In-Plane Thermal Diffusivity of Semitransparent Thin Films by Lock-In Thermography: An Extension of the Slopes Method.
   A. Philipp, N. W. Pech-May, B. A. F. Kopera, A. M. Lechner, S. Rosenfeldt, M. Retsch, *Analytical Chemistry* **2019**, 91(13), 8476-8483.

5. The Accuracy of Laser Flash Analysis Explored by Finite Element Modeling and Numerical Fitting.
   A. Philipp, J. Eichinger, R. C. Aydin, A. Georgiadis, C. J. Cyron, M. Retsch, *Heat and Mass Transfer* **2020**, 56, 811-823.

6. Tunable Thermoelastic Anisotropy in Hybrid Bragg Stacks with Extreme Polymer Confinement.
   Z. Wang, K. Rolle, T. Schilling, P. Hummel, **A. Philipp**, B. A. F. Kopera, A. M. Lechner, M. Retsch, J. Breu, G. Fytas, *Angewandte Chemie International Edition* **2020**, 59(3), 1286-1294.

7. Anisotropic Thermal Transport in Spray-Coated Single-Phase Two-Dimensional Materials: Synthetic Clay vs. Graphene Oxide.
   A. Philipp, P. Hummel, T. Schilling, P. Feicht, S. Rosenfeldt, M. Ertl, M. Schöttle, A. M. Lechner, Z. Xu, C. Gao, J. Breu, M. Retsch, *ACS Applied Materials & Interfaces* **2020**, 12, 18785-18791.

Peer-Reviewed Publications not Included in this Thesis:

1. Mechanical Behaviour of Micro-Capsules and their Rupture under Compression.
   A. Ghaemi, **A. Philipp**, A. Bauer, K. Last, A. Fery, S. Gekle, *Chemical Engineering Science* **2016**, 142, 236-243.

2. On the Interplay of Shell Structure with Low- and High-Frequency Mechanics of Multifunctional Magnetic Microbubbles.
   M. Pöhlmann, D. Grishenkov, S. V. V. N. Kothapalli, J. Harmark, H. Hebert, **A. Philipp**, R. Hoeller, M. Seuss, C. Kuttner, S. Margheritelli, G. Paradossi, A. Fery, *Soft Matter* **2014**, 10(1), 214-226.

List of Contributions

1. Poster presentation: *Finite Element Modeling of Thermal Losses in Laser Flash Analysis,* Workshop Hot Nanostructures: Thermal Transport and Radiation at the Nanoscale, **2015**, Mainz (DE).

2. Poster presentation: *Finite Element Modeling of Thermal Transport in Colloidal Assemblies,* Conference of the European Colloid and Interface Society, **2017**, Madrid (ES).

3. Poster presentation: *Binary Colloidal Mixtures: Influence of the Order on the Thermal Conductivity,* Conference of the European Colloid and Interface Society, **2017**, Madrid (ES).

4. Poster presentation: *Thermal Conductivity of Polymeric Colloidal Assemblies: Experiment and Simulation,* Particle-Based Materials Symposium, **2017**, Saarbrücken (DE). **3rd poster prize for my poster presentation.**

Abbreviations and Symbols

AC	alternating current
ATR	attenuated total reflection
AMM	acoustic mismatch model
CC	colloidal crystal
DMM	diffuse mismatch model
EOM	electro-optic modulator
EM	electromagnetic
FEM	finite element method
fcc	face-centered cubic
GO	graphene oxide
HSNP	hollow silica nanoparticle
IR	infrared
LDPE	low-density polyethylene
LIT	lock-in thermography
LW	long-wave
MD	molecular dynamics
MFP	mean free path
MMA	methyl methacrylate
MW	mid-wave
NaHec	sodium hectorite
n-BA	*n*-butyl methacrylate
PEEK	polyether ether ketone
PR	phenol red
PS	polystyrene
PVP	polyvinylpyrrolidone
PMMA	poly(methyl methacrylate)
RT	room temperature
SiO_2	silica
SW	short-wave
THF	tetrahydrofuran
UV-vis	ultraviolet-visible
XFA	xenon flash analysis
1D	one-dimensional
2D	two-dimensional
3D	three-dimensional

A	(cross-sectional) area
c	specific heat capacity/ speed of light
d	pore size
D	diameter/ thermal diffusivity

f	frequency
F	view factor/ incoming frames
h	heat transfer coefficient/ cube edge length/ Planck constant
k_{B}	Boltzmann constant
K	weighting factor
Kn	Knudsen number
l	collision diameter of gas molecule/ sample thickness
m	slope
M	emissive power
M_{λ}	spectral specific irradiation
n	number of frames per lock-in period/ exponent of heat propagation dimensionality
N	number of lock-in periods
P	gas pressure
q	heat flux density
Q	heat flux/heat flow rate
r	radius/ radial distance
S	output signal
T	amplitude of lock-in signal/ temperature
ΔT	temperature difference
∇T	temperature gradient vector field
T_{g}	glass transition temperature
v	velocity
$[K]$	global matrix
$\{f\}$	global load vector
$\{u\}$	global unknown vector

α	absorption coefficient/ thermal diffusivity
β	energy transfer parameter
ε	correction factor
θ_{D}	Debye temperature
κ	thermal conductivity
λ	wavelength
Λ	mean free path
μ	thermal diffusion length
υ	frequency
ρ	density/ reflection coefficient
σ	Stefan-Boltzmann constant
τ	transmission coefficient
φ	volume fraction
Ψ	phase shift of lock-in signal

1. Motivation

Thermal transport is a ubiquitous phenomenon which even plays an important role in everyday life, for example for clothing, cooking, and heating. However, heat management is also crucial for technological materials, such as thermal interface, electronic packaging, and thermal insulation materials. The latter are used for steady-state thermal insulation like building insulation and for non-steady-state thermal insulation like fire protection and refrigeration.[1-2] Electrically insulated thermal interface materials are used to prevent the formation of hotspots and thus to increase the life time and reliability of electronic materials.[3-4] A current example of the use of heat spreading materials is E-mobility. Here, the cooling of the battery by dissipating excess heat to a heat sink while preventing the neighboring electronic parts from heat is the key task to significantly increase the lifetime of the battery cells.

The ongoing miniaturization of, for example, electronic devices led to an increased interest in nanostructured materials for thermal transport applications. Overall, two phenomenological properties are especially important for the application of nanostructured materials: thermal insulation (*i.e.*, a low thermal conductivity) and heat dissipation (*i.e.*, a high thermal conductivity) as wells as the combination of both in form of materials with directional thermal conductivity. Furthermore, nanostructured materials are important, since the thermal conductivity can be tailored by its nano-, meso-, or microstructure. Porous, nanostructured materials[5-8] and fully dense, nanostructured materials[9-14] are efficient candidates for thermal insulation and heat dissipation, respectively. Promising porous materials are colloidal assemblies since they represent an ideal model system to study thermal transport in particulate materials. Exemplary effects which have already been studied are the influence of the geometrical constrictions of the interparticle contact points, and the material of the particles[15-17]. Besides the introduction of porosity and, therefore, of a high volume fraction of a gaseous phase[18], an

increased interface density on small length scales in fully dense materials lowers also the thermal conductivity. Prominent examples are thin, layered structures[9-10] which inherently exhibit structural anisotropy and consequently possess an anisotropic thermal conductivity.

Two powerful methods to investigate these nanostructured materials are the finite element method (FEM) and lock-in thermography (LIT). The great advantage of the FEM is that thermal transport phenomena can be studied which are not or only hardly accessible by experiments. In addition, a deeper understanding of underlying effects can be achieved. Finally, FEM studies save resources and in most cases time. LIT, on the other hand, is a versatile experimental method to determine the in-plane thermal transport properties of thin, free-standing samples[19-23]. Advantages of this method are its non-contact and non-invasive material characterization, the relatively simple measurement set-up and data evaluation, and small sample sizes (dependent on the thermal properties) in contrast to steady-state methods.

In this work, these two methods are applied to investigate thermal transport in well-defined, nanostructured materials. In the first part of this thesis, the FEM is established and used to quantify the accuracy of the laser flash analysis (LFA) technique. Then, the FEM in combination with experimental studies based on the LFA is conducted to investigate heat transport through colloidal assemblies. In the second part of this thesis, the accuracy of a home-built LIT set-up is demonstrated. Furthermore, its application is extended to semitransparent thin films. Then, single-phase and hybrid, layered films are studied with regard to their anisotropic thermal transport properties. In all studies, the governing structure-property relationships are clarified.

2. Theoretical Overview

2.1. Thermal Transport in Dielectric Materials

2.1.1. Macroscopic Heat Transfer Modes

Heat is a form of energy transferred between two systems due to a temperature difference. In line with the second law of thermodynamics, heat always flows from hot areas to cold ones. Heat transfer is usually divided into three modes: heat conduction, heat convection, and thermal radiation.[24-25]

(1) *Heat Conduction*

The mode of heat transfer in static materials (solids or static fluids) is referred to as heat conduction. Steady-state heat conduction is analytically described by Fourier's law. The one-dimensional (1D) equation reads as follows:[24]

$$q = -\kappa \frac{dT}{dx} \tag{1}$$

Here, q is the heat flux density ([Wm^{-2}]), *i.e.*, the heat transfer rate Q per unit area A normal to the direction of heat flow, $-\frac{dT}{dx}$ is the negative temperature gradient along the x-direction. The thermal conductivity κ ([$Wm^{-1}K^{-1}$]) is the most important quantity of steady-state heat conduction. κ is a measure of how much energy is transferred through a material per unit time due to a steady-state temperature gradient. The three-dimensional (3D) form is given by:[24]

$$\vec{q} = -\kappa \nabla T \tag{2}$$

Here, $\vec{q}$ is the heat flux vector, ∇T the 3D temperature gradient vector field.

By combining Equation (1) and the first law of thermodynamics (conservation of energy), the 1D heat diffusion equation to describe transient heat conduction is obtained:[24]

$$\frac{\partial^2 T}{\partial x^2} = \frac{1}{\alpha}\frac{\partial T}{\partial t} \tag{3}$$

T is the temperature distribution $T(x,t)$, and t is the time. In the transient case, the thermal diffusivity α ([m^2s^{-1}]) is the decisive property. α is a measure of how fast energy is transferred through a material. The thermal diffusivity depends on the material's thermal conductivity, specific heat capacity c, and density ρ:

$$\alpha = \frac{\kappa}{c \cdot \rho} \tag{4}$$

(2) *Heat Convection*

Heat convection is defined as the transfer of heat by a moving fluid.[24] Although conduction and convection are usually considered separately, convective heat transfer occurs only together with conduction.[26]

There are two different kinds of convection: natural convection and forced convection. Natural convection is the movement of fluid molecules induced by a temperature gradient. The temperature gradient causes a density gradient in the fluid. Forced convection arises from the forced movement of fluid molecules by an external force, *e.g.*, a pump or a fan.[27]

The cooling of a solid body through convection can be expressed by Newton's law (steady-state form):

$$q = \bar{h}\left(T_{\mathrm{body}} - T_{\infty}\right), \tag{5}$$

where T_{body} is the surface temperature of the body, T_{∞} the temperature of the fluid far away from the surface, and $\bar{h}$ the heat transfer coefficient averaged over the surface of the body ([$Wm^{-2}K^{-1}$]).[24-25]

The heat transfer coefficient depends on the properties of the fluid, the flow field, and the geometry of the body. Usually, h is extracted from experiments or numerical simulations.[27] Furthermore, the heat transfer coefficient can vary with the temperature difference ($\Delta T = T_{\mathrm{body}} - T_{\infty}$), especially in the case of natural convection. If forced convection (*i.e.*, a small ΔT) is present, the coefficient is independent of the temperature difference.[24]

(3) *Thermal Radiation*

Thermal radiation is the emission of electromagnetic (EM) radiation in the infrared (IR) spectral range of 0.78 – 1000 μm. Each body with a temperature above absolute zero (> 0 K) emits energy in the form of EM waves. The EM waves lie in case of natural and technological processes in the IR wavelength region.[28-29] Convection and conduction are often the predominant heat transfer modes. Nevertheless, thermal radiation plays a significant role at high temperatures and in vacuum.[24]

The radiation heat flux density between body 1 and body 2 is given by

$$q = \sigma(T_1^4 - T_2^4), \tag{6}$$

where σ is the Stefan-Boltzmann constant ($5.670 \cdot 10^{-8}$ $Wm^{-2}K^{-4}$), T_1 and T_2 the temperatures of body 1 and 2, respectively.[27]

Equation (6) is only valid if thermal energy is solely exchanged radiatively between body 1 and 2. Furthermore, both bodies are treated as black bodies. A black body transmits or reflects no EM radiation independent of the wavelength. Thus, it is an ideal absorber and thermal radiator. However, real bodies radiate less than a black body. This influence is considered by introducing the so-called view factor F_{1-2}:

$$q = F_{1-2}\sigma(T_1^4 - T_2^4) \tag{7}$$

F_{1-2} corrects additionally for radiative influences of other objects.[24]

2.1.2. Microscopic Heat Conduction in Solids

In dielectric materials, thermal energy is carried from one area to another through the coupled vibration of atoms. In Figure 1a, the well-known mass-spring model for a crystalline material is shown. Here, each atom is interconnected via a spring. Due to the interatomic interactions, vibrations of an atom result in lattice waves in the whole system. The lattice vibrational energy is discrete and a multiple of $h\upsilon$, where h is Planck's constant ($6.626 \cdot 10^{-34}$ Js) and υ the frequency of the lattice wave. A phonon is the quantized energy of the collective lattice vibration ($h\upsilon$). Phonon wave packets, *i.e.*, the superposition of phonons of multiple frequencies,

can be treated as quasi-particles if the wave packets are much smaller than the crystal size. Thus, instead of the mass-spring system, the phonon gas model can be used (Figure 1b). The phonon gas model treats the heat transport through phonons as equivalent to the transport through gas molecules.[27]

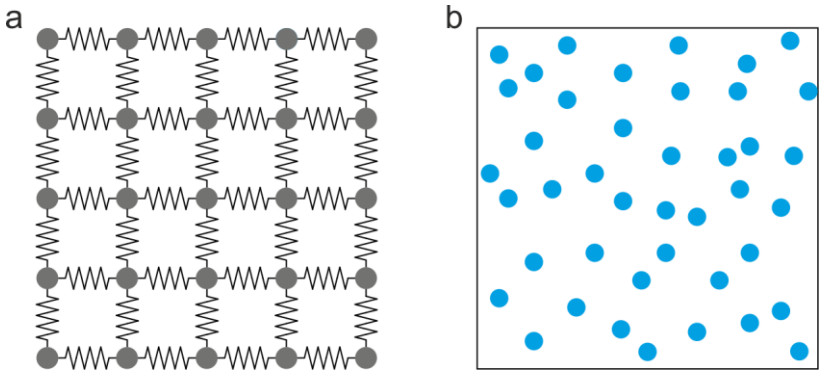

Figure 1. a) Mass-spring system: atoms in a crystal interconnected via springs. b) Phonon gas model: mass-spring system is replaced by a box of phonon particles. Adapted from Chen.[27]

Based on the quasi-particle concept and kinetic theory, the thermal conductivity κ of a dielectric solid can be expressed by the Debye equation:

$$\kappa = \frac{1}{3} c_v v \Lambda \tag{8}$$

Here c_v is the volumetric specific heat at constant volume, v the average random phonon velocity, and Λ the average phonon mean free path.[27]

The mean free path (MFP) is the average distance a phonon travels freely until scattering occurs. The phonon MFP of dielectric solids lies in the range of 0.3 nm to 1 μm.[25] The phonon MFP depends not only on the material, but also on the temperature and scattering processes. In general, the MFP is large at low temperatures and decreases with increasing temperature.[30]

The different phonon scattering mechanism in a dielectric, crystalline solid are schematically depicted in Figure 2: phonon-boundary, phonon-imperfection, phonon-impurity, phonon-grain boundary, and phonon-phonon scattering. Depending on the temperature, either phonon-boundary scattering, defect scattering (includes imperfection, impurity, and grain boundary scattering), or

phonon-phonon scattering is the prevailing process that determines the MFP and therefore the thermal conductivity.[25, 31]

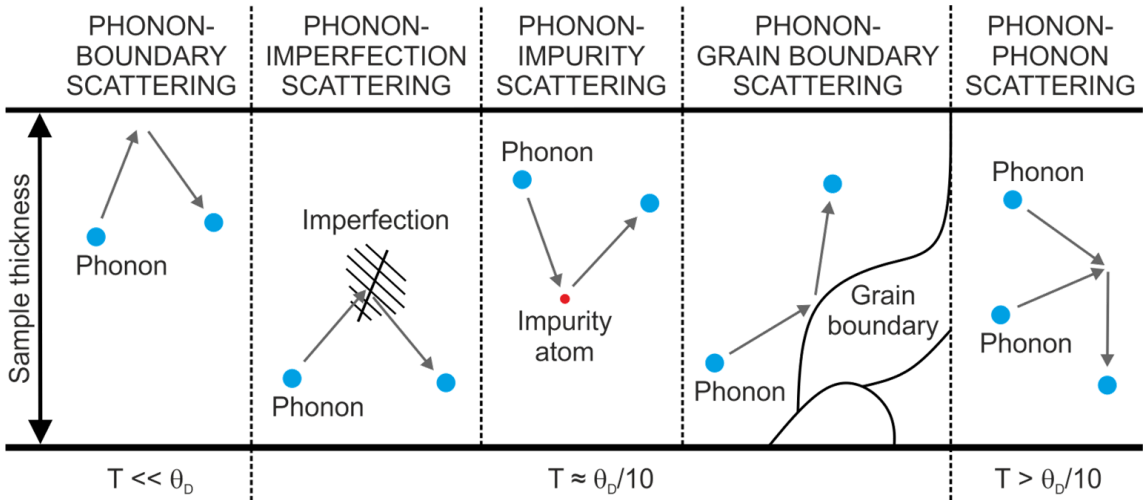

Figure 2. Phonon scattering mechanisms in dielectric, crystalline solids: Phonon-boundary scattering, phonon-imperfection scattering, phonon-impurity scattering, phonon-grain boundary scattering, and phonon-phonon scattering. At temperatures below the Debye temperature (θ_D), phonon-boundary scattering plays a dominant role, at a temperature around $\theta_D/10$, defect scattering is important, whereas at temperatures above $\theta_D/10$, phonon-phonon scattering prevails. Adapted from Asheghi.[31]

The thermal conductivity of a crystalline, dielectric solid shows the following temperature-dependent behavior:

At temperatures far below the Debye temperature θ_D, the thermal conductivity is proportional to T^3. θ_D is a material-specific temperature which depends on the chemical bond strength and the mass of the atoms. The T^3 increase arise from the heat capacity, which follows as $c_v \propto T^3$.[25, 32-34] The wavelengths of the phonons at these temperatures are very large. Thus, the MFP is only limited by phonon-boundary scattering due to a finite size of the sample (Figure 2, $T \ll \theta_D$).[35] Boundary scattering results in a reduced thermal conductivity. At a temperature around $\theta_D/10$, the thermal conductivity reaches a maximum. Here, the phonon wavelength is comparable to the separation distance between two defects. Thus, phonons are scattered on defects, such as imperfections, impurities, and grain boundaries (Figure 2, $T \approx \theta_D/10$). Due to the reduction of the MFP, the thermal conductivity decreases with increasing defect density.[31, 35-38] If the sample is

significantly thinner than bulk, the position of the maximum shifts with decreasing film thickness to higher temperatures.[30] At temperatures above $\theta_D/10$, the thermal conductivity of a dielectric crystal drops due to two effects: First, with increasing temperatures, the rise of the volumetric specific heat deviates from the T^3 relation and approaches a constant value at high temperatures. Second, phonon-phonon scattering (Figure 2, $T > \theta_D/10$), more precisely Umklapp scattering, prevails at high temperatures leading to a reduced phonon MFP. In general, phonon-phonon scattering occurs from the anharmonicity of the atomic interactions. During an Umklapp process, the phonon energy is conserved, but the momentum of the phonons changes. Umklapp scattering is highly temperature dependent and the probability increases exponentially with temperature. If Umklapp scattering is the dominant process, the thermal conductivity decreases as T^{-1}.[25, 39] Finally, at very high temperatures, the thermal conductivity reaches a plateau.

The temperature-dependent thermal conductivity of amorphous, dielectric solids behaves completely different as for crystalline materials. However, there is also a general trend of the temperature dependence for amorphous solids.[40] At low temperatures, the thermal conductivity scales with T^n, where n is $1.8 - 2$ depending on the chemical composition. Between ~5 - 30 K, the thermal conductivity stays almost constant. Then, it increases again, but monotonically with temperature. Furthermore, at each temperature, the thermal conductivity of an amorphous solid is significantly lower compared to its crystalline counterpart (*e.g.*, amorphous *vs.* crystalline silica).[41-44]

In addition, due to the disordered structure of amorphous materials, the concept of phonons is not fully applicable.[45] Instead, Allen and Feldman[46-47] developed the model of vibrons to describe the transport of thermal energy through vibrations in an amorphous material. The classification of vibrons is depicted in Figure 3. The vibrational modes in an amorphous solid are divided into extendons and locons. Locons are localized, non-propagating vibrational modes.[47] It has been shown that

they do not transfer heat but affect the specific heat capacity.[48] Extendons, on the other hand, are extended, *i.e.*, delocalized, modes and contribute to the thermal transport. Extendons can be subdivided into delocalized, propagating modes (propagons) and delocalized, non-propagating modes (diffusons). Propagons show phonon-like propagation and have an MFP of a few interatomic spacings. They are responsible for the thermal conductivity increase of amorphous solids at low temperatures (T^n, $n = 1.8 - 2$). Diffusons show diffusive transport and propagate only across small distances.[46]

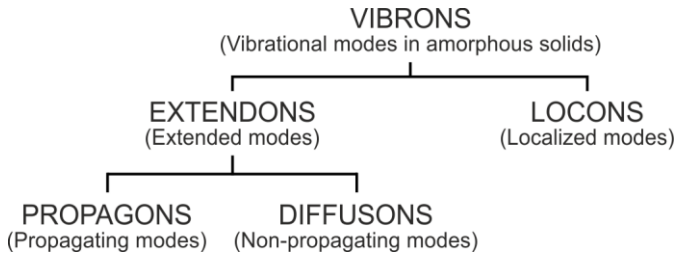

Figure 3. Concept of vibrons in amorphous solids and its classification in extendons (propagons and diffusons) and locons. Adapted from Allen *et al*.[47]

Although the microscopic structure of a polymer deviates from other solids, amorphous polymers exhibit a similar temperature-dependent thermal conductivity behavior as described above for amorphous solids.[49] At low temperatures, the thermal conductivity exhibits a T^2 dependence, stays constant between 5 – 15 K, and rises again but more slowly with increasing temperature. Above 60 K, the thermal conductivity increases proportionally to the specific heat.[50] Due to the random-coiled and entangled polymer chains, the propagation of vibrational waves through an amorphous polymer is considerably hindered by detours.[49] Furthermore, on the basis of the phonon model, several scattering events are present: structural scattering, intramolecular scattering, intermolecular scattering, and boundary scattering. Structural scattering arises from the random curvilinear shape of the polymer chains.[51] It is the main reason for the low MFP of < 10 nm and thus for the low thermal conductivity (0.1 – 1.0 $Wm^{-1}K^{-1}$). However, boundary scattering, *i.e.*, scattering at the end of a polymer chain, also affects the

thermal conductivity. Shorter polymer chains lead to a reduction in the thermal conductivity.[49-50, 52]

Semi-crystalline polymers consist of amorphous and crystalline regions. In the crystalline regions, the polymer chains are highly ordered and densely packed. Consequently, the propagation of vibrations along an extended polymer chain is less hindered than in amorphous regions. Furthermore, heat conduction is more efficient along the aligned polymer chains than perpendicular to them (weak interactions instead of covalent bondings).[49-50] Owing to the crystalline regions, semi-crystalline polymers have higher thermal conductivities at moderate temperatures as amorphous polymers. Furthermore, they show a different thermal conductivity *vs.* temperature dependence. Up to a temperature of around 20 K, the thermal conductivity of semi-crystalline polymers follows a T^n dependence, where n is $1-3$. Then, the thermal conductivity typically rises more slowly up to the respective glass transition. However, the thermal conductivity of highly crystalline polymers rises up to 100 K, and then decreases slightly with temperature.[50]

2.1.3. Heat Transfer in Nanostructured Materials

In this thesis, I investigate the heat transfer in two different kinds of dielectric, nanostructured materials: three-dimensional colloidal assemblies and layered, two-dimensional nanomaterials. This chapter covers the basics of thermal transport in these two material classes.

(1) *Three-Dimensional Colloidal Assemblies*

Three-dimensional (3D) colloidal assemblies comprise colloidal building blocks (*i.e.*, particles with sizes from several nm to μm) which are organized in a 3D structure.[53] Here, the focus lies on the thermal transport through colloidal assemblies made of dielectric, spherical particles with monodisperse sizes.

Due to the porous structure, gas in the pores contributes to the total thermal transport through colloidal assemblies. However, the contribution of convection becomes only relevant when pores exceed a size of 4 mm.[54] The radiative conductivity κ_{rad} is proportional to the temperature to the power of three and to the inverse density of the assembly ($\kappa_{\mathrm{rad}} \propto T^3 \rho^{-1}$). Furthermore, it depends on the absorbance of thermal radiation of the used material.[55-56] Altogether, thermal radiation can usually be neglected, since colloidal assemblies have a rather high density and the used materials a strong infrared absorbance. Consequently, the effective thermal conductivity κ_{eff} of a colloidal assembly is given by:

$$\kappa_{\mathrm{eff}} = \kappa_{\mathrm{cond,solid}} + \kappa_{\mathrm{cond,gas}} \tag{9}$$

Thus, the thermal conductivity of a colloidal assembly depends only on heat conduction of the solid material ($\kappa_{\mathrm{cond,solid}}$) and the gaseous phase ($\kappa_{\mathrm{cond,gas}}$).
The bulk gas thermal conductivity can be expressed by the kinetic gas theory:

$$\kappa_{\mathrm{gas,bulk}} = \frac{1}{3} c_{\mathrm{v}} \upsilon \Lambda_{\mathrm{gas}} \varepsilon \tag{10}$$

Here, c_{v} is the volumetric specific heat of the gas, υ the gas root mean square velocity, and ε is the correction factor of the kinetic theory expression for viscosity and thermal conductivity. Exemplary values for ε are 2.50 for noble gases, 1.47 for hydrogen gas (H_2), and 1.95 for nitrogen gas (N_2).[8, 57] The bulk MFP of a gas molecule Λ_{gas} (*i.e.*, the average travelling distance of a gas molecule until it is scattered) is

$$\Lambda_{\mathrm{gas}} = \frac{k_{\mathrm{B}} T}{\sqrt{2} \pi P l^2}, \tag{11}$$

where k_{B} is the Boltzmann constant ($1.380 \cdot 10^{-23}$ JK^{-1}), T the temperature, P the gas pressure, and l the collision diameter of the gas molecule.[57] Under ambient conditions, the MFP of gases lies in the range of several tens to hundred nm (*e.g.*, ~70 nm in air, ~200 nm in helium).[58] In a free gas, the gas thermal conductivity is independent of the gas pressure.[8]

However, in a colloidal assembly the MFP is limited by the pore size which is in the nanometer range. The Knudsen number Kn is the ratio of the bulk gas MFP and the characteristic pore size d:[59]

$$Kn = \frac{\Lambda_{\text{gas}}}{d} \tag{12}$$

If $Kn > 1$, *i.e.*, d is smaller than Λ_{gas}, the mean free path of the gas molecules is affected by the confinement due to molecule-interface collisions. The gas thermal conductivity in confined space $\kappa_{\text{gas,conf}}$ is given by:[8, 60]

$$\kappa_{\text{gas,conf}} = \frac{\kappa_{\text{gas,bulk}}}{1 + Kn} = \frac{c_{\text{v}} v \varepsilon}{3} \left(\frac{\sqrt{2}\pi P l^2}{k_{\text{B}} T} + \frac{1}{d} \right)^{-1} \tag{13}$$

Thus, the thermal conductivity depends strongly on the gas pressure and the pore size, as exemplarily shown in Figure 4 for helium gas. In confined space, $\kappa_{\text{gas,conf}}$ decreases with decreasing gas pressure (Figure 4a). Furthermore, the onset of the thermal conductivity decrease depends on the pore size. The smaller the pores, the lower the gas thermal conductivity at ambient pressure (Figure 4b).

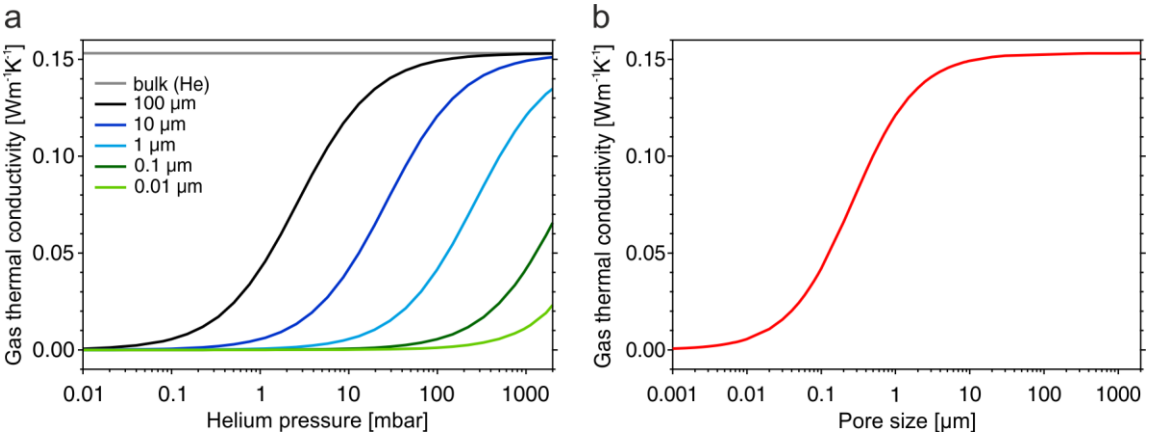

Figure 4. a) Dependency of the thermal conductivity of helium on the pressure and pore size (100 – 0.01 µm). b) Influence of the pore size on the thermal conductivity of helium at ambient pressure of 1000 mbar. The curves were calculated according to Equation (13).

To calculate κ_{eff} of the assembly according to Equation (9), the porosity Π of the porous structure (*i.e.*, the ratio of the pore volume to the total sample volume) has to be taken into account. Furthermore, the parameter β is introduced, which considers the energy transfer through collisions between the gas molecules and the

solid phase.[60] Typical values lie between 1.5 and 2.[61] The gas thermal conductivity $\kappa_{\mathrm{cond,gas}}$ writes as follows:

$$\kappa_{\mathrm{cond,gas}} = \frac{\kappa_{\mathrm{gas,bulk}} \cdot \Pi}{1 + 2\beta \cdot Kn} \tag{14}$$

Colloidal assemblies represent a versatile model system to study heat transfer in nanostructured materials. There are several parameters which can be varied to tune the thermal conductivity of the solid material in vacuum ($\kappa_{\mathrm{cond,solid}}$):

- Material of the particles (*e.g.*, polymers or silica)
- Material composition of the assembly (one material or mixture)
- Particle geometry (full sphere, hollow sphere, or core-shell particle)
- Symmetry of the assembly (ordered or disordered)
- Interface properties (interface density, thermal boundary conductance, contact resistance, …)

Some exemplary studies on the thermal conductivity of 3D colloidal assemblies will be discussed in the following.

The thermal transport properties of polystyrene (PS) colloidal crystals (CCs) have been investigated by Nutz *et al.*[16] (Figure 5a). The CCs exhibited a thermal conductivity of 0.051 $\mathrm{Wm^{-1}K^{-1}}$ in vacuum and room temperature (RT). This value is relatively low for a material of low porosity (~ 74 %) and rather high density (750 $\mathrm{kgm^{-3}}$). Upon heating above the glass transition temperature T_{g}, $\kappa_{\mathrm{cond,solid}}$ increased significantly, as demonstrated in Figure 5b. This was due to the loss of the colloidal microstructure, *i.e.*, an enlargement of the interparticle contact points, and an increase of the density. After heating, a non-reversible thermal conductivity in the range of bulk PS was obtained. Furthermore, κ_{eff} of the open-porous material was only slightly affected by the surrounding atmosphere due to the low porosity and small pore sizes (~ 100 nm).

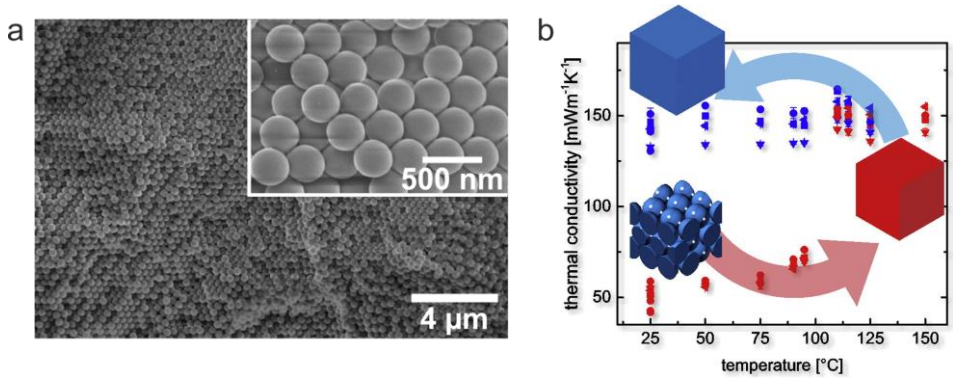

Figure 5. a) Side-view scanning electron microscope images of a three-dimensional polystyrene colloidal crystal. b) Temperature-dependent thermal conductivity of the colloidal crystal. Adapted from Nutz *et al*.[16] with the permission of Elsevier.

In further thermal transport studies on CCs, Nutz and Retsch used copolymer particles consisting of *n*-butyl methacrylate (*n*-BA) and methyl methacrylate (MMA).[15, 62] By varying the *n*-BA content, the T_g of the copolymer changed. This offered Nutz *et al*. great flexibility to tune the temperature-dependent thermal conductivity of the CCs, as summarized schematically in Figure 6.[62]

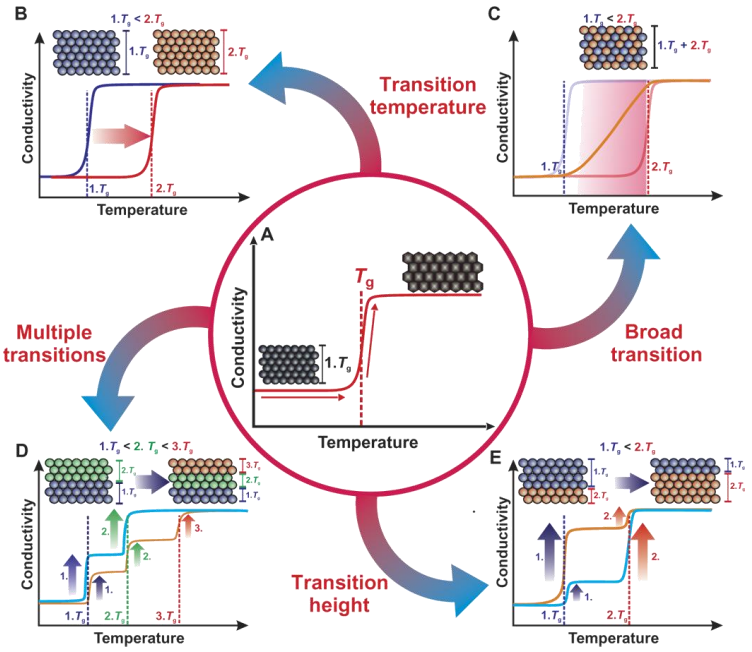

Figure 6. Tailor-made temperature-dependent thermal conductivity of colloidal crystals consisting of *n*-butyl methacrylate-*co*-methyl methacrylate particles. By heating upon the glass transition T_g, the thermal conductivity rises due to the enlargements of contact points (A). Four aspects can be varied using particles having different T_gs or by mixing particles having different T_gs: transition temperature (B), transition width (C), transition number (D), and transition height (E). Reprinted from Nutz et al.[62] with the permission of American Association for the Advancement of Science (http://creativecommons.org/licenses/by-nc/4.0/).

Ruckdeschel *et al.* explored the role of the microstructure and interparticle contact points of hollow silica nanoparticle (HSNP) CCs. 3D monoliths were prepared in two different ways. First, the CCs were calcined at different temperatures after self-assembly of the particles (solid symbols in Figure 7a). Second, core-shell particles were calcined at 950 °C, self-assembled into CCs, and then annealed at different temperatures (open symbols in Figure 7a). As depicted in the inset of Figure 7a, $\kappa_{\mathrm{cond,solid}}$ increases with higher calcination/annealing temperature. This increase could be related, on the one hand, to a decrease in the BET surface area (Figure 7a, solid symbols). The corresponding changes in the internal structure of the HSNPs are schematically shown in Figure 7b, I *vs.* III. Upon high temperature calcination, the microporosity and surface area of the shell decreased, whereas the rigidity increased. Furthermore, the calcination of the CCs led to higher interfacial adhesion. On the other hand, the increase of $\kappa_{\mathrm{cond,solid}}$ with annealing temperature (Figure 7b, open symbols) was only attributed to a higher interfacial adhesion between the particles (Figure 7b, II *vs.* III). Within their study, Ruckdeschel *et al.* found a remarkable low $\kappa_{\mathrm{cond,solid}}$ of 0.071 $Wm^{-1}K^{-1}$ for an inorganic, rather dense (1.04 kgm^{-3}) material.

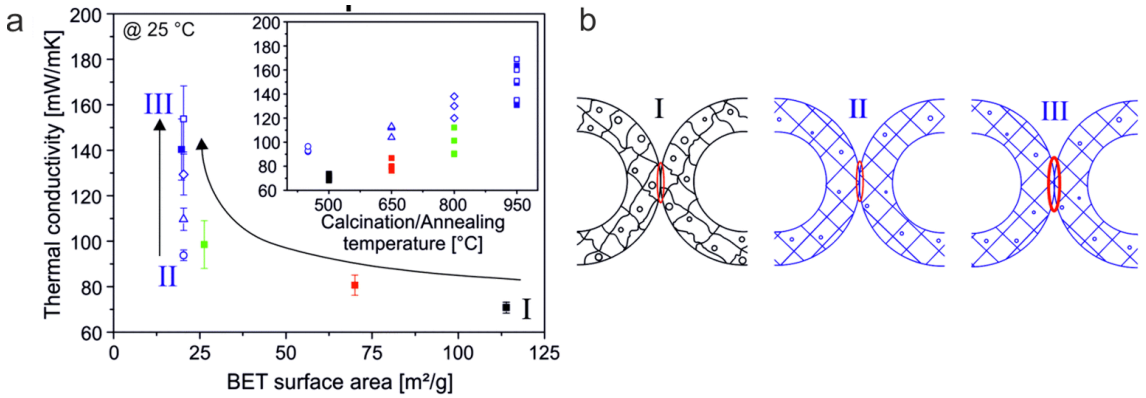

Figure 7. a) Thermal conductivity of hollow silica nanoparticle (HSNP) colloidal crystals (CCs) in dependence of the BET surface area and calcination/annealing temperature (inset). Closed symbols represent calcined HSNP CCs, open symbols annealed HSNP CCs. b) Schematic illustration of the corresponding internal structure and interfacial adhesion within a CC. Adapted from Ruckdeschel *et al.*[17] with the permission of Royal Society of Chemistry (https://creativecommons.org/licenses/by/3.0/).

Furthermore, the thermal conductivity of CCs made from core-shell nanoparticles has been investigated by Ruckdeschel and Retsch.[63] PS-silica/core-shell particles with varying size but constant shell thickness (15 nm), and particles with varying shell thickness but constant size (265 nm) were synthesized. The morphology has a high impact on $\kappa_{cond,solid}$ which increases from 0.044 to 0.091 $Wm^{-1}K^{-1}$ with higher silica amount (Figure 8b, solid squares). Heating up to 200 °C led to PS leakage through 15 nm silica shells (Figure 8a). The leakage led to improved interparticle contact points and, thus, to a higher $\kappa_{cond,solid}$ (Figure 8b, open squares). The influence of helium gas on the thermal transport properties is depicted in Figure 8c. As expected, the total thermal conductivity of the CCs was higher in helium than under vacuum conditions. Furthermore, the difference was more pronounced for large particles, since larger pore sizes are present.

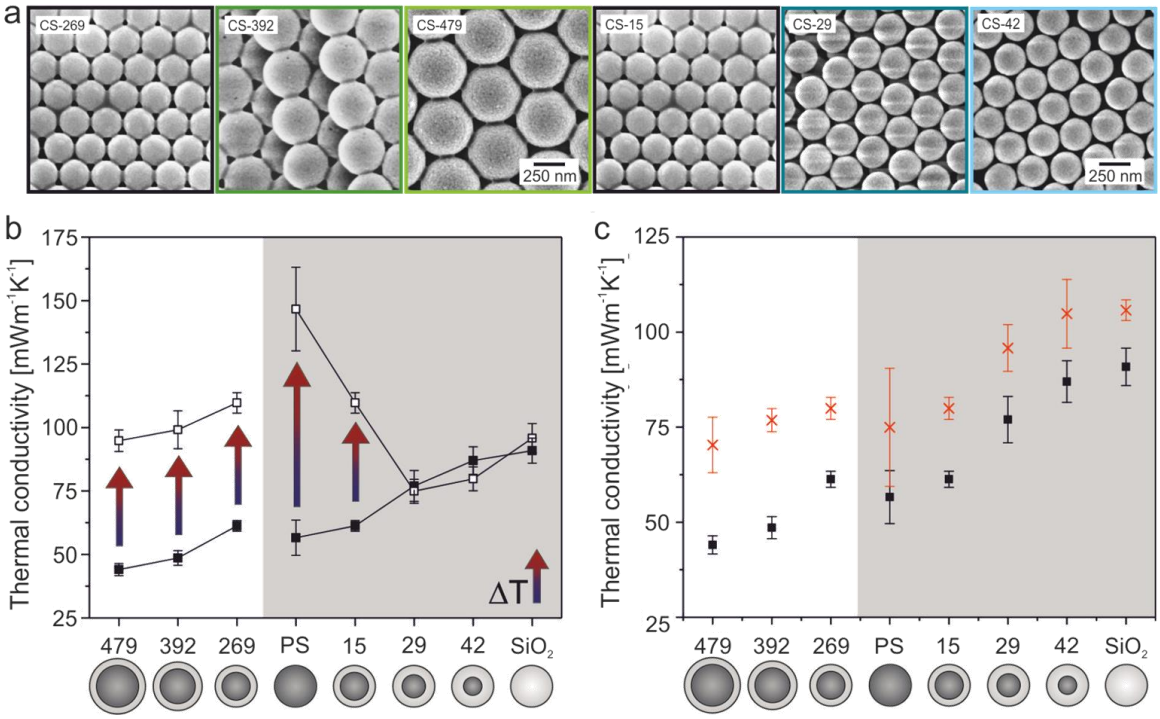

Figure 8. a) Scanning electron images of the polystyrene (PS)-silica/core-shell particles after heating up to 200 °C. b) Thermal conductivity of the core-shell, PS, and silica colloidal crystals before (solid squares) and after heating up to 200 °C (open squares). Measurements were conducted in vacuum. Particles with varying sizes (left side) have a comparable shell thickness of 15 nm, particles with varying shell thicknesses (right side) have a comparable size of 265 nm. c) Thermal conductivity of the core-shell, PS, and silica colloidal crystals before heating measured in vacuum (solid squares) and in helium at 1000 mbar (crosses). Adapted from Ruckdeschel and Retsch[63] with the permission of WILEY-VCH Verlag GmbH & Co. KGaA, Weinheim.

(2) *Layered, Two-Dimensional Nanomaterials*

Layered nanomaterials consist of multiple layers, each of them with a thickness on the nanoscale.[10] In this thesis, the focus lies on two-dimensional (2D), layered nanomaterials where the total thickness of the nanoscale multilayer is significantly smaller than the other two dimensions. Furthermore, the investigated nanomaterials are made either from one material which inherently has a layered structure (*e.g.*, clays) or from two alternating materials to obtain a layered structure.

A layered film consisting of two components is schematically depicted in Figure 9a. Since layered nanomaterials are fully dense materials, solid conduction is the predominating heat transfer mode. Furthermore, due to the layered structure, nanolaminates typically exhibit a strong thermal conductivity anisotropy. As illustrated in Figure 9a, the cross-plane thermal conductivity, $\kappa_{\text{cross-plane}}$ or $\kappa_{\perp}$, is defined as the effective thermal conductivity normal to the layers, whereas the in-plane thermal conductivity, $\kappa_{\text{in-plane}}$ or $\kappa_{\parallel}$, represents the effective thermal conductivity parallel to the layers.

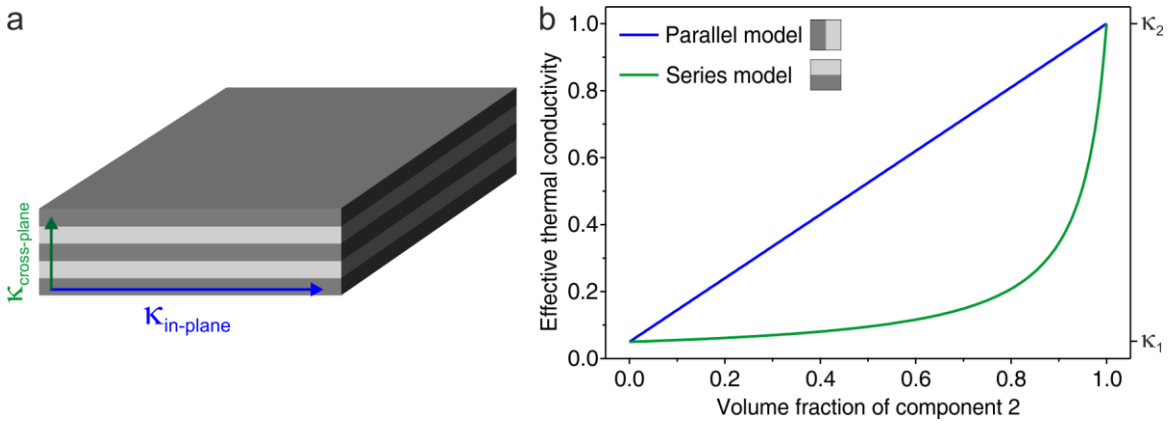

Figure 9. a) Schematic depiction of a layered nanomaterials consisting of two alternating components. The cross-plane thermal conductivity $\kappa_{\text{cross-plane}}$ characterizes heat conduction normal to the layers, whereas the in-plane thermal conductivity $\kappa_{\text{in-plane}}$ characterizes heat conduction parallel to the layers. b) Effective thermal conductivity of a two-component system described by the parallel model and series model.

There are several mixing models to calculate the effective thermal conductivity of heterogeneous, two-component materials. The parallel and series models describe

the effective thermal conductivity of a material where the two components are arranged parallel to each other (Figure 9b). In case of the parallel model, the heat flows only parallel to the layers. The effective thermal conductivity κ_{eff} is defined as:

$$\kappa_{\text{eff,parallel}} = (1 - \varphi_2)\kappa_1 + \varphi_2\kappa_2 \tag{15}$$

On the contrary, the series model considers heat flow normal to the layers:

$$\kappa_{\text{eff,series}} = \frac{1}{(1 - \varphi_2)/\kappa_1 + \varphi_2/\kappa_2}, \tag{16}$$

where φ_2 is the volume fraction of component 2, κ_1 and κ_2 are the thermal conductivities of component 1 and 2, respectively.[64]

Those two macroscopic mixing models do not consider any interface effects, such as thermal contact resistance or thermal boundary resistance. In case of in-plane thermal transport, interface effects play not a major role since heat flows parallel to the boundaries. Thus, the parallel model can represent a simple model to predict $\kappa_{\text{in-plane}}$ of layered nanomaterials, provided that the respective in-plane thermal conductivities of the two components are used for κ_1 and κ_2 in Equation (15). However, cross-plane thermal transport in a layered structure is strongly affected by the interfaces due to the high interface density in direction of the heat flow. Consequently, $\kappa_{\text{cross-plane}}$ will be significantly lower than the effective thermal conductivity predicted by the series model.

Thermal contact resistance arises from an imperfect junction between two contacting solid materials and reduces the heat flow across the boundary. Parameters which influence the thermal contact resistance are for example contact pressure, surface roughness, and interstitial materials (*e.g.*, air or vacuum).[65-66] However, even materials with an ideal contact, *i.e.*, no thermal contact resistance, have a certain resistance at the interface. The so-called thermal boundary resistance, or Kapitza resistance, arises from phonon scattering at the interface. Especially in the case of nanoscale materials, thermal boundary conductance determines the thermal transport.

Thermal boundary conductance between dielectric materials is commonly modelled by the acoustic mismatch model (AMM) or diffuse mismatch model (DMM).[67] The AMM is based on differences in the speed of sound of the materials in contact. Furthermore, the model assumes a specular scattering of the phonons during transmission of the boundary.[68] The DMM, on the other hand, is based on differences in the phonon density of states. Here, the phonons are scattered diffusively, *i.e.*, randomly, at the interface between two materials.[69] Based on these assumptions, the AMM predicts a higher thermal boundary conductance than the DMM.

In the following, exemplary studies on the thermal conductivity of nanoscale layered thin films are presented.

The lowest known $\kappa_{\mathrm{cross-plane}}$ for a fully dense solid has been reported for tungsten diselenide (WSe_2) films with an atomic-scale laminate structure.[9] An ultralow cross-plane thermal conductivity of 0.05 $Wm^{-1}K^{-1}$ was obtained for a WSe_2 film with a thickness of 62 nm fabricated by molecular beam deposition. The WSe_2 film had a disordered, layered structure that was obtained from a randomly stacking of 2D crystalline WSe_2 sheets. This laminate structure led to a localization of lattice vibrations and, thus, to an ultralow cross-plane thermal conductivity. Furthermore, Chiritescu *et al.* destroyed the crystalline order in the films by ion irradiation. Interestingly, $\kappa_{\mathrm{cross-plane}}$ increased with ion beam damage. This rise was attributed to a reduced localization of lattice vibrations due to the introduced disorder.

Losego *et al.* studied the cross-plane thermal transport properties of organically modified montmorillonite clays.[10] The focus of their work was on the influence of the alkyl chain length of the intercalated primary alkylammonium cation and the effect of the head group chemistry. An exemplary cross-section through an organoclay nanolaminate is depicted in Figure 10a. Losego *et al.* found that

$\kappa_{cross-plane}$ of the organoclay nanolaminates is rather independent of the organic layer thickness in the range of the investigated interface densities of 1 – 1.5 nm^{-1} (Figure 10b). All organoclay nanolaminates had a low $\kappa_{cross-plane}$, especially for a fully dense solid, of around 0.09 $Wm^{-1}K^{-1}$. The unmodified sodium montmorillonite clay, however, had an obviously higher thermal conductivity of 0.48 $Wm^{-1}K^{-1}$. This trend is attributed to the lower interface density (0.85 nm^{-1}) and higher thermal boundary conductance compared to the organoclay systems. The highest $\kappa_{cross-plane}$ and, therefore, also the highest thermal boundary conductance was obtained for the organoclay intercalated with trimethyl terminated dodecylammonium cations (Figure 10c).

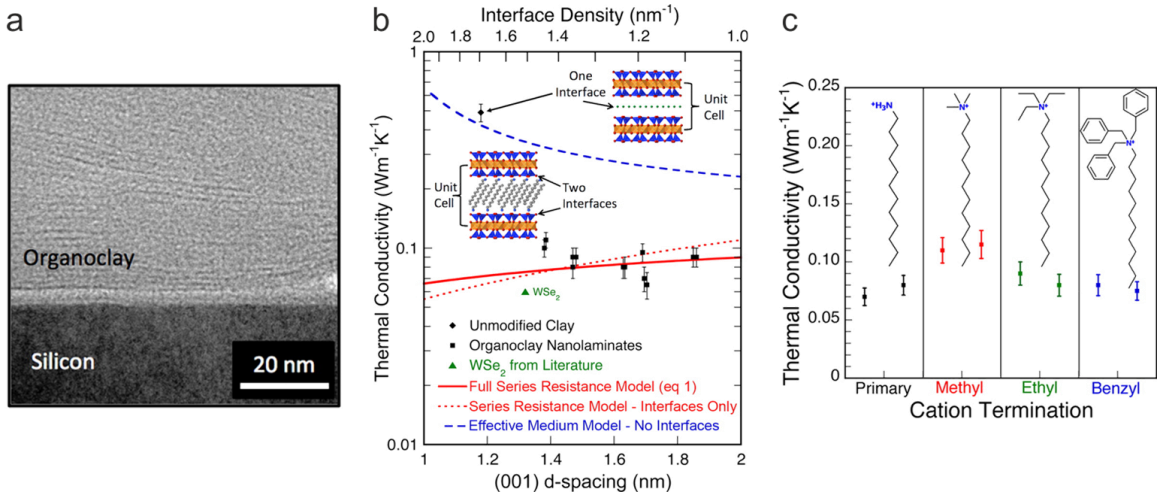

Figure 10. a) Cross-section transmission electron microscopy image of an organoclay nanolaminate on silicon substrate. b) Cross-plane thermal conductivities of unmodified clay and organoclay nanolaminates with varying organic layer thickness. c) Cross-plane thermal conductivities of nanolaminates with varying head group chemistry. Adapted with permission from Losego *et al.*[10]. Copyright 2013 American Chemical Society.

Renteria *et al.*[70] investigated the anisotropic thermal transport properties of free-standing, thin (40 – 170 μm) graphene oxide (GO) and reduced GO (rGO) films which exhibit a layered structure. Both the in-plane and cross-plane thermal conductivity were determined by the laser flash technique using a special in-plane sample holder and the standard cross-plane configuration, respectively. As depicted in Figure 11a, the thermal annealing of the GO films led to a significant rise of the in-plane thermal conductivity from ~3 $Wm^{-1}K^{-1}$ to ~61 $Wm^{-1}K^{-1}$ at room

temperature. This strong increase was explained by restoration of C sp^2 bonds, reduced phonon scattering on oxygen-containing functional groups and other impurities, as well as an increase in the sp^2 grains due to the thermal annealing. Furthermore, only the rGO film annealed at 1000 °C showed a strong temperature dependence similar to a crystalline sample (decrease with increasing temperature due to Umklapp phonon scattering). The cross-plane thermal conductivity showed an opposing trend and decreased from ~0.18 $Wm^{-1}K^{-1}$ to a low value of ~0.09 $Wm^{-1}K^{-1}$ at room temperature (Figure 11b). This decrease after high temperature annealing is due to softening of the restoring forces in the cross-plane direction and the appearance of "air pockets" (Figure 11c). The simultaneous increase of the in-plane thermal conductivity and decrease of the cross-plane thermal conductivity upon thermal treatment led to an exceptionally high thermal conductivity ratio ($\kappa_{\parallel}/\kappa_{\perp}$) of ~675.

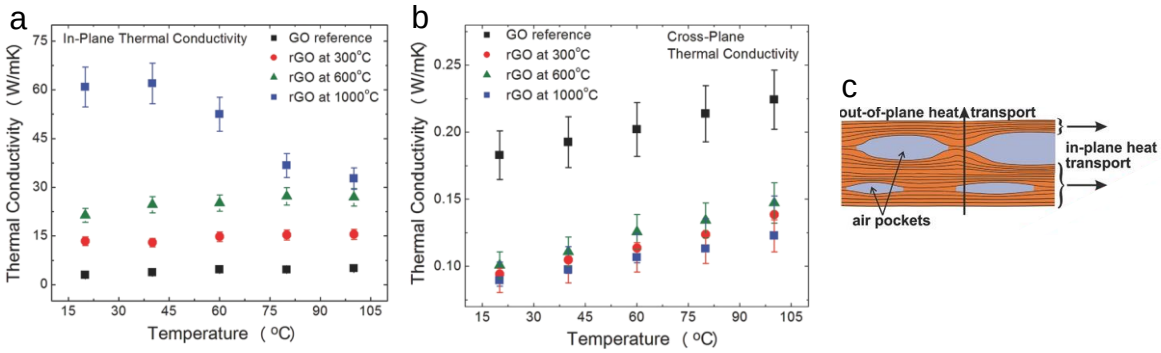

Figure 11. a) In-plane thermal conductivity of graphene oxide (GO) and reduced GO (rGO) films in dependence of the temperature. b) Cross-plane thermal conductivity of GO and rGO films in dependence of the temperature. d) Appearance of air pockets in rGO films due to the thermal annealing. Adapted from Renteria *et al.*[70] with the permission of WILEY-VCH Verlag GmbH & Co. KGaA, Weinheim.

2.2. Basics of the Finite Element Method

The finite element method (FEM) is a numerical analysis technique to solve problems in fields like heat transfer and fluid flow, as well as multiphysics problems.[71-73] Although only analytical methods give absolutely exact solutions, in many situations these analytical solutions are very complicated or even not possible to obtain. This is especially the case when the geometry of interest is irregular or the boundary conditions are too complex. As the name FEM suggests, the geometry is subdivided into a finite number of small regions called elements, as illustrated in Figure 12. Each element is formed by a specific number of points which are referred to as nodes (Figure 12). The FEM computes an approximated solution only at these nodes, whereas an analytical method would give an exact solution for any point of the geometry.[71]

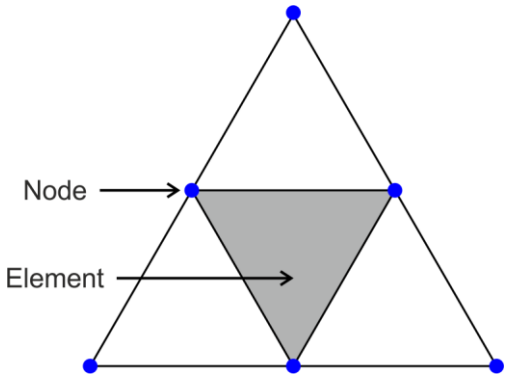

Figure 12. Two-dimensional geometry with triangular finite element mesh: each element is created by the connection of a specific number of nodes. Adapted from Nithiarasu *et al.*[71]

The flow diagram in Figure 13 summarizes the subsequent steps of a numerical model. The basis for each numerical study is a physical problem to be solved. The physical problem is expressed by mathematical models, usually in terms of partial differential equations.[71]

Subsequently, the finite element discretization of the geometry as well as the underlying equations (spatial or temporal) is carried out. As mentioned above, the complete object of interest is divided into non-overlapping finite elements bounded by nodes (Figure 12).[71-73]

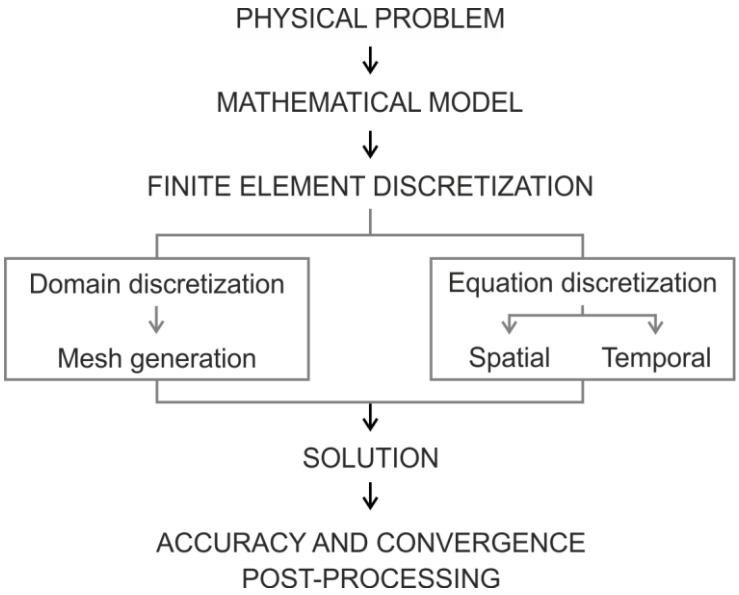

Figure 13. Subsequent steps of a numerical model. Adapted from Nithiarasu *et al.*[71]

The unknown variables are defined and computed in these nodal points, variables in the domain are obtained by interpolation.[74] The number of nodes depend on the used mesh element and interpolation function. The domain discretization is referred to as mesh generation and can be either manual, semi-automatic, or fully-automatic.[71] One-dimensional (1D) objects are meshed with lines, areas with triangles or rectangles, and volumes with tetrahedra, hexahedra, pyramids or triangular prisms. Generally, there are two different mesh generation techniques: the mapped meshing and free-form meshing procedure. The mapped meshing technique generates a structured mesh and is therefore only suitable for rather regular geometries. The used mesh elements and element spacings are defined by the user. Usually, mapped meshes lead to a high accuracy of the solution. In case of the free-form meshing procedure, almost any geometry can be meshed, whereas an unstructured mesh is built. Typical mesh elements are triangles for two-dimensional (2D) and tetrahedral for three-dimensional (3D) objects. Although the user can specify the size range of the elements, he has little influence on the generated mesh.[72] The mesh generation is one of the most important steps, since the mesh determines the accuracy of the numerical solution and the needed computation time.[71] A measure for the mesh quality is a good agreement of the

mesh elements with the prescribed element shape and edge lengths, *e.g.*, highly distorted elements must be avoided.[71-72] There are several methods for automatic mesh generation available. However, methods are often used that are based on advancing front methodology or on Delaunay triangulation.[71-72] In brief, in the advancing front technique, the meshing starts from the boundaries to the inside of the domains, whereas in the Delaunay triangulation, the complete domain is directly meshed from coarse to fine using triangles (2D) or tetrahedra (3D).[72]

After the domain discretization, the element formulation, *i.e.*, the development of equations for the elements, takes place. Typically, the equations are formulated by partial differential equations and rewritten into a weak form (integral form). The individual matrix element equations are assembled into a system of equations in form of a global matrix:[71, 74]

$$[K]\{u\} = \{f\}, \tag{17}$$

where $[K]$ is the global matrix, $\{u\}$ is the global unknown vector, and $\{f\}$ the global load vector. After the assembly, all essential boundary conditions are implemented.[71]

The next step is the solution of the equations and thus the computation of the nodal values of the unknown variable (*e.g.*, temperature in steady-state heat transfer).

Finally, accuracy and convergence studies are performed. During post-processing, secondary quantities, such as heat flux and thermal conductivity, are calculated and responses can be visualized.[73]

All numerical studies are an approximation and the exact solution will only be obtained with a mesh size of zero. Furthermore, the accuracy of the FEM solution depends highly on the chosen mesh. Thus, mesh convergence studies should always be carried out to ensure mesh-independent results. A schematic mesh convergence study is depicted in Figure 14. Several studies were done on different meshes, whereas the size of the mesh elements was decreased and thus the number of mesh elements/nodes increased. Here, a coarse mesh results in an

underestimation of the thermal conductivity. With increasing number of nodes, the solution approaches the exact value, *i.e.*, the solution is converged.[71]

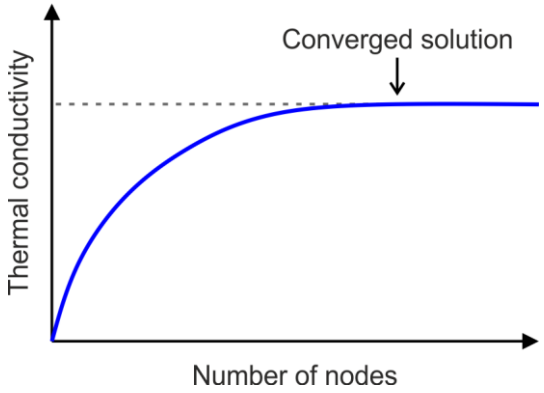

Figure 14. Exemplary mesh convergence study: a converged solution, *i.e.*, a good approximation to the real solution, is obtained above a certain number of nodes. Adapted from Nithiarasu *et al.*[71]

Beside the use of smaller elements, the accuracy can also be improved by keeping the number and size of mesh elements constant and increasing the displacement interpolations or by combining both possibilities. Whereas detailed mesh convergence studies are rather easy for 2D geometries, this can be difficult or too costly for complicated 3D structures. In this case, numerical solutions can be compared with experimental data (or analytical data if available).[71]

2.3. Infrared Lock-In Thermography

2.3.1. Fundamentals of Infrared Thermography

Infrared (IR) thermography, also called thermal imaging, determines the surface temperature distribution of an object under investigation.[28] The main advantages over other temperature detection systems are its non-contacting, non-intrusive working principle and the provision of two-dimensional images in real-time.[75]

IR thermography is based on the heat transfer mode thermal radiation (Chapter 2.1.1). As illustrated in Figure 15, IR thermography uses only a certain wavelength range within the IR spectral region that is called thermal infrared (0.78 µm – 14 µm). Typically, the spectral range is divided into three parts: the short-wave region from 0.9 – 1.7 µm, the mid-wave region from ~3 – 5 µm, and the long-wave region from ~7 – 14 µm.[29]

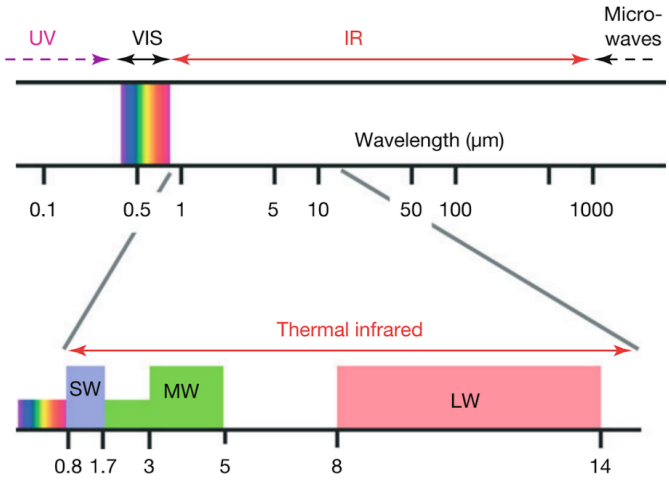

Figure 15. Selection of the electromagnetic spectrum showing the infrared (IR) and its adjacent spectral regions. Typically, in IR thermography the so-called thermal infrared spectral range is used. This range is divided into short-wave (SW), mid-wave (MW), and long-wave (LW) region. Reprinted from Vollmer and Möllmann[29] with the permission of WILEY-VCH Verlag GmbH & Co. KGaA.

There are three possible interactions of a specimen with EM radiation: reflection, absorption, and transmission. The corresponding dimensionless probabilities of these processes are specified by the absorption coefficient $\alpha(\lambda)$, the transmission

coefficient $\tau(\lambda)$, and the reflection coefficient $\rho(\lambda)$. They depend on the wavelength of the EM radiation and their sum is unity:

$$\alpha(\lambda) + \tau(\lambda) + \rho(\lambda) = 1 \tag{18}$$

As mentioned in Chapter 2.1.1, a black body transmits or reflects no EM radiation independent of the wavelength. Thus, its coefficient of absorption is unity ($\alpha = 1$).[28-29] The black body serves as model system for the following radiation laws.

Planck's law (Equation (19)) defines the spectral specific irradiation $M_\lambda(T)$ ([$Wm^{-2}\mu m^{-1}$]) of a black body of given temperature T as a function of the wavelength λ. The spectral specific irradiation is the total radiant power per wavelength unit that is irradiated by a plane unit area into a hemisphere.[29]

$$M_\lambda(T) = \frac{2\pi hc^2}{\lambda^5}\left(e^{\frac{hc}{\lambda k_B T}} - 1\right)^{-1} \tag{19}$$

Here, h is Planck's constant ($6.626 \cdot 10^{-34}$ Js), c the speed of light, and k_B the Boltzmann constant ($1.380 \cdot 10^{-23}$ JK^{-1}).

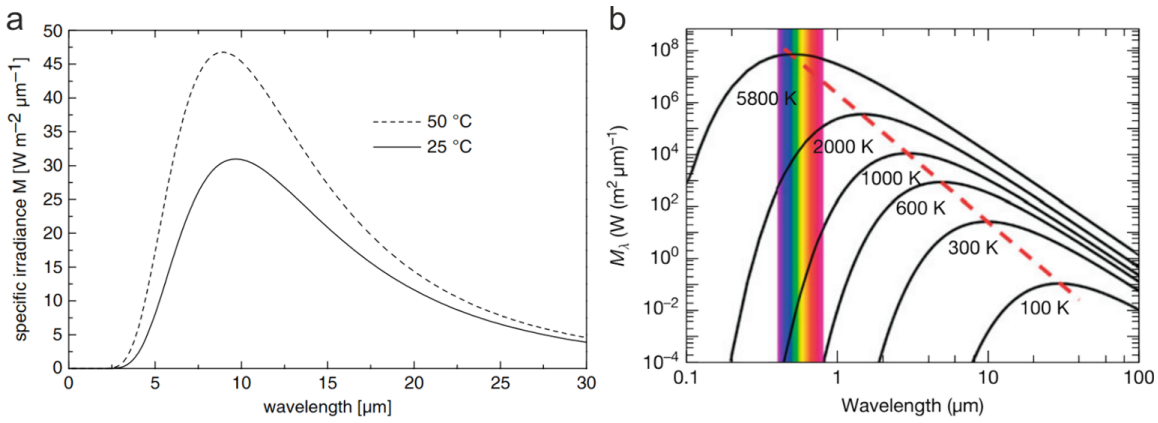

Figure 16. a) Radiation of black bodies of 25 °C and 50 °C according to Planck's law (Equation (19)). Adapted from Breitenstein *et al*.[28] with the permission from Springer-Verlag Berlin Heidelberg. b) Radiation of black bodies of temperatures between 100 – 5800 K in a double log plot. The maximum of the distribution shifts to lower wavelengths with increasing temperature. The red dashed line represents the maxima displacement according to Wien's law (Equation (20)). Adapted from Vollmer and Möllmann[29] with the permission of WILEY-VCH Verlag GmbH & Co. KGaA.

In Figure 16a, the distributions of EM radiation emitted by a black body with a temperature of 25 °C and 50 °C, respectively, are shown. The maximum radiation of the specimen at room temperature is located around 10 µm.[28] The position of the

maximum shifts to lower wavelengths with increasing temperature, as illustrated in the double log plot in Figure 16b. Thus, at extremely high temperatures, like for example 5800 K (sun light), the maximum of Planck's black body spectra lies in the visible range.[29]

The relation between the location of the maximum λ_{max} and the temperature T is described by Wien's law:

$$\lambda_{max} \cdot T = 2897.8\ \mu mK \tag{20}$$

This result is obtained by setting the first derivate of Planck's law (Equation (19)) to zero.[29,76] The maxima displacement with temperature is illustrated as red dashed line in Figure 16b.

The total emissive power $M(T)$ of a black body is given by integrating Planck's law (Equation (19)) over the whole spectrum. The emissive power is proportional to the fourth power of the temperature. This relation is called Stefan-Boltzmann law:

$$M(T) = \sigma T^4 \tag{21}$$

According to Kirchhoff's law, the coefficient of absorption is equal to the coefficient of emission $\varepsilon(\lambda)$ at a specific wavelength:

$$\alpha(\lambda) = \varepsilon(\lambda) \tag{22}$$

The coefficient of emission is the probability of a surface to emit radiation and is usually referred to as emissivity. Since a black body is an ideal absorber, its emissivity is $\varepsilon = 1$. However, the emissivity of a real specimen lies in the range of $0 < \varepsilon < 1$. The emissivity is a material property and depends on the material itself, the surface roughness, and the surface geometry.[29]

If the emissivity of a specimen is wavelength independent but below 1, the object is called grey emitter. A specimen with a wavelength dependent emissivity is referred to as selective emitter. The spectral specific irradiation of a real specimen is obtained by multiplying Planck's law (Equation (19)) by the emissivity $\varepsilon(\lambda)$.[28] The corresponding radiation spectra of a grey body and selective emitter in comparison to the spectra of an ideal black body are shown in Figure 17. The

emissivity of the specimen has a strong influence on the radiation spectra. Thus, it is important to know the correct emissivity of a specimen to determine the actual surface temperature from the measured thermal radiation.

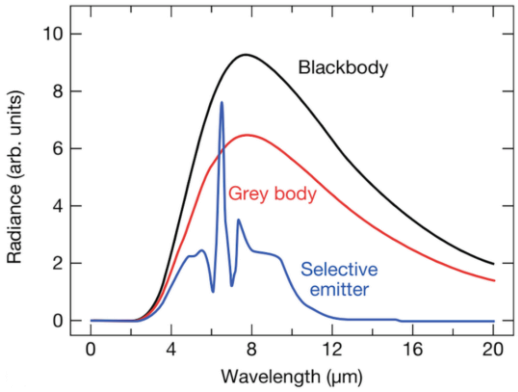

Figure 17. Radiation spectra of an ideal black body according to Planck's law (Equation (19)) and the spectra of realistic specimens like a grey body and selective emitter. Reprinted from Vollmer and Möllmann[29] with the permission of WILEY-VCH Verlag GmbH & Co. KGaA.

Furthermore, the IR camera detects not only the thermal radiation emitted from the specimen but also radiation coming from other sources: transmitted background radiation (if $\tau > 0$), reflected background radiation (if $\rho > 0$), and radiation from the atmosphere. Transmitted and reflected background radiation can be reduced or even neglected, if the surface of the object is coated with a high emissive material (*e.g.*, graphite). IR cameras usually work within one of the two wavelength windows ($\sim 3 - 5$ μm or $\sim 8 - 14$ μm) where the atmosphere is mainly transparent, especially for short working distances. Thus, atmospheric radiation can often be ignored.

Most of the modern thermographic systems consist of a focal plane array, *i.e.*, a two-dimensional array, of IR detectors. In general, there are two different detector types: thermal detectors and photon detectors. Thermal detectors, like a microbolometer, are uncooled detectors. Here, the detector absorbs the thermal radiation that is converted into heat. Then, the change of a physical property, *e.g.*, resistance, due to the temperature increase is measured. On the other hand, photon

detectors count individual photons using the photoelectric effect. These detectors need to be cooled to suppress thermal noise.[29]

2.3.2. Basics of Lock-In Thermography

Lock-in thermography is an active thermography method.[77] In general, the sample under investigation is heated periodically with a certain frequency, the lock-in frequency ($f_{\mathrm{lock-in}}$). The temperature distribution of the sample surface is detected and a lock-in correlation is conducted. This means that only the oscillating (alternating current, AC) parts of the temperature signal are evaluated.

There are two different measurement systems: serially probing systems and camera-based systems. In serially probing systems, a single temperature detector, *e.g.*, an infrared (IR) detector, is scanned across the sample surface. The other option uses an IR camera to record two-dimensional temperature data with a certain frame rate ($f_{\mathrm{frame\ rate}}$). Usually, a camera-based lock-in measurement averages over several lock-in periods N to improve the detection sensitivity.[28]

Since an IR camera as well as a sinusoidal heating are most commonly used, I will explain only the lock-in procedure for this configuration:

A digital two phase image correlation, which uses both a sine-function and a negative cosine-function, is applied (Figure 18). The correlation functions are split into n weighting factors K^{0°(sin-function) and K^{-90° (-cos-function). Here, n is the number of frames per lock-in period recorded by the camera. This number depends on the camera-specific frame rate and the used lock-in frequency:

$$n = \frac{f_{\mathrm{frame\ rate}}}{f_{\mathrm{lock-in}}} \tag{23}$$

All incoming frames F are multiplied twice in parallel by the two weighting factors. A subsequent summation gives the output signals S^{0° and S^{-90°:

$$S^{0°} = \frac{1}{nN}\sum_{i=1}^{N}\sum_{j=1}^{n} K_j^{0°} F_{i,j} \tag{24}$$

$$S^{-90°} = \frac{1}{nN}\sum_{i=1}^{N}\sum_{j=1}^{n} K_j^{-90°} F_{i,j} \tag{25}$$

Here, $S^{0°}$ is the output signal of the sine-correlation and $S^{-90°}$ the ouput signal of the negative cosine-correlation. The corresponding images are called in-phase/0°- and quadrature/-90°-image, respectively.[28]

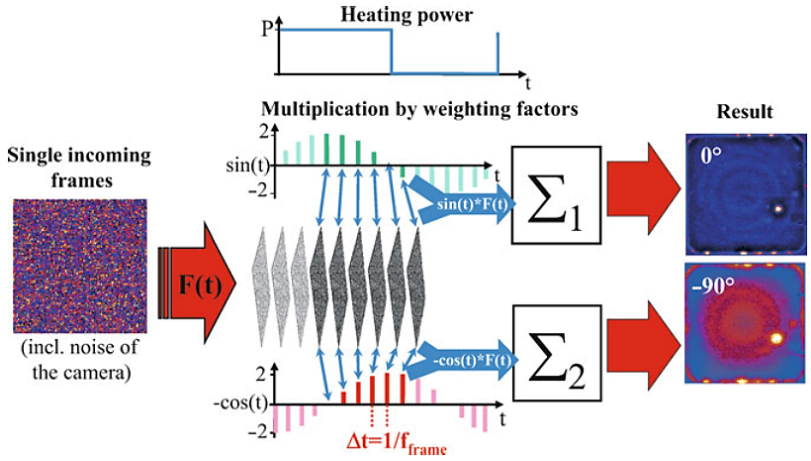

Figure 18. Principle of sin/-cos lock-in image correlation for $n = 16$ frames per lock-in period: All incoming frames are multiplied separately by the two weighting factors (sin and –cos). The summation gives the 0°-image (in-phase image) and the -90°-image (quadrature image). From these, the corresponding phase and amplitude images are calculated. Reprinted from Breitenstein *et al.*[28] with the permission from Springer-Verlag Berlin Heidelberg.

Then, the amplitude T and phase Ψ of the oscillating temperature can be calculated for the whole image using the following equations:

$$T = \sqrt{(S^{0°})^2 + (S^{-90°})^2} \tag{26}$$

$$\Psi = \arctan\left(\frac{-S^{-90°}}{S^{0°}}\right) \ (-180° \text{ if } S^{0°} \text{ is negative}) \tag{27}$$

According to the Nyquist-Shannon sampling theorem, at least four frames per lock-in period ($n = 4$) are needed for the two-phase lock-in correlation. Consequently, there is a maximum possible lock-in frequency $f_{\text{lock-in,max}}$:

$$f_{\text{lock-in,max}} \leq \frac{f_{\text{frame rate}}}{4} \tag{28}$$

If a frequency above this limit is used, undersampling occurs. All the equations above are valid for a synchronous correlation, *i.e.*, n is an integer. However, also asynchronous correlation is possible. The difference of both correlation principles is demonstrated in Figure 19.

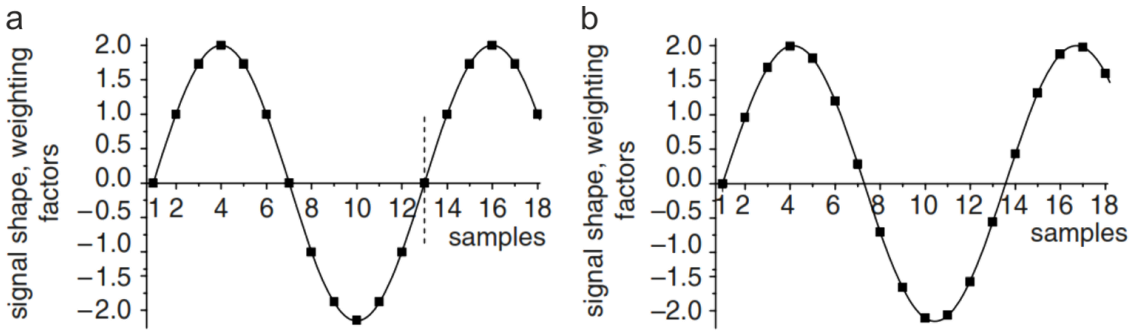

Figure 19. Timing diagrams: a) synchronous correlation ($n = 12$) and b) asynchronous correlation ($n > 12$). The vertical dashed line marks the beginning of the next lock-in period. The solid line represents the signal shape, the black squares the measurement events. Adapted from Breitenstein *et al*.[28] with the permission from Springer-Verlag Berlin Heidelberg.

2.3.3. Lock-In Thermography for Determination of the Thermal Diffusivity of Thin Samples

Lock-in thermography (LIT) is a versatile, non-destructive method to determine the in-plane thermal diffusivity of solids. A major advantage of this technique is that the thermal transport properties of thermally thin, anisotropic and isotropic slabs as well as thin filaments can be studied.[19-23, 78-81]

A typical lock-in measurement works as follows. The sample is heated by an intensity-modulated light beam at a known frequency, the lock-in frequency. In equilibrium, the temperature of the sample oscillates with the same frequency. However, the phase and amplitude of these oscillations are position dependent. The surface temperature oscillations are detected by an infrared (IR) camera connected to a lock-in module.[28] An exemplary LIT set-up is depicted in

Figure 20.[19] In this case, the intensity of a laser beam is modulated using an acousto-optic modulator. A lens focuses the laser beam on the sample surface and an IR camera detects the emitted thermal radiation in rear-face configuration. Typically, the software provided with the IR camera calculates the amplitude and phase of the temperature oscillations. There are also experimental set-ups, where the surface temperature oscillations are measured in front-face configuration, where a line-shaped laser beam or a different kind of modulator (*e.g.*, electro-optic modulator) is used.

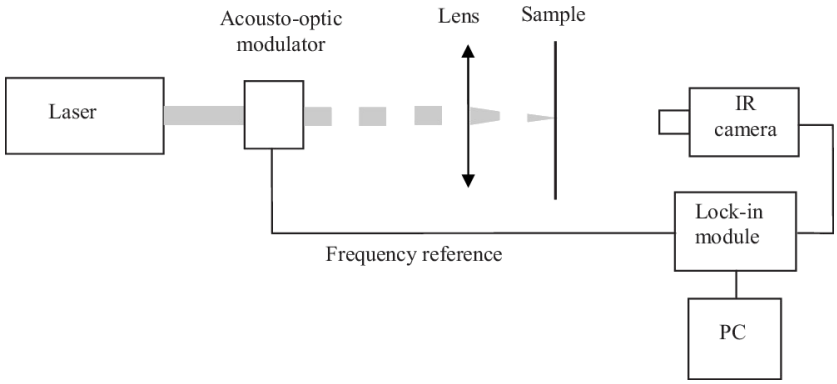

Figure 20. Scheme of an exemplary lock-in thermography set-up for thermal diffusivity measurements under ambient conditions. Reprinted from Mendioroz *et al.*[19] with the permission of AIP Publishing.

If heat losses to the surrounding air are negligible, the thermal diffusivity can easily be obtained using the so-called slope method.[20, 78] The phase of the surface temperature Ψ changes linearly with the distance to the illuminated heating spot (or line) r. The slope m_Ψ of this linear relation and the used lock-in frequency $f_{\mathrm{lock-in}}$ give the thermal diffusivity D:

$$m_\Psi = -\sqrt{\frac{\pi f_{\mathrm{lock-in}}}{D}} \tag{29}$$

Interestingly, the linear relation of the natural logarithm of the amplitude T multiplied by r^n ($\ln(Tr^n)$) yields the same slope ($m_{\ln(Tr^n)} = m_\Psi$) under ideal conditions, like negligible heat losses.[20-21, 78] The exponent n depends on the dimensionality of heat propagation and is n = 0, 0.5, and 1 for one-dimensional

(1D), two-dimensional (2D), and three-dimensional (3D) heat transport, respectively.[21]

It was shown that the slope method cannot be used for thin slabs and filaments. The presence of heat losses leads to an overestimation of the thermal diffusivity, which rises with increasing surface to volume ratio of the investigated sample.[19-21] Furthermore, the effect of heat losses is especially crucial for poor thermal conductors. However, in case of thermally high conductive materials and 1D (*i.e.*, point illumination of a thin filament or line-shaped illumination of a thin slab) or 2D (*i.e.*, point illumination of a thin slab) heat transfer, the product of both slopes

$$m_{\Psi} \cdot m_{\ln(Tr^n)} = \frac{\pi f_{\mathrm{lock-in}}}{D} \tag{30}$$

leads to correct thermal diffusivities.[19-20, 22, 79, 82-83] Here, heat conduction to the gas plays no role. Convection and radiation induce an increase in m_{Ψ} and a decrease in $m_{\ln(Tr^n)}$. However, the influence of these two heat loss processes is cancelled out using the product of both slopes.

Mendioroz *et al.*[19] and Salazar *et al.*[23] proved that under vacuum conditions (10^{-3} - 10^{-2} mbar) correct thermal diffusivity values are obtained - even for thermally thin, low conductive slabs and filaments. However, it is important to extract the slopes from the linear regions of the profiles (far enough away from the heating spot).

If measurements are conducted in vacuum, the thermal diffusivity of an opaque, thermally thin sample (sample thickness $l \ll$ thermal diffusion length μ, where $\mu = \sqrt{D/\pi f_{\mathrm{lock-in}}}$) can be calculated using the following equations:[19]

(a) *1D heat propagation in a thermally thin slab (illuminated by a line shaped light beam[22]) or filament*:

$$m_{\Psi} \cdot m_{\ln(T)} = \frac{\pi f_{\mathrm{lock-in}}}{D} \tag{31}$$

(b) *2D heat propagation in a thermally thin, isotropic slab (point excitation):*

$$m_{\Psi} \cdot m_{\ln(Tr^{0.5})} = \frac{\pi f_{\text{lock-in}}}{D} \tag{32}$$

(c) *2D heat propagation in a thermally thin, anisotropic slab, i.e., a sample with a thermal diffusivity varying with x, y, and/or z-direction ($l \ll \mu_z$)*

$$m_{\Psi} \cdot m_{\ln(Tx^{0.5})} = \frac{\pi f_{\text{lock-in}}}{D_x} \tag{33}$$

$$m_{\Psi} \cdot m_{\ln(Ty^{0.5})} = \frac{\pi f_{\text{lock-in}}}{D_y} \tag{34}$$

Although LIT is a rather simple method, some sources of error – in addition to *heat losses* - can lead to inaccurate thermal diffusivity values. In the following, the effects of other parameters are discussed:

(a) *Excitation Diameter*

An excitation diameter of zero is used for the derivations of Equations (29) - (34). A finite spot size changes the phase and amplitude profiles close to the excitation spot. At large distances r, the linear relations are still valid and the slopes of both profiles are unaffected.[19-20] Thus, the actual spot size is not decisive as long as the profiles are fitted in the linear region.

(b) *Heating Power*

High heating powers lead to large temperature variations in the sample, especially near the excitation area. Since the IR emission behaves nonlinearly with temperature (Stefan-Boltzmann law), distortions in the detected IR intensity distribution will be obtained. It is therefore recommended to use heating powers as low as possible producing a temperature rise of a few Kelvins.[19, 84-85]

(c) *Diffraction Effects*

Diffraction effects are produced by the optics of the IR detectors. The phase and amplitude profiles are affected in such a way that an overestimated

thermal diffusivity is obtained. This overestimation increases for poor conductors and high frequencies.[84-88] However, the use of low lock-in frequencies (< 10 Hz) avoids this problem.[19]

(d) *Sample Size*

All models assume infinite sample sizes and, therefore, boundary effects are not considered. In a real experiment, the sample size is an important parameter. In case of too small sample dimensions, thermal waves reach the edges of the sample. The phase and amplitude profiles are deformed which results in an overestimation of the thermal diffusivity. Furthermore, the thermal diffusivity rises with decreasing modulation frequency, since the diffusion length of the thermal wave ($\mu = \sqrt{D/\pi f}$) increases for low frequencies. Consequently, the sample size has to be adjusted for different thermal diffusivities and frequencies.[19] Typically, experiments are performed at several frequencies. If the thermal diffusivity is independent of the frequency, an influence of the sample size can be excluded.

(e) *Sample Coating*

To obtain a better signal to noise ratio, it can be necessary to coat the sample, *e.g.*, with carbon or graphite. The black layer enhances the absorption of the light beam and the emission of IR radiation. The coating has to be significantly thinner than the thickness of the free-standing sample. Otherwise, the thermal transport properties of the coating lead to an over- or underestimation.[19]

3. Materials and Methods

3.1. Materials

The following section provides the fabrication of dyed polymeric samples which have been used for the studies in Chapter 10. Sodium hectorite (Hec), Hec/polyvinylpyrrolidone (PVP), and graphene oxide (GO) thin films investigated in Chapter 11 and Chapter 12 have been prepared by a collaboration partner.

All chemicals were used as received:
Poly(methyl methacrylate) Plexiglas® 7N (PMMA; Evonik), low-density polyethylene Purell PE 1840H (LDPE; LyondellBasell), tetrahydrofuran (THF; > 99.9 %; Sigma Aldrich), and phenol red (PR; Alfa Aesar).

Preparation of Thick PMMA Samples for Xenon Flash Analysis:
Thick PMMA samples were fabricated by compounding and injection molding. PMMA pellets and PR powder were mixed under nitrogen gas flow in a twin screw compounder with a stirring speed of 40 rpm and at a temperatures of 240 °C. Then, the compounded material was directly filled into the injection unit. Disks with a diameter of ~27 mm and a thickness of ~1 mm were fabricated using an injection force of 6 kN and a tool temperature of 20 °C. In this way, PMMA disks with 0 wt%, 2 wt%, and 6 wt% PR, respectively, were prepared.

Preparation of Thick LDPE Samples for Xenon Flash Analysis:
Thick LDPE samples were also fabricated by compounding and injection molding. First, LDPE pellets and PR powder were mixed under nitrogen gas flow in a twin screw compounder with a stirring speed of 40 rpm and at a temperature of 200 °C. Second, the compounded material was directly filled into the injection unit. Disks with a diameter of ~27 mm and a thickness of ~1 mm were fabricated using an injection force of 6 kN and a tool temperature of 20 °C.

Preparation of Thin, Free-Standing PMMA Films for Lock-In Thermography:

Free-standing PMMA films were prepared from solution. Therefore, 30 wt% PMMA were dissolved in THF under magnetic stirring. To obtain red-colored PMMA films 2 wt% and 6 wt% PR (with regard to the amount of PMMA), respectively, were added to PMMA before dissolving in THF. Then, the PMMA solution was casted on a glass substrate with a speed of 7.5 mms^{-1} using the doctor-blade method. After drying for 48 h, the film was removed from the glass substrate and cut into pieces with appreciate sizes. The thickness of the PMMA films was measured to be around 200 μm.

Preparation of Thin, Free-Standing LDPE Films for Lock-In Thermography:

The fabrication of the free-standing LDPE films is composed of the following steps: compounding, injection molding, and hot pressing. First, LDPE pellets and PR powder were mixed under nitrogen gas flow in a twin screw compounder with a stirring speed of 40 rpm and at a temperature of 200 °C. Second, the compounded material was directly filled into the injection unit. Disks with a diameter of ~27 mm and a thickness of ~1 mm were fabricated using an injection force of 6 kN and a tool temperature of 20 °C. Finally, thin, free-standing LDPE films were obtained by hot pressing of the disks at a temperature of 200 °C and subsequent cooling to room temperature. In this way, LDPE film with 0 wt%, 2 wt%, and 6 wt% PR, respectively, were prepared. The thickness of the LDPE films was around 200 μm.

3.2. Methods

3.2.1. Finite Element Method

Finite Element Method Modeling

Various heat transfer problems have been solved using the commercial finite element method (FEM) software COMSOL Multiphysics®. The general procedure for setting up a model comprises the following steps:

1. Selection of the spatial dimension and physical interfaces
2. Creation/ import of the geometry
3. Assignment of material parameters
4. Assignment of physical properties (domain and boundary conditions)
5. Meshing
6. Solution
7. Convergence studies and evaluation of the results

In this thesis, heat transfer in solids was studied in two-dimensional (2D) or three-dimensional (3D) objects. In the case of simple 2D objects (Chapter 6), the geometries were directly created in COMSOL Multiphysics®. Complex 3D structures as used in Chapter 7 - 9 were first created in the commercial computer-aided design software AutoCAD and then imported to COMSOL Multiphysics®. Material parameters were taken from the material library or new materials were defined based on literature values or experimental data. To conduct heat transfer simulations in solids, the material's thermal conductivity, density, and specific heat capacity has to be known. Which and how many domain and boundary conditions are assigned to the model depends on the heat transfer problem to be solved. The meshes were always generated fully automatic, whereas the free-form meshing procedure using triangles (2D) and tetrahedra (3D) was applied. Finally, the models were solved either time-dependent or stationary. Then, convergence studies were performed to ensure a mesh independent and time-step independent

result (in case of time-dependent studies). During the post-processing, secondary variables like heat flux and temperature profiles were evaluated and 2D or 3D images were exported from COMSOL Multiphysics®.

In the following, some key aspects as well as major problems and their solution are discussed which arose during the conduction of the heat transfer simulations presented in Chapter 6 - 9.

Time Steps in Time-Dependent Heat Transfer Simulations:

In Chapter 6, time-dependent heat transfer simulations were performed. The objective of these simulations was to simulate a typical laser flash experiment and to extract the thermal diffusivity from temperature-rise curves. In the simplest case, the lower surface of a thermally insulated disk was excited by a short triangular heat pulse. After solution of the model, the average temperature rise of the upper surface of the disk in dependence of the time was evaluated.

The major difficulty of this numerical model arose during the evaluation of the temperature-rise curves. Without changing any settings of the time-dependent solver, a temperature-rise curve with several kinks was obtained (green solid line in Figure 21a). The standard setting of the time-dependent solver is that the steps taken by the solver are "free", *i.e.*, the time-stepping method chooses the time steps freely. In this case, too few time steps were taken to obtain a smooth curve close to an analytical solution. However, the setting of the solver can be changed to "intermediate" where the solver takes at least one step in each time interval, or to "strict" where the time-stepping method is forced to take steps at the defined time steps (in addition to further steps if necessary). In Figure 21a, the resulting temperature-time curves of each setting mentioned above are compared. Altough all curves yield the same final temperature, smooth curves were only obtained for "intermediate" and "strict" time steps where more time steps are computed.

However, there are also small differences in the course of these two curves, as illustrated in the inset of Figure 21a. Thus, in further studies, the time steps were reduced from 1 ms to 0.5 ms, whereas strict time steps were taken by the solver. The additional time steps lead to slight changes in the first milliseconds of the temperature-time curve (Figure 21b).

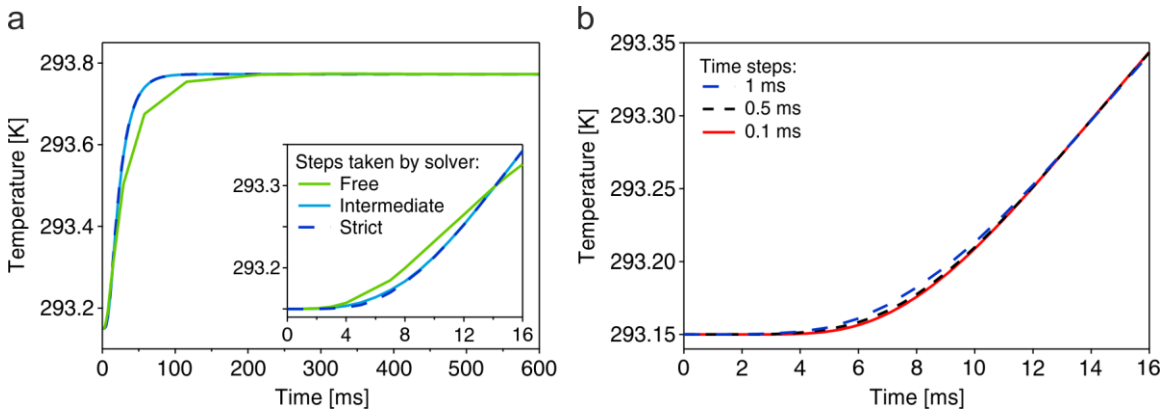

Figure 21. Temperature-time curves for different solver settings: a) Time steps of 1 ms were chosen for the computation. The time-stepping was set to free, intermediate, and strict. b) Strict time stepping was chosen and time steps of 1 ms, 0.5 ms, and 0.1 ms, respectively, were used.

How small the time steps should be chosen depends on the aim of the time-dependent simulation. The accuracy is usually defined in convergence studies.

Extraction of the Effective Thermal Conductivity from Steady-State Simulations:

In Chapter 7 - 9, steady-state heat transfer simulations were performed to obtain the effective thermal conductivity of the investigated three-dimensional structures. Figure 22 explains the general procedure based on a symmetric structure (face-centered cubic unit cell consisting of silica hollow spheres surrounded by gas) which has been used in Chapter 7.

A constant hot and cold temperature is applied to the entire upper and lower face of the cube. Thermal insulation boundary conditions are imposed on all other surfaces. Thus, a temperature gradient forms, with a heat flow in the direction of the cold face. To obtain the effective thermal conductivity κ_{eff}, the integrated heat flux normal to the upper surface is extracted from the simulation result. Then, the

effective thermal conductivity is calculated using Fourier's law of steady-state heat conduction (compare Equation (1)):

$$\kappa_{\text{eff}} = \frac{Q/A}{\Delta T/h}, \tag{35}$$

where Q is the heat flow rate normal to the cross-sectional area A of the cube, ΔT the temperature difference ($T_{\text{hot}} - T_{\text{cold}}$), and h the cube edge length.

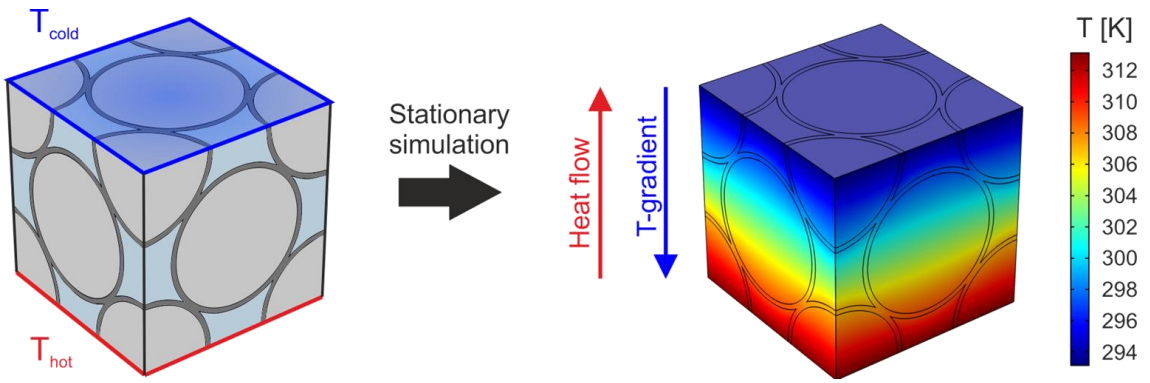

Figure 22. General procedure to extract the thermal conductivity: A constant temperature is applied to the lower (T_{hot}) and upper (T_{cold}) face of the cube. All other faces are thermally insulated. The stationary solution of this model yields a temperature gradient in direction of the hot face. The heat flow normal to the upper surface is evaluated.

In Chapter 8 and 9, non-symmetric geometries were used. In both cases, the underlying particle structures were generated with molecular dynamics (MD) simulations. Since the whole MD particle assembly was too large for FEM, a smaller volume in form of a cube was cut out of the structure, as exemplarily shown in Figure 23. However, due to the disordered particle structure, a non-symmetric geometry was obtained. Thus, stationary heat transfer simulations as described above were conducted in all three spatial directions (x, y, and z). For better statistics, three cubes were cut out of three different positions of the particle structure obtained from MD simulations.

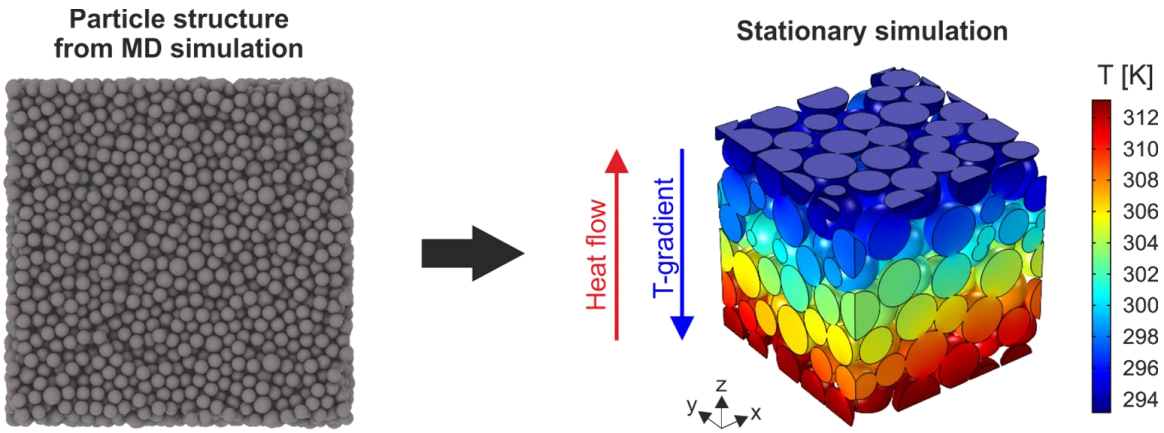

Figure 23. Particle structures were obtained from molecular dynamics (MD) simulations. Since the total geometry was too large for FEM, three cubes located at different positions were cut out of the particle structure. Stationary simulations were conducted in all three spatial directions.

In Chapter 9, it was proven that three positions are sufficient to calculate a meaningful average value. The corresponding data are shown in Figure 24.

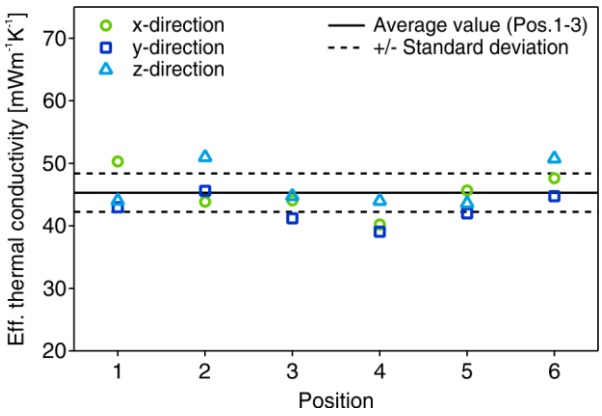

Figure 24. Thermal conductivities of a disordered particle assembly obtained for six cubes cut out of different positions of the amorphous particle structure. Simulations were conducted in each spatial direction. The black solid line represents the average effective thermal conductivity calculated from the first three positions, the dashed line is the corresponding standard deviation.

Assignment of Several Material Parameters in Complex, Non-Symmetric Three-Dimensional Structures

As already mentioned, steady-state heat transfer simulations through rather complex, non-symmetric particle geometries were conducted in Chapter 8. The difficulty here was that the total geometry of interest consisted of two particle types, silica hollow spheres and polymer particles, which were randomly

distributed, as illustrated in Figure 25. Thus, two different materials had to be assigned to the individual particles in COMSOL Multiphysics®. However, this was impossible due to the complex 3D structure. Consequently, first the hollow spheres were imported to COMSOL Multiphysics® and the material properties were assigned. Then, the polymer particles were imported and the respective material properties were added. Afterwards, the particle geometry was united into one object.

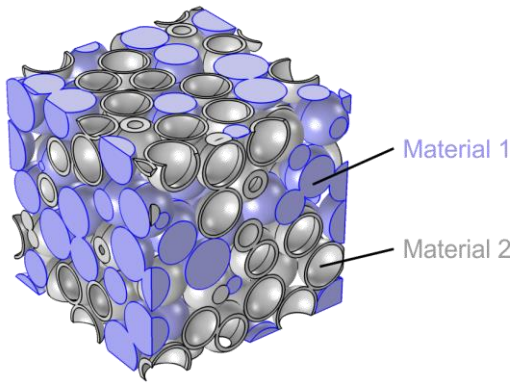

Figure 25. Geometry of a disordered particle assembly consisting of two particle types (hollow spheres and full spheres) made of different materials which are randomly distributed.

Meshing of Complex, Non-Symmetric Three-Dimensional Structures:

The most challenging and time-consuming part of the simulations presented in Chapter 8 and 9 was the meshing of the particle assemblies. The geometries are rather complex, non-symmetric, and contain large size variations. Two examples of these geometries are depicted in Figure 23 and Figure 25. As mentioned in the beginning, all meshes were generated with the automatic free-form meshing procedure using triangles for faces and tetrahedra for domains. Here, the generated mesh can be controlled by the size range of the elements. If the mesh elements were chosen small enough, a complete mesh was generated. However, due to the high number of mesh elements, the model could not be solved due to the limited physical memory of the computer (128 GB). On the other hand, in most cases, large mesh elements lead to several error messages, since small features

could not be meshed. These error messages were typically related to faces, since the automatic procedure meshes in the following order: first, boundaries, then faces, and finally, domains. This issue could be solved by forcing the automatic meshing procedure to start with the problematic faces. Therefore, the concerned faces were selected manually and meshed with appropriate size ranges of the elements. Afterwards, the remaining geometry was meshed.

3.2.2. Lock-In Thermography

Set-Up for Lock-In Thermography Measurements

The first step was the development of the lock-in thermography (LIT) set-up for measuring the thermal diffusivity of thermally thin, free-standing samples.

In this thesis, I used two slightly different LIT set-ups. Both set-ups are schematically depicted in Figure 26. The general working principle is the same as explained in Chapter 2.3.3. In the first variant (a), an electro-optic modulator (EOM 350-160, Conoptics), a signal generator (DG1022A, Rigol), and a laser with a wavelength of 488 nm (Genesis MX 488-1000 SLM OPS, Coherent) was used. In the second variant (b), the intensity of a laser with a wavelength of 532 nm (Genesis MX 532-1000 SLM OPS, Coherent) was modulated using a shutter (SH05/M, Thorlabs) and shutter controller (SC10, Thorlabs). An Infratec VarioCAM HD research infrared (IR) camera (7.5 – 14 μm) equipped with a close-up objective was used in both cases. The minimum spatial resolution of this camera system is 29 μm at a working distance of 33 mm. To avoid heat losses to the environment, all samples were measured under vacuum conditions (~$3 \cdot 10^{-3}$ mbar). All measurements were performed using Infratec's IRBISactiveonline software which automatically calculates the amplitude and phase of the temperature oscillations.

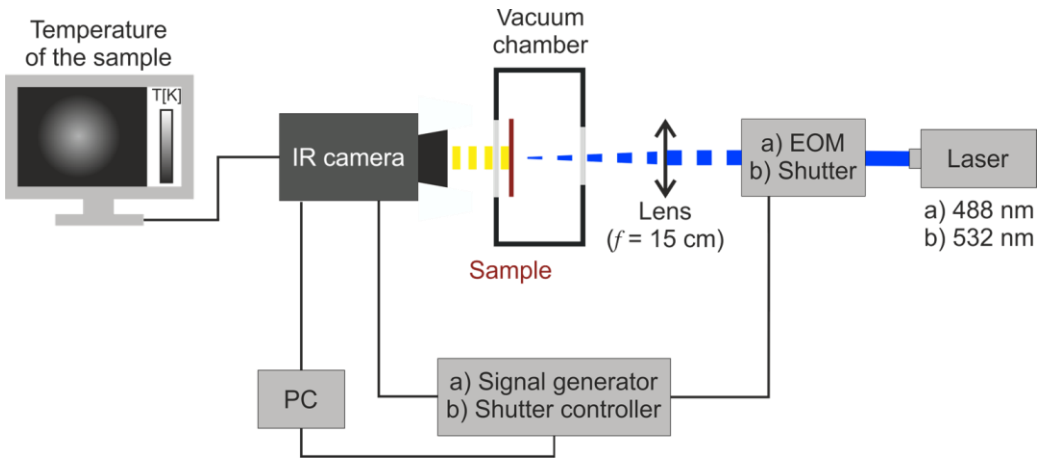

Figure 26. Schematic lock-in thermography set-up for measuring the thermal diffusivity of free-standing thin films.

The final set-up mounted on an optical table is shown in Figure 27. A lens (3) with a focal length of 15 cm focuses the laser beam (1) on the sample surface. Here, the focused laser has a spot size of around 85 µm. Due to the rather large focal length, small changes in the position of the sample surface influence only slightly the size of the laser spot. If necessary, an absorptive neutral density filter (2) is mounted prior to the optical lens. The sample is put into a self-constructed vacuum chamber (4) which has an optical window in direction of the laser and an IR window (sodium chloride) in direction of the IR camera. The sample is fixed on the self-constructed sample holder depicted in Figure 28a by means of magnets. Then, the sample holder is put in the vacuum chamber using the guide highlighted in Figure 28b. This sample holder is suitable for samples with various sizes, since the distance of the plates is adjustable. The vacuum chamber is mounted on an xyz-stage which enables a simple alignment of the vacuum chamber, and thus of the sample. The handheld IR camera is fixed using the self-constructed mount shown in Figure 28c. The distance between sample and IR camera can be adjusted by means of the x-stage. The smallest working distance of around 33 mm was used.

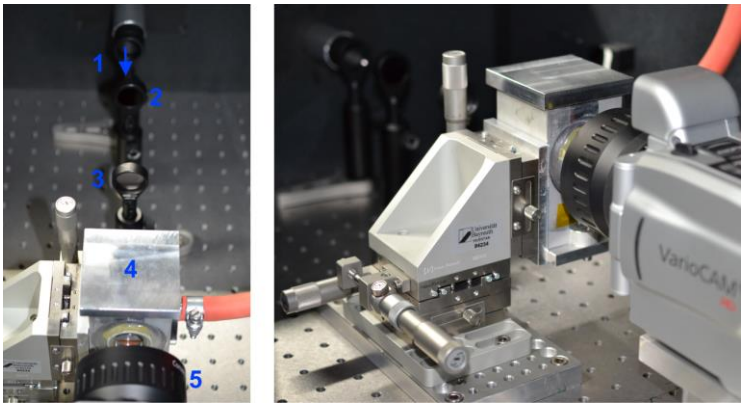

Figure 27. Lock-in thermography set-up: Laser (1), absorptive neutral density filter (if necessary) (2), lens (3), vacuum-chamber on xyz-stage (4), and infrared camera on x-stage (5).

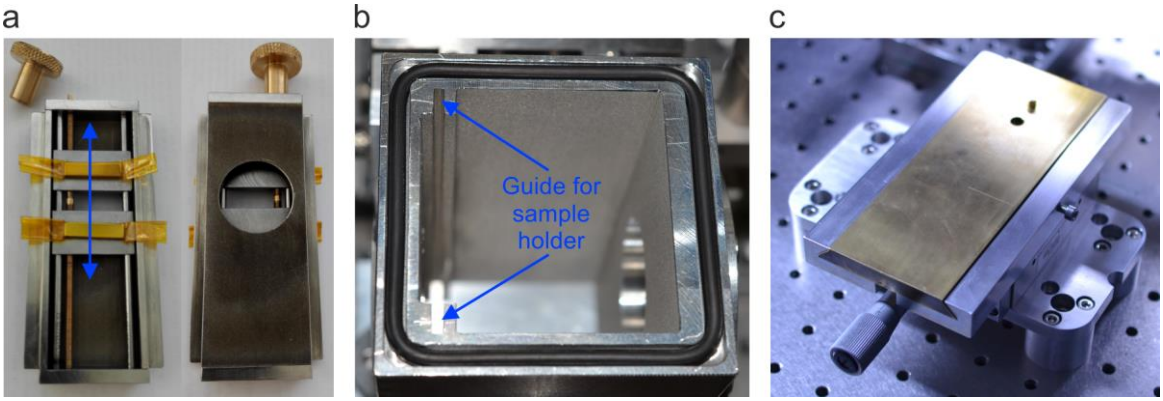

Figure 28. Detailed lock-in thermography set-up: a) Sample holder with adjustable plate distance for various sample sizes. b) Top view of the vacuum-chamber showing the guide for the sample holder. c) Mount for the infrared camera.

Lock-In Thermography Measurements and Data Evaluation

Lock-in thermography measurements were conducted in this way:

1. Sample preparation
2. Evacuation of sample in vacuum chamber
3. Focusing of IR camera on sample surface
4. LIT measurements (at several frequencies)
5. IR image of calibration grid
6. Data evaluation

Typically, the sample is cut into an appropriate size, cleaned, and if necessary coated with a thin layer of carbon (~ 20 nm). The carbon layer enhances the

absorption of the laser light and slightly the emission of IR radiation. Since the measurements are conducted in vacuum, water-containing samples are dried in a vacuum oven before measuring. Then, the sample is fixed on the sample holder, put into the vacuum chamber, and the vacuum chamber is evacuated. The evacuation takes around 20 – 30 min until a rather constant pressure of ~$3 \cdot 10^{-3}$ mbar is reached. Subsequently, one of the most important steps follows: the manual focusing on the sample surface. After directing the laser beam on the sample, the actual LIT measurements are conducted. Therefore, a specific lock-in freqency, typically between 0.1 – 2 Hz depending on the thermal transport properties of the sample, and a certain number of lock-in periods are chosen. The averaging over several periods enhance the signal to noise ratio. Usually, the first 60 – 100 periods are dropped, then 300 – 2000 lock-in periods are recorded. Furthermore, measurements at three to five lock-in frequencies are performed. After removal of the sample, the pixel calibration of the IR images is done. Therefore, the self-fabricated calibration grid (Figure 29a) glued on a 3D printed sample holder is inserted into the vacuum chamber. The calibration grid is a silicon wafer with a line pattern made of photoresist, whereas each photoresist line has a width of 600 μm and a separation distance of 600 μm. Since the silicon wafer is transparent and the photoresist opaque to the wavelength range of the IR camera, a good contrast is visible in the IR image as shown in Figure 29b. A cross-section over several black and white lines is extracted from this image using the software ImageJ (highlighted in blue in Figure 29b) . Then, a Phython script written by Bernd Kopera, University of Bayreuth, determines automatically the factor for the conversion from pixel to μm. Due to the used working distance, the pixel scale factor is always around 29 μm/pixel.

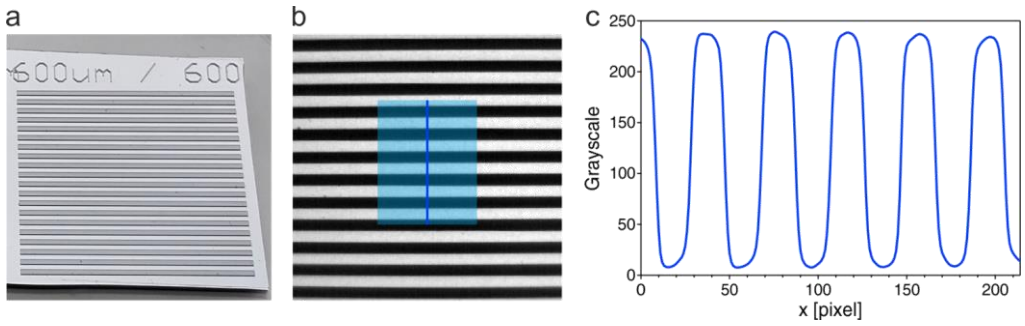

Figure 29. Pixel calibration of infrared images: a) Photograph of the calibration grid with a 600 µm line pattern. b) IR image section of the calibration grid. c) Cross-section over several black and white lines.

Finally, the actual lock-in data is evaluated. For this, a Python script (written by Bernd Kopera, University of Bayreuth) is used which extracts radial profiles for the phase and amplitdue images (Figure 31a). Exemplary phase and amplitude images obtained from lock-in measurements are depicted in Figure 30. The red point marks the midpoint of the laser excitation and thus the midpoint of the radial distribution.

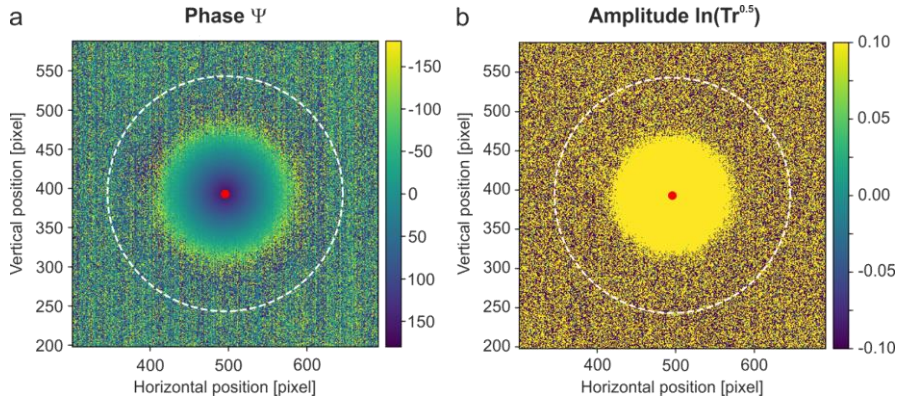

Figure 30. Lock-in thermography raw data of a 250 µm PEEK film measured at a frequency of 0.219 Hz: Phase (a) and amplitude (b) image. Red point marks the midpoint of the radial distribution.

The script converts automatically the radial distance from pixel to mm, the phase from ° to rad, and calculates the natural logarithm of the amplitude multiplied by the square root of the radial distance in mm (ln ($Tr^{0.5}$)). However, the fitting of the phase and amplitude profiles has to be done manually by selecting the lower and upper boundaries of the linear fit. Then, the thermal diffusivity is calculated from the phase and amplitude slopes using Equation (32) (Chapter 2.3.3).

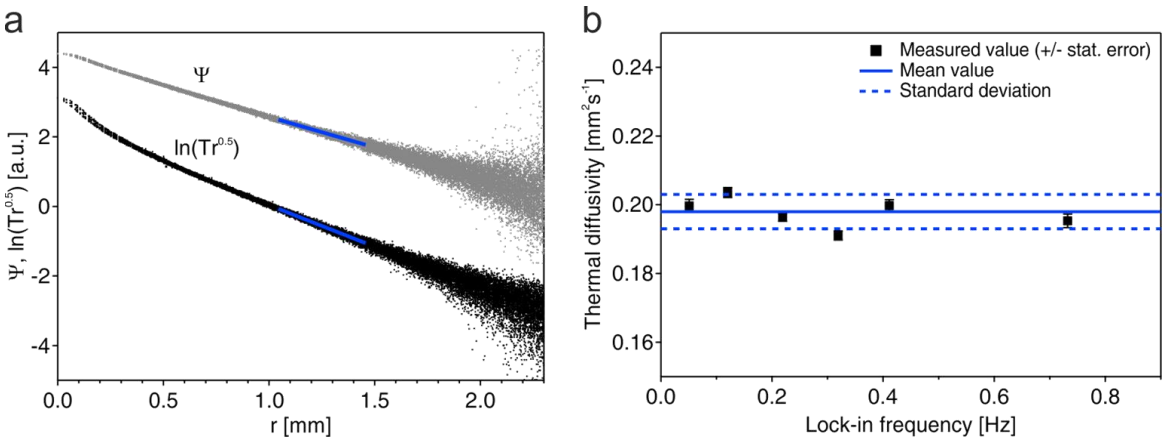

Figure 31. Exemplary data of a 250 µm PEEK film: a) Radial phase and amplitude profiles with linear fits (measured at a frequency of 0.219 Hz). b) Thermal diffusivity with statistical error determined for several lock-in frequencies as well as mean value with standard deviation.

Since measurements are conducted at several frequencies, a thermal diffusivity value for each frequency is obtained. If there are no edge effects or other error sources, the thermal diffusivity is independent of the frequency (Figure 31b). Then, an average thermal diffusivity with standard deviation is calculated.

3.2.3. Further Characterization Methods

Xenon Flash Analysis

In Chapter 6 and 10, the cross-plane thermal diffusivity was determined using xenon flash analysis (XFA). All measurements were performed on an XFA500 xenon flash apparatus from Linseis equipped with an InSb infrared detector. Before the measurement, the bottom and top surface of the sample was coated with a thin graphitic layer. The graphite coating ensures a good absorbance of the xenon flash and a high infrared emissivity. Since the coating is significantly thinner than the sample thickness, it does not affect the measured thermal diffusivity. The precise sample thickness was measured with a Litematic VL-50 (Mitutoyo). The obtained temperature rise-time data were evaluated using the fitting framework developed in Chapter 6.

Differential Scanning Calorimetry

In Chapter 11 and 12, the specific heat capacity was obtained from differential scanning calorimetry (DSC). The measurements were performed on a Discovery DSC 2500 (TA instruments) according to the ASTM E1269 standard. Prior to the measurements, the samples were freeze ground and dried in a vacuum oven at 100 °C for 7 d. Additionally, an isothermal step (1 h, 100 °C) was conducted. Two heating cycles were performed, whereas only the second cycle was evaluated.

Helium Pycnometry

The density of the samples characterized in Chapter 11 and 12, was determined using Helium pycnometry, which measures the sample volume. Therefore, an Ultrapyc 1200e (Quantachrome Instruments) was used. Prior to the measurements, small pieces of the free-standing films were dried in a vacuum oven at 100 °C for 7 d. After measuring the volume of the measurement cell, the volume of the weighed films was measured at room temperature. The software calculates automatically the density from the known mass of the sample.

Ultraviolet-Visible Spectroscopy

Ultraviolet-visible (UV-vis) spectroscopy detects the attenuation of light in the UV-vis wavelength range after passing through a sample. In Chapter 10, an Agilent Cary 5000 spectrometer was used to record absorbance spectra from 380 – 800 nm. A suitable reference sample was used for each measured sample.

Infrared Spectroscopy

Infrared (IR) spectroscopy measures the attenuation of IR light after passing through a sample. In Chapter 10, a Bruker Vertex 70 FT-IR spectrometer was used for infrared (IR) absorption spectra acquisition. Therefore, either transmission-IR using an appropriate reference or attenuated total reflection (ATR)-IR was applied.

4. Thesis Overview

4.1. Synopsis

This thesis deals with the development and application of two methods for thermal transport studies in well-defined, nanostructured materials. On the one hand, a theoretical approach based on the finite element method (FEM, Part A), and, on the other hand, an experimental approach based on lock-in thermography (LIT, Part B) is used. Overall, the thesis comprises seven manuscripts, which have already been published in peer-reviewed journals. Figure 32 provides a graphical overview of the content of the individual manuscripts.

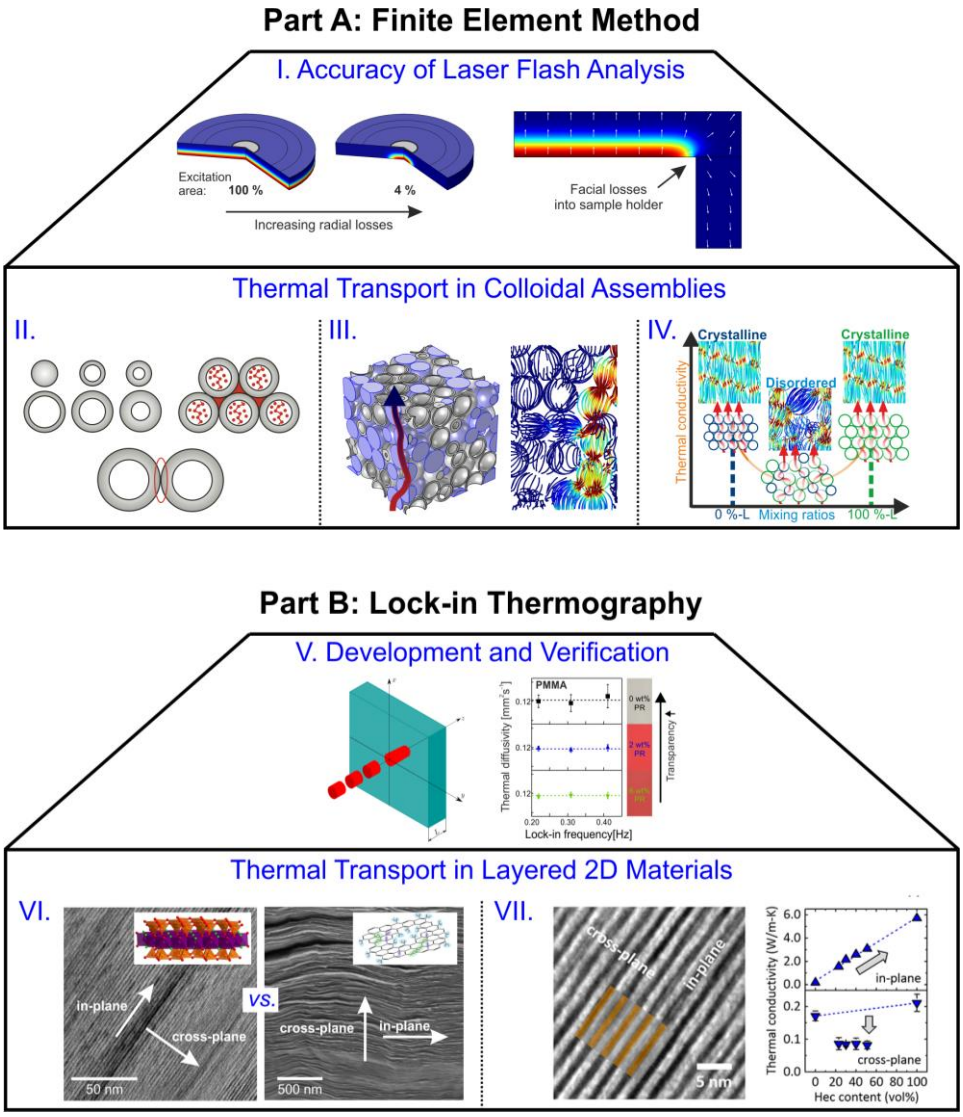

Figure 32. Content of the seven manuscripts with regard to FEM (Part A) and LIT (Part B).

In Chapter 6 (Figure 32, A.I), heat transfer simulations were performed to estimate the sensitivity of the laser flash analysis (LFA) to non-ideal experimental conditions. The LFA is a widely used method to determine the cross-plane thermal diffusivity of solid samples. The simulations showed among other things that also samples which do not perfectly fit on the sample holder can be measured with the LFA with great precision. Due to this versatility, the LFA was applied to determine the thermal transport properties of nanostructured, three-dimensional colloidal assemblies in the experimental parts of Chapter 7 – 9. Here, additional FEM studies were performed to gain a deeper understanding of the experimentally examined thermal transport processes. The investigated colloidal assemblies were obtained from assembled spherical nanoparticles resulting in a porous, nanostructured material. This material class offers the possibility to study the influence of various, well-controlled parameters on the final thermal transport properties as a model system for similar nanomaterials. Thermal transport properties of various silica hollow sphere assemblies (made of monodisperse particles) were studied in Chapter 7 (Figure 32, A.II) to reach a thermal conductivity as low as possible. The FEM particularly helped to clarify the influence of the individual contributions of the solid and gaseous conduction as well as to show the importance of the interparticle thermal conduction. Besides colloidal assemblies consisting of the same particle type, it is also possible to fabricate colloidal assemblies from two different particle types as it was shown in Chapter 8 and 9. In Chapter 8 (Figure 32, A.III), thermal transport in binary colloidal glasses based on randomly mixed, similarly sized polymer particles and silica hollow spheres was investigated. By means of FEM, the composition dependent thermal conductivity was assigned to an existing mixing model. Moreover, the onset of thermal transport percolation was assessed. Binary colloidal assemblies fabricated from two monodisperse, differently sized polystyrene particles were studied in Chapter 9 (Figure 32, A.IV). Again, the focus lied on reaching a minimum thermal conductivity. The FEM

helped to understand the underlying effects. Using this knowledge, assemblies with an ultralow thermal conductivity could be fabricated.

LIT is a relatively simple method to determine the in-plane thermal diffusivity of thin solids. However, the underlying equations of the data evaluation assume a complete opaqueness of the sample to both the exciting laser light as well as the emitted infrared radiation. In the first LIT chapter (Figure 32, B.V), it was shown that the standard evaluation procedure is also valid for semitransparent thin films. This was proven by numerical simulations and by actual measurements of semitransparent polymer films using a home-built LIT setup (see Chapter 3.2.2.). This finding paved the way for the determination of the in-plane thermal conductivity of nanostructured materials carried out in Chapter 11 and 12. More precisely, two-dimensional, layered films, each layer with a thickness on the nanoscale, have been characterized with regard to their thermal conductivity anisotropy. These nanomaterials were again fabricated in a highly controlled way and can therefore serve as a model system for other fully dense materials. In both studies, the in-plane thermal conductivity of these materials was determined by LIT, and the cross-plane thermal conductivity using the photoacoustic method. First of all, in Chapter 11 (Figure 32, B.VI), the anisotropic thermal transport properties of a synthetic clay sodium fluorohectorite (Hec) consisting of different platelet sizes was compared to graphene oxide samples. Then, the introduction of a matrix material on the thermal properties was investigated in Chapter 12 (Figure 32, B.VII). Here, stacks of strongly alternating layers of Hec and polyvinylpyrrolidone were fabricated with varying polymer content. Finally, a wholistic thermomechanical analysis was conducted.

Chapter 6: The Accuracy of Laser Flash Analysis Explored by Finite Element Modeling and Numerical Fitting

The laser flash analysis (LFA) is a standard method to determine the thermal diffusivity of solid samples. In a typical laser flash experiment, the entire bottom face of a sample is illuminated by a short laser flash. The sample surface absorbs the heat which is transferred through the sample. The time-dependent temperature rise of the top face of the sample is recorded by an infrared detector. Finally, a curve fitting procedure is applied to obtain the thermal diffusivity from the temperature rise-time curves. Ideally, the mathematical model of this fitting procedure compensates for any deviations from the ideal, theoretical case. First of all, we developed our own state-of-the-art computational framework for the evaluation of LFA measurements. This gives us full control with regard to the assumptions and requirements of the used mathematical models. A schematic overview of this computational framework is illustrated in Figure 33.

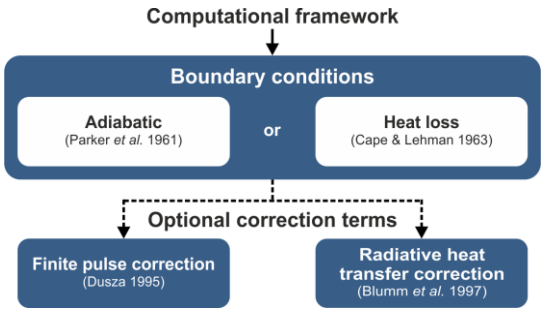

Figure 33. Overview of the computational framework for laser flash analysis. The underlying mathematical model depends on the choice of boundary conditions as well as optional correction terms. Adapted from Philipp *et al.*[89] with the permission of Springer-Verlag GmbH Germany.

Subsequently, we used the finite element software COMSOL Multiphysics® to simulate laser flash experiments with non-ideal experimental conditions. Subsequently, we evaluated the simulated experiments using our self-developed computational framework. Overall, we studied the following side effects as well as combinations of some of these side effects: (a) the ideal adiabatic case, where no heat losses occur, (b) convective and radiative heat losses to the environment, (c) radial losses which arise from an incomplete excitation of the lower sample surface

by the heat pulse that leads to radial heat flow away from the sample center towards its edges, (d) radiative heat transfer, and (e) facial losses which occur if a sample is put on a sample holder, which can serve as a heat sink. The influences of radial and facial losses as well as radiative heat transfer are exemplarily shown in Figure 34. Figure 34a illustrates that the smaller the excitation area, the larger are the radial losses. Radial losses have a strong impact on the temperature-time curves (Figure 34b): the absolute temperature after reaching a maximum value decreases and the half-time shifts to lower times. The influence of radiative heat transfer was simulated using a second heat source (Figure 34c). This leads to a sharp temperature peak at $t \approx 0$ ms (Figure 34d) which has to be taken into account by the mathematical model. The influence of facial losses are comparitively low as it can be seen in Figure 34e.

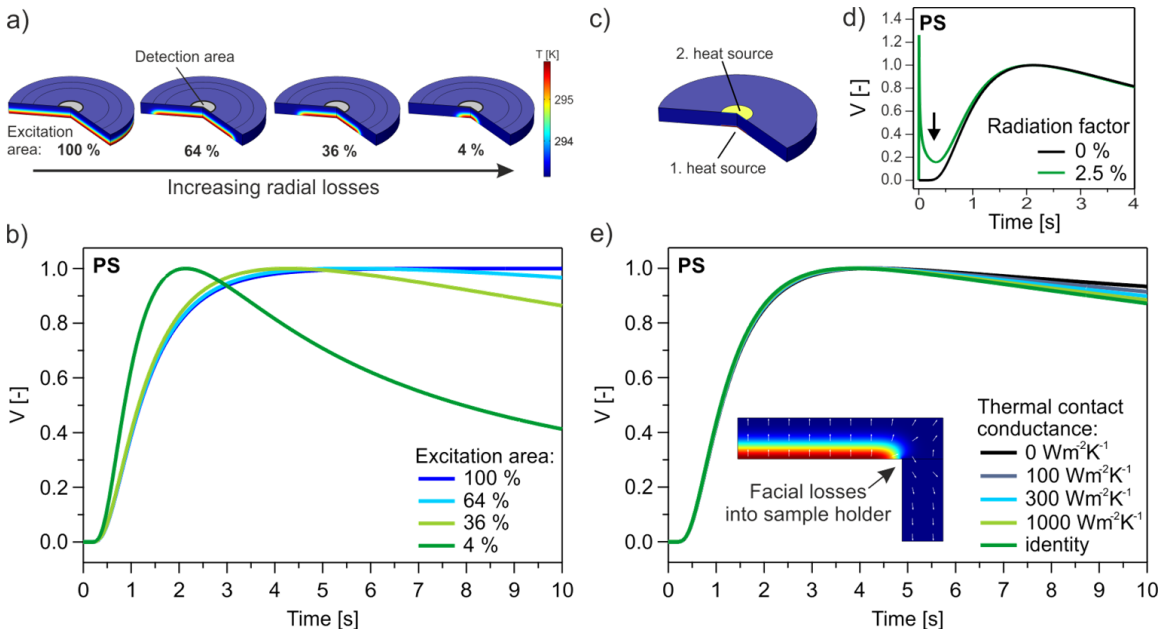

Figure 34. **Influence of radial losses:** a) 3D COMSOL images for different excitation areas. b) Corresponding normalized temperature rise-versus-time curves exemplarily shown for polystyrene (PS). **Influence of radiative heat transfer:** c) 3D COMSOL image illustrates the second heat source. d) Corresponding normalized temperature-rise-versus-time curves of PS with radiative heat transfer. The jump in the temperature evolution is highlighted by an arrow. **Influence of facial losses**: e) 2D COMSOL image illustrating heat flow into the sample holder. Corresponding normalized temperature rise-versus-time curves of PS for different thermal contact conductances. Adapted from Philipp *et al.*[89] with the permission of Springer-Verlag GmbH Germany.

Finally, we confirmed our findings experimentally by measuring a reference sample with certified thermal diffusivity value using a xenon flash apparatus.
Overall, these studies showed that a state-of the art computational framework allows a determination of thermal diffusivities for a broad range of materials and experimental conditions with a relative error of typically less than 4 %. This finding enabled the performance of xenon flash measurements for the thermal characterization of colloidal assemblies as shown in the following three chapters.

Chapter 7: Understanding Thermal Insulation in Porous, Particulate Materials

In this Chapter, thermal insulation capabilities of silica hollow sphere colloidal assemblies have been studied with regard to the following aspects: a) nanoparticle geometry, b) surrounding gas, c) symmetry of assembly, and d) interparticle bonding strength.
For this holistic study, we first self-assembled colloidal crystals from five types of silica hollow spheres which differ either in their size or in their shell thickness. As can be seen in Figure 35a, the thermal conductivity of the colloidal crystals shows a strong dependence on the nanoparticle geometry. In vacuum, where only solid conduction contributes to the thermal transport, the lowest thermal conductivity of 27 $mWm^{-1}K^{-1}$ was found for the colloidal crystal with the largest particles (HS-469/17). The thermal conductivity rises significantly for measurements in air, nitrogen, and helium due to the additional contribution of gaseous conduction in the porous structure. Here, the absolute rise depends strongly on the pore size due to the size dependency of the gaseous phonon mean free path. In general, the FEM data (Figure 35b) show the same trend as the experimental one.
With the help of heat flux analysis (Figure 35c), we further clarified the individual contributions of solid conduction, open-pore and closed-pore volume gaseous conduction. Due to the higher thermal conductivity of silica, the predominating contribution to the overall heat transport is across the silica network (Figure 35c,

high heat flux density). Moreover, the open-pore volume gaseous conduction dominates over the closed-pore gaseous conduction.

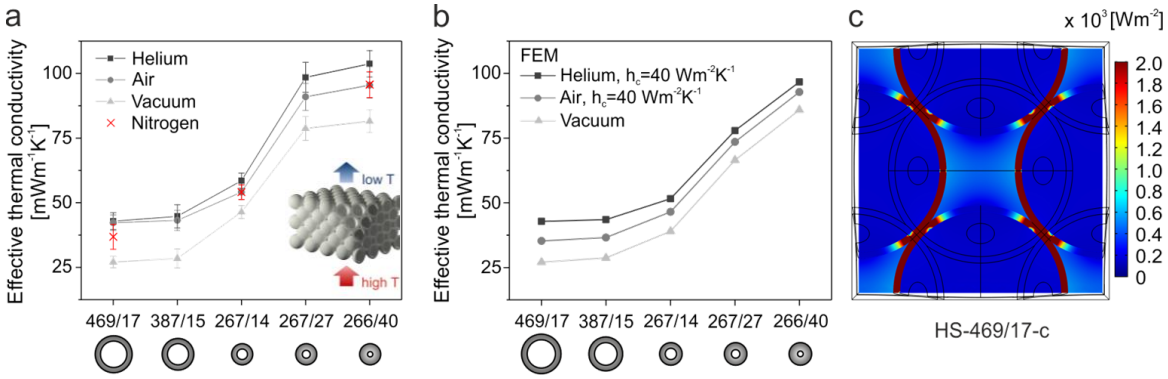

Figure 35. Influence of particle geometry and surrounding atmosphere on the thermal transport in hollow silica sphere colloidal crystals: thermal conductivity in helium and air at 1000 mbar as well as vacuum obtained from a) experiments and b) finite element modeling. c) Heat flux density distribution in a silica hollow sphere colloidal crystal surrounded by helium gas. Adapted from Ruckdeschel *et al.*[90] with permission from Wiley VCH.

Next, we investigated the influence of the symmetry of the particle assembly and the interparticle bonding strength on the thermal insulation properties. In Figure 36a, the helium pressure-dependent thermal conductivity is compared for a crystalline assembly (HS-469/17-c), an amorphous (randomly close-packed) assembly (HS-469/17-a), and an amorphous assembly with reduced interparticle bonding strength (HS-469/17-aa). In helium at 1000 mbar, all assemblies have a comparable thermal conductivity of around 40 $mWm^{-1}K^{-1}$. This demonstrates again the high impact of the gaseous conduction on the overall thermal transport. With decreasing helium pressure, significant differences become visible. The strongest reduction of the thermal conductivity was obtained for the amorphous assembly with reduced interparticle bonding strength (8 $mWm^{-1}K^{-1}$). The strong influence of the interparticle bonding strength on the thermal conductivity was emphasized by further simulations (Figure 36b).

Thus, besides the particle geometry and assembly geometry, the interparticle bonding strength is one of the promising tools to obtain a highly insulating material (in vacuum). However, gaseous conduction deteriorates the extreme thermal insulation of silica hollow sphere assemblies.

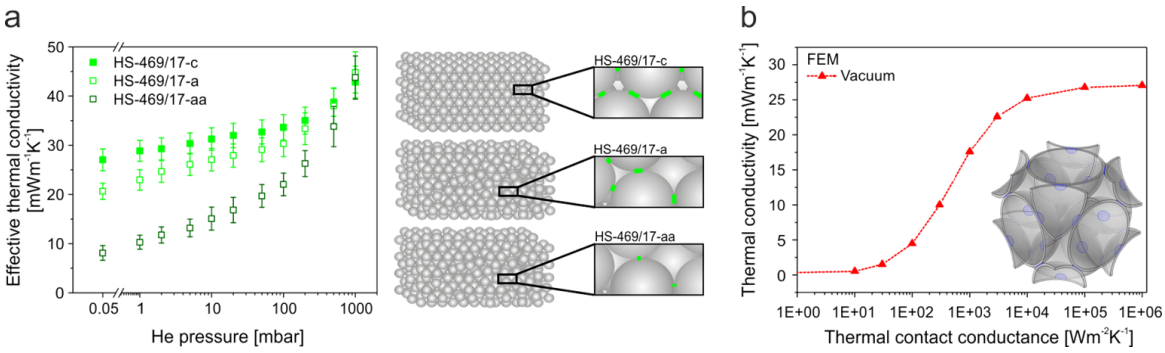

Figure 36. Influence of assembly symmetry and interparticle bonding strength: a) Experimental data of a crystalline assembly (HS-469/17-c), an amorphous assembly (HS-469/17-a), and an amorphous assembly with reduced interparticle bonding strength (HS-469/17-aa). b) Simulated data show the strong impact of the thermal contact conductance of adjacent particles. Adapted from Ruckdeschel *et al.*[90] with permission from Wiley VCH.

Chapter 8: Thermal Transport in Binary Colloidal Glasses: Composition Dependence and Percolation Assessment

Whereas in the previous chapter the focus lied on pure silica hollow sphere colloidal assemblies, we explored here the effects of mixing two particle types on the thermal transport. Therefore, binary amorphous colloidal assemblies, so-called binary colloidal glasses, were assembled from silica hollow spheres and poly(methyl methacrylate-*co*-*n*-butyl acrylate) [P(MMA-*co*-nBA)] particles with similar sizes (≈ 400 nm). We found for both experiments and simulations that the thermal conductivity (in vacuum) increases monotonically from 13 $mWm^{-1}K^{-1}$ to 57 $mWm^{-1}K^{-1}$ with increasing polymer particle content (Figure 37a).

Furthermore, the simulated data are in good agreement to the effective medium theory (EMT) and the Maxwell-Eucken 1 model (ME1). Thus, the mixing of two unlike particles led neither to a reduced thermal conductivity due to additional interfacial resistances, nor to a percolation threshold. However, in further simulations with diamond particles (high thermal conductivity) instead of polymer particles, we observed such a distinct percolation threshold at around 30 % diamond particles (Figure 37b). This steplike increase in the thermal conductivity is only well described by the percolation theory and the simple EMT model. Using the EMT model we found that the thermal conductivity difference

between the respective components ($\kappa_1 : \kappa_2$) should at least be 1:500 to obtain a percolating behavior of the colloidal assembly.

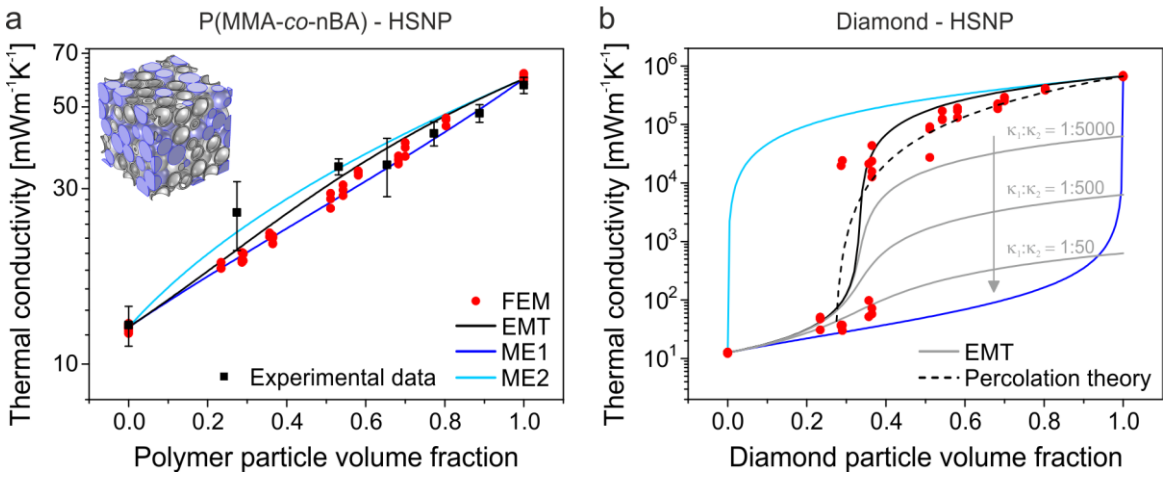

Figure 37. Composition dependent thermal conductivity of a binary colloidal glass: a) Polymer particles mixed with silica hollow spheres. Data from experiment and FEM is compared to effective medium theory (EMT), Maxwell-Eucken 1 (ME1), and Maxwell-Eucken 2 (ME2). Inset shows an exemplary geometry used for FEM. b) Diamond particles mixed with silica hollow spheres. Data from FEM is compared to EMT and percolation theory. Adapted from Ruckdeschel *et al.*[91] with permission from American Physical Society.

Chapter 9: Low Thermal Conductivity through Dense Particle Packings with Optimum Disorder

Besides mixing two similarly sized particle types made of different materials, in this chapter, we mixed two monodisperse, differently sized polystyrene (PS) particles in a well-defined way. First of all, the effects of mixing PS particles with a size ratio of around 0.8 were experimentally studied in dependence of the large particle volume ratio. We found that the crystallinity of the colloidal assemblies decreases gradually from the highly crystalline homo-particle assemblies to intermediate mixing ratios where a random packing of the particles is observed. Consequently, there is a transition from order to disorder by adding the other particle type. Interestingly, the determined thermal conductivity follows the order of the colloidal assembly: the thermal conductivity is highest for the ordered homo-particle assemblies, and then decreases gradually with increasing disorder until a reduction of around 20 % is observed for intermediate mixing ratios

(Figure 38a). Thereby, the overall drop of the thermal conductivity is 10 % more than expected from the density. To understand the additional contribution of the thermal conductivity reduction, we conducted molecular dynamics (MD) simulations, which provided the virtual colloidal assemblies, in combination with FEM simulations. We found that due to the short assembly time-scale used for the MD simulations, disordered structures are already obtained for small mixing ratios. This is also observed by the average number of particles surrounding a center particle (*i.e.*, the number of next neighbors) which drops from 12 for the homo-particle assemblies to 10 for all other mixing ratios. Interestingly, the thermal conductivity of these virtual assemblies decreases rapidly in an asymmetric manner with a minimum thermal conductivity (reduction by 45 %) at a large particle volume ratio of 16 % (Figure 38b). Analysis of the heat flux streamlines across the colloidal assemblies revealed that there is a direct correlation of the thermal conductivity and the mean streamline length. Whereas the thermal transport pathways in ordered structures are rather straight, strongly bended, elongated streamlines are observed in the disordered cases (insets in Figure 38b).

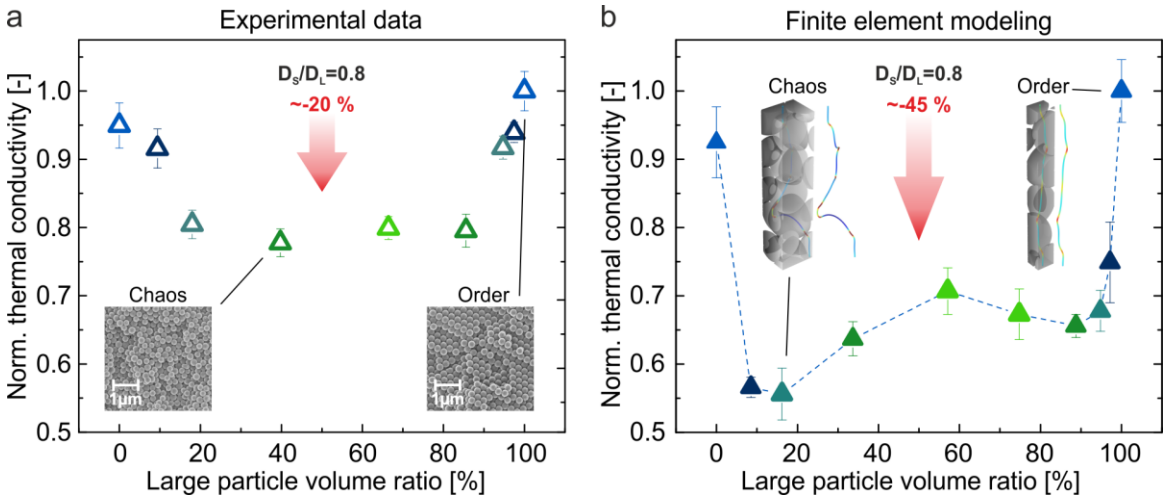

Figure 38. Effect of mixing two monodisperse, differently-sized particles with a size ratio of 0.8 on the thermal transport: Normalized thermal conductivity of binary PS colloidal assemblies with different mixing ratios obtained from a) experiments and b) FEM. The red arrows indicate the reduction of the thermal conductivity due to disorder. The insets show exemplarily scanning electron images (a) and heat flux streamlines (b) of an ordered and disordered colloidal assembly; respectively. Adapted from Nutz *et al.*[92] with permission from Wiley VCH.

We attributed the appearance of the global minimum to the local particle environment: A few large particles are surrounded by several small particles. This leads obviously to a strong disturbance of the streamline length and consequently to an even stronger reduced thermal conductivity.

As illustrated in Figure 39a, further FEM simulations showed that the bending of the heat flux streamlines is even stronger for a lower size ratio. Furthermore, the distributions of the relative streamline length (Figure 39b) and number of next neighbors (Figure 39c) broaden with decreasing size ratio. Interestingly, a second population of next neighbors between 20 and 30 arises for the smallest size ratio of 0.54. Due to the effects of the local particle environment, the thermal conductivity from both experiment and simulation decreases with decreasing size ratio (Figure 39d). Finally, by the introduction of disorder with an optimized size mismatch, a reduced thermal conductivity of 44 % compared to the ordered homo-particle colloidal assembly is obtained.

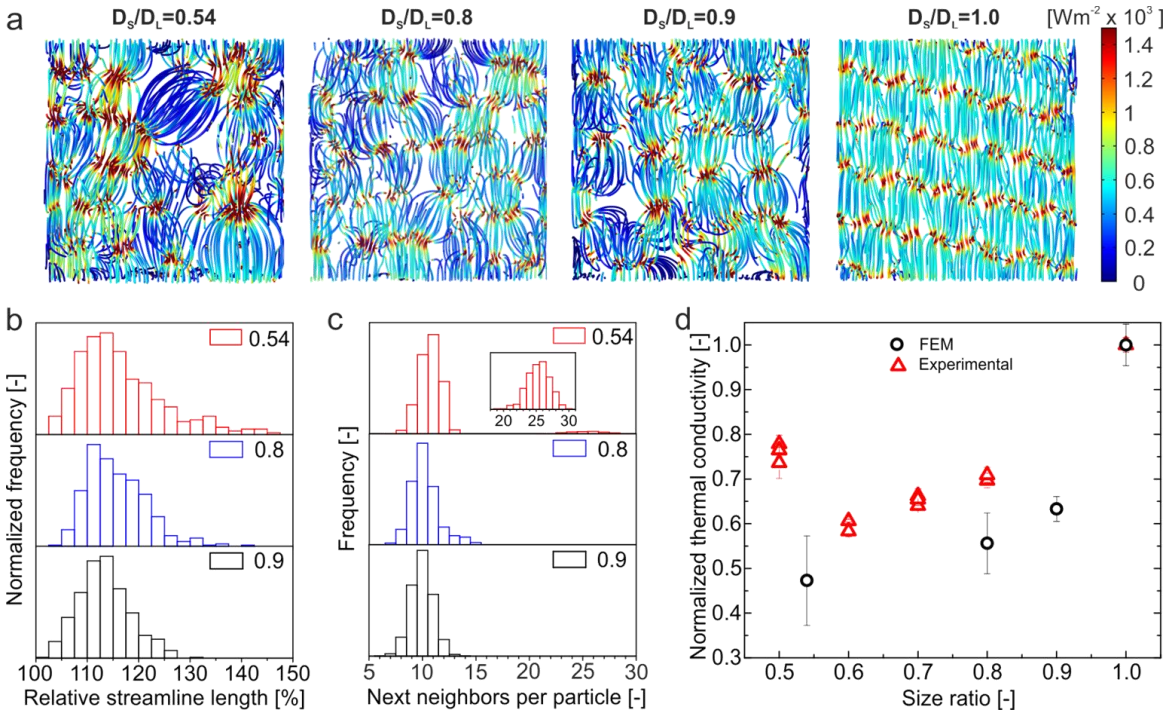

Figure 39. Influence of the size ratio (D_S/D_L) on the thermal transport at a large particle volume ratio of around 20 %: a) Heat flux streamlines across colloidal assemblies with varying size ratio. b) Distribution of the relative streamline length and c) number of next neighbors. d) Thermal conductivity obtained from FEM and experiment in dependence of the size ratio. Reprinted from Nutz *et al.*[92] with permission from Wiley VCH.

Chapter 10: Direct Measurement of the In-Plane Thermal Diffusivity of Semitransparent Thin Films by Lock-In Thermography: An Extension of the Slopes Method

As introduced in Chapter 2.2.3., LIT is a non-destructive method which can be used for the characterization of the in-plane thermal diffusivity of thermally thin solids. In brief, a free-standing sample is periodically heated by a focused laser beam and the surface temperature oscillations are detected by an infrared (IR) camera. The amplitude and phase of the temperature oscillations are calculated from the detected IR images. The well-known slopes method is used to calculate the in-plane thermal diffusivity from the product of the slopes of the linear phase and amplitude radial profiles.

First, we developed a two-dimensional model for heat conduction through a semitransparent film. Using this model, we conducted numerical simulations for a thin polymeric film. We found that the slopes method, which was developed for optically opaque films, gives far from the heating spot ($\geq \mu$) also accurate thermal diffusivity values for semitransparent thin films.

In the second part of this Chapter, we conducted measurements on thin polymeric films with our home-built LIT set-up. A red dye (phenol red, PR) was added to poly(methyl methacrylate) (PMMA) and low-density polyethylene (LDPE) to vary the optical absorption coefficient of these polymers in the visible wavelength range (semitransparent to opaque). We used polyether ether ketone (PEEK) with varying film thickness to tune the optical absorption coefficient of this polymer in the IR wavelength range (semitransparent to opaque). On the basis of our theoretical finding, we evaluated the LIT measurements far from the heating spot ($> 2\mu$). Most importantly, we found no dependence of the thermal diffusivity on the optical properties of the polymer films. Furthermore, all values are in good agreement to literature values (Figure 40). This confirms that the slopes method gives accurate values even for semitransparent, thin films.

Additionally, since literature values of PEEK films bought from the same company are available[19, 93], the investigated PEEK films serve as reference material. The accuracy of our LIT setup and evaluation procedure is validated by a slight deviation of only 5 % from the average value from Mendioroz *et al.*[19]

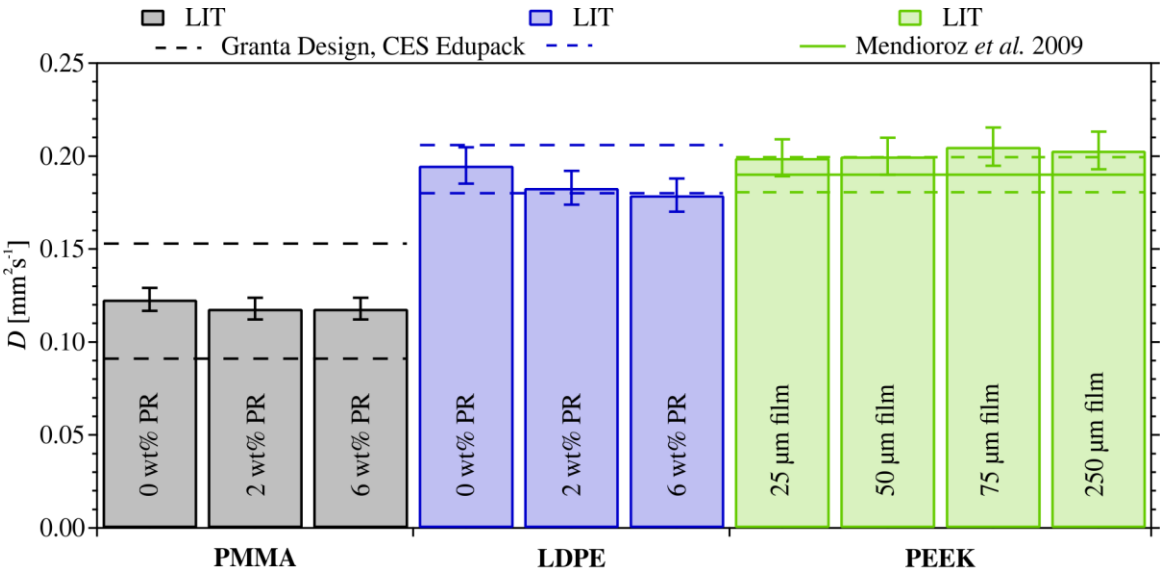

Figure 40. In-plane thermal diffusivities of the investigated polymer films with varying optical properties: PMMA and LDPE with 0, 2, and 6 wt% phenol red (PR), respectively, and PEEK films with a thickness of 25, 50, 75, and 250 µm (error bars are 5 % uncertainty). The black and blue dashed lines represent the lower and upper limits of the reference values for unmodified PMMA and LDPE. The solid green line represents the literature value of PEEK measured with LIT. The green dashed lines are the 5 % uncertainty range given by Mendioroz *et al.*[19] Adapted from Philipp *et al.*[94] with permission from American Chemical Society.

The extension of the slopes method to semitransparent films enables the use of LIT for a wide range of materials. In the following two chapters, we applied the slopes method to layered, two-dimensional nanomaterials. Due to their structural anisotropy, these nanomaterials exhibit strong anisotropic thermal transport properties.

Chapter 11: Anisotropic Thermal Transport in Spray-Coated Single-Phase Two-Dimensional Materials: Synthetic Clays vs. Graphene Oxide

In this study, we compare the anisotropic thermal transport properties of two different single phase materials which were prepared via spray-coating of a dilute

aqueous dispersion: synthetic sodium fluorohectorite (Hec, $[Na_{0.5}]^{inter}[Mg_{2.5}Li_{0.5}]^{oct}[Si_4]^{tet}O_{10}F_2$) and graphene oxide (GO). Electron microscopy images (Figure 41) demonstrate the macroscopically stacked Hec and GO platelets (the so-called Bragg stacks), respectively. The insets depict the chemical structures and the 2D natures of these two materials.

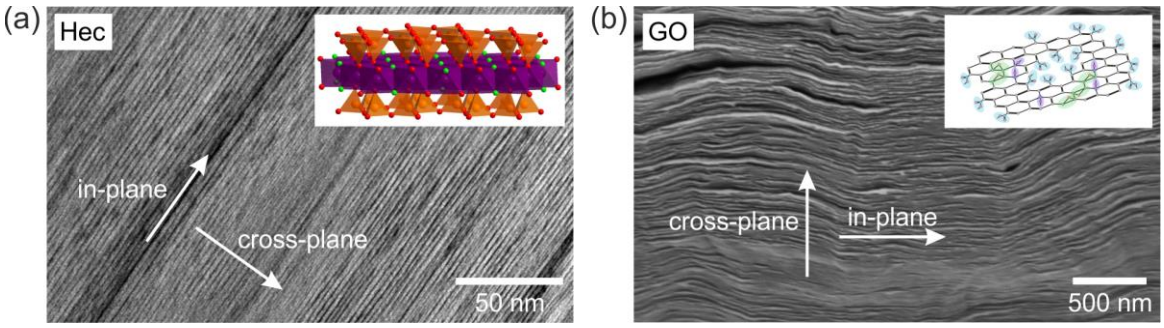

Figure 41. Single-phase, two-dimensional materials: a) Transmission electron microscopy image of perfectly aligned Hec nanoplatelets. The inset shows the chemical structure of the Hec platelets, where the red atoms are oxygen, the green ones are fluoride, the orange ones are silicone, and the purple ones magnesium and lithium. b) Scanning electron image of stacked GO nanoplatelets. The inset depicts an exemplary chemical structure of graphene oxide with various functional groups and defects. Adapted from Philipp *et al.*[95] with permission from American Chemical Society.

Overall, two different samples per material class were prepared: synthetic Hec consisting of large nanoplatelets (Hec-L), synthetic Hec consisting of smaller platelets (Hec-S) fabricated from Hec-L via ultrasonication, synthetic GO (GO-syn), and commercial GO (GO-com). Since the thermal transport properties depend on several factors, a holistic characterization of the structural properties and chemical composition of all samples was conducted. These analyses revealed that both Hec samples consist of Hec platelets with the same chemical composition. Furthermore, their structures are homogeneous, one-dimensional crystalline (in the cross-plane direction) and the platelets have the same thickness of ~10 Å, *i.e.*, the stacks have the same periodicity. Thus, the structural properties are independent of the platelet size. As expected, the platelet areas of the nanoplatelets are significantly different, more precisely $\approx 800\ \mu m^2$ in case of Hec-L, and $\leq 0.4\ \mu m^2$ in case of Hec-S. The GO samples, on the other hand, were found both to be chemically different (different degrees of oxidation) and have various sizes/size

distributions. Furthermore, in contrast to the Hec samples, the GO samples have a less well-defined order and thinner platelets (~6 Å).

The anisotropic thermal transport properties were determined by lock-in thermography and the photoacoustic method. These measurements yield the in-plane ($\kappa_{\parallel}$) and cross-plane thermal conductivity ($\kappa_{\perp}$), respectively. The results are summarized in Figure 42, where the grey numbers are the anisotropy ratio ($\kappa_{\parallel}/\kappa_{\perp}$). In case of the two Hec samples we found comparable thermal properties with a high in-plane thermal conductivity of around 5.7 $Wm^{-1}K^{-1}$ and a low cross-plane thermal conductivity of around 0.2 $Wm^{-1}K^{-1}$. This gives compared to natural clays and other synthetic ordered clays a relatively high anisotropy ratio of ≈ 30 for both samples independent of the platelet size. This independence can be explained by the small phonon mean free path of Hec, which is significantly smaller than the platelet size. In contrast, the two GO samples have lower in-plane thermal conductivities. Furthermore, GO-syn has a higher in-plane thermal conductivity than GO-com. The literature values of the in-plane thermal conductivity exhibit also a high variability. In our case, the reason lies in the different amounts of oxygen-containing groups, (the higher the degree of oxidation, the less the in-plane thermal conductivity). Low cross-plane thermal conductivities of around 0.1 $Wm^{-1}K^{-1}$ were obtained which are in good agreement to literature values.

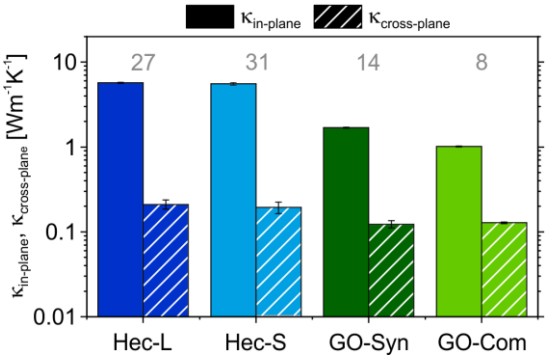

Figure 42. In-plane and cross-plane thermal conductivities. The grey numbers are the thermal conductivity ratios. Adapted from Philipp *et al.*[95] with permission from American Chemical Society.

Chapter 12: Tunable Thermoelastic Anisotropy in Hybrid Bragg Stacks with Extreme Polymer Confinement

Finally, the anisotropic thermomechanical properties of strongly alternating clay nanosheets/polymer Bragg stacks were studied as a model system for other hybrid nanomaterials. Therefore, the same clay sample consisting of 20 μm large sodium fluorohectorite (Hec) nanoplatelets as investigated in Chapter 11 has been used. Polyvinylpyrrolidone (PVP) chains are highly confined in between these Hec nanosheets. These long-range 1D ordered materials were again fabricated with Angstrom precision via a simple spray-coating process. By varying the volume fraction of the polymer, the thickness of the PVP layer (9 – 28 Å), and thus the periodicity of the hybrid stacks, was adjusted. In this way, four hybrid materials with 49, 60, 69, and 77 vol% PVP have been prepared beside the two single-phase samples (100 vol% Hec and 100 vol% PVP). All stacked samples are macroscopically aligned with translational symmetry in the cross-plane direction. However, only the samples with 60 and 69 vol% PVP are mostly defect free. This is due to their gallery heights (1.3 nm and 2.0 nm, respectively) which corresponds to the thickness of an individual PVP monolayer and bilayer, respectively. All other hybrid Bragg stacks have random interstratifications of these gallery spacings. The specific heat capacity and density of all samples have a linear relation to the Hec volume fraction (Figure 43a and b). These dependences follow an effective medium model of the bulk properties of the two single-phase materials independent of the extreme polymer confinement. Similar to the density and heat capacity, the in-plane thermal conductivity shows also a linear relation to the Hec content. It increases from a low value of 0.2 $Wm^{-1}K^{-1}$ to an exceptionally high value of 5.7 $Wm^{-1}K^{-1}$ (Figure 43c). This increase is in very good agreement to a parallel mixing model calculated from the bulk Hec and PVP in-plane thermal conductivities. Consequently, the extreme confinement of the PVP chains does not affect the in-plane thermal conductivity of the hybrid samples. The cross-plane

thermal conductivity deviates from an effective medium behavior. This disagreement is due to the Hec/PVP interfaces leading to a higher thermal interface resistance. Here, the phonon mean free path is in the same order of the stack periodicity. Thus, the Bragg stacks show a lower cross-plane thermal conductivity of 0.09 $Wm^{-1}K^{-1}$ independent of the exact Hec content (Figure 43d). However, the thermal conductivity anisotropy ($\kappa_{\parallel}/\kappa_{\perp}$) depends on the hybrid composition and has its record high maximum of 38 at 51 vol% Hec (Figure 43e).

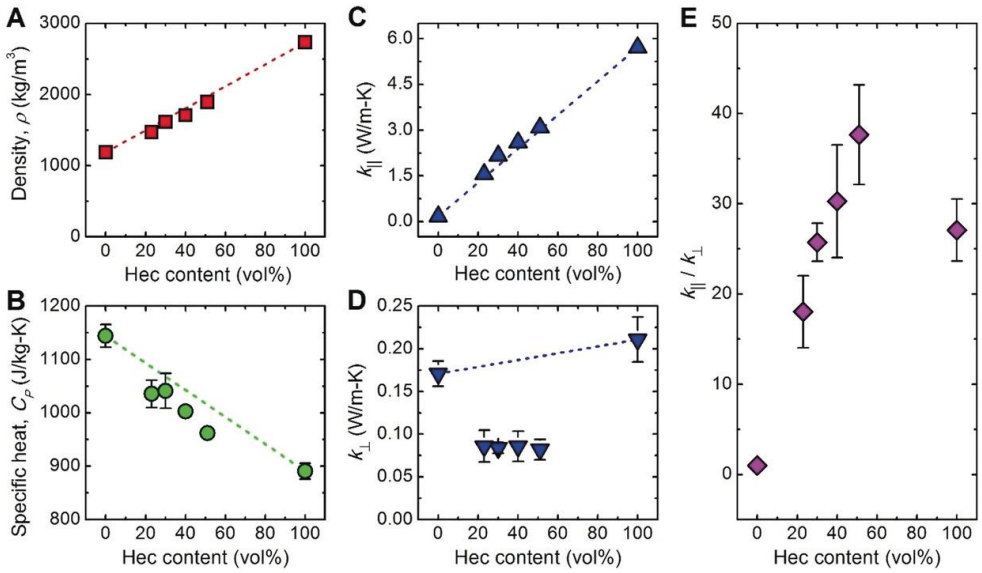

Figure 43. Thermal transport properties of all Bragg stacks: a) Density, b) Specific heat capacity, c) Cross-plane thermal conductivity $\kappa_{\perp}$., d) In-plane thermal conductivity $\kappa_{\parallel}$, and e) Thermal conductivity anisotropy ratio $\kappa_{\parallel}/\kappa_{\perp}$. Reprinted from Wang et al.[96] with permission from Wiley VCH.

Analogous to the thermal conductivity, the mechanical properties, which are measured by Brillouin light scattering, show a strong direction dependence. Despite the extreme Angstrom-level polymer confinement, all derived mechanical moduli (Young's moduli $E_{\perp}$ and $E_{\parallel}$, torsional shear modulus, and sliding shear modulus) follow an effective medium behavior which can be obtained from the pure one-phase components. The Young's moduli and torsional shear modulus increase with increasing Hec content, whereas the sliding shear modulus slightly decrease with increasing Hec content. The decrease of the sliding shear modulus could be explained by a reduced polymer chain entanglement. Furthermore, the

structural anisotropy explains the anisotropic Young's moduli, which increase from 1 to 7 for 0 to 100 vol% Hec.

A correlation of the anisotropic mechanical moduli and thermal conductivities revealed that the in-plane thermal conductivity is directly related to the Young's moduli and the torsional shear modulus. Contrary, the direction-dependent mechanical properties do not influence the cross-plane thermal conductivity. Here, the interfacial resistance (Hec/PVP) dominates over the mechanical properties.

4.2. Individual Contributions to Joint Publications

Chapter 6: "The Accuracy of Laser Flash Analysis Explored by Finite Element Modeling and Numerical Fitting"

This work is submitted as a full paper in the journal Heat and Mass Transfer by Alexandra Philipp, Jonas Eichinger, Roland. C. Aydin, Argyrios Georgiadis, Christian. J. Cyron and Markus Retsch.

I planned and performed all finite element simulations, did the data evaluation, and wrote the major part of the manuscript. Argyrios Georgiadis conducted XFA measurements. I evaluated the XFA data and wrote the corresponding section in the manuscript. Jonas Eichinger, Roland C. Aydin, and Christian J. Cyron developed the computational fitting framework and took part in scientific discussions. Jonas Eichinger wrote the corresponding section in the manuscript. Markus Retsch supervised the work. Christian J. Cyron and Markus Retsch corrected the manuscript.

Chapter 7: "Understanding Thermal Insulation in Porous, Particulate Materials"

This work is published as a full paper in the journal Advanced Functional Materials by Pia Ruckdeschel, Alexandra Philipp, and Markus Retsch.

I planned and performed all finite element simulations, did the data evaluation, and wrote the corresponding section in the supporting information. Furthermore,

I was involved in scientific discussions and did proofreading of the manuscript. Pia Ruckdeschel synthesized and characterized the particles as well as particle assemblies, took part in scientific discussions, and wrote the manuscript. Markus Retsch supervised the project and corrected the manuscript.

Chapter 8: "Thermal Transport in Binary Colloidal Glasses: Composition Dependence and Percolation Assessment"

This work is published as a full paper in the journal Physical Review E by Pia Ruckdeschel, Alexandra Philipp, Bernd A. F. Kopera, Flora Bitterlich, Martin Dulle, Nelson W. Pech-May, and Markus Retsch.

I planned and performed all finite element simulations, did the data evaluation, and wrote the corresponding sections in the manuscript and supporting information. Furthermore, I was involved in scientific discussions and did proofreading and revisions of the manuscript. Pia Ruckdeschel synthesized and characterized the particles as well as particle assemblies, took part in scientific discussions, and wrote the manuscript. Bernd A. F. Kopera and Martin Dulle supported the finite element simulations. Flora Bitterlich was involved in scientific discussions. Nelson W. Pech-May formatted and corrected the manuscript. Markus Retsch supervised the project and corrected the manuscript.

Chapter 9: "Low Thermal Conductivity Through Dense Particle Packings with Optimum Disorder"

This work is published as a full paper in the journal Advanced Materials by Fabian A. Nutz, Alexandra Philipp, Bernd A. F. Kopera, Martin Dulle, and Markus Retsch.

I planned and performed all finite element simulations, did the data evaluation, and wrote the corresponding sections in the manuscript and supporting information. Furthermore, I was involved in scientific discussions and did proofreading and revisions of the manuscript. Fabian A. Nutz synthesized and

characterized the particle assemblies, took part in scientific discussions and wrote the manuscript. Bernd A. F. Kopera supported this work with self-written Phython scripts and took part in scientific discussions.
Martin Dulle conducted molecular dynamics simulations, wrote the corresponding section in the supporting information and was involved in scientific discussions. Markus Retsch supervised the project and corrected the manuscript.

Chapter 10: "Direct Measurement of the In-Plane Thermal Diffusivity of Semitransparent Thin Films by Lock-In Thermography: An Extension of the Slopes Method"

This work is published as a full paper in the journal Analytical Chemistry by Alexandra Philipp, Nelson W. Pech-May, Bernd A. F. Kopera, Anna M. Lechner, Sabine Rosenfeldt, and Markus Retsch.

I synthesized and characterized the polymeric samples, planned and performed all lock-in measurements and did the data evaluation. Furthermore, I wrote major parts of the manuscript. Nelson W. Pech-May was responsible for numerical simulations, wrote the corresponding section in the manuscript, helped with UV-vis measurements and was involved in scientific discussions. Bernd A. F. Kopera helped with the automation of the evaluation of the lock-in measurements. Anna M. Lechner did the thermal annealing of the polymeric samples. Sabine Rosenfeldt measured XRD and SAXS, analyzed the data, and was involved in scientific discussions. Markus Retsch supervised the project and corrected the manuscript.

Chapter 11: "Anisotropic Thermal Transport in Spray-Coated Single-Phase Two-Dimensional Materials: Synthetic Clay vs. Graphene Oxide"

This work is published as a full paper in the journal ACS Applied Materials & Interfaces by Alexandra Philipp, Patrick Hummel, Theresa Schilling, Patrick Feicht, Sabine Rosenfeldt, Michael Ertl, Marius Schöttle, Anna M. Lechner, Zhen Xu, Chao Gao, Josef Breu, and Markus Retsch.

I conducted and analyzed the lock-in thermography measurements to obtain the in-plane thermal conductivity. Furthermore, Patrick Hummel and I prepared the samples for DSC and measured the density using helium pycnometry. Moreover, Patrick Hummel and I wrote the manuscript. Patrick Hummel performed and analyzed photoacoustic measurements to determine the cross-plane thermal conductivity. Theresa Schilling synthesized the Hec nanoplatelets and fabricated the stacked Hec and GO samples. Furthermore, Theresa Schilling performed IR measurements. Patrick Feicht synthesized the GO used to fabricate GO-syn. Sabine Rosenfeldt performed and analyzed SAXS measurements. Michael Ertl conducted and analyzed XPS measurements. Marius Schöttle performed Raman spectroscopy. Anna M. Lechner conducted and analyzed DSC measurements to obtain the specific heat. Zhen Xu and Chao Go provided the commercial GO used to fabricate GO-com. Markus Retsch and Josef Breu initialized the idea, supervised this work, and corrected the manuscript.

Chapter 12: "Tunable Thermoelastic Anisotropy in Hybrid Bragg Stacks with Extreme Polymer Confinement"

This work is published as a full paper in the journal Angewandte Chemie International Edition by Zuyuan Wang, Konrad Rolle, Theresa Schilling, Patrick Hummel, Alexandra Philipp, Bernd A. F. Kopera, Anna M. Lechner, Markus Retsch, Josef Breu, and George Fytas.

I conducted and analyzed the lock-in thermography measurements to obtain the in-plane thermal conductivity. Furthermore, I prepared the samples for DSC and helium pycnometry measurements. Theresa Schilling explored and optimized the Hec/PVP system, fabricated the hybrid Bragg stacks, and characterized their structures. Konrad Rolle conducted the BLS experiments. Patrick Hummel performed and analyzed the photoacoustic characterization to obtain the cross-plane thermal conductivity and measured the sample densities. Bernd A. F. Kopera

conducted additional lock-in thermography measurements and contributed to the lock-in thermography analysis. Anna M. Lechner conducted and analyzed the DSC measurements to obtain the specific heat. Zuyuan Wang analyzed the BLS data and established the correlation between the mechanical moduli and thermal conductivity. Zuyuan Wang, Markus Retsch, Josef Breu and George Fytas wrote the manuscript. All authors have given approval to the final version of the manuscript. Markus Retsch, Josef Breu, and George Fytas initialized the idea and supervised this work.

5. References

1. Ma, H.-Y.; Tong, L.-F.; Xu, Z.-B.; Fang, Z.-P., Functionalizing carbon nanotubes by grafting on intumescent flame retardant: Nanocomposite synthesis, morphology, rheology, and flammability. *Advanced Functional Materials* **2008,** *18* (3), 414-421.

2. Dong, L.; Hu, C.; Song, L.; Huang, X.; Chen, N.; Qu, L., A large-area, flexible, and flame-retardant graphene paper. *Advanced Functional Materials* **2016,** *26* (9), 1470-1476.

3. Xia, Y.; Gates, B.; Yin, Y.; Lu, Y., Monodispersed colloidal spheres: Old materials with new applications. *Advanced Materials* **2000,** *12* (10), 693-713.

4. Moore, A. L.; Shi, L., Emerging challenges and materials for thermal management of electronics. *Materials Today* **2014,** *17* (4), 163-174.

5. Notario, B.; Pinto, J.; Solorzano, E.; De Saja, J. A.; Dumon, M.; Rodríguez-Pérez, M., Experimental validation of the Knudsen effect in nanocellular polymeric foams. *Polymer* **2015,** *56*, 57-67.

6. Koebel, M.; Rigacci, A.; Achard, P., Aerogel-based thermal superinsulation: an overview. *Journal of Sol-Gel Science and Technology* **2012,** *63* (3), 315-339.

7. Lu, X.; Arduini-Schuster, M. C.; Kuhn, J.; Nilsson, O.; Fricke, J.; Pekala, R. W., Thermal conductivity of monolithic organic aerogels. *Science* **1992,** *255* (5047), 971-2.

8. Schiffres, S. N.; Kim, K. H.; Hu, L.; McGaughey, A. J. H.; Islam, M. F.; Malen, J. A., Gas diffusion, energy transport, and thermal accommodation in single-walled carbon nanotube aerogels. *Advanced Functional Materials* **2012,** *22* (24), 5251-5258.

9. Chiritescu, C.; Cahill, D. G.; Nguyen, N.; Johnson, D.; Bodapati, A.; Keblinski, P.; Zschack, P., Ultralow thermal conductivity in disordered, layered WSe_2 crystals. *Science* **2007,** *315* (5810), 351-353.

10. Losego, M. D.; Blitz, I. P.; Vaia, R. A.; Cahill, D. G.; Braun, P. V., Ultralow thermal conductivity in organoclay nanolaminates synthesized via simple self-assembly. *Nano Letters* **2013,** *13* (5), 2215-2219.

11. Moon, J.; Minnich, A. J., Sub-amorphous thermal conductivity in amorphous heterogeneous nanocomposites. *RSC Advances* **2016,** *6* (107), 105154-105160.

12. Mizuno, H.; Mossa, S.; Barrat, J. L., Beating the amorphous limit in thermal conductivity by superlattices design. *Scientific Reports* **2015,** *5*, 14116.

13. Zhang, H.; Minnich, A. J., The best nanoparticle size distribution for minimum thermal conductivity. *Scientific Reports* **2015,** *5*, 8995.

14. Kim, W.; Zide, J.; Gossard, A.; Klenov, D.; Stemmer, S.; Shakouri, A.; Majumdar, A., Thermal conductivity reduction and thermoelectric figure of merit increase by embedding nanoparticles in crystalline semiconductors. *Physical Review Letters* **2006,** *96* (4), 045901.

15. Nutz, F. A.; Retsch, M., Interfacial and volumetric sensitivity of the dry sintering process of polymer colloidal crystals: a thermal transport and photonic bandgap study. *Phys. Chem. Chem. Phys.* **2017,** *19* (24), 16124-16130.

16. Nutz, F. A.; Ruckdeschel, P.; Retsch, M., Polystyrene colloidal crystals: Interface controlled thermal conductivity in an open-porous mesoparticle superstructure. *Journal of Colloid and Interface Science* **2015,** *457*, 96-101.

17. Ruckdeschel, P.; Kemnitzer, T. W.; Nutz, F. A.; Senker, J.; Retsch, M., Hollow silica sphere colloidal crystals: insights into calcination dependent thermal transport. *Nanoscale* **2015,** *7* (22), 10059-10070.

18. Suh, K. W.; Park, C. P.; Maurer, M. J.; Tusim, M. H.; Genova, R. D.; Broos, R.; Sophiea, D. P., Lightweight cellular plastics. *Advanced Materials* **2000,** *12* (23), 1779-1789.

19. Mendioroz, A.; Fuente-Dacal, R.; Apinaniz, E.; Salazar, A., Thermal diffusivity measurements of thin plates and filaments using lock-in thermography. *Review of Scientific Instruments* **2009,** *80* (7), 074904.

20. Zhang, B.; Imhof, R. E., Theoretical analysis of the surface thermal wave technique for measuring the thermal diffusivity of thin slabs. *Applied Physics A* **1996,** *62* (4), 323-334.

21. Salazar, A.; Mendioroz, A.; Fuente, R.; Celorrio, R., Accurate measurements of the thermal diffusivity of thin filaments by lock-in thermography. *Journal of Applied Physics* **2010,** *107* (4), 043508.

22. Wolf, A.; Pohl, P.; Brendel, R., Thermophysical analysis of thin films by lock-in thermography. *Journal of Applied Physics* **2004,** *96* (11), 6306.

23. Salazar, A.; Mendioroz, A.; Fuente, R., The strong influence of heat losses on the accurate measurement of thermal diffusivity using lock-in thermography. *Applied Physics Letters* **2009,** *95* (12), 121905.

24. Lienhard IV, J. H. a. L. V., John. H., A heat transfer textbook. *Phlogiston Press* **2012,** *4th ed.*

25. Rohsenow, W. M.; Hartnett, J. P.; Cho, Y. I., *Handbook of heat transfer*. McGraw-Hill Education: 1998.

26. Nußelt, W., Das Grundgesetz des Wärmeübergangs. *Gesundheits-Ingenieur* **1915,** *38*, 872.

27. Chen, G., *Nanoscale energy transport and conversion: A parallel treatment of electrons, molecules, phonons, and photons*. Oxford University Press: 2005.

28. Breitenstein, O.; Warta, W.; Langenkamp, M., *Lock-in thermography: Basics and use for evaluating electronic devices and materials*. Springer: 2010.

29. Vollmer, M.; Möllmann, K.-P., *Infrared thermal imaging: Fundamentals, research and applications*. Wiley-VCH: 2013.

30. Marconnet, A. M.; Asheghi, M.; Goodson, K. E., From the Casimir limit to phononic crystals: 20 years of phonon transport studies using silicon-on-insulator technology. *Journal of Heat Transfer* **2013,** *135* (6), 061601-061601-10.

31. Asheghi, M.; Kurabayashi, K.; Kasnavi, R.; Goodson, K. E., Thermal conduction in doped single-crystal silicon films. *Journal of Applied Physics* **2002,** *91* (8), 5079-5088.

32. Kittel, C., *Introduction to solid state physics*. John Wiley & Sons: New York, 1986.

33. Ziman, J. M., *Electrons and phonons*. Oxford University Press: London, 1960.

34. Berman, R., *Thermal conduction in solids*. Oxford University Press: Oxford, 1976.

35. Berman, R.; Foster, E. L.; Ziman, J. M., Thermal conduction in artificial sapphire crystals at low temperatures I. Nearly perfect crystals. *Proceedings of the Royal Society of London. Series A. Mathematical and Physical Sciences* **1955,** *231* (1184), 130-144.

36. Chávez-Ángel, E.; Reparaz, J. S.; Gomis-Bresco, J.; Wagner, M. R.; Cuffe, J.; Graczykowski, B.; Shchepetov, A.; Jiang, H.; Prunnila, M.; Ahopelto, J.; Alzina, F.; Torres, C. M. S., Reduction of the thermal conductivity in free-standing silicon nano-membranes investigated by non-invasive Raman thermometry. *APL Materials* **2014,** *2* (1), 012113.

37. Hochbaum, A. I.; Chen, R.; Delgado, R. D.; Liang, W.; Garnett, E. C.; Najarian, M.; Majumdar, A.; Yang, P., Enhanced thermoelectric performance of rough silicon nanowires. *Nature* **2008,** *451*, 163.

38. Zhou, Y.; Hu, M., Record low thermal conductivity of polycrystalline Si nanowire: breaking the Casimir limit by severe suppression of propagons. *Nano Letters* **2016,** *16* (10), 6178-6187.

39. Peierls, R., Zur kinetischen Theorie der Wärmeleitung in Kristallen. *Annalen der Physik* **1929,** *395* (8), 1055-1101.

40. Phillips, W. A.; Weaire, D. L.; Pohl, R. O.; Anderson, A. C.; Hunklinger, S.; v. Schickfus, M.; Golding, B.; Graebner, J. E.; Jäckle, J., *Amorphous solids: Low-temperature properties*. Springer: Berlin, 1981.

41. Cahill, D. G.; Pohl, R. O., Lattice vibrations and heat transport in crystals and glasses. *Annual Review of Physical Chemistry* **1988,** *39* (1), 93-121.

42. Shenogin, S.; Bodapati, A.; Keblinski, P.; McGaughey, A. J., Predicting the thermal conductivity of inorganic and polymeric glasses: The role of anharmonicity. *Journal of Applied Physics* **2009,** *105* (3), 034906.

43. Alexander, S.; Entin-Wohlman, O.; Orbach, R., Phonon-fracton anharmonic interactions: The thermal conductivity of amorphous materials. *Physical Review B* **1986,** *34* (4), 2726-2734.

44. Zeller, R.; Pohl, R., Thermal conductivity and specific heat of noncrystalline solids. *Physical Review B* **1971,** *4* (6), 2029.

45. Wingert, M. C.; Zheng, J.; Kwon, S.; Chen, R., Thermal transport in amorphous materials: a review. *Semiconductor Science and Technology* **2016,** *31* (11), 113003.

46. Allen, P. B.; Feldman, J. L., Thermal conductivity of disordered harmonic solids. *Physical Review B* **1993,** *48* (17), 12581-12588.

47. Allen, P. B.; Feldman, J. L.; Fabian, J.; Wooten, F., Diffusons, locons and propagons: Character of atomic vibrations in amorphous Si. *Philosophical Magazine B* **1999,** *79* (11-12), 1715-1731.

48. Wang, X.; Liman, C. D.; Treat, N. D.; Chabinyc, M. L.; Cahill, D. G., Ultralow thermal conductivity of fullerene derivatives. *Physical Review B* **2013,** *88* (7), 075310.

49. Henry, A., Thermal transport in polymers. *Annual Review of Heat Transfer* **2013,** *17*, 485-520.

50. Choy, C. L., Thermal conductivity of polymers. *Polymer* **1977,** *18* (10), 984-1004.

51. Klemens, P. G., The thermal conductivity of dielectric solids at low temperatures (theoretical). *Proceedings of the Royal Society A: Mathematical, Physical and Engineering Sciences* **1951,** *208* (1092), 108-133.

52. Anderson, D. R., Thermal conductivity of polymers. *Chemical Reviews* **1966,** *66* (6), 677-690.

53. Vogel, N.; Retsch, M.; Fustin, C.-A.; del Campo, A.; Jonas, U., Advances in colloidal assembly: The design of structure and hierarchy in two and three dimensions. *Chemical Reviews* **2015,** *115* (13), 6265-6311.

54. Hrubesh, L. W.; Pekala, R. W., Thermal properties of organic and inorganic aerogels. *Journal of Materials Research* **1994,** *9* (3), 731-738.

55. Lu, X.; Caps, R.; Fricke, J.; Alviso, C. T.; Pekala, R. W., Correlation between structure and thermal conductivity of organic aerogels. *Journal of Non-Crystalline Solids* **1995,** *188* (3), 226-234.

56. Siegel, R.; Howell, J. R., *Thermal radiation heat transfer*. Taylor & Francis: New York, 2002.

57. Jeans, S. J., *An introduction to the kinetic theory of gases*. Cambridge University Press: Cambridge, 1940.

58. Haynes, W. M., *CRC Handbook of chemistry and physics*. 97th ed.; CRC Press: 2016.

59. Knudsen, M., Die Gesetze der Molekularströmung und der inneren Reibungsströmung der Gase durch Röhren. *Annalen der Physik* **1909,** *333* (1), 75-130.

60. Hu, F.; Wu, S.; Sun, Y., Hollow-structured materials for thermal insulation. *Advanced Materials* **2018**, e1801001.

61. Baetens, R.; Jelle, B. P.; Gustavsen, A., Aerogel insulation for building applications: A state-of-the-art review. *Energy and Buildings* **2011,** *43* (4), 761-769.

62. Nutz, F. A.; Retsch, M., Tailor-made temperature-dependent thermal conductivity via interparticle constriction. *Science Advances* **2017,** *3* (11).

63. Ruckdeschel, P.; Retsch, M., Interface and morphology control of the thermal conductivity in core-shell particle colloidal crystals. *Advanced Materials Interfaces* **2017,** *4* (24).

64. Carson, J. K.; Lovatt, S. J.; Tanner, D. J.; Cleland, A. C., Thermal conductivity bounds for isotropic, porous materials. *International Journal of Heat and Mass Transfer* **2005,** *48* (11), 2150-2158.

65. Fletcher, L. S., Recent developments in contact conductance heat transfer. *Journal of Heat Transfer* **1988,** *110* (4b), 1059-1070.

66. Cooper, M.; Mikic, B.; Yovanovich, M., Thermal contact conductance. *International Journal of Heat and Mass Transfer* **1969,** *12* (3), 279-300.

67. Hopkins, P. E., Thermal transport across solid interfaces with nanoscale imperfections: effects of roughness, disorder, dislocations, and bonding on thermal boundary conductance. *ISRN Mechanical Engineering* **2013,** *2013*.

68. Little, W. A., The transport of heat between dissimilar solids at low temperatures. *Canadian Journal of Physics* **1959,** *37* (3), 334-349.

69. Swartz, E. T.; Pohl, R. O., Thermal boundary resistance. *Reviews of Modern Physics* **1989,** *61* (3), 605-668.

70. Renteria, J. D.; Ramirez, S.; Malekpour, H.; Alonso, B.; Centeno, A.; Zurutuza, A.; Cocemasov, A. I.; Nika, D. L.; Balandin, A. A., Strongly anisotropic thermal conductivity of free-standing reduced graphene oxide films annealed at high temperature. *Advanced Functional Materials* **2015,** *25* (29), 4664-4672.

71. Nithiarasu, P.; Lewis, R. W.; Seetharamu, K. N., *Fundamentals of the finite element method for heat and mass transfer*. John Wiley & Sons: 2016.

72. Bathe, K.-J., Finite element method. In *Wiley Encyclopedia of Computer Science and Engineering*, John Wiley & Sons: 2008.

73. Fish, J.; Belytschko, T., *A first course in finite elements*. John Wiley & Sons New York: 2007; Vol. 1.

74. Nielsen, C. V.; Zhang, W.; Alves, L. M.; Bay, N.; Martins, P., *Modeling of thermo-electro-mechanical manufacturing processes - Applications in metal formin and resitance welding*. Springer: 2013.

75. Gade, R.; Moeslund, T. B., Thermal cameras and applications: A survey. *Machine Vision and Applications* **2013,** *25* (1), 245-262.

76. Carosena, M.; Giovanni, M. C., Recent advances in the use of infrared thermography. *Measurement Science and Technology* **2004,** *15* (9), R27.

77. Maldague, X. P. V., *Theory and practice of infrared technology for nondestructive testing*. Wiley: 2001.

78. Fabbri, L.; Fenici, P., Three-dimensional photothermal radiometry for the determination of the thermal diffusivity of solids. *Review of Scientific Instruments* **1995,** *66* (6), 3593-3600.

79. Pradère, C.; Goyhénèche, J. M.; Batsale, J. C.; Dilhaire, S.; Pailler, R., Thermal diffusivity measurements on a single fiber with microscale diameter at very high temperature. *International Journal of Thermal Sciences* **2006,** *45* (5), 443-451.

80. Fuente, R.; Rodríguez, S.; Mendioroz, A.; Salazar, A.; Zhukov, A.; Zhukova, V., Thermal conductivity and diffusivity measurements of glass-coated magnetic microwires using lock-in thermography. *International Journal of Thermophysics* **2014,** *36* (5-6), 1137-1141.

81. Fuente, R.; Mendioroz, A.; Salazar, A., Revising the exceptionally high thermal diffusivity of spider silk. *Materials Letters* **2014,** *114*, 1-3.

82. Muscio, A.; Bison, P. G.; Marinetti, S.; Grinzato, E., Thermal diffusivity measurement in slabs using harmonic and one-dimensional propagation of thermal waves. *International Journal of Thermal Sciences* **2004,** *43* (5), 453-463.

83. Oksanen, M.; Scholz, R.; Fabbri, L., On the longitudinal thermal diffusivity of SiC-based fibres. *Journal of Materials Science Letters* **1997,** *16* (13), 1092-1094.

84. Bisson, J. F.; Fournier, D., Influence of diffraction on low thermal diffusivity measurements with infrared photothermal microscopy. *Journal of Applied Physics* **1998,** *83* (2), 1036-1042.

85. Bisson, J. F.; Fournier, D., The coupled influence of sample heating and diffraction on thermal diffusivity estimate with infrared photothermal microscopy. *Journal of Applied Physics* **1998,** *84* (1), 38-43.

86. Walther, H. G.; Kitzing, T., Systematic errors of locally resolved photothermal radiometric measurements. *Journal of Applied Physics* **1998,** *84* (3), 1163-1167.

87. Paoloni, S.; Fournier, D., Spectral dependence of signal distortions in spatially resolved photothermal radiometry. *Journal of Applied Physics* **2002,** *92* (10), 5950-5954.

88. Paoloni, S.; Fournier, D., Semi-empirical approach for the analysis of infrared photothermal microscopy. *Journal of Applied Physics* **2002,** *92* (10), 5955-5958.

89. Philipp, A.; Eichinger, J. F.; Aydin, R. C.; Georgiadis, A.; Cyron, C. J.; Retsch, M., The accuracy of laser flash analysis explored by finite element method and numerical fitting. *Heat and Mass Transfer* **2019,** *56* (3), 811-823.

90. Ruckdeschel, P.; Philipp, A.; Retsch, M., Understanding thermal insulation in porous, particulate materials. *Advanced Functional Materials* **2017,** *27*, 1702256.

91. Ruckdeschel, P.; Philipp, A.; Kopera, B. A. F.; Bitterlich, F.; Dulle, M.; Pech-May, N. W.; Retsch, M., Thermal transport in binary colloidal glasses: Composition dependence and percolation assessment. *Physical Review E* **2018,** *97* (2-1), 022612.

92. Nutz, F. A.; Philipp, A.; Kopera, B. A. F.; Dulle, M.; Retsch, M., Low thermal conductivity through dense particle packings with optimum disorder. *Advanced Materials* **2018,** *30* (14), 1704910.

93. Pech-May, N.; Mendioroz, A.; Salazar, A., Simultaneous measurement of the in-plane and in-depth thermal diffusivity of solids using pulsed infrared thermography with focused illumination. *NDT & E International* **2016,** *77*, 28-34.

94. Philipp, A.; Pech-May, N. W.; Kopera, B. A. F.; Lechner, A. M.; Rosenfeldt, S.; Retsch, M., Direct measurement of the in-plane thermal diffusivity of semitransparent thin films by lock-in thermography: An extension of the slopes method. *Analytical Chemistry* **2019,** *91* (13), 8476-8483.

95. Philipp, A.; Hummel, P.; Schilling, T.; Feicht, P.; Rosenfeldt, S.; Ertl, M.; Schöttle, M.; Lechner, A. M.; Xu, Z.; Gao, C.; Breu, J.; Retsch, M., Anisotropic

thermal transport in spray-coated single-phase two-dimensional materials: Synthetic clay versus graphene oxide. *ACS Applied Materials & Interfaces* **2020,** *12* (16), 18785-18791.

96. Wang, Z.; Rolle, K.; Schilling, T.; Hummel, P.; Philipp, A.; Kopera, B. A. F.; Lechner, A. M.; Retsch, M.; Breu, J.; Fytas, G., Tunable thermoelastic anisotropy in hybrid bragg stacks with extreme polymer confinement. *Angewandte Chemie International Edition* **2020,** *59* (3), 1286-1294.

Part A:

Finite Element Method

6. The Accuracy of Laser Flash Analysis Explored by Finite Element Modeling and Numerical Fitting

Alexandra Philipp[1], Jonas Eichinger[2,3], Roland C. Aydin[4], Argyrios Georgiadis[1], Christian J. Cyron[3,4*], Markus Retsch[1*]

[1]University of Bayreuth, Department of Chemistry, Universitaetsstr. 30, 95447 Bayreuth, Germany

[2]Technical University of Munich, Institute for Computational Mechanics, Boltzmannstr. 15, 85748 Garching b. Munich, Germany

[3]Institute of Continuum Mechanics, Hamburg University of Technology, Eissendorfer Str. 42 (M), 21073 Hamburg, Germany

[4]Institute of Materials Research, Materials Mechanics, Helmholtz-Zentrum Geesthacht, Max-Planck-Str. 1, 21502 Geesthacht, Germany

Reprinted with permission from Philipp *et al.*, *Heat Mass Transfer*, **2020**, *56*, 811-823.

Abstract

Laser flash analysis (LFA) has become over the last decades a widely used standard technique to measure the thermal diffusivity of bulk materials under various conditions like different gases, atmospheric pressures, and temperatures. A curve fitting procedure forms the heart of LFA. This procedure bases on a mathematical model that should ideally account for inherent shortcomings of the experimental realization such as: duration of the heating pulse, heat losses to the environment and sample holder, non-opaque samples, and radiative heat transfer. The accuracy of the mathematical model and curve fitting algorithm underlying LFA defines an upper bound of the accuracy of LFA in general. Unfortunately, not much is known about the range of parameters and conditions for which this accuracy is acceptable. In this paper, we examine the limits of accuracy of LFA resulting from its underlying computational framework. To this end, we developed a particularly accurate and comprehensive computational framework and applied it to data from simulated experiments. We quantify the impact of different (simulated) experimental conditions on the accuracy of the results by comparing the fit results of our computational framework to the known simulation input parameters. This way we demonstrate that a state-of-the-art computational framework for LFA admits determining thermal conductivities of materials in a broad range from at least 0.16 $Wm^{-1}K^{-1}$ to 238 $Wm^{-1}K^{-1}$ with relative errors typically well below 4 % even in the presence of common undesired experimental side effects.

1. Introduction

Laser/light flash analysis (LFA) is a simple and widely used technique for the determination of the thermal properties of solid samples with uniform thickness. LFA represents a transient characterization method and provides fast access to the thermal diffusivity of a given material.

LFA has several advantages which have made this method increasingly popular since its invention more than 50 years ago: short measurement time, small sample size compared to steady-state methods, non-destructive measurement, assessment of temperature-, pressure-, gas composition-dependence, and high throughput. Additionally, it is possible to measure the specific heat capacity.[1-10]

The wide range of materials and thermal transport phenomena, which have been investigated in literature, demonstrates the versatility of the LFA. Some specific and recent examples are: high temperature thermal insulation properties of carbon aerogels (measured up to 1500 °C in argon and vacuum atmosphere)[11], designed temperature-dependence of the thermal conductivity of colloidal crystals[12], percolation assessment of colloidal glasses[13], anisotropic thermal conductivity of fiber-based nanowood[14] as well as of 3D printed boron nitride-polymer composites[15], and switchable anisotropy in polymer foams[16].

In a typical flash experiment, the front surface of the sample is heated by a short-duration light pulse created by a laser or flash lamp. The time-dependent temperature increase on the rear surface of the sample is measured by a contactless infrared detector. In an ideal adiabatic case, the thermal diffusivity α can be directly determined from the half-rise time $t_{1/2}$ using a formula derived by Parker *et al.*[1]:

$$\alpha = (1.38 \cdot L^2)/(\pi^2 \cdot t_{1/2}). \quad (1)$$

Here L is the thickness of the sample. Parker's model is only applicable in case of a negligibly short heat pulse that is uniformly irradiated as well as uniformly absorbed by the full front surface of the sample. Furthermore, the sample must be opaque (optically, to block the light flash and thermally, to prevent radiative heat transfer), isotropic, uniform in thickness, and thermally insulated from the environment. Parker *et al.* recommend a black coating of the sample's rear and front face to ensure a homogenous absorption of the heat pulse as well as to make the sample opaque.[1]

Practically, an adiabatic measurement, as assumed implicitly in the derivation of Parker's formula, cannot be conducted, since thermal losses to the environment are inevitable. The time-dependent temperature on the rear sample surface deviates from Parker's ideal case due to such thermal losses. Instead of reaching a steady temperature plateau, the temperature decreases at long measurement times and the half-rise-time shifts to lower times. Thus, the prefactor of 1.38 in Equation (1) and therefore Equation (1) as a whole is no longer valid.[17]

To yet enable the applicability of the flash method under practical conditions, a host of theoretical models has been developed. These models consider heat losses due to radiation and/or natural convection.[3,18-24] In addition to heat loss effects, it can also be important to take the actual pulse length and shape into account. This is particularly relevant for thin samples and/or samples with a high thermal diffusivity, and consequently fast temperature diffusion. Thus, refinements to Parker's model have been developed, which consider the so-called finite pulse effect.[25-28] Ultimately, one needs to combine all loss mechanisms and the finite pulse lengths for a realistic description of actual measurements.[29-31]

Radiative heat transfer leads to an additional and strong contribution to the effective temperature-time-curve in the case of (semi-)transparent samples. Examples of such materials are glasses or ceramics where heat is not only transferred through conduction but also *via* radiation, especially at high temperatures.[32] Also, porous materials at room temperature can be affected. Numerous research groups have focused on the physics of laser flash measurements of semi-transparent materials and enabled the correct determination of the thermal diffusivity of these materials.[32-41]

The accuracy of the computational framework, that is, of the mathematical model and curve fitting algorithm, underlying LFA naturally defines an upper bound of the accuracy of LFA in general. This problem matters in particular if practical constraints result in experimental conditions which deviate from the ideal

conditions assumed in the mathematical model of the experimental conditions underlying LFA. For example, these models typically assume cylindrical material samples, a complete sample surface illumination, and negligible heat losses through the sample holder whereas in practice these conditions can often not be ensured in experiments. The impact of such deviations from ideal experimental conditions on the accuracy of LFA remains poorly understood to date.

In this paper, we first introduce and describe in detail a state-of-the-art computational framework for LFA, which is based on the equations of Parker *et al.*[1], Cape and Lehman[19], Dusza[31] and Blumm *et al.*[32] and which thus in general accounts at least to a certain extent for aspects such as thermal losses, finite pulse length and potential radiative contributions. For this state-of-the-art computational framework, we analyzed the associated inherent accuracy limitations, in particular, due to deviations from ideal experimental conditions. To this end, we performed finite element simulations of laser flash experiments. The output data of these simulations were analyzed as usually experimental data in LFA. From the differences between the thermal conductivity values retrieved by such an inverse analysis and the original input parameters of the simulations, we could determine the inherent accuracy limitations of the employed computational framework and its sensitivity to deviations from ideal experimental conditions. This way we can conclude that a state-of-the-art computational framework for LFA admits – if considering only the error associated with the computational framework itself - measurement of thermal conductivity parameters in a broad range (at least 0.16 $Wm^{-1}K^{-1}$ to 238 $Wm^{-1}K^{-1}$) with relative errors mostly well below 4 % even in the presence of common deviations from ideal experimental conditions.

2. Methods

2.1. Computational Framework for LFA

Based on the work of Parker *et al.*[1], Cape and Lehman[19], Dusza[31] and Blumm *et al.*[32] we developed a new computational framework using the software package Matlab for computing the thermal diffusivity from temperature rise curves obtained from (real or simulated) laser flash measurements. Our framework includes multiple optional corrections terms, which can be switched on when using the framework (Figure 1). This way it is capable of calculating the thermal diffusivity under adiabatic as well as non-adiabatic conditions accounting also for radiative heat transfer if required. Finite pulse effects depending on the actual length and shape of the laser pulse can be considered. A pulse correction function of predefined shapes (exponential, triangular, linear-exponential) can be chosen, and the length of the pulse can be defined.

The following section briefly illustrates the basic equations of the developed framework for adiabatic and non-adiabatic boundary conditions and explains how they can be extended by optional correction terms to account for effects like radiative heat transfer.

The subsequent section describes key aspects that ensure the robustness and accuracy of our computational framework.

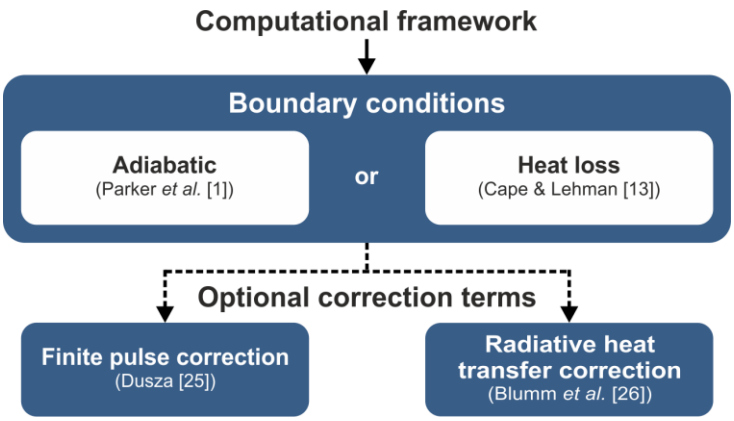

Figure 1. Overview of the computational framework. The basic form of the equation describing heat transfer in the sample is determined by the choice of boundary conditions. Either effects resulting from the finite laser pulse or radiative heat transfer can be considered by additional correction terms.

2.1.1. Basic Equations

Adiabatic conditions are assumed in our computational framework if the temperature decrease is less than 1 % in the last 20 % of the given temperature data points. In the adiabatic case, Parker's[1] temperature rise function

$$T^{A}(x = L, r = 0, t) = 1 + 2\sum_{i=1}^{\infty}(-1)^{i}\, e^{-\frac{i^2\pi^2\alpha t}{L^2}}, \tag{2}$$

with x being the distance from the front to the rear surface of the sample, L the sample length and t the time is used to determine the thermal diffusivity of a given sample material. To account for effects resulting from the laser flash impulse the model can be extended according to Dusza[31]:

$$T^{A,PSF}(x = L, r = 0, t) = P(1) + 2\sum_{i=1}^{\infty}(-1)^{i}\, e^{-\frac{i^2\pi^2\alpha t}{L^2}}\, P\left(-\frac{i^2\pi^2\alpha}{L^2}\right), \tag{3}$$

with P being a certain pulse shape function as defined by Dusza[31]. In case of very thin samples or samples with a high thermal diffusivity, often radiative heat transfer rather than finite pulse effects are considered, which leads according to Blumm *et al.* [32] to

$$T^{A,R}(x = L, r = 0, t) = \underbrace{1 + 2\sum_{i=1}^{\infty}(-1)^{i}\, e^{-\frac{i^2\pi^2\alpha t}{L^2}}}_{adiabatic\ heat\ transfer} + \underbrace{A + 2A\sum_{i=1}^{\infty} e^{-\frac{i^2\pi^2\alpha t}{L^2}}}_{radiative\ heat\ transfer}, \tag{4}$$

with A being a factor that must be fitted describing effects of properties like the energy of the laser pulse.

As adiabatic conditions are experimentally barely realizable due to convection and radiation, Cape and Lehman[19] introduced a new model where they added heat loss correction terms to the method proposed by Parker *et al.* [1]. We will show in the following, that the model is also capable of yielding good results regarding additional loss mechanism that are unavoidably present in the experimental setup due to the sample holder and non-ideal sample geometry. Cape and Lehman[19]

introduced the following model including terms describing heat losses to the environment:

$$T^{HL}(x = L, r = 0, t) = \sum_{m=0}^{\infty} C_{\mathrm{m}}\, \xi_{\mathrm{m}} \sum_{i=1}^{\infty} D_i(H_1) e^{(\omega_{\mathrm{im}} t/t_{\mathrm{c}})}, \tag{5}$$

with $C_{\mathrm{m}} = (-1)^m \frac{2\xi_{\mathrm{m}}}{{\xi_{\mathrm{m}}}^2 + 2H_2 + {H_2}^2}$, $D_i(H_1) = \frac{2H_1}{({H_1}^2 + \lambda_i^2) J_0(\lambda_i)}$, $\omega_{\mathrm{im}} = -(L/\pi)^2 \left(\frac{{\xi_{\mathrm{m}}}^2}{L^2} + \frac{\lambda_i^2}{R_{\mathrm{s}}^2}\right)$, $t_{\mathrm{c}} = L^2/(\pi^2 \alpha)$ and λ_i being the solution of $H_1 J_0(\lambda_i) - \lambda_i J_1(\lambda_i) = 0$. J_0 and J_1 are the Bessel functions of the zeroth and first degree. ξ_m is the solution of

$$\left({\xi_{\mathrm{m}}}^2 - {H_2}^2\right) \tan(\xi_{\mathrm{m}}) = 2\xi_{\mathrm{m}} H_2. \tag{6}$$

Given that heat loss effects and finite pulse effects can be present simultaneously, Dusza[31] expanded the model of Cape and Lehman[19] by adding a pulse shape function adjustable to shape and length of the pulse used in the respective experiment:

$$T^{HL,PSF}(x = L, r = 0, t) = \sum_{m=0}^{\infty} C_{\mathrm{m}}\, \xi_{\mathrm{m}} \sum_{i=1}^{\infty} D_i(H_1) e^{(\omega_{\mathrm{im}} t/t_{\mathrm{c}})}\, P(\omega_{\mathrm{im}}/t_{\mathrm{c}}), \tag{7}$$

with *P* being a pulse shape function as described by Dusza[31].

Analogously to the adiabatic case, transmitted radiation from the irradiated front surface to the detector can be incorporated into the model according to Blumm *et al.* [32]

$$T^{HL,R}(x = L, r = 0, t) = T^{HL}(x = L, r = 0, t) + \underbrace{A \sum_{m=0}^{\infty} C_{\mathrm{m,rad}}\, \xi_{\mathrm{m}} \sum_{i=1}^{\infty} D_i(H_1) e^{(\omega_{\mathrm{im}} t/t_{\mathrm{c}})}}_{radiative\ heat\ transfer}, \tag{8}$$

with

$$C_{\mathrm{m,rad}} = \frac{2\xi_{\mathrm{m}}}{{\xi_{\mathrm{m}}}^2 + 2H_2 + {H_2}^2}. \tag{9}$$

In our computational framework, the user can choose initially which optional corrections (Figure 1) should be taken into account in the mathematical model used to fit a temperature rise data set.

2.1.2. Key Mathematical Aspects

Independently of the chosen equation we identified some crucial aspects to obtain a robust computational framework. In the following, we briefly summarize these crucial aspects. The code of our computational framework, as well as an exemplary input file, are provided in the Supplementary Material.

1) In case heat losses are considered when determining the thermal diffusivity of a sample material, the roots of Equation (6) must be calculated. Cape and Lehman[19] stated an approximate formula for the computation of these roots for cases where $H_2 < 1$. However, the formula was shown to be wrong by Josell *et al.*[24] who presented a corrected version.

Unfortunately, in cases of Biot numbers $H_2 > 1$, also the solution of Josell *et al.* [24] yields wrong results. As we observed that Biot numbers $H_2 > 1$ may appear at least at some point during the iterative fitting process, the equations of Josell *et al.* alone are not sufficient for a robust algorithm.

To overcome this problem, we implemented a robust and efficient algorithm for finding all required roots of Equation (6) without restrictions regarding the Biot number H_2. The algorithms are based on an analytically gained understanding of how many roots must exist in certain subdomains. Most importantly it takes into consideration that two roots exist in the neighborhood of H_2 in case of $H_2 > \pi/2$, see Figure 2. Using both of these roots in Equations (5), (7), and (8) was identified to be crucial for accurate computation of the thermal diffusivity α.

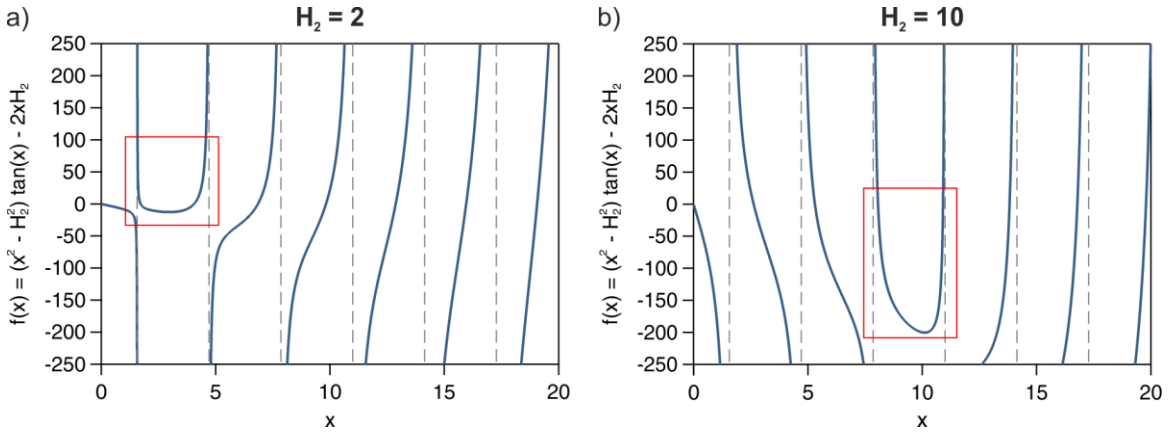

Figure 2. Plot of Equation (6) for Biot numbers $H_2 > 1$: a) $H_2 = 2$, b) $H_2 = 10$. Red rectangles show critical intervals for numerical determination of roots.

2) All temperature rise data obtained from experiments, or numeric simulations are normalized for a smoothed maximum temperature as well as shifted so that the temperature rise equals zero at time $t = 0$. In addition, all equations mentioned above describing the temperature rise at the rear surface of a sample are formulated for absolute temperature values and therefore have to be normalized in every iteration of the fitting process by the maximum temperature of the current iteration.

3) To ensure that our fitting algorithm yields parameters which represent a global optimum with respect to the quality of the fit, it is important to start the iterative calculations underlying to the fitting procedure with an initial guess sufficiently close to this global optimum. We found that Equation (1) provides a suitable initial guess for the thermal diffusivity α.

4) If the half maximum time of a sample is larger than 100 times the length of the pulse, the pulse correction function is deactivated as the influence, in that case, is negligible. Parasitic effects in the curve fitting procedure were observed otherwise.

5) In case of heat loss boundary conditions, the specimen radius R_s can either be specified by a numeric value or fitted just like the thermal diffusivity α. The latter was found to be beneficial in case of an arbitrarily shaped sample geometry for which the exact sample radius is unknown.

6) Both the Levenberg-Marquard as well as the Trust-Region-Reflective algorithm as pre-implemented in Matlab were found to perform well for computing the best fit thermal diffusivity. In the computations performed for this paper, both worked equally robust.

2.2. Framework for Simulation of LFA Measurements

To clarify the nomenclature used in this paper, we want to define the following terms: heat losses to the environment, radial losses, and facial losses.

Here, *heat losses to the environment* refer to radiative or convective heat losses from all external boundaries except for the ones, where the sample is in contact with a sample holder. *Radial losses* arise from an incomplete excitation of the lower sample surface by the heat pulse that leads to radial heat flow away from the sample center towards its edges. We note that this is not a loss of heat to the environment, but merely a distribution of heat and consequently temperature within the entire sample volume. If the sample is put on a sample holder, *facial losses* into the sample holder occur, since the sample holder can be perceived as a heat sink.

2.2.1. General Setup

To quantify the accuracy of the computational framework used in LFA, we applied this framework to data from simulated rather than real experiments. The motivation of this approach is twofold. On the one hand, analyzing the data from simulated experiments has the advantage that the correct solutions for the parameters to be identified with the LFA framework are already known because they are simply the input parameters of the performed computer simulations. This enables a straightforward quantification of the error associated with the computational framework used in LFA. On the other hand, deviations from ideal experimental conditions can easily be applied and controlled in computer simulations so that their respective impact on the accuracy of LFA can be examined in detail. To simulate experiments, we performed time-dependent heat transfer

simulations using the finite element (FE) software COMSOL Multiphysics®. To study the radial losses separately from the facial losses, two different geometries were chosen: a disk (Figure 3a) representing the sample and a disk on a sample holder (Figure 3b). In all our simulations we assumed axisymmetric geometries. The disk-shaped sample has a thickness of 1 mm and a radius R_{sample} of 5 mm.

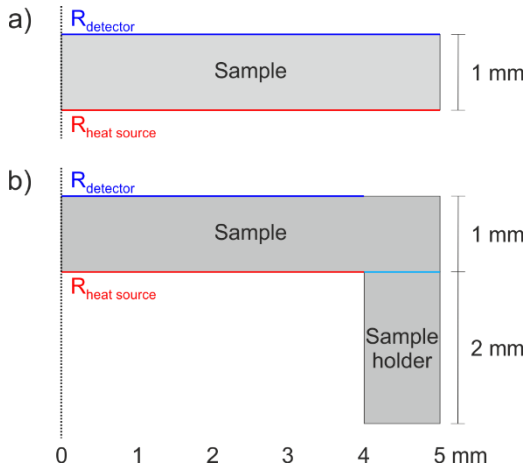

Figure 3. General set-up a) Simple case without sample holder and b) geometry with a sample holder; the dotted line at R=0 represents the axis of symmetry. The heat source is marked in red, the evaluation range in dark blue.

A heat source in the form of a (temporally) triangular heat pulse with a pulse duration of $\tau = 2$ ms was imposed on the lower edge of the sample disk (red line in Figure 3a and b). The intensity of the heat pulse was assumed to be uniform within a disk of radius $R_{\mathrm{heat\,source}}$. We used various heat source radii $R_{\mathrm{heat\,source}}$ for the investigation of radial heat losses into the sample using the geometry depicted in Figure 3a. A heat source radius of 5 mm corresponds to a complete excitation area (100 %) of the lower sample surface, 4 mm to an excitation area of 64 %, 3 mm to 36 %, and 1 mm to 4 %. Furthermore, we modeled radiative heat transfer using a second heat source imposed on the upper edge of the sample disk opposite the first heat source. To study the facial losses into the sample holder (Figure 3b), a heat source radius of 4 mm was used. These facial losses were adjusted by the magnitude of the thermal contact conductance at the interface between the sample and sample holder (light blue line in Figure 3b).

In adiabatic cases, *i.e.*, without any heat losses to the environment, all external boundaries were assumed to be thermally insulating. In other studies, heat losses to the environment were considered, with heat loss boundary conditions being applied to all external boundaries.

We used sample materials covering a *broad range of thermal conductivities* (0.16 – 238 $Wm^{-1}K^{-1}$) to examine the applicability of the LFA procedure over a large parameter range. Due to its high thermal conductivity, copper was used as the material for the sample holder. The material parameters used for the simulations are listed in Table 1.

Table 1. Material parameters used for the FE simulations.

Material	κ [$Wm^{-1}K^{-1}$]	C_p [$Jkg^{-1}K^{-1}$]	ρ [kgm^{-3}]	ε
Aluminum (Al)	238	900	2700	-
Titanium (Ti)	7.5	710	4940	-
Quartz (SiO_2)	1.4	730	2210	-
Polystyrene (PS)	0.16	1300	1050	0.9
Copper (Cu)	400	385	8700	0.05

κ: thermal conductivity, C_p: heat capacity at constant pressure, ρ: density, ε: emissivity

Mesh convergence tests were performed to ensure mesh size independent results (Figure S1, Supplementary Material). Furthermore, suitable time ranges and time steps of the solver were chosen for the different sample materials (Figure S2 and S3, Supplementary Material).

Subsequently, the time-dependent average temperature rise at the upper boundary of the sample was extracted from the simulation result. The radius of the region over which the temperature average was computed, *i.e.*, the detector radius R_{detector} (Figure 3a and b, blue line), was varied from 5 to 1 mm. This procedure mimics another experimental pre-requisite: confining the detection area to small radii allows measuring specimen, which are difficult to scale up and/or to produce with a high confidence regarding the sample thickness L. One should note that we

determine the average temperature across the detector area, whereas the mathematical framework only considers the temperature in the center (r = 0). One can, therefore, expect that a higher deviation occurs for heat loss/detection area combinations that evoke large temperature gradients in the sample's top surface.

2.2.2. Numerical Studies

- *Ideal Adiabatic Case and Heat Losses to the Environment ($R_{\text{heat source}} = R_{\text{sample}}$)*

Firstly, the ideal adiabatic case was simulated for all samples to validate consistency between the FE method and the numerical fitting procedure. Thereby, the entire lower boundary of the disk-shaped sample (Figure 3a) was excited by a 2 ms heat pulse, and no heat losses were assumed to occur. Since adiabatic conditions cannot be realized experimentally, heat losses to the environment, *i.e.*, thermal radiation and convection to air, were exemplarily modeled for polystyrene (PS). The heat loss boundary conditions were applied to all external boundaries. Results are summarized in Section 3.1.

- *Radial Losses and Radiative Heat Transfer ($R_{\text{heat source}} < R_{\text{sample}}$)*

The influence of radial losses into the sample, which arises from an incomplete excitation of the lower sample surface, was studied under adiabatic conditions using excitation areas smaller than 100 % of the lower sample surface. In addition to the excitation area, the detector radius was also varied. Experimentally, the detection area can be adjusted by differently sized sample apertures. Again, we used the geometry depicted in Figure 3a. Radiative heat transfer was simulated by introducing a second heat source on the upper sample surface. The amount of radiation was adjusted by the power of the heat source and varied between 0.25 – 2.5 % of the initial power. This study was only conducted for PS using an excitation area of 4 % and $R_{\text{detector}} = 1\ mm$. Results are summarized in Section 3.2.

- *Facial Losses and Heat Losses to the Environment ($R_{\text{heat source}} < R_{\text{sample}}$)*

Experimentally, if the sample is put on a sample holder (Figure 3b), radial losses are increased due to facial losses into the sample holder. Facial losses (without heat losses to the environment) were modeled using an excitation area of 64 %; different detector radii were used for the evaluation. First, the thermal contact conductance between the sample and sample holder was varied exemplarily for PS. Then, the highest possible thermal contact conductance was applied to all materials. Finally, the most realistic case with facial losses as well as heat losses to the environment was modeled for PS. Results are summarized in Section 3.3.

2.2.3. Data Evaluation

From the evaluation of the simulation results, temperature-rise-versus-time curves were obtained. First, we normalized the temperature values to the maximum temperature ($V = \Delta T/\Delta T_{\text{max}}$). Then, we interpolated the data using the software Igor Pro to obtain data points evenly spaced in time to avoid overweighting of specific time periods in the fitting due to increased density of interpolation points. This is necessary because finer time steps were used for the first part of the simulation. Negative time data was added as a baseline. Subsequently, we fitted the normalized temperature-rise-versus-time curves with the developed computational framework (Figure 1). A triangular pulse correction function and a pulse duration of 2 ms were used for all computations. As described above, in case of a negligible influence of pulse shape and duration, no pulse correction term is added to the equations to avoid parasitic effects during fitting. Dependent on the extent of temperature losses, equations considering either adiabatic or heat loss boundary conditions were used. Radiative heat transfer correction terms were accounted for in the fitting procedure in cases where part of the illumination flash was simulated to transmit to the top sample surface. The fit yields the thermal diffusivity α_{fit} that is used to calculate the thermal conductivity κ_{fit}:

$$\kappa_{\mathrm{fit}} = \alpha_{\mathrm{fit}} \cdot \rho \cdot C_{\mathrm{p}} \tag{10}$$

where ρ is the density and C_{p} the specific heat capacity (Table 1). Then, the relative deviation of the thermal conductivity κ chosen as the input parameter for the respective simulation (Table 1) and the thermal conductivity κ_{fit} retrieved from an inverse analysis of the simulation output data was computed as

$$relative\ deviation = ((\kappa_{\mathrm{fit}} - \kappa)/\kappa) \cdot 100\ \% \tag{11}$$

2.3. Application of Computational Framework to Experimental LFA Data

The focus of this paper is to analyze the accuracy of LFA by applying the developed computational framework to the output data of our simulated experiments. To demonstrate the applicability of our computational framework to real measurement data, we also performed LFA experiments and used the exact same numerical fitting procedure to evaluate the measured data. The measurements were performed with an XFA500 xenon flash apparatus (Linseis), equipped with an InSb infrared detector. The apparatus is schematically depicted in Figure 4a. To obtain similar (non-ideal) conditions as the simulated ones, we intentionally introduced loss scenarios using different, self-fabricated sample holders and lids. A schematic illustration of the sample configuration, *i.e.*, a brass sample holder, graphite coated sample, and graphite coated Teflon lid, are shown in Figure 4b.

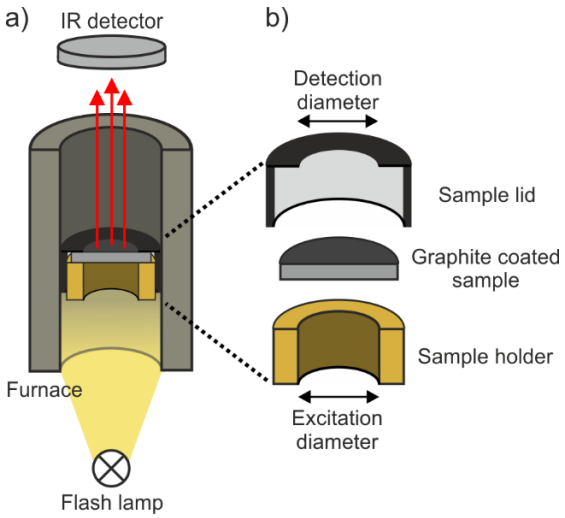

Figure 4. a) Simplified LFA set-up. b) Schematic illustration of the sample configuration consisting of sample holder, graphite coated sample, and sample lid. The excitation and detection diameter determine the excitation and detection area, respectively.

The smaller the hole in the sample holder and lid, respectively, the smaller is the excitation and detection area. We used a reference sample with certified thermal diffusivity value (BCR-724). The sample had a radius of 6.35 mm and a thickness of around 1.5 mm. The sample was coated with a thin graphitic layer on each side, which is a standard procedure in LFA measurements. The graphite coating ensures a good absorbance of the xenon flash and a high IR emissivity. The precise sample thickness was measured with a Litematic VL-50 (Mitutoyo). All measurements were performed in air and at room temperature (295 K). The obtained data were evaluated using the computational framework discussed above (with triangular pulse correction function, a pulse duration of 2 ms, no radiative heat transfer).

3. Results and Discussion

3.1. Ideal Adiabatic Case and Influence of Heat Losses to the Environment

The ideal adiabatic case was simulated for all sample materials. Here, the sample geometry depicted in Figure 3a was used. The complete lower sample surface was excited by a short heat pulse, and no heat losses to the environment were considered. Thus, purely one-dimensional heat transfer in the thickness direction of the sample occurs. Figure 5a shows the resulting temperature rise versus time

curves. In general, the temperature increases with time until a plateau is reached. As expected, the half-time shifts to longer times for samples with low thermal conductivity.

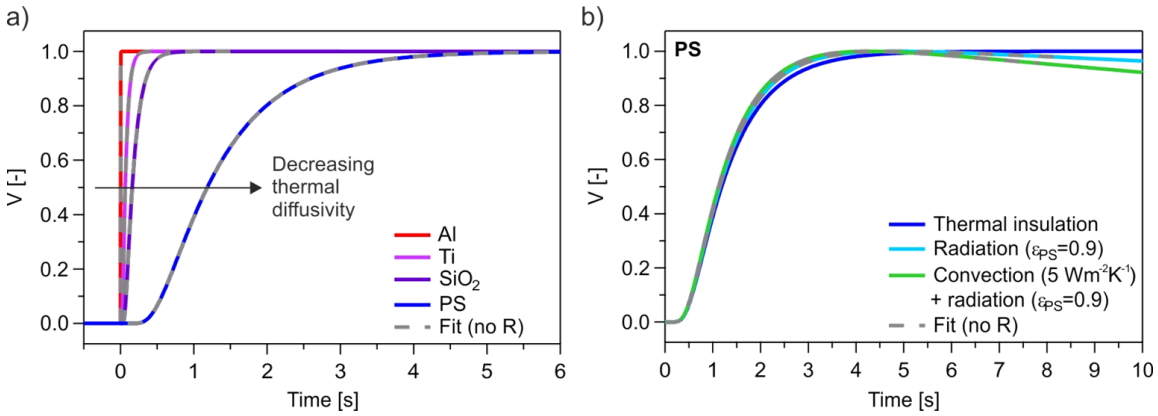

Figure 5. Normalized temperature-rise-versus-time curves and corresponding fits. a) Ideal adiabatic case without losses. b) Influence of heat losses on the normalized temperature-rise-versus-time curve for PS.

We used the computational framework from Section 2.1.1 to extract the thermal diffusivity from the simulation data. The corresponding fits are also shown in Figure 5a (grey dashed lines). As can be seen, they fit the simulated curves perfectly. In Table 2, the obtained thermal diffusivity α_{fit}, the calculated thermal conductivity κ_{fit}, the reference value κ, and the calculated relative deviation are listed. Relative deviations on the order of 0.1 % were obtained for all materials. Thus, the developed computational framework is applicable even for highly conducting materials like Al, where the finite pulse correction is important (pulse duration: 2 ms, half-time: 2.45 ms).

Table 2. Fitting results of the temperature-rise-versus-time curves for the ideal adiabatic case (Figure 5a) in comparison to the input values.

	Combined fit		Input	*Rel. dev. [%]*
	α_{fit} *[cm^2s^{-1}]*	κ_{fit} *[$Wm^{-1}K^{-1}$]*	κ *[$Wm^{-1}K^{-1}$]*	
Al	0.980709	238	238	0.13
Ti	0.021418	7.51	7.50	0.16
SiO_2	0.008704	1.40	1.40	0.30
PS	0.001172	0.160	0.160	-0.01

α_{fit}: fitted thermal diffusivity, κ_{fit}: thermal conductivity calculated from α_{fit}, κ: input thermal conductivity.

In Figure 5b, the ideal adiabatic curve of PS is compared to more realistic cases. We introduced heat losses due to thermal radiation (solid light blue line) which occur under vacuum conditions. In the air, radiation and natural convection (solid light green line) lead to heat losses during the experiment. Because of these heat losses, the half-time shifts to slightly shorter times and the temperature decreases after reaching a maximum. The effect of heat losses to the environment is small since there is only a small temperature difference between the sample and the surrounding (room temperature). Furthermore, short measurement time and thin sample thickness are used. Again, the fitted results are in very good agreement with the simulation curves (Figure 5b, grey dashed line). This results in negligible relative deviations of the thermal conductivity (Table 3).

Table 3. Relative deviation of the thermal conductivity fitting results of PS with heat losses (Figure 5b) from the input parameters used in the FEM simulation.

	Thermal insulation	*Radiation*	*Convection + radiation*
PS	-0.01 %	-0.10 %	-0.18 %

Thus, by exciting the total surface area and measuring in air or vacuum at room temperature, one can expect to obtain very good fits for the thermal conductivity

with negligible relative deviations from the real values due to the computational framework used for evaluation of the experimental data.

3.2. Radial Losses and Radiative Heat Transfer

An incomplete excitation of the lower sample surface by the heat pulse leads to radial heat flow into the sample. These radial losses increase with decreasing excitation area as shown in Figure 6a. To study the influence of radial losses into the sample due to an incomplete excitation, the geometry depicted in Figure 3a was used. The heat source and detector radius were varied from 4 mm to 1 mm. The different detection areas are marked in grey in Figure 6a. No heat losses to the environment were considered.

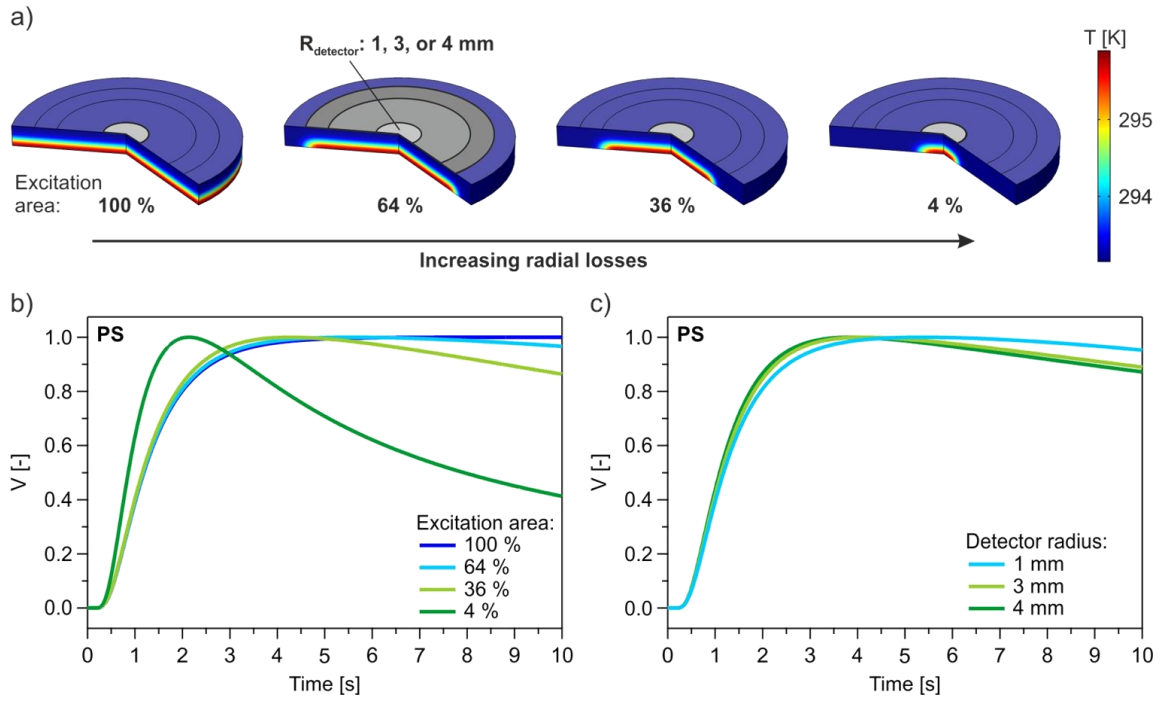

Figure 6. Influence of radial losses: a) COMSOL images for different excitation areas. Radial losses arise from an incomplete excitation of the sample surface and increase with decreasing excitation area. No radial losses are present for a complete excitation. b,c) Normalized temperature-rise-versus-time curves are exemplarily shown for PS. b) Influence of the excitation area ($R_{detector}$: 1 mm). c) Influence of the detector radius (excitation area: 64 %).

In Figure 6b, the normalized temperature rise versus time curves for different excitation areas are exemplarily shown for PS. For the evaluation, a detector radius

of 1 mm was used. Similar to the heat losses to the environment, the radial losses into the sample lead to a decrease in the temperature after reaching a maximum value and the half-time shifts to lower times. The stronger the radial losses, the more pronounced are these changes. Besides the excitation area, we also studied the influence of the detector radius. The resulting curves for an excitation area of 64 % and different detector radii are again exemplarily plotted for PS (Figure 6c). The strongest temperature decrease after the maximum is obtained for a detector radius that is equal to the excitation radius (4 mm). The smaller the detector radius (compared to the excitation radius), the lower is the influence of the radial losses.

In Figure 7, the relative deviation of all materials is plotted against the excitation area. The used detector radius is depicted as differently sized circles; a small circle represents a small detection area and vice versa. Relative deviations from the input value below 4 % were obtained for all configurations, except for the material with the highest thermal conductivity and the highest radial losses (5.6 %). Thus, the combined fitting model leads to reliable results, especially for low conductive materials, even with radial losses present.

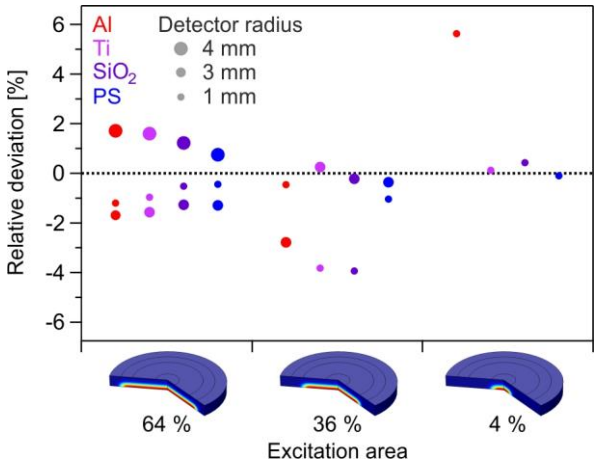

Figure 7. Influence of radial losses: Relative deviation in dependence on the excitation and detection area.

If the sample is not completely opaque to the excitation source (*e.g.*, laser or xenon lamp) or it exhibits a porous structure, the light energy is not only absorbed at the

lower sample surface but in the entire sample volume or at the upper sample surface. This leads to a sharp temperature peak at $t \approx 0$ ms. To obtain reliable fitting results, this radiative heat transfer has to be considered in the fitting procedure. Here, in addition to radial losses, the influence of radiative heat transfer was studied using a second heat source on the upper sample surface (Figure 8a). This study was only conducted for PS using the smallest excitation area (4 %) and detector radius (1 mm), *i.e.*, the most demanding specimen geometry regarding radial losses.

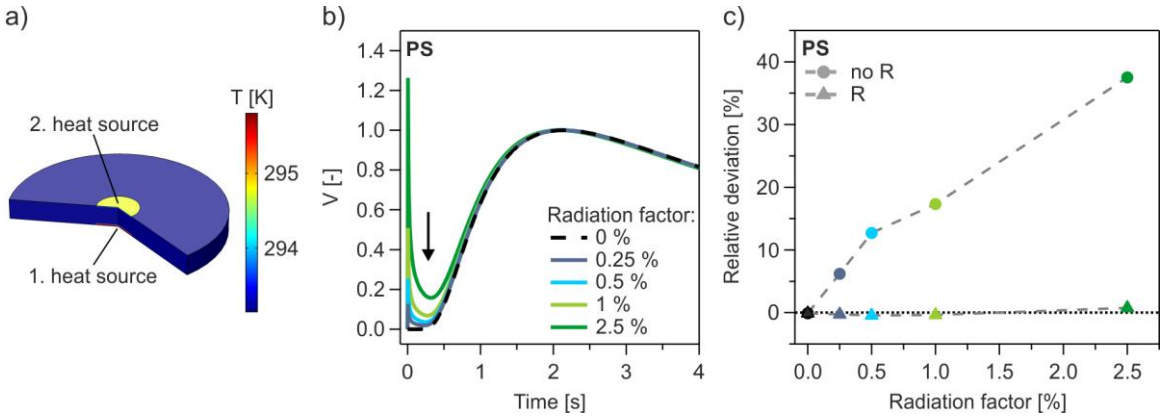

Figure 8. Influence of radiative heat transfer: a) COMSOL snapshot at $t = 1$ ms illustrates the second heat source on the upper sample surface (excitation area: 4 %). b) Normalized temperature-rise-versus-time curves of PS with radiative heat transfer. The jump in the temperature evolution is highlighted by an arrow. c) Comparison of the relative deviation obtained from the fit with ("R") and without ("no R") correction for radiative heat transfer.

The temperature-rise-time-curves for different radiation factors are compared in Figure 8b. The temperature at $t \approx 0$ ms rises when the radiation factor is increased. Also, the temperature after this initial peak increases and the half-time shifts to lower times. These changes lead to inaccurate results in case of fitting without corrections for radiative heat transfer. For the lowest radiation factor, a relative deviation above 6 % is obtained, which increases up to around 38 % for the highest radiation factor. In contrast, fitting with corrections for radiative heat transfer yields negligible relative deviations for all studied radiation factors combined with high radial losses due to an incomplete excitation. Thus, in this case, radiative heat transfer has to be considered in the fitting model.

3.3. Facial Losses and Influence of Heat Losses

By adding a sample holder to the geometry (Figure 3b) and enabling the heat flow through the sample/sample holder interface, facial losses into the sample holder occur and consequently enhance the radial losses. The direction of heat flow is illustrated by arrows in Figure 9a.

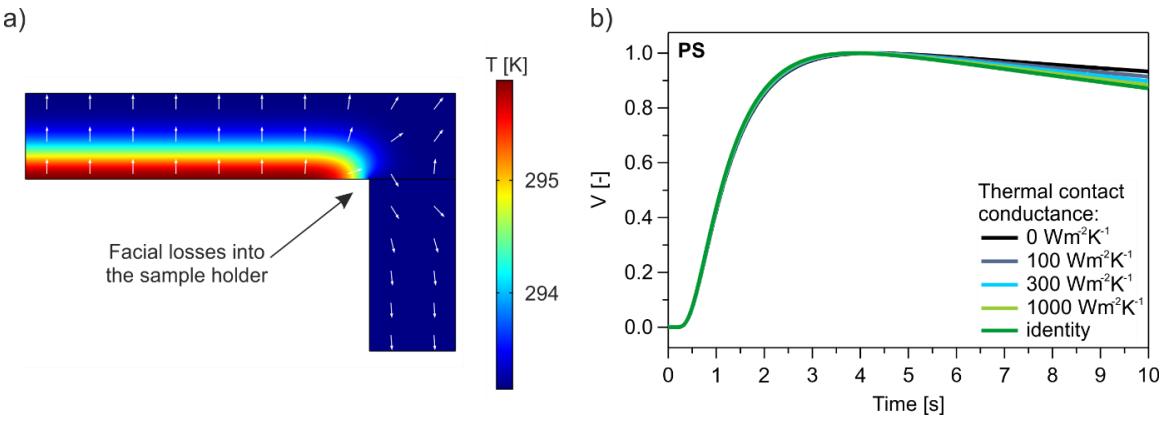

Figure 9. Influence of facial losses: a) COMSOL image illustrating facial losses into the sample holder, arrows display the direction of heat flow. b) Normalized temperature-rise-versus-time curves of polystyrene for different thermal contact conductances (excitation area: 64 %, R_{detector}: 4 mm). No facial losses occur at a thermal contact conductance of 0 $Wm^{-2}K^{-1}$, while the maximum heat flow into the holder is present at the identity boundary condition.

We performed the simulations for an excitation area of 64 %. The thermal contact conductance between the sample and the copper sample holder was varied from zero (no facial losses) to identity (maximum facial losses). In Figure 9b, the corresponding normalized temperature-rise-versus-time curves for a detector radius of 4 mm are exemplarily plotted for PS. The temperature after reaching the maximum value drops to a lower value as the thermal contact conductance increases. However, this is a rather small effect compared to the influence of the radial losses. This effect is even smaller for smaller detector radii. The corresponding relative deviations of all curves are below 1 % (Figure 10a).

Similar simulations were performed for all the other samples using the same detector radius and the maximum thermal contact conductance. As can be seen from Figure 10b, relative deviations below 3 % are obtained for all materials. Thus,

one can conclude that facial losses into the sample holder are insignificant even for materials with high thermal conductivity.

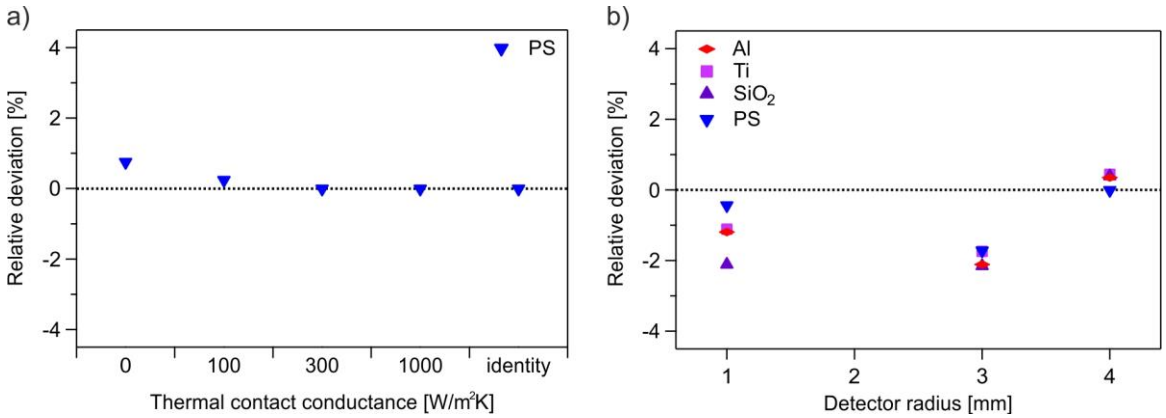

Figure 10. Influence of facial losses: a) Relative deviation of the thermal conductivity of PS obtained from fit and the preset thermal conductivity for different thermal contact conductance values. b) Relative deviation of all samples for maximum facial losses (identity boundary condition).

Heat losses are always present. Therefore, we studied the combined influence of all heat loss types: radiation, convection, and conduction into the sample holder (Figure 11a). Again, we chose PS as the material. Relative deviations below 2 % were obtained for all investigated configurations (Figure 11b). Furthermore, there are almost no differences between the relative deviation obtained from the simulation with thermal insulation and with heat losses.

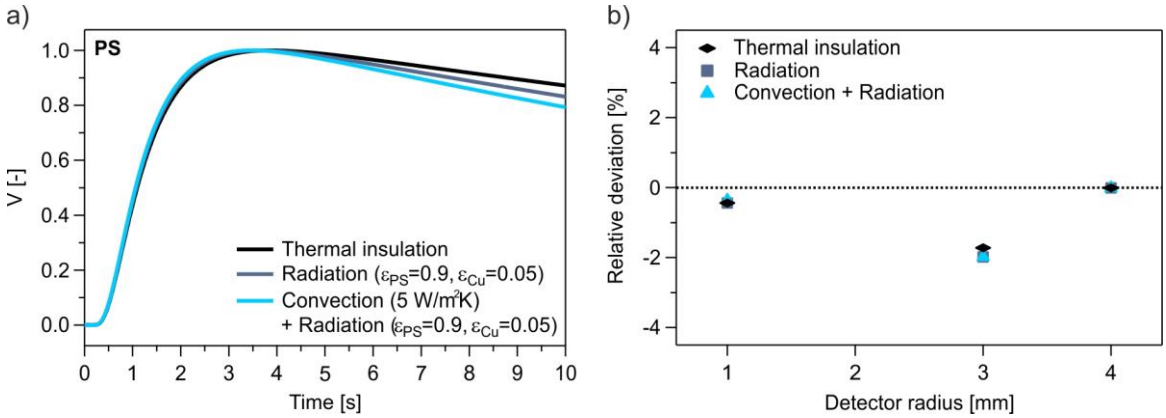

Figure 11. a) Normalized temperature rise versus time curves for PS with and without heat losses (detector radius: 4mm). b) Relative deviation obtained for no heat losses and with heat losses due to radiation or convection as well as radiation.

Our results demonstrate the remarkable robustness of the laser flash method to yield accurate values of the thermal diffusivity even for experimental conditions, which substantially deviate from optimal measurement conditions. This is a very positive result as it corroborates the confidence in thermal diffusivity results reported from laser flash analysis.

3.4. Experimental Validation

In the above sections we concluded by means of simulated experiments that the computational framework of LFA enables high accuracy measurements for a large variety of experimental conditions. To confirm this conclusion experimentally, we measured a reference sample (BCR-724 with certified thermal diffusivity value) using a xenon flash apparatus. Thereby, we used different sample holders to vary the excitation area (100 % - 10 %) and different sample covers to adjust the detection area (40 % - 10 %). The received raw data and the corresponding fit (solid black line) are shown in Figure 12a. A reduction in the excitation or detection area leads to a lower maximum temperature rise. The fitted thermal diffusivity agrees very well with the certified thermal diffusivity of BCR-724 (Figure 12b) independently of the chosen sample holder/cover. This confirms our expectation from FE modeling that the computational framework underlying LFA is – if based on a state-of-the-art mathematical model – fairly robust to deviations from ideal experimental conditions. For whereas the measured raw data of the overall temperature increase (reflected by the voltage change of the InSb detector) vary significantly depending on the experimental conditions, the thermal diffusivity was consistently and correctly fitted.

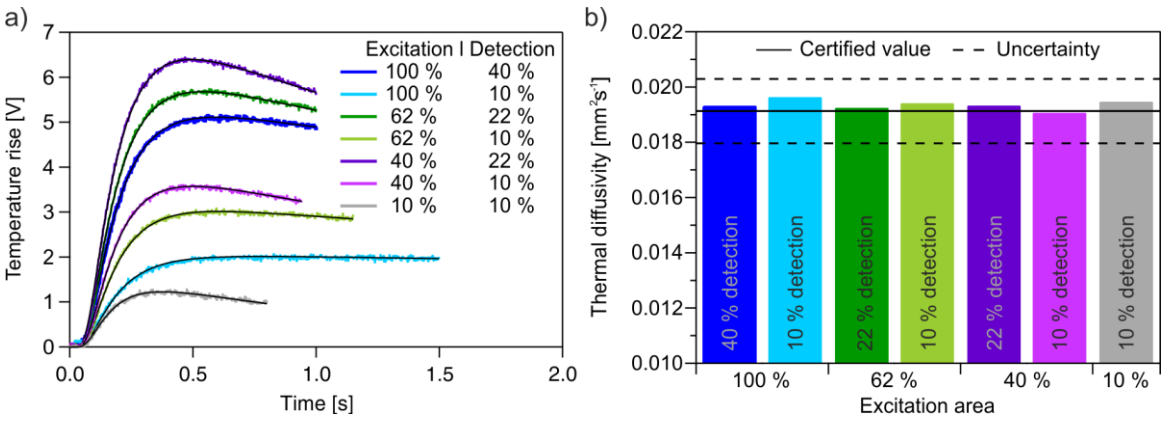

Figure 12. a) Temperature-rise-versus-time curves obtained from LFA measurements of BCR-724 and corresponding fit (solid black line). b) Thermal diffusivity of BCR-724 measured using different sample holders and covers; the solid black line represents the certified value of BCR-724, the dashed black lines the upper/lower limit of the uncertainty range.

4. Conclusion

The computational framework (*i.e.*, mathematical model and fitting procedure) underlying laser flash analysis (LFA) naturally limits the accuracy of LFA. So far, the impact of this limitation is poorly understood. To quantify this impact, we developed a state-of-the-art computational framework for LFA based on the work of Parker *et al.*[1], Cape and Lehman[19], Dusza[31] and Blumm *et al.*[32]. This framework can account for heat losses to the environment, radial losses within the sample, facial losses into the sample holder, radiative heat transfer, as well as combinations of these processes. It operates robustly even for Biot numbers $H_2 > 1$.

We applied this state-of-the-art computational framework to analyze the output data of experiments. Thereby we focused on simulated rather than real experiments. We did so for two reasons. First, for simulated experiments, the error that results from the computational framework underlying LFA can easily and accurately be quantified. It is the difference between the known simulation input parameters and the parameter values which the computational framework yields when applied in an inverse analysis of the simulation output data. The second reason why we used simulated rather than real experiments is that in computer simulations different experimental conditions can easily be mimicked and

controlled so that the impact of deviations from ideal experimental conditions can be examined conveniently. Our computational studies revealed that a state-of-the-art computational framework for LFA as we used it herein allows a determination of thermal conductivities for a broad range of materials and experimental conditions with a relative error of typically less than 4 %. This result confirms that LFA is a robust and reliable method for determining thermal diffusivity of materials even if an ideal sample preparation is practically in certain cases not possible.

Acknowledgements

This project was funded by the Lichtenberg Professorship provided by the Volkswagen Foundation.

Conflict of Interest

The authors declare no conflict of interest.

References

1. Parker, W. J.; Jenkins, R. J.; Butler, C. P.; Abbott, G. L., Flash method of determining thermal diffusivity, heat capacity, and thermal conductivity. *Journal of Applied* Physics **1961**, *32* (9), 1679-1684.

2. Righini, F.; Cezairliyan, A., Pulse method of thermal diffusivity measurements. High Temperatures-High Pressures **1973**, *5*, 481-501.

3. Degiovanni, A., Diffusivité et méthode flash. *Revue générale de thermique* **1971**, *185*, 420-442.

4. Taylor, R. E., Heat-pulse thermal diffusivity measurements. *High Temperatures-High Pressures* **1979**, *11* (1), 43-58.

5. Balageas, D. L., Thermal diffusivity measurement by pulsed methods. *High Temperatures-High Pressures* **1989**, *21*, 85-96.

6. Maglić, K.; Taylor, R., The apparatus for thermal diffusivity measurement by the laser pulse method. *In: Compendium of thermophysical property measurement methods.* Springer **1992**, pp 281-314.

7. Sheindlin, M.; Halton, D.; Musella, M.; Ronchi, C., Advances in the use of laser-flash techniques for thermal diffusivity measurement. *Review of Scientific Instruments* **1998**, *69* (3), 1426-1436.

8. Baba, T.; Ono, A., Improvement of the laser flash method to reduce uncertainty in thermal diffusivity measurements. *Measurement Science and Technology* **2001**, *12* (12), 2046.

9. Vozár, L., Flash method for thermal diffusivity measurement: Theory and Praxis. *Constantine the Philosopher University* **2001**

10. Vozár, L.; Hohenauer, W., Flash method of measuring the thermal diffusivity. A review. *High Temperatures-High Pressures* **2004**, *36* (3), 253-264.

11. Wiener, M.; Reichenauer, G.; Braxmeier, S.; Hemberger, F.; Ebert, H.-P., Carbon aerogel-based high-temperature thermal insulation. *International Journal of Thermophysics* **2009**, *30* (4), 1372-1385.

12. Nutz, F. A.; Retsch, M. Tailor-made temperature-dependent thermal conductivity via interparticle constriction. *Science Advances* **2017**, *3* (11).

13. Ruckdeschel, P.; Philipp, A.; Kopera, B. A. F.; Bitterlich, F.; Dulle, M., Pech-May N. W.; Retsch, M., Thermal transport in binary colloidal glasses: Composition dependence and percolation assessment. *Physical Review E* **2018**, *97* (2-1), 022612.

14. Li, T.; Song, J.; Zhao, X.; Yang, Z.; Pastel, G.; Xu, S.; Jia, C.; Dai, J.; Chen, C.; Gong, A.; Jiang, F.; Yao, Y.; Fan, T.; Yang, B.; Wågberg, L.; Yang, R.; Hu, L.,

Anisotropic, lightweight, strong, and super thermally insulating nanowood with naturally aligned nanocellulose. *Science Advances* **2018**, *4* (3).

15. Quill, T. J.; Smith, M. K.; Zhou, T.; Baioumy, M. G. S.; Berenguer, J. P.; Cola, B. A.; Kalaitzidou, K.; Bougher, T. L., Thermal and mechanical properties of 3D printed boron nitride – ABS composites. *Applied Composite Materials* **2018**, *25* (5), 1205-1217.

16. Chau, M.; Kopera, B. A. F.; Machado, V. R.; Tehrani, S. M.; Winnik, M. A.; Kumacheva, E.; Retsch, M., Reversible transition between isotropic and anisotropic thermal transport in elastic polyurethane foams. *Materials Horizons* **2017**, *4* (2), 236-241.

17. Mendelsohn, A. R., The effect of heat loss on the flash method of determining thermal diffusivity. *Applied Physics Letters* **1963**, *2* (1), 19-21.

18. Cowan, R. D., Pulse method of measuring thermal diffusivity at high temperatures. *Journal of Applied Physics* **1963**, *34* (4), 926-927.

19. Cape, J. A.; Lehman, G. W., Temperature and finite pulse-time effects in the flash method for measuring thermal diffusivity. *Journal of Applied Physics* **1963**, *34* (7):1909-1913.

20. Watt, D. A., Theory of thermal diffusivity by pulse technique. *British Journal of Applied Physics* **1966**, *17* (2), 231.

21. Clark III, L. M.; Taylor, R. E., Radiation loss in the flash method for thermal diffusivity. *Journal of Applied Physics* **1975**, *46* (2), 714-719.

22. Degiovanni, A., Identification de la diffusivité thermique par l'utilisation des moments temporels partiels. *High Temperatures-High Pressures* **1985**, *17*, 683-689.

23. Balageas, D. L., Nouvelle méthode d'interprétation des thermogrammes pour la détermination de la diffusivité thermique par la méthode impulsionnelle (méthode «flash»). *Revue de Physique Appliquée* **1982**, *17* (4), 227-237.

24. Josell, D.; Warren, J.; Cezairliyan, A., Comment on ''Analysis for determining thermal diffusivity from thermal pulse experiments''. *Journal of Applied Physics* **1995**, *78* (11), 6867-6869.

25. Larson, K. B.; Koyama, K. Correction for finite-pulse-time effects in very thin samples using the flash method of measuring thermal diffusivity. *Journal of Applied Physics* **1967**, *38* (2), 465-474.

26. Taylor, R. E.; Clark III, L. M., Finite pulse time effects in flash diffusivity method. *High Temperatures-High Pressures* **1974**, *6*, 65-72.

27. Azumi, T.; Takahashi, Y., Novel finite pulse-width correction in flash thermal diffusivity measurement. *Review of Scientific Instruments* **1981**, *52* (9), 1411-1413.

28. Xue, J.; Liu, X.; Lian, Y.; Taylor, R., The effects of a finite pulse time in the flash thermal diffusivity method. *International Journal of Thermophysics* **1993**, *14* (1), 123-133.

29. Heckman, R. C. Finite pulse-time and heat-loss effects in pulse thermal diffusivity measurements. *Journal of Applied Physics* **1973**, *44* (4), 1455-1460.

30. Lechner, T.; Hahne, E., Finite pulse time effects in flash diffusivity measurements. *Thermochimica Acta* **1993**, *218*, 341-350.

31. Dusza, L., Combined solution of the simultaneous heat loss and finite pulse corrections with the laser flash method. *High Temperatures-High Pressures* **1995**, *27/28* (5), 467-473.

32. Blumm, J.; Henderson, J.; Nilsson, O.; Fricke, J., Laser flash measurement of the phononic thermal diffusivity of glasses in the presence of ballistic radiative transfer. *High Temperatures-High Pressures* **1997**, *29*, 555-560.

33. Tischler, M.; Kohanoff, J. J.; Rangugni, G. A.; Ondracek, G., Pulse method of measuring thermal diffusivity and optical absorption depth for partially transparent materials. *Journal of Applied Physics* **1988**, *63* (5), 1259-1264.

34. Araki, N., Effect of radiation heat transfer on thermal diffusivity measurements. *International Journal of Thermophysics* **1990**, *11* (2), 329-337.

35. Andre, S.; Degiovanni, A., A theoretical study of the transient coupled conduction and radiation heat transfer in glass: phonic diffusivity measurements by the flash technique. *International Journal of Heat and Mass Transfer* **1995**, *38* (18), 3401-3412.

36. Hofmann, R.; Hahn, O.; Raether, F.; Mehling, H.; Fricke, J., Determination of thermal diffusivity in diathermic materials by the laser-flash technique. *High Temperatures-High Pressures* **1997**, *29* (6), 703-710.

37. Hahn, O.; Raether, F.; Arduini-Schuster, M. C.; Fricke, J., Transient coupled conductive/radiative heat transfer in absorbing, emitting and scattering media: application to laser-flash measurements on ceramic materials. *International Journal of Heat and Mass Transfer* **1997**, *40* (3), 689-698.

38. Andre, S.; Degiovanni, A., A new way of solving transient radiative-conductive heat transfer problems. *Journal of Heat Transfer* **1998**, *120* (4):943-955.

39. Mehling, H.; Hautzinger, G.; Nilsson, O.; Fricke, J.; Hofmann, R.; Hahn, O., Thermal diffusivity of semitransparent materials determined by the laser-flash method applying a new analytical model. *International Journal of Thermophysics* **1998** ,*19* (3), 941-949.

40. McMasters, R. L.; Beck, J. V.; Dinwiddie, R. B.; Wang, H., Accounting for penetration of laser heating in flash thermal diffusivity experiments. *Journal of Heat Transfer* **1999**, *121* (1), 15-21.

41. Lazard, M.; André, S.; Maillet, D.; Degiovanni, A., Radiative and conductive heat transfer: a coupled model for parameter estimation. *High Temperatures-High Pressures (UK)* **2000**, *32* (1), 9-17.

Supporting Information

1. Finite Element Modeling

Mesh Convergence Test

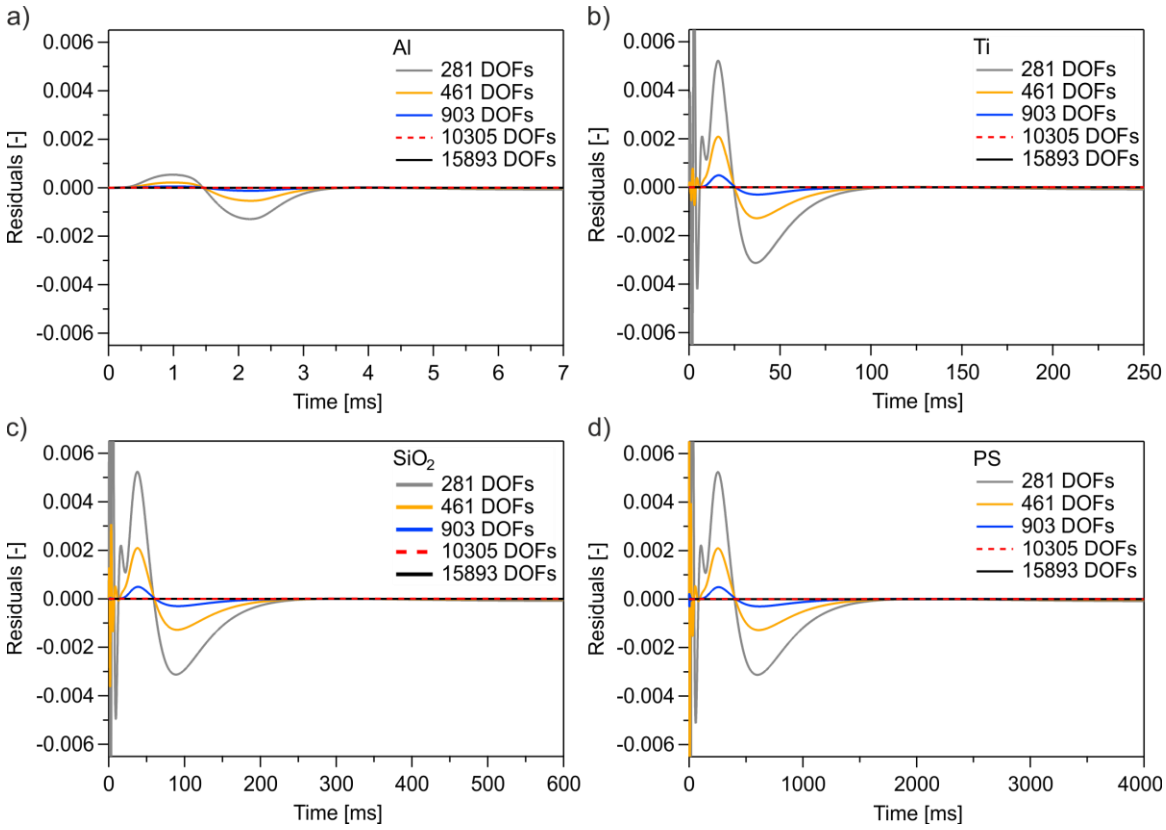

Figure S1. For the mesh convergence tests, the geometry without sample holder (Figure 3a) and a heat source radius of 1 mm were used, whereas the number of mesh elements was varied. The time-dependent temperature increase for a detector radius of 1 mm was evaluated. Finally, the residuals compared to the finest mesh (15983 DOFs, black straight line) were calculated. Since there are no significant differences between the mesh with 10305 DOFs (dashed red line) and the finest mesh, a mesh with 10305 DOFs was used for all simulations (and samples)

Convergence Test of Time Steps

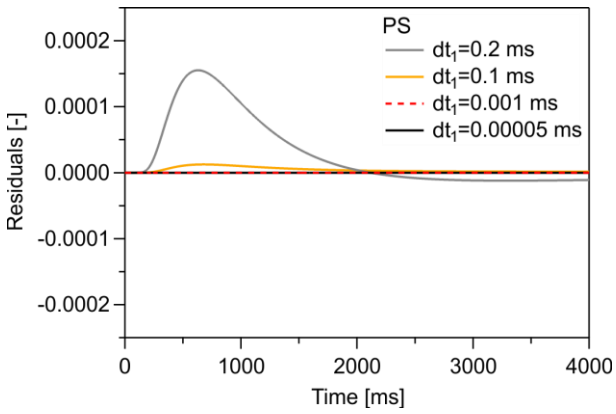

Figure S2. Besides the mesh size, the time steps used for the time-dependent simulations are also necessary to adjust fine enough, especially in the time range of the 2 ms triangular heat pulse. For the convergence tests, again the geometry without sample holder (Figure 3a) and a heat source radius of 1 mm was used. The time-dependent temperature increase for a detector radius of 1 mm was evaluated. Here, exemplarily shown for PS, the time steps within the first 2 ms were varied and the residuals compared to the smallest time steps were calculated. For PS, 0.001 ms time steps for the first 2 ms were used for all simulations.

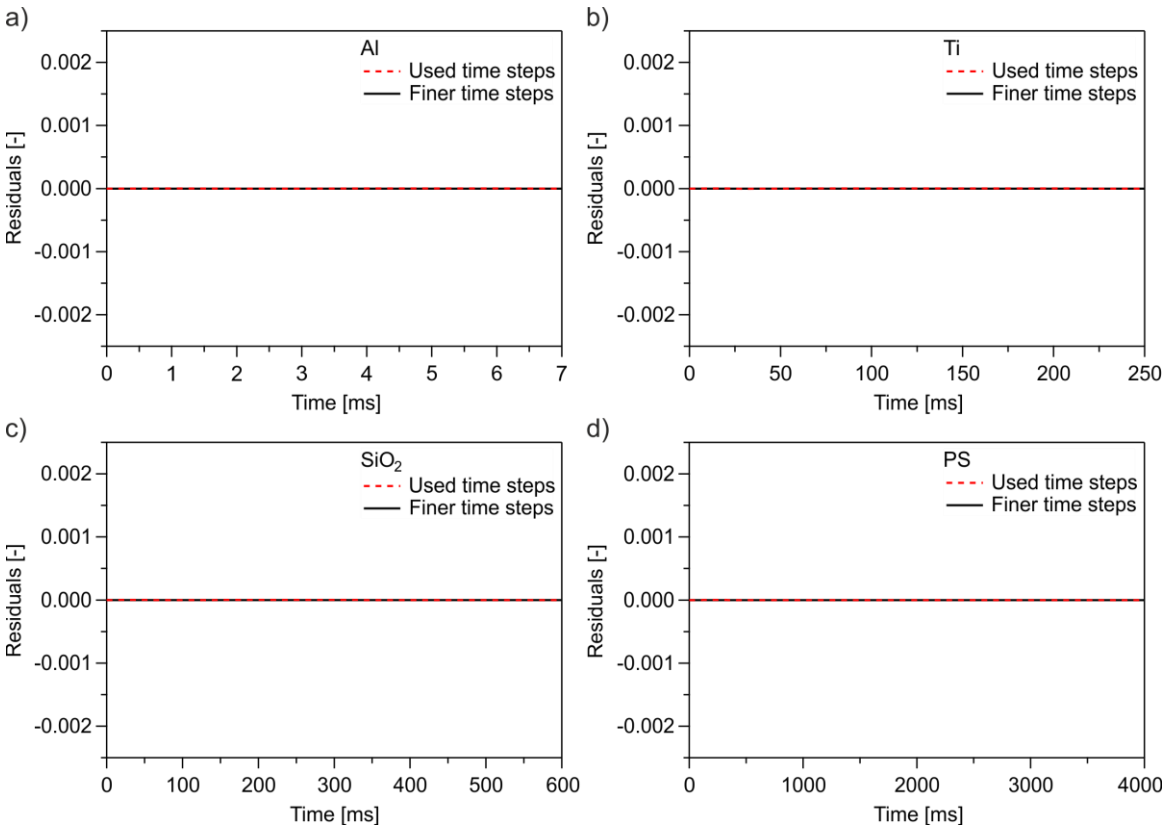

Figure S3. For the convergence tests, again the geometry without sample holder (Figure 3a) and a heat source radius of 1 mm was used. The time-dependent temperature increase for a detector radius of 1 mm was evaluated and the residuals compared to the smallest time steps (black straight line) were calculated. Since there are no significant differences between the two curves, the used time steps (red dashed line) are chosen fine enough.

Radial Losses into the Sample

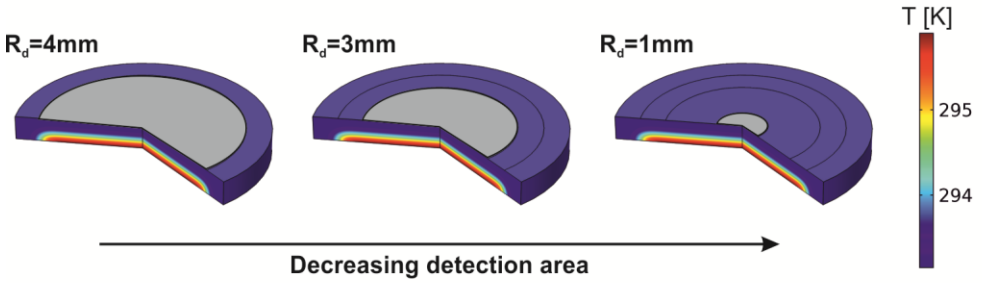

Figure S4. Influence of radial losses: COMSOL images for the same excitation area, but different detector radii. The smaller the detector radius, the smaller the detection area.

Influence of Measurement Time

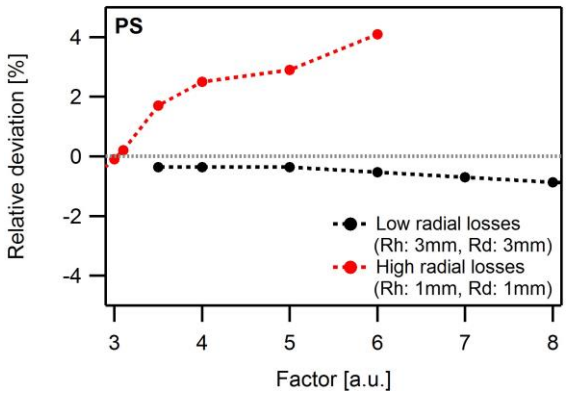

Figure S5. Exemplary plot of relative deviation versus factor (factor times the half-time $t_{1/2}$). In the case of low radial losses, the fit will also lead for longer measurement times to good results (relative deviation < 1 %). However, for high radial losses, long measurement times increase the relative deviation. Thus, to obtain always the smallest error, short measurement times should be used in any case (low or high radial losses).

7. Understanding Thermal Insulation in Porous, Particulate Materials

Pia Ruckdeschel, Alexandra Philipp, and Markus Retsch*

Physical Chemistry – Polymer Systems, University of Bayreuth, Universitätsstraße 30, 95447 Bayreuth, Germany

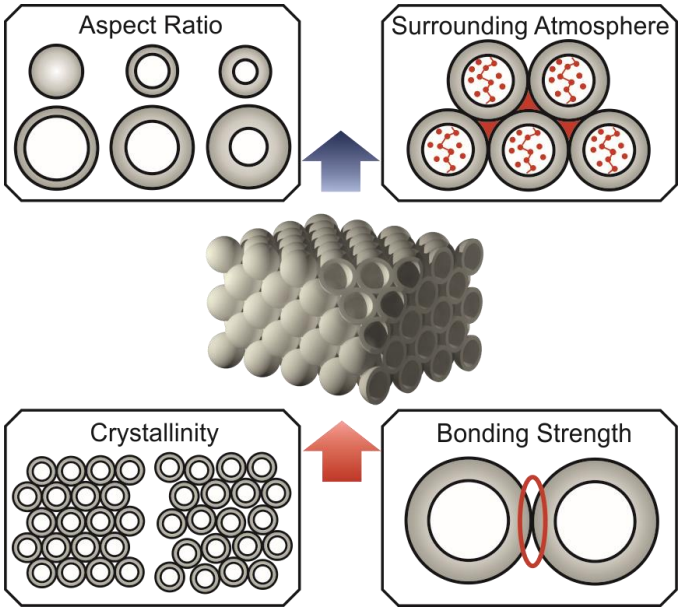

Reprinted with permission from Ruckdeschel *et al.*, *Adv. Funct. Mater.*, **2017**, 27, 1702256.

Abstract

Silica hollow nanosphere colloidal crystals feature a uniquely well-defined structure across multiple length scales. This contribution elucidates the intricate interplay between structure and atmosphere on the effective thermal diffusivity as well as the effective thermal conductivity. Using silica hollow sphere assemblies, one can independently alter the particle geometry, the density, the packing symmetry, and the interparticle bonding strength to fabricate materials with ultralow thermal conductivity.

Whereas the thermal diffusivity decreases with increasing shell thickness, the thermal conductivity behaves inversely. However, the geometry of the colloidal particles is not the only decisive parameter for thermal insulation. By a combination of reduced packing symmetry and interparticle bonding strength, the thermal conductivity is lowered by additionally 70 % down to only 8 $mWm^{-1}K^{-1}$ in vacuum. The contribution of gaseous transport, even in these tiny pores (< 200 nm), leads to minimum thermal conductivities of ~35 $mWm^{-1}K^{-1}$ and ~45 $mWm^{-1}K^{-1}$ for air and helium atmosphere, respectively. The influence of the individual contributions of the solid and (open- and closed-pore) gaseous conductions was further clarified by using finite element modeling. Consequently, these particulate materials can be considered as a non-flammable and dispersion processable alternative to commercial polymer foams.

1. Introduction

In our age of limited energy resources, a strong need for sustainable and efficient thermal insulation technologies has evolved. Thus, the ability to thermally insulate pipes, walls, entire houses, or even ourselves from extreme cold and hot conditions is of high importance. Hence, humans have been developing insulating materials for thousands of years, trying to reduce their thermal conductivity as efficiently as possible. Insulation materials have the natural capacity to inhibit the transmission of heat by exhibiting high volume fractions of a gaseous phase or by introducing a

large number of interfaces, leading to an efficient thermal insulation.[1-2] Conventional insulation materials are fiberglass, mineral wool, and polymer foams.[2] The decisive performance quantity is given by the thermal conductivity κ, which describes the steady-state amount of thermal energy (heat) that can be transferred along a given temperature gradient. Current polymer foam-based materials possess thermal conductivities of about $20 - 40\ \mathrm{mWm^{-1}K^{-1}}$.[3] One approach to achieve even higher thermal insulation properties is the implementation of the Knudsen effect by (i) the replacement of air with other gases or vacuum, or by (ii) reducing the pore size below the mean free path of air.[3] However, maintaining a certain gas or even vacuum inside a porous material is challenging. Thus, the reduction of the pore size seems to be a more promising way to obtain a super-insulating material. An example for nanoporous materials are aerogels, which in most cases comprise silica (SiO_2) as the solid skeleton backbone.[4-8]

Whereas silica aerogels are excellent materials for thermal insulation due to their nanoporosity, their widespread application is still limited compared to polymer foams or organic fibers and fleeces. Major obstacles are their poor mechanical properties and their laborious and energy intensive fabrication, which in most cases involves supercritical drying using carbon dioxide.[9] The good insulation properties of silica aerogels inspired researchers to find other nanomaterials with similar or better properties.[9-13] Among these materials, silica hollow spheres are a promising insulation material, due to their structural analogy to silica aerogels. Their high thermal insulation capability has already been shown in powder measurements of silica hollow spheres.[14] However, from these measurements, conclusions about the influence of the size and shell thickness are impossible due to the ill-defined order within the powder specimens. Furthermore, it is not possible to detect any influences of the contact area and bonding strength between the silica hollow spheres. In contrast, our contribution unleashes for the first time the full potential of colloidal crystals for the understanding of thermal transport

on small length scales. This is based on their periodically ordered structure, their large number of interfaces, and the possibility to adjust the surface chemistry.[15] Whereas the optical properties are well known for colloidal crystals, the thermal properties are far from being fully understood.[16] Recent contributions in this field are investigations on nanocrystal arrays, inverse opals[17-18], organoclay nanolaminates[1] and colloidal nanoparticle assemblies[12-13, 19-20].

Understanding thermal transport in nanomaterials is not only essential for steady-state thermal insulation, but also for non-steady-state insulation like refrigeration or fire protection.[21-22] In both cases, the aim is to minimize the temperature increase in a closed area, surrounded by heat or fire for a certain time. Thus, there are two requirements for a material used for non-steady-state insulation. First, the material's thermal conductivity should be as low as possible to minimize the amount of energy conducted into the system. Second, the volumetric heat capacity (density and specific heat capacity) should be large, so that the accumulated energy is absorbed to minimize the temperature increase. The material specific property for characterizing the non-steady-state heat conduction is the thermal diffusivity. It is defined as the ratio of thermal conductivity to volumetric heat capacity. Materials with low thermal diffusivities are polymer materials. However, these materials are inherently not flame-retardant without modifying the polymer or incorporating flame retardant compounds.[23] Silica hollow sphere colloidal crystals could contribute to the solution of this problem due to their low thermal diffusivities as shown later.

In this paper, we will address the following questions: What is the fundamental limit of the thermal conductivity that can be achieved by such hollow sphere ensembles? What are the governing structure-property relationships? Therefore, we will present a holistic study of the thermal insulation capabilities of hollow silica nanoparticle assemblies. Our findings are of general importance to rationally understand and improve the thermal insulation capability of nanoporous materials. We will investigate the influence of (i) the aspect ratio of the hollow

particles (size and shell thickness), (ii) the symmetry of the colloidal assembly (crystalline *vs.* amorphous packing), (iii) the surrounding atmosphere by gas pressure-dependent thermal conductivity measurements, (iv) the closed- and open-porous volume and (v) the bonding strength between adjacent spheres in the assembly.

2. Results and Discussion

2.1. Silica Hollow Sphere Colloidal Crystals

The synthesis of monodisperse core-shell particles is divided into two steps: (i) the synthesis of polystyrene (PS) template particles via emulsifier-free emulsion polymerization[24] and (ii) the coating of the PS spheres with a silica shell using a templated Stoeber condensation process[25]. The well-defined colloids are subsequently crystallized into superstructures via a simple evaporation-induced self-assembly process (see schematic illustration in the Supporting Information in Scheme S1), followed by a calcination step (heat treatment at 500 °C) to burn out the PS core of the core-shell particles. As a result, hollow silica nanoparticle colloidal crystals are obtained. Further experimental details are described in the Experimental Section.

The narrow size distribution of the core-shell particles leads to ordered colloidal crystals (CCs) with a high packing density straightforwardly and reproducibly. Exemplary photographic images of such hollow sphere (HS) colloidal crystals with different shell thicknesses are shown in Figure S1. All three samples exhibit a purple color due to their same outer particle diameter of ~270 nm. However, the CCs become more and more opaque with increasing shell thickness (from left to right), resulting from an increased scattering. Thus, the CCs become more and more opaque.

The thermal transport properties and the density of the assembled HS structures are governed by two structural parameters: the shell thickness and the size of the particles. Our synthetic protocol allows adjusting these two quantities

independently and thus, to study their influence on the macroscopic thermal transport. We base our investigation on five different hollow silica nanoparticles as depicted in Figure 1.

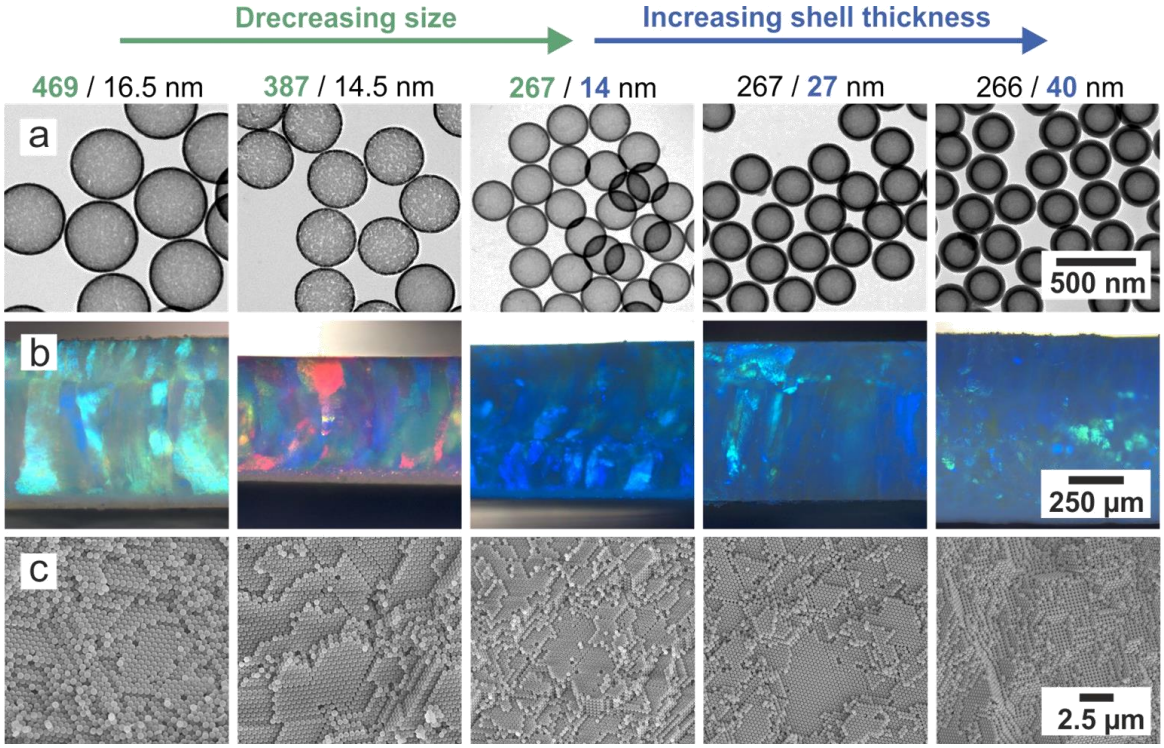

Figure 1. Hollow silica nanoparticles and their corresponding colloidal crystals. a) Transmission electron microscopy (TEM) images of the individual particles, b) side-view optical microscopy images, and c) scanning electron microscopy (SEM) images of the colloidal crystals.

To highlight the contribution of the overall particle size and the shell thickness separately, we prepared two different series. In the first, the diameter of the particles was altered between 267 and 469 nm with a constant shell thickness of about 15 nm (size series). In a second set, the size of the particles was kept constant at ~270 nm, while the shell thickness was adjusted between 14 nm and 40 nm (shell thickness series). The relevant structural parameters obtained from transmission electron microscopy (TEM) are summarized in Table 1. All samples exhibit a low polydispersity of about 1 %. Besides TEM measurements, the monodispersity is also confirmed by small-angle X-ray scattering (SAXS, Figure S2). The low polydispersity of the particle size results in narrowly spaced form factor minima, which are superimposed by further minima, which indicate the low polydispersity of the shell thickness.[26] The analysis of these scattering curves gives comparable

values for the size and shell thickness as the evaluation of the TEM images (Table 1). In the following, the values obtained from SAXS analysis are used for the nomenclature of the hollow spheres: HS-xxx/yy, where xxx is the diameter and yy is the shell thickness.

Table 1. Summary of data received from TEM, and SAXS measurements, as well as density measurements of the colloidal crystals.

	TEM		*SAXS* [a)]		*Density* [b)]
	d **[nm]**	***t*** **[nm]**	***d*** **[nm]**	***t*** **[nm]**	$\boldsymbol{\rho(c)}$ **[gcm^{-3}]**
HS-469/17	468.8 ± 3.0	18.2 ± 1.2	469.0	16.5	0.235 ± 0.009
HS-387/15	383.5 ± 5.3	15.2 ± 1.1	387.0	14.5	0.244 ± 0.014
HS-267/14	264.4 ± 2.6	12.9 ± 0.6	267.0	14.0	0.370 ± 0.006
HS-267/27	270.5 ± 4.1	26.9 ± 1.0	267.0	27.0	0.702 ± 0.007
HS-267/40	268.7 ± 3.8	40.4 ± 1.4	266.0	40.0	0.883 ± 0.022

[a)]The fitting was performed using the software Scatter with a vesicle model.[36] The standard deviation of the outer radius is 0.014 - 0.022 and for the inner radius 0.06 - 0.15. [b)] The density of the silica shell can be found in Table S1.

Figure 1b shows optical microscopy side-view images of the CCs of the hollow nanospheres. A bright opalescence is visible in all samples pointing to a close-packed structure. We label these colloidal assemblies with the appendix *c*, referring to the crystalline state (*e.g.*, HS-469/17-c). For the shell thickness series (HS-267/14-c, HS-267/27-c, and HS-266/40-c) the observed color is identical due to the same outer diameter of ~270 nm, as mentioned beforehand (Figure S1). In contrast, the size series exhibits different colors depending on the particle diameter. The long-range order of the nanospheres in a hexagonal close-packed structure is further confirmed by scanning electron microscopy (SEM) images (Figure 1c). Based on the optical microscopy and SEM images, the volume fraction of the particles in the CCs can, therefore, be assumed to be close to 74 %, which is the theoretical value for an ideal close-packed structure. The densities of the colloidal crystals $\rho(c)$ were determined by measuring the volume, and weight of the CCs (for details see Supporting Information) and are summarized in Table 1.

Here, values between 0.235 gcm^{-3} for HS-469/17-c and 0.883 gcm^{-3} for HS-266/40-c were obtained. Hence, a broad range of densities below conventional bulk materials ($\rho > 1$ gcm^{-3}) is covered. The density of the silica shell can be calculated with the help of the effective density of the colloidal crystals yielding values between 1.7 and 1.9 gcm^{-3} (see Table S1). The sample HS-387/15 exhibits a slightly lower silica density (1.5 gcm^{-3}) caused by an increased microporosity as depicted in the nitrogen sorption data in Figure S3 and Table S2. The BET surface area (246 m^2g^{-1}) and the pore volume (0.41 cm^3g^{-1}) of HS-387/15 are slightly higher compared to the other hollow silica spheres, for which the BET surface area ranges between 150 – 180 m^2g^{-1} and the pore volume amounts to 0.18 – 0.33 cm^3g^{-1}. Thereby, the micropore diameter shows a broad distribution with a maximum < 5 nm for the different silica hollow nanospheres. Overall, no significant influence of the microporosity on the thermal transport is expected.

2.2. Thermal Transport Properties of Silica Hollow Sphere Colloidal Assemblies

We investigated the thermal transport properties by the Xenon flash analysis (XFA). The setup and a common measurement signal along with its radiation fit are provided in Figure S4. In brief, a sample, coated with a thin graphitic layer on both sides, is subjected to a temperature increase due to a short Xenon light flash illuminating the bottom surface of the specimen. The absorbed heat is conducted through the sample. At the upper surface, an infrared (IR) detector measures the time-dependent temperature increase. Subsequently, the measurement signal is fitted with an appropriate one-dimensional heat diffusion model (*i.e.*, the radiation model), giving the effective thermal diffusivity of the measured sample. The great advantage of this method is the possibility to control the temperature and the surrounding atmosphere (pressure, gas type) in a precise manner.

The individual contributions of the heat transport in porous materials are solid conduction, open- and closed-pore volume gaseous conduction, radiative

transport, and convection. The different mechanisms are depicted in Scheme 1. The contribution from convection is negligible due to the small pore sizes. Additionally, radiative thermal transport can be neglected due to the transient measurement and the small temperature difference applied in an XFA. Thus, the heat transport is mainly governed by solid and gaseous conduction. We want to point out that Xenon flash analysis measures the *effective* thermal diffusivity owing to the porosity of the colloidal ensemble. For reasons of readability, however, we will talk about thermal diffusivity and conductivity, respectively, throughout this paper. In the following sections, we will describe the individual contributions of the thermal transport as a function of the structure of the silica hollow sphere colloidal crystals.

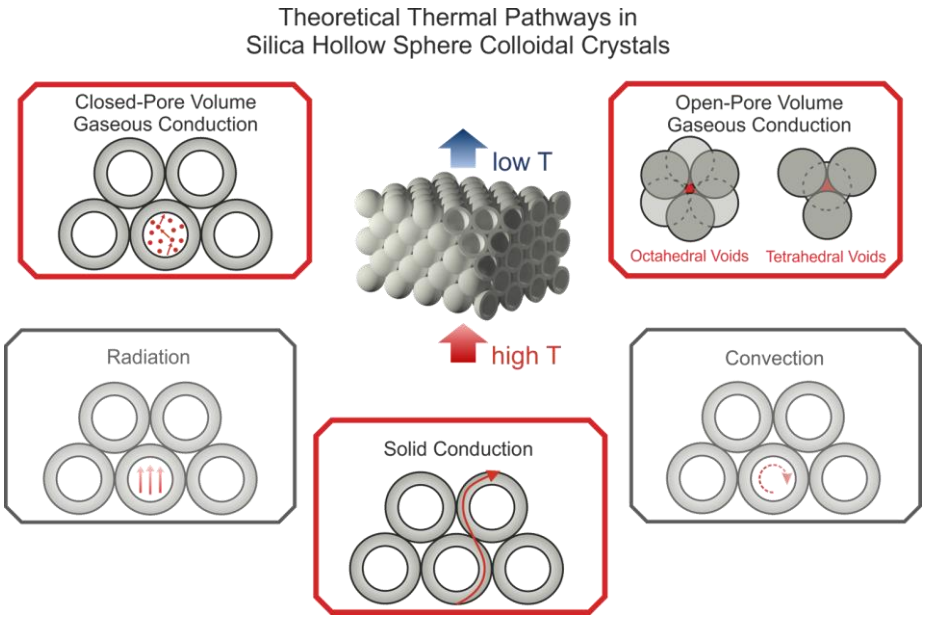

Scheme 1. Thermal transport pathways in a silica hollow sphere colloidal crystal: Solid conduction, gaseous conduction through the open-pore and closed-pore volume, radiative transport, and convection. The red framed boxes mark the thermal pathways critical for silica hollow sphere colloidal crystals.

2.2.1. Thermal Diffusivity of Silica Hollow Sphere Colloidal Crystals

How fast is temperature diffusing through a hollow sphere colloidal crystal? Considering that, the thermal diffusivity has to be considered. For an understanding of the contribution of the solid and the gaseous conduction through

the colloidal assemblies, the experiments were conducted in vacuum (0.05 mbar) and in helium in the range between 1 – 1000 mbar.

The thermal diffusivity under vacuum conditions (0.05 mbar) is solely governed by the thermal conduction across the solid silica network. It should be noted that the contact area between two adjacent spheres was measured to be comparable for all particles (0.60 – 0.77 % of the particle surface area). Hence, an influence of the contact area can be excluded.[13] Our data show that the actual size of the hollow spheres does not strongly affect the thermal diffusivity, which remains constant at around $1.6 \cdot 10^{-3}$ cm^2s^{-1} (Figure 2a). Conversely, the shell thickness exerts a strong impact on the thermal diffusivity, with a systematic decrease by about 27 % when increasing the shell thickness (Figure 2b). Thus, a larger amount of material slows down the temperature diffusion. These low thermal diffusivity values are comparable to common bulk polymer materials.[27]

Quite expectedly, for both, the size series (Figure 2a) and the shell thickness series (Figure 2b), the thermal diffusivity increases with increasing helium pressure. This is due to the additional temperature diffusion pathway through the gaseous phase at high helium pressures. However, it is interesting to consider the quantitative changes. The increase of the thermal diffusivity is more pronounced for larger particles than for smaller ones. It amounts to 37 % ($\alpha = 9.0 \cdot 10^{-4}$ cm^2s^{-1}) for the samples HS-469/17-c and HS-387/15-c and only 20 % ($\alpha = 4.3 \cdot 10^{-4}$ cm^2s^{-1}) for HS-267/14-c when decreasing the particle size. An explanation for the different sensitivity to helium atmosphere can be given by comparing the interparticle void sizes[28] (see Table S3) with the mean free path of helium (~ 200 nm).[29] The octahedral voids, as a measure for the upper limit, range from 194 nm to 110 nm for the largest and smallest hollow sphere, respectively. Consequently, the mean free path of helium is comparable or greater than the open-pore volume of the voids. This implies that gas-wall interactions predominate over the collision of the gas molecules with each other (Knudsen diffusion).[30] The confinement effect is the strongest for the smallest particles, resulting in the smallest additional temperature

conduction across the gaseous phase, whereas a higher amount of temperature transfer can be expected for the larger particles.

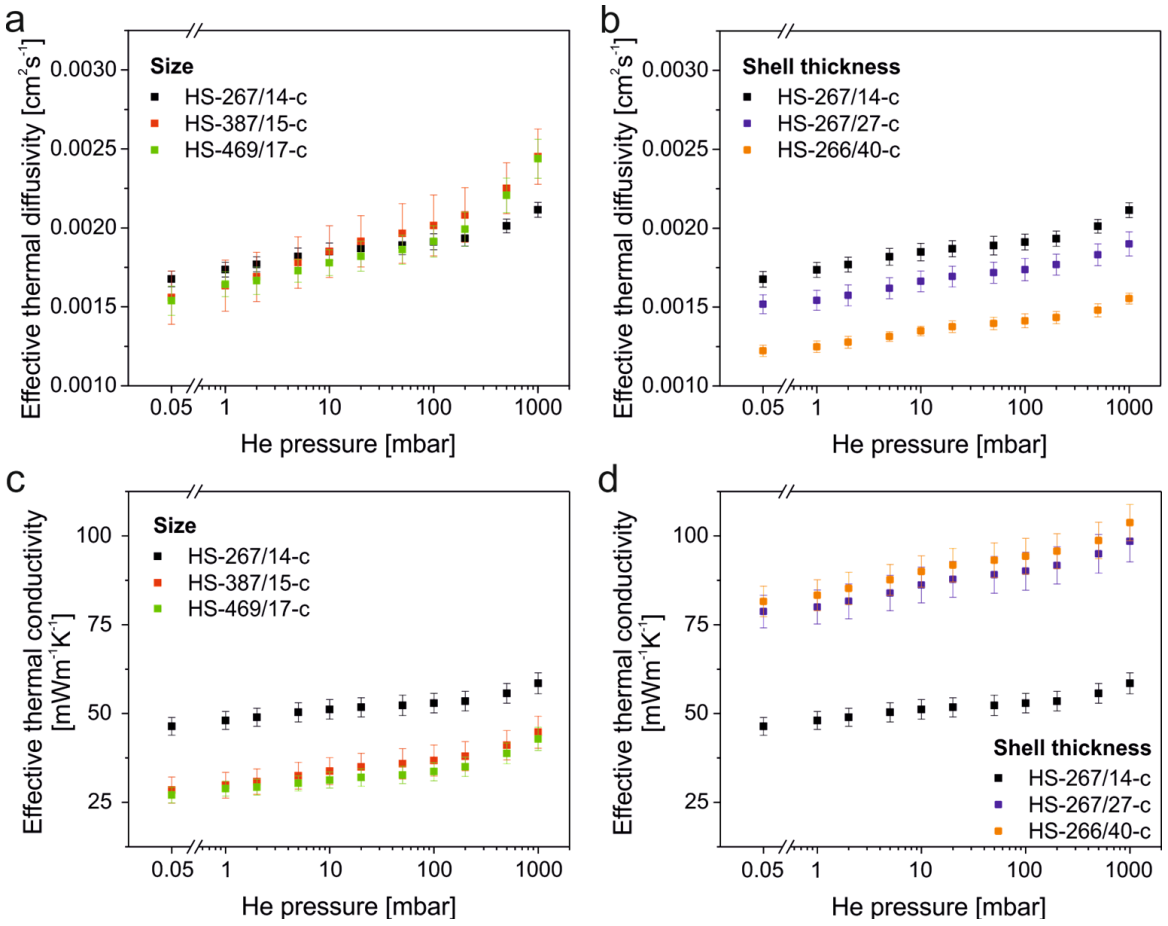

Figure 2. Thermal transport properties of silica hollow sphere colloidal crystals. a, b) Pressure-dependent thermal diffusivity of the size series (a), and the shell thickness series (b). c, d) Pressure-dependent thermal conductivity of the size series (c), and the shell thickness series (d).

In contrast, the thermal diffusivity increases from vacuum (0.05 mbar) to helium at 1000 mbar by about 20 % for all shell thicknesses. This corresponds to a thermal diffusivity difference $\Delta\alpha$ of $4.3 \cdot 10^{-4}$ cm^2s^{-1} for the thinnest shell to $3.3 \cdot 10^{-4}$ cm^2s^{-1} for the thickest shell. Hence, the increase of the thermal diffusivity from vacuum to helium is rather similar for all shell thicknesses due to the same outer diameter. Slight differences can be explained by the impact of the decreasing inner pore volume. A more detailed investigation on how the heat spreads between the solid phase and the internal and external pore volume is given in the Chapter 2.2.3 by finite element modeling.

2.2.2. Thermal Conductivity of Silica Hollow Sphere Colloidal Crystals

How much energy is conducted across a hollow sphere colloidal crystal? For this, we determined the *effective* thermal conductivity κ, which can be calculated based on the *effective* thermal diffusivity α, the heat capacity c_p, and the density ρ of the colloidal crystal using the following equation:

$$\kappa = \alpha \cdot c_p \cdot \rho \quad (1)$$

The heat capacity was averaged over four different silica hollow spheres with different sizes and shell thicknesses (see Figure S5). Its mean value at 25 °C amounts to (0.748 ± 0.031) $Jg^{-1}K^{-1}$. The density values are summarized in Table 1. In Figure 2c and d, the resulting pressure-dependent thermal conductivities are given.

The lowest thermal conductivity values are observed in vacuum due to the absence of heat transport pathways through the gaseous phase. While the thermal diffusivity is more or less size independent, the thermal conductivity exhibits a clear size dependence (Figure 2c). The lowest thermal conductivity is obtained for the colloidal crystal comprising the largest particles (HS-469/17-c). In vacuum, a value of 27 $mWm^{-1}K^{-1}$ is achieved, and in helium, at 1000 mbar the thermal conductivity amounts to 43 $mWm^{-1}K^{-1}$. The comparable density of HS-387/15-c and HS-469/17-c results in a very similar thermal conductivity, whereas the thermal conductivity of HS-267/14-c is significantly higher.

We also found a shell thickness dependent thermal conductivity (Figure 2d). In contrast to the thermal diffusivity, an opposing trend is present: The thermal conductivity in vacuum increases by about 43 % from 46 $mWm^{-1}K^{-1}$ to 82 $mWm^{-1}K^{-1}$ with increasing shell thickness. When using helium as a gas medium, the thermal conductivity ranges from 59 $mWm^{-1}K^{-1}$ to 104 $mWm^{-1}K^{-1}$. For decreasing particle sizes, a reduction in the thermal conductivity difference between vacuum and helium is found ($\Delta\kappa$ = 15.8 $mWm^{-1}K^{-1}$ for HS-469/17-c to $\Delta\kappa$ = 12.1 $mWm^{-1}K^{-1}$ for HS-267/14-c). This agrees with the thermal diffusivity data,

and can be traced back to the more pronounced Knudsen effect for the smaller particles. On the other hand, for the shell thickness series, a constant difference between vacuum and helium is expected due to the same outer pore diameter. However, we find that the increase from vacuum to helium is more pronounced for the thickest shell ($\Delta\kappa = 22.1\ mWm^{-1}K^{-1}$) compared to the thinnest shell ($\Delta\kappa = 12.1\ mWm^{-1}K^{-1}$). This can be explained by a slight densification of the silica shell with increasing shell thickness. The role of the inner pore volume will be elucidated in the next chapter by FEM simulation.

Figure 3 summarizes the thermal diffusivity and thermal conductivity properties of our hollow silica spheres colloidal crystals. From that, insights into the fundamental limit of thermal insulation, solely based on the hollow sphere geometry, can be deduced. From the vacuum measurements, it is apparent that larger shell thicknesses are needed to reduce the thermal diffusivity. However, the reduction in thermal diffusivity is over-compensated by the concomitant density increase. Consequently, the thermal conductivity increases with shell thickness and tends towards a plateau. Increasing the size of the hollow spheres does not strongly influence the thermal diffusivity. Therefore, the density of the colloidal ensemble governs the effective thermal conductivity. Lower thermal conductivities ($< 27\ mWm^{-1}K^{-1}$) could be achieved by larger particles with thin shells. However, this would come at a compromised structural integrity of the colloidal ensemble, since the stiffness of hollow silica particles scales with the square of the shell thickness t^2 and inversely with the radius of the particle R^{-1}.[31] Overall, the thermal diffusivity and thermal conductivity cannot be lowered simultaneously just by the appropriate particle design.

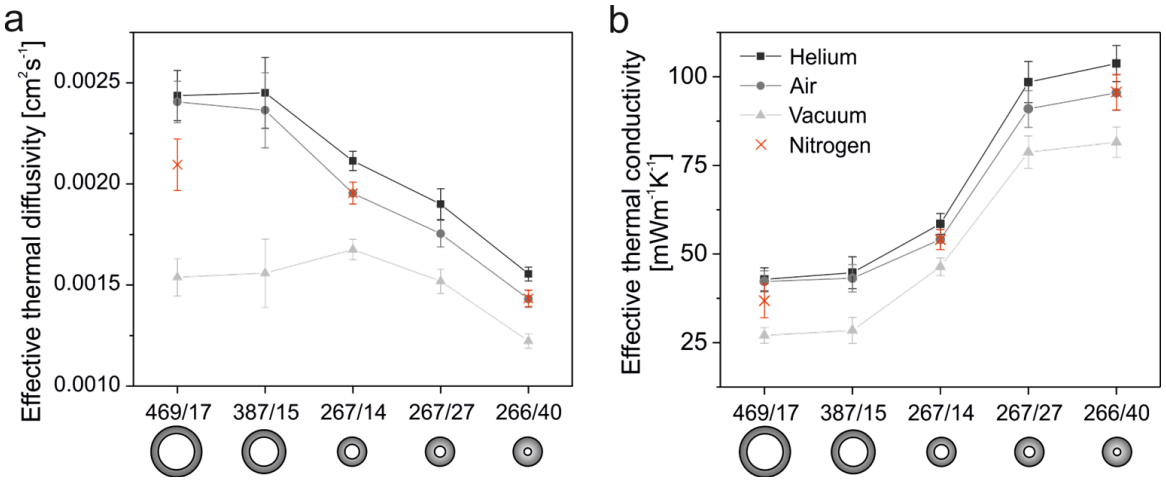

Figure 3. Atmosphere-dependent thermal transport properties of silica hollow sphere colloidal crystals. a) Thermal diffusivity and b) thermal conductivity in helium and air at 1000 mbar as well as vacuum at 0.05 mbar. The lines are a guide to the eye.

Additional thermal transport pathways in the open-porous structure are opened by using nanoporous systems in air or helium. The thermal transport properties in ambient air are located between the helium and vacuum measurements due to a lower gaseous thermal conductivity compared to helium (air: 25 $mWm^{-1}K^{-1}$ compared to helium: 153 $mWm^{-1}K^{-1}$).[32] However, this is not the case for the larger particle diameter, especially for sample HS-469/17-c, where a similar thermal conductivity is obtained in air and helium. An explanation for this is water condensation, which can be adsorbed by the hygroscopic silica network during measurement in ambient air. The incorporation of water does not occur in helium and vacuum due to preconditioning of the samples at 200 °C in vacuum before the thermal transport determination. When conducting the experiments with dry nitrogen, the thermal conductivity of the assembly with the largest spheres (HS-469/17-c) is reduced by 13 %, compared to moist air, yielding a thermal conductivity of 37 $mWm^{-1}K^{-1}$ in nitrogen (red crosses in Figure 3). Altogether, our measurements indicate a fundamental limit of the thermal conductivity at around 35 $mWm^{-1}K^{-1}$ for hollow silica nanoparticle ensembles in air. This is based on the interplay between solid and gaseous heat conduction. Furthermore, care has to be taken to avoid vapor condensation, which will further increase the overall thermal conductivity. Whereas the measured values of the thermal conductivity are higher

compared to silica aerogels, they are well comparable to commercial polymer foams. Yet, these hollow sphere ensembles possess several advantageous features: breathable due to their open porous structure, dispersion-processable like spraying or painting, and non-flammable based on the SiO_2 network.

2.2.3. Finite Element Modeling of the Thermal Transport in HS Colloidal Crystals

In the following, we compare our experimental results to the data obtained from finite element modeling (FEM). The aim of the FEM simulation is to gain insights into the contribution of the open- and closed-pore volume to the total heat transport through silica hollow sphere colloidal assemblies.

For the steady-state simulations, hollow spheres were arranged in a face-centered cubic (*fcc*) unit cell packing (see Figure S7). A constant hot and cold temperature is imposed on the entire lower and upper face, while all other boundaries are set thermally insulating. Thus, a temperature gradient is formed, with a heat flux in the direction of the cold face. The effective thermal conductivity is calculated according to Fourier's equation of heat conduction:

$$\kappa = \frac{Q/A}{\Delta T/h} \tag{2}$$

where Q is the numerically computed heat flow rate normal to the cross-sectional area A ($= h^2$) of the unit cell, ΔT the temperature difference ($T_{\mathrm{hot}} - T_{\mathrm{cold}}$), and h the unit cell edge length. Further details about the model are described in the Supporting Information.

Figure 4a shows the calculated thermal conductivity for the different silica hollow sphere geometries in vacuum and helium, with different thermal contact conductances h_c between silica and helium (0 $Wm^{-2}K^{-1}$ – continuity). The solid/gas thermal contact conductance is an unknown variable and needs to be reasonably estimated, while the thermal contact resistance between adjacent spheres is assumed to be zero. In the absence of gas, heat is only transported through the silica network. For this case, the thermal conductivity of the silica shell material

was adjusted such that similar values were obtained for the simulation and the experimental data. We found a thermal conductivity of the silica shell material of $\kappa = 331$ mWm^{-1}K^{-1} to describe our system adequately. This is comparable to nanostructured silica thin films reported by Coquil *et al.*[33]. By introducing helium to the network, additional heat conduction pathways arise. The thermal conductivity of helium was reduced compared to its bulk value due to the Knudsen effect occurring in small pores. The applied thermal conductivities in the open- and closed-pores are summarized in Table S5.

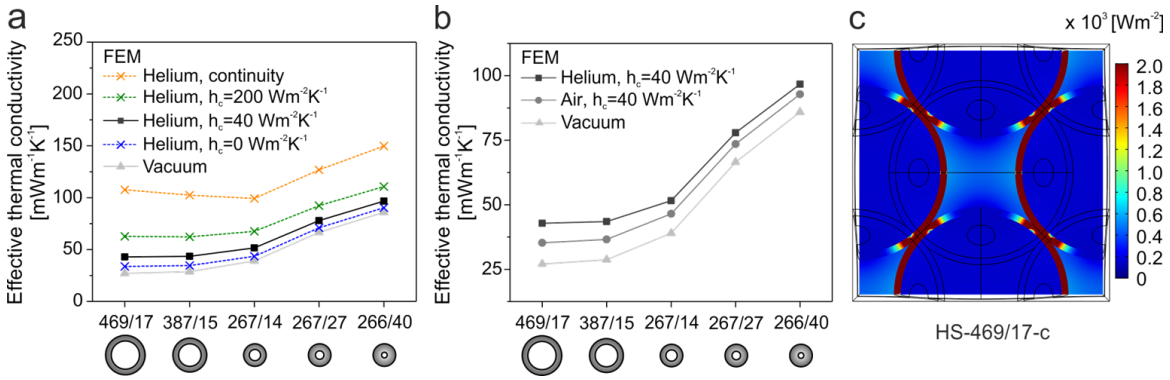

Figure 4. Finite element method modeling. a) Influence of the thermal contact conductance h_c between silica and helium on the total thermal conductivity of silica hollow sphere colloidal crystals and comparison to vacuum. b) Thermal conductivity of silica hollow sphere colloidal crystals in vacuum, helium, and air assuming a thermal contact conductance h_c of 40 Wm^{-2}K^{-1}. The input data used for the simulations in a) and b) can be found in Table S4 and Table S5, respectively. c) Heat flux density analysis for a thermal contact conductance of 40 Wm^{-2}K^{-1} between the silica network and helium for HS-469/17-c. The thermal conductivity values used for helium in the open- and closed-pores are listed in Table S5. The integrated heat flux densities of the different phases are listed in Table S7.

At a thermal contact conductance of 0 Wm^{-2}K^{-1}, only the gas in the open-pore volume can contribute to the total heat transport. For this case, the increase in the thermal conductivity was found to be too low compared to the experimentally determined data in helium. Thus, a small amount of the heat has to be also transferred through the closed-pore volume. We found a relatively low thermal contact conductance of 40 Wm^{-2}K^{-1} between the solid spheres and their gaseous environment to be suitable for our system. Higher thermal contact conductance values of 200 Wm^{-2}K^{-1} (green crosses) and continuity (orange crosses), which

means that no thermal contact resistance exists, are also shown in Figure 4a. It is apparent that these parameters overestimate the thermal conductivity of the colloidal crystals. They also do not replicate the geometry-dependent trend adequately.

The thermal transport properties are plotted in Figure 4b for different gases, using a thermal contact conductance of 40 $Wm^{-2}K^{-1}$. The theoretically obtained values are in good agreement with the measured ones (Figure 3). For all surrounding atmospheres, the thermal conductivity decreases with decreasing shell thickness and increasing particle diameter. The additional thermal transport through the gaseous phase increases the thermal conductivity from vacuum to helium. The simulations in (dry) air are located between helium and vacuum. By looking at the helium and vacuum data, it can be seen that the relative change in thermal conductivity is lower for smaller particles. This is based on an increased thermal conductivity reduction of the gas phase due to the geometric constriction. Consequently, the highest increase is obtained for the largest particle diameter and thus, the largest interstitial pore sizes in the assembly (HS-469/17-c). For the shell thickness series, *i.e.*, the same open pore sizes, the increase in the thermal conductivity between vacuum and helium is comparable. This again demonstrates the important interplay between thermal conductance along the solid silica backbone and the gaseous environment. Whereas the specific particle design could greatly reduce the thermal conductivity of the hollow silica nanoparticle network, this high thermal insulation capacity is counteracted by thermal transport across the increased gas volume.

Moreover, heat flux densities and heat flux streamlines can be deduced from the FEM simulation. In Figure 4c, the distribution of the heat flux density is shown for a cross-section through HS-469/17-c. One can infer a lower contribution of the closed-pore volume (gas encapsulated in the hollow sphere) to the total thermal conductivity compared to the open-pore volume. Still, thermal transport through the silica shell is preferred. The predominating heat transport through the solid

phase is further emphasized by the heat flux streamlines (Figure S7b, bottom), which are bent towards the silica shell. Additionally, heat flux density images and streamlines for different helium gas thermal conductivities (153 $mWm^{-1}K^{-1}$ for bulk helium, 95 $mWm^{-1}K^{-1}$ for 436 nm pores, and 50 $mWm^{-1}K^{-1}$ for 135 nm pores) are compared in Figure S7a. The decrease of the helium thermal conductivity due to an increased confinement, leads to a decreased heat flux in the open-pore volume, whereas the heat flux in the closed-pore volume stays at a low level. Integration of the heat flux densities provides a quantitative impression of the respective transport pathways. The values are summarized in Table S7. For the colloidal crystals consisting of the particles HS-469/17 and a thermal contact conductance of 40 $Wm^{-2}K^{-1}$, 67 % of the heat is transported through the silica, and 33 % through the gaseous phase. From that, 18 % of the heat transport occurs through the open-pore volume and 15 % through the closed-pore volume.

2.2.4. Lower Limit of Thermal Transport Properties of Silica Hollow Sphere Colloidal Assemblies

How can the thermal diffusivity be further reduced in hollow sphere ensembles? Without changing the particle geometry, there are two possibilities: 1) the reduction of the interparticle contact points from 12 (close packing) to ~6 (random close packing) and 2) the reduction of the interparticle bonding strength. The first option can be realized by reducing the packing parameter from a colloidal crystal towards a colloidal glass with a random close-packed (*rcp*) structure. The structures of such colloidal glasses are shown in Figure 5. In contrast to the crystalline assemblies, these colloidal glasses are labeled with the appendix *a* referring to the amorphous symmetry (*e.g.*, HS-469/17-a).

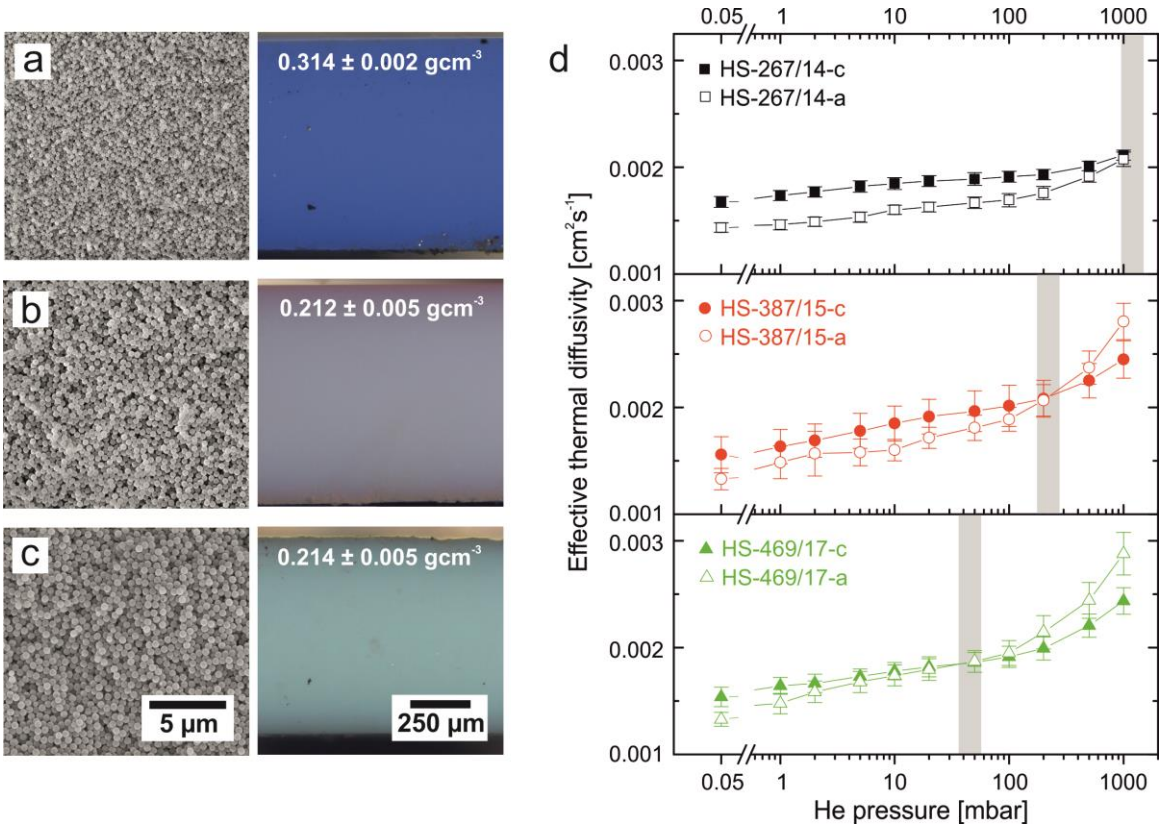

Figure 5. Silica hollow sphere colloidal glasses. a-c) SEM and side-view optical microscopy images of colloidal glasses consisting of hollow spheres a) HS-267/14, b) HS-387/15, and c) HS-469/17. d) Pressure-dependent thermal diffusivity data of amorphous assemblies (open symbols) in comparison to colloidal crystals (closed symbols).

The SEM images show the random packing of the hollow nanospheres, which causes a diffuse scattering in the optical microscopy image (see Figure 5a – c).[34] Thus, due to the missing crystallinity, no Bragg reflections are visible. For these colloidal glasses, the density was measured to be 0.208 – 0.314 gcm^{-3}, which is a reduction of 9 – 15 % compared to the colloidal crystals. The influence of the packing parameter on the thermal diffusivity is shown in Figure 5d. In vacuum, the temperature diffusion is slower and causes a drop of the thermal diffusivity by about 15 %. This can be explained by the lower density and the reduction of the interparticle contact points due to the glassy structure. In helium at 1000 mbar, the thermal diffusivity of colloidal glasses is comparable or even higher than the temperature diffusion through the crystalline counterpart. Thus, while a reduced solid conduction persists in the glassy state, an increased gaseous conduction originates due to the greater open-pore volume. The increased gaseous conduction

is especially noticeable for large particles (HS-387/15-a and HS-469/17-a). For smaller particles, the Knudsen effect is still dominating and thus, reduces the thermal diffusivity in helium. Noteworthy, the point at which the temperature diffusion of the amorphous glass is higher than the colloidal crystal shifts to lower pressures with increasing pore sizes. In the following, the influence of the density reduction and thermal diffusivity changes on the thermal conductivity will be discussed.

Figure 6a gives the helium pressure-dependent thermal conductivity of hollow nanosphere colloidal crystals (closed symbols) and colloidal glasses (open symbols). Indeed, the reduction of the packing density reduces the solid thermal conduction by 23 – 27 % in vacuum due to the decreasing density and decreasing amount of contact points for all particles under investigation. The lowest thermal conductivity was measured to be 21 $mWm^{-1}K^{-1}$ for HS-469/17-a. However, for the gaseous thermal conductivity, one needs to distinguish between small and large hollow silica nanoparticle packings. The small particles (HS-267/14-a), the thermal conductivity is reduced over the whole pressure range. This is different for the colloidal glasses consisting of the larger particles (HS-387/15-a and HS-469/17-a). For these, the thermal conductivity is comparable or even higher than for the crystalline assemblies, after exceeding a certain helium pressure. This intersection point is located at lower pressures for larger particles due to the increasing pore sizes. Besides the measurements in vacuum and helium, we also determined the thermal conductivity in air. The comparison of the different surrounding atmospheres is shown in Figure 6b. Analogous to the crystalline samples, the thermal conductivity in helium and air are comparable for the colloidal glasses. Only in the case of the smallest particles, a significant difference between the measurements in air and helium atmosphere is observed. This can be traced back to the adsorption of water, as discussed beforehand.

Overall, the transition to a colloidal glass resulted in a lower thermal conductivity and lower thermal diffusivity for all particles in vacuum. However, this reduction

in temperature and heat transport is counteracted by the additional gaseous transport through the concomitantly generated free volume. After all, the lowest thermal conductivity (42 $mWm^{-1}K^{-1}$) in helium and air was measured for a colloidal crystal with 469 nm large hollow nanospheres (HS-469/17-c).

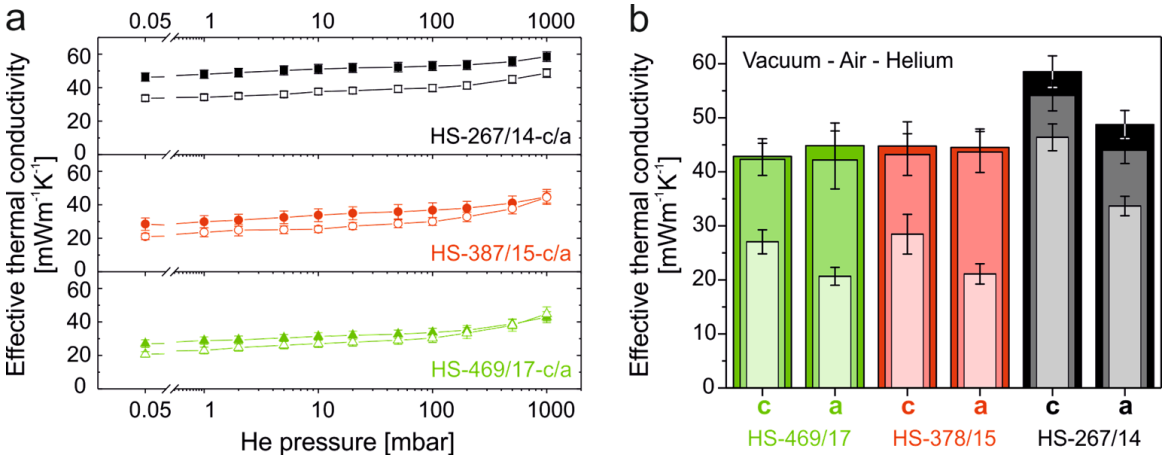

Figure 6. Thermal conductivity of silica hollow sphere colloidal crystals and amorphous glasses. a) Pressure-dependent thermal conductivity of amorphous assemblies (open symbols) in comparison to colloidal crystals (closed symbols). b) Comparison of different surrounding atmospheres (from bright to dark: vacuum, air (1000 mbar), and helium (1000 mbar)).

The adjustment of the bonding strength between adjacent spheres is another possibility to reduce the transport of thermal energy further. The influence of the interparticle bonding strength, and therefore, the interfacial thermal conductance was already shown in an earlier contribution.[12] In this, the bonding strength was enhanced by increasing calcination temperatures from 500 to 950 °C. This led to stronger covalent bonding between adjacent spheres and hence, resulted in an increased thermal conductivity. Here, we want to decrease the interfacial bonding between the hollow silica spheres to reduce heat transport. Thus, we calcined the hollow silica spheres *before* the assembly process. As a result, the spheres will only possess weak van der Waals contact forces. Thus, altered heat transport properties are expected by the reduction of the bonding strength.[35] To access the lower limit of the thermal conductivity for such a colloidal assembly, the hollow spheres with the largest diameter (469 nm) and the lowest packing density (colloidal glass) were utilized. The resulting structure is called HS-469/17-aa (Figure 7). Its thermal

conductivity in helium at 1000 mbar is comparable to the colloidal glass structure HS-469/17-a and the crystalline assembly HS-469/17-c, introduced beforehand. This shows the predominant thermal transport through the gaseous phase, independent from the symmetry of the assembly. The influence of the contact strength becomes dominant for measurements at lower gas pressures. In vacuum, the thermal conductivity of the colloidal glass (HS-469/17-aa) shows an extremely low thermal conductivity of about 8 $mWm^{-1}K^{-1}$. Thus, a thermal conductivity reduction of 61 % is achieved solely by reducing the interparticle bonding strength. This significant decrease of the heat transport can be traced back to a simultaneously drastic reduction of the thermal diffusivity (see Figure S8). The heat capacity remains unchanged, and the density of 0.190 gcm^{-3} is comparable. Compared to the hollow spheres assembled in a crystalline symmetry and calcined after the assembly (HS-469/17-c), the thermal conductivity in vacuum is even reduced by 70 % by combining the effect of reduction of interparticle contact points and reducing their bonding strength.

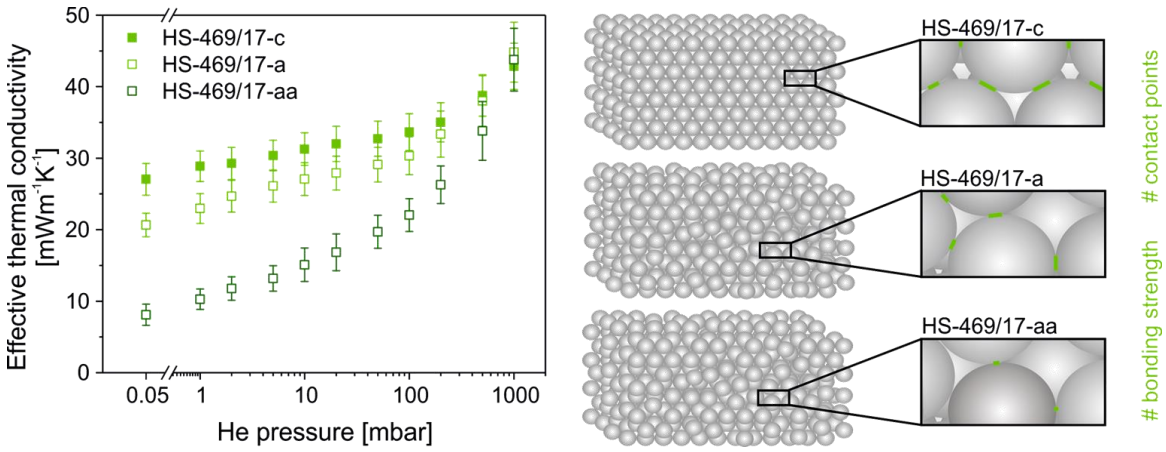

Figure 7. Influence of the number of contact points and the interparticle bonding strength on the thermal conductivity for assemblies with 469 nm-sized hollow spheres. HS-469/17-c is a colloidal crystal, HS-469/17-a is an amorphous colloidal glass, and HS-469/17-aa is an amorphous colloidal glass without covalent interparticle bonds.

The effect of the bonding strength can also be rationalized by FEM simulating a thermal contact conductance between individual spheres (see blue circular areas in Figure S9a). By increasing the thermal resistance, the thermal conductivity

decreases significantly (see Figure S9b). Thus, very low thermal conductivities and diffusivities can be achieved by reducing the bonding strength, and consequently by lowering the thermal contact conductance between adjacent hollow spheres. Nevertheless, this material engineering will be only effective under vacuum conditions, as gaseous conduction will be the path of the least resistance and therefore be the dominant contribution.

3. Conclusion

In summary, we presented a holistic picture of the thermal transport properties of dense silica hollow nanoparticle packings. At first, we focused on the influence of the geometry of the hollow spheres: size and shell thickness. The thermal diffusivity is mainly influenced by the shell thickness. An increasing shell thickness lowers the temperature diffusion. An opposing trend was found for the thermal conductivity. Here, the thermal conductivity is decreased by increasing the size of the particles and by reducing the shell thickness. Thus, the lower the density, the lower the thermal conductivity. A concomitant reduction of the thermal diffusivity and conductivity by the particle geometry is not possible. Furthermore, using finite element modeling, we were able to show that the heat transport through the gas phase is mainly dependent on the open-pore volume. The internal particle volume plays a less significant role.

In the second part, we focused on the number and strength of the interparticle contact points. Here, we changed the packing density of the spheres in the assembly and the bonding strength between adjacent particles. The combination of both effects resulted in a strong reduction of 70 % of the thermal conductivity and diffusivity in vacuum. This can be advantageous for both, steady- and non-steady-state state, thermal insulation applications. For a colloidal crystal consisting of 469 nm hollow spheres with a shell thickness of 16.5 nm, we found a thermal conductivity of only 8 $mWm^{-1}K^{-1}$ in vacuum. This ultra-low thermal conductivity, however, cannot be maintained under atmospheric conditions due

to the overwhelming thermal transport through the gaseous phase. Nevertheless, a low thermal conductivity (~35 $mWm^{-1}K^{-1}$) can be achieved with this material class, which is comparable to established polymer-based insulation materials. Altogether, this comprehensive study about the interplay of vacuum and gas-dependent thermal diffusivity and thermal conductivity in nanostructured materials will help to create novel insulation materials.

4. Experimental Section

Materials: Styrene (≥99 %, Aldrich) , 2,2′-azobis(2-methylpropionamidine)-dihydrochloride (AIBA; 97 %, Aldrich), 2-methacryloxyethyltrimethyl-ammoniumchloride (MTC; 70 % solution in water, Polyscience), polyvinylpyrrolidone K30 (PVP; Mw ~ 55 $kgmol^{-1}$, Aldrich), tetraethylorthosilicate (TEOS; ≥ 99 %, Aldrich), and ammonium hydroxide solution (30 – 33 % in water, Aldrich) were used as received. Ethanol (EtOH) was used in technical grade, and water was taken from a Millipore Direct Q3UV unit for the entire synthesis and purification steps.

Synthesis of Silica Hollow Spheres: Monodisperse polystyrene (PS) particles were synthesized by emulsifier-free emulsion polymerization. The synthesis was carried out in a three-necked flask, equipped with a reflux condenser and a gas inlet, under a slight argon flow. For the polystyrene template synthesis of sample HS-267/14, 100 mL water, 13 mL styrene, 100 µL MTC, and 0.9 g PVP K-30 were heated to the reaction temperature of 70 °C at a stirring speed of 850 rpm. After an equilibration time of 30 min, 0.3 g AIBA, dissolved in 20 mL water, were added to initiate the polymerization. After nucleation, the stirring speed was reduced to 450 rpm. The reaction was carried out overnight. Seeds of varying diameter were obtained by using different amounts of MTC, PVP, and AIBA.

The polystyrene particles were used as seeds for coating with a thin silica shell by the Stoeber process. For sample HS-267/14, 2.2 vol.% TEOS were added to an

81.3 vol.% EtOH, 10.5 vol.% water, 6.0 vol.% ammonium hydroxide solution containing 93 mgmL^{-1} PS latex particles. Core-shell particles with thicker shell thicknesses were obtained by increasing the TEOS volume.
The polystyrene core was removed by calcining the particles at 500 °C for 12 h in air. For the thermal transport measurements, the core-shell particles were assembled into colloidal assemblies before the calcination process.

Assembly into Colloidal Crystals and Glasses: The colloidal crystals were obtained by slow evaporation of a concentrated particle dispersion (7 wt.%) in a Teflon beaker with a diameter of 2 cm under ambient conditions. To obtain colloidal glasses ~ 1 mL ammonia hydroxide solution was added in several steps during the evaporation process.

Characterization Methods: Transmission electron microscopy (TEM) measurements were performed with a JEOL JEM-2200FS EFTEM electron microscope operated at an acceleration voltage of 200 kV. Zero-loss filtered micrographs (ΔE ~ 0 eV) were recorded with a bottom mounted CMOS camera system (OneView, Gatan) and processed with DM 3.11 image processing software (Gatan).
Scanning electron microscopy (SEM) images were taken on a Zeiss Leo 1530 instrument using InLens SE detection as well as Everhart-Thornley detection at acceleration voltages of 2 and 3 kV.
Small-angle X-ray scattering (SAXS) data were measured using the small-angle X-ray system Double Ganesha AIR (SAXSLAB). The X-ray source of this laboratory-based system is a rotating copper anode (MicroMax 007HF, Rigaku Corporation) providing a micro-focused beam at $\lambda = 0.154$ nm. The data were recorded by a position-sensitive detector (PILATUS 300 K, Dectris). To cover the range of scattering vectors between 0.026 and 2.6 nm^{-1} different detector positions were used. The measurement was performed at room temperature, using a

powder of hollow silica nanoparticles packed in a capillary tube. The scattering data were evaluated with a vesicle fit in the program SCATTER.[36]

Nitrogen sorption measurements were recorded on a Quantachrome Autosorb AS-1 pore analyzer at 77 K. All samples were preconditioned in vacuum at 350 °C for 12 hours before the measurements. For the data evaluation, the Quantachrome ASiQ v3.0 software was used. The specific surface areas were calculated using the Brunauer-Emmett-Teller (BET) method. Pore volumes and pore size distributions were obtained by applying the nonlocal density functional theory (NLDFT) adsorption branch model for silica materials with cylindrical pore geometry.

Differential scanning calorimetry (DSC) measurements were carried out using a Discovery DSC 2500 (TA Instruments). Compressed powders of the hollow spheres (10 – 16 mg) were scanned in covered aluminum pans under a dry nitrogen purge of 50 $mLmin^{-1}$ over a temperature range from -50 to 210 °C with a heating rate of 20 $°Cmin^{-1}$. The heat capacity was determined according to the ASTM E1269 standard test method using a standard sapphire sample. Two heating cycles on each sample were conducted. For the evaluation, the second heating cycle was used.

Thermal diffusivity measurements of the colloidal crystals were performed on an XFA 500 XenonFlash apparatus (Linseis) equipped with an InSb infrared detector. Before the measurements, the samples were coated with a thin graphite layer (approx. 15 μm) on each side to ensure a good absorbance at the bottom and a high emissivity at the top side of the sample. The thickness of the graphite layer is negligible compared to the thickness of the colloidal crystals (600 – 1100 μm). The samples were preconditioned at 200 °C for 15 min in vacuum to eliminate any potential contribution from intercalated water inside the silica network. The measurements were performed on at least three samples at 25 °C in vacuum (~ 0.05 mbar), helium (1– 1000 mbar), nitrogen (~1000 mbar), and air (~ 1000 mbar). The pressure-dependent measurements in helium are possible by controlling

ventilation valves and two pressure gauges (coarse and fine vacuum). The received data were evaluated by the software AproSoft Laser Flash Evaluation v1.06 using the radiation fit model (see Figure S4).

The thicknesses of the colloidal crystals were determined with a Litematic VL-50 (Mitutoyo).

The density of the colloidal crystals was determined from the mass and volume of the monoliths. The volume was measured using a 3D digital surface profiler (Keyence V-3100) and the mass was determined by weighing the colloidal crystals.

Supporting Information

Supporting Information is available from the Wiley Online Library or from the author.

Acknowledgements

This project was funded by a Lichtenberg Professorship provided by the Volkswagen Foundation. P.R. acknowledges support by the Elite Network Bavaria (ENB). Anna Lechner and Fabian Nutz are acknowledged for DSC measurements. Markus Drechsler is acknowledged for TEM measurements. Additional support was provided by the Bavarian Polymer Institute, BPI, the SFB840, and DFG project RE3550/2-1.

Conflict of Interest

The authors declare no conflict of interest.

Keywords

colloidal assembly, hollow spheres, nanoinsulation materials, thermal conductivity, thermal diffusivity

References

1. Losego, M. D.; Blitz, I. P.; Vaia, R. A.; Cahill, D. G.; Braun, P. V., Ultralow thermal conductivity in organoclay nanolaminates synthesized via simple self-assembly. *Nano Letters* **2013,** *13* (5), 2215-2219.

2. Suh, K. W.; Park, C. P.; Maurer, M. J.; Tusim, M. H.; Genova, R. D.; Broos, R.; Sophiea, D. P., Lightweight Cellular Plastics. *Advanced Materials* **2000,** *12* (23), 1779-1789.

3. Jelle, B. P., Traditional, state-of-the-art and future thermal building insulation materials and solutions – Properties, requirements and possibilities. *Energy and Buildings* **2011,** *43* (10), 2549-2563.

4. Kistler, S. S., Coherent expanded-aerogels. *Journal of Physical Chemistry* **1931,** *36* (1), 52-64.

5. Fricke, J.; Emmerling, A., Aerogels. *Journal of the American Ceramic Society* **1992,** *75* (8), 2027-2035.

6. Fricke, J.; Tillotson, T., Aerogels: production, characterization, and applications. *Thin Solid Films* **1997,** *297* (1–2), 212-223.

7. Fricke, J.; Emmerling, A., Aerogels. *Advanced Materials* **1991,** *3* (10), 504-506.

8. Hüsing, N.; Schubert, U., Aerogels - airy materials: Chemistry, structure, and properties. *Angewandte Chemie International Edition* **1998,** *37* (1-2), 22-45.

9. Thapliyal, P. C.; Singh, K., Aerogels as promising thermal insulating materials: An overview. *Journal of Materials* **2014,** *2014*, 10.

10. Cahill, D. G.; Ford, W. K.; Goodson, K. E.; Mahan, G. D.; Majumdar, A.; Maris, H. J.; Merlin, R.; Sr, P., Nanoscale thermal transport. *Journal of Applied Physics* **2003,** *93* (2), 793-818.

11. Cahill, D. G.; Braun, P. V.; Chen, G.; Clarke, D. R.; Fan, S. H.; Goodson, K. E.; Keblinski, P.; King, W. P.; Mahan, G. D.; Majumdar, A.; Maris, H. J.; Phillpot, S. R.; Pop, E.; Shi, L., Nanoscale thermal transport. II. 2003-2012. *Applied Physical Reviews* **2014,** *1* (1).

12. Ruckdeschel, P.; Kemnitzer, T. W.; Nutz, F. A.; Senker, J.; Retsch, M., Hollow silica sphere colloidal crystals: insights into calcination dependent thermal transport. *Nanoscale* **2015,** *7* (22), 10059-10070.

13. Nutz, F. A.; Ruckdeschel, P.; Retsch, M., Polystyrene colloidal crystals: Interface controlled thermal conductivity in an open-porous mesoparticle superstructure. *Journal of Colloid and Interface Science* **2015,** *457*, 96-101.

14. Gao, T.; Jelle, B. P.; Sandberg, L. I. C.; Gustavsen, A., Monodisperse hollow silica nanospheres for nano insulation materials: Synthesis, characterization, and life cycle assessment. *ACS Applied Materials and Interfaces* **2013,** *5* (3), 761-767.

15. Xia, Y.; Gates, B.; Yin, Y.; Lu, Y., Monodispersed colloidal spheres: Old materials with new applications. *Advanced Materials* **2000,** *12* (10), 693-713.

16. Aguirre, C. I.; Reguera, E.; Stein, A., Tunable colors in opals and inverse opal photonic crystals. *Advanced Functional Materials* **2010,** *20* (16), 2565-2578.

17. Barako, M. T.; Sood, A.; Zhang, C.; Wang, J.; Kodama, T.; Asheghi, M.; Zheng, X.; Braun, P. V.; Goodson, K. E., Quasi-ballistic electronic thermal conduction in metal inverse opals. *Nano Letters* **2016,** *16* (4), 2754-2761.

18. Ma, J.; Parajuli, B. R.; Ghossoub, M. G.; Mihi, A.; Sadhu, J.; Braun, P. V.; Sinha, S., Coherent phonon-grain boundary scattering in silicon inverse opals. *Nano Letters* **2013,** *13* (2), 618-624.

19. Albrecht, J. D.; Knipp, P. A.; Reinecke, T. L., Thermal conductivity of opals and related composites. *Physical Review B* **2001,** *63* (13), 134303.

20. Nutz, F. A.; Retsch, M., Interfacial and volumetric sensitivity of the dry sintering process of polymer xolloidal xrystals: A thermal transport and photonic bandgap study. *Physical Chemistry Chemical Physics* **2017**.

21. Ma, H.-Y.; Tong, L.-F.; Xu, Z.-B.; Fang, Z.-P., Functionalizing carbon nanotubes by grafting on intumescent flame retardant: Nanocomposite synthesis, morphology, rheology, and flammability. *Advanced Functional Materials* **2008,** *18* (3), 414-421

22. Dong, L.; Hu, C.; Song, L.; Huang, X.; Chen, N.; Qu, L., A large-area, flexible, and flame-retardant graphene paper. *Advanced Functional Materials* **2016,** *26* (9), 1470-1476.

23. Bourbigot, S.; Duquesne, S., Fire retardant polymers: recent developments and opportunities. *Journal of Materials Chemistry* **2007,** *17* (22), 2283-2300.

24. Goodwin, J. W.; Hearn, J.; Ho, C. C.; Ottewill, R. H., Studies on the preparation and characterisation of monodisperse polystyrene latices. *Colloid and Polymer Science* **1974,** *252* (6), 464-471.

25. Graf, C.; Vossen, D. L. J.; Imhof, A.; van Blaaderen, A., A general method to coat colloidal particles with silica. *Langmuir* **2003,** *19* (17), 6693-6700.

26. Ruckdeschel, P.; Dulle, M.; Honold, T.; Förster, S.; Karg, M.; Retsch, M., Monodisperse hollow silica spheres: An in-depth scattering analysis. *Nano Research* **2016,** *9* (5), 1366-1376.

27. Nunes dos Santos, W.; Mummery, P.; Wallwork, A., Thermal diffusivity of polymers by the laser flash technique. *Polymer Testing* **2005,** *24* (5), 628-634.

28. Wang, J.; Ahl, S.; Li, Q.; Kreiter, M.; Neumann, T.; Burkert, K.; Knoll, W.; Jonas, U., Structural and optical characterization of 3D binary colloidal crystal and inverse opal films prepared by direct co-deposition. *Journal of Materials Chemistry* **2008,** *18* (9), 981-988.

29. Haynes, W. M., CRC Handbook of Chemistry and Physics, 97th Edition. CRC Press: 2016.

30. Knudsen, M., Die molekulare Wärmeleitung der Gase und der Akkommodationskoeffizient. *Annalen der Physik* **1911,** *339* (4), 593-656.

31. Yin, J.; Retsch, M.; Thomas, E. L.; Boyce, M. C., Collective mechanical behavior of multilayer colloidal arrays of hollow nanoparticles. *Langmuir* **2012,** *28* (13), 5580-5588.

32. Schiffres, S. N.; Kim, K. H.; Hu, L.; McGaughey, A. J. H.; Islam, M. F.; Malen, J. A., Gas diffusion, energy transport, and thermal accommodation in single-walled carbon nanotube aerogels. *Advanced Functional Materials* **2012,** *22* (24), 5251-5258.

33. Coquil, T.; Richman, E. K.; Hutchinson, N. J.; Tolbert, S. H.; Pilon, L., Thermal conductivity of cubic and hexagonal mesoporous silica thin films. *Journal of Applied Physics* **2009,** *106* (3).

34. Retsch, M.; Schmelzeisen, M.; Butt, H.-J.; Thomas, E. L., Visible mie scattering in nonabsorbing hollow sphere oowders. *Nano Letters* **2011,** *11* (3), 1389-1394.

35. Losego, M. D.; Grady, M. E.; Sottos, N. R.; Cahill, D. G.; Braun, P. V., Effects of chemical bonding on heat transport across interfaces. *Nature Materials* **2012,** *11* (6), 502-506.

36. Foerster, S.; Apostol, L.; Bras, W., Scatter: software for the analysis of nano- and mesoscale small-angle scattering. *Journal of Applied Crystallography* **2010,** *43* (3), 639-646.

Supporting Information

Corresponding to Chapter 2.1.: Silica Hollow Sphere Colloidal Crystals

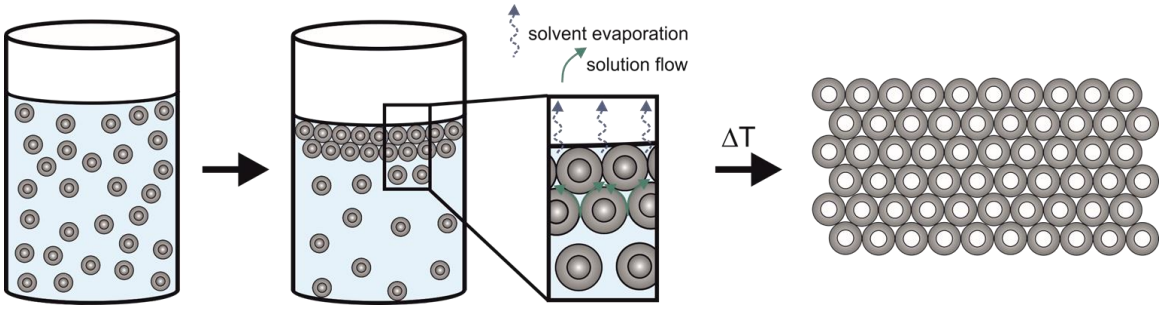

Scheme S1. Schematic illustration of the evaporation-induced self-assembly of hollow silica sphere colloidal crystals and subsequent calcination to obtain silica hollow sphere colloidal crystals.

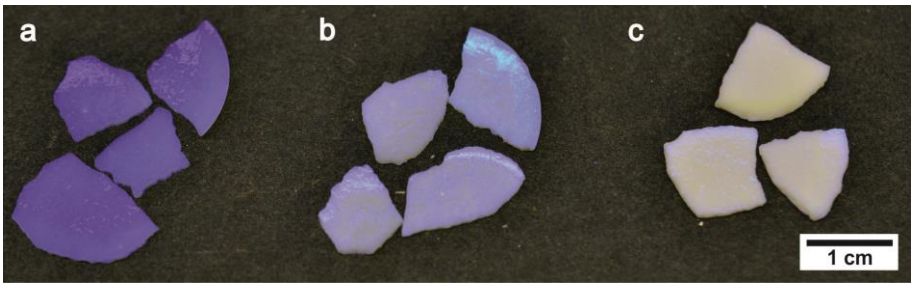

Figure S1. Photographic image of silica hollow sphere colloidal crystals with a particle diameter of ~270 nm and shell thicknesses of a) 14 nm (HS-267/14), b) 27 nm (HS-267/27), and c) 40 nm (HS-266/40).

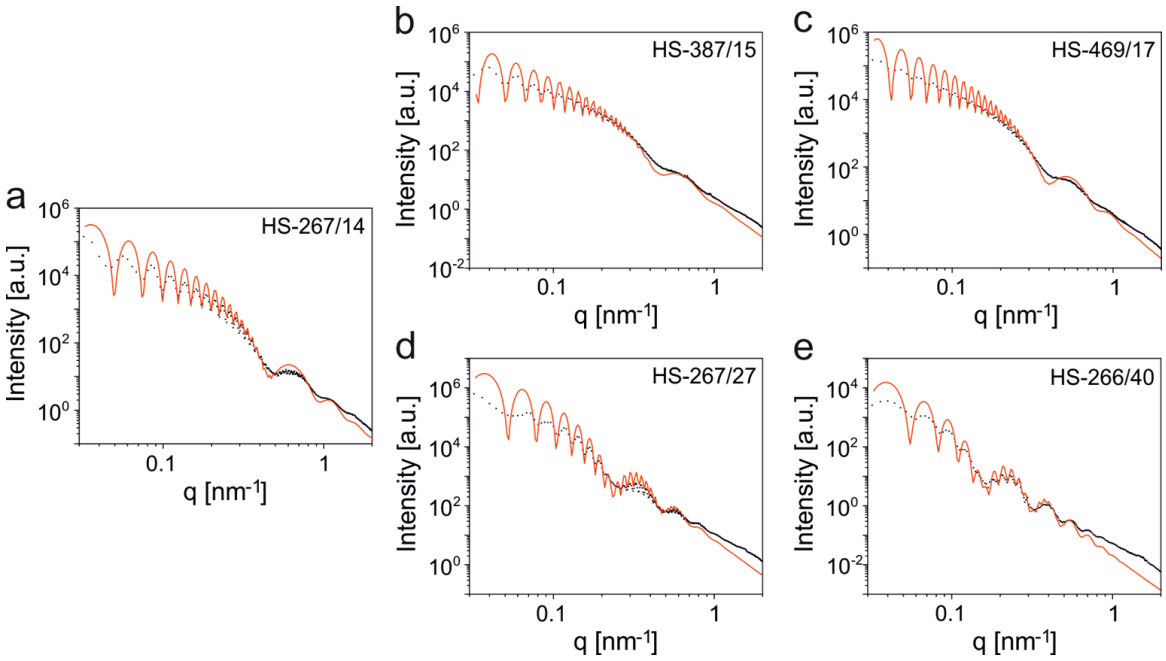

Figure S2. Small angle X-ray scattering (SAXS) analysis of silica hollow nanospheres (black dots) and the corresponding fits using a form factor for spherical core-shell particles (red lines). a, b, c) Size series, a, d, e) Shell thickness series.

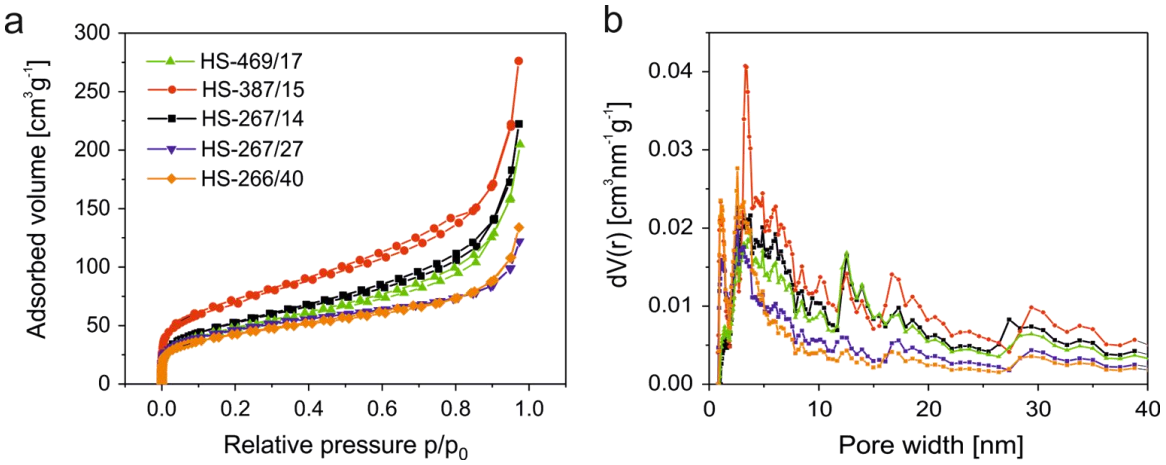

Figure S3. Nitrogen sorption data of silica hollow spheres. a) Nitrogen adsorption/desorption isotherms, and b) pore size distribution calculated by DFT method. The lines are a guide to the eye.

Table S1. Density of the silica shell considering the porosity.[a)]

	HS-469/17	**HS-387/15**	**HS-267/14**	**HS-267/27**	**HS-267/40**
Calculated density of the shell including meso- and micropores [gcm^{-3}]	1.68	1.52	1.83	1.93	1.81

[a)] Recalculation of the density of the silica shell: The density of the bulk silica measured by helium pycnometry gives a value of 2.2 gcm^{-3}. The bulk silica density has to be corrected due to the porosity of the shell. The recalculation is based on a 74 % volume filling and the geometric parameters of the individual silica spheres.

Table S2. Summary of data received from nitrogen sorption measurements.

	N_2 sorption measurements			
	BET surface area [m^2g^{-1}]	DFT surface area [m^2g^{-1}]	Pore volume [cm^3g^{-1}]	Pore size [nm]
HS-469/17	169.4	142.1	0.30	3.8
HS-387/15	246.3	224.9	0.41	3.3
HS-267/14	184.8	155.0	0.33	2.6
HS-267/27	152.2	136.1	0.20	2.6
HS-266/40	164.5	147.4	0.18	2.6

Table S3. Voids in silica hollow sphere colloidal crystals with a packing parameter of 74 %.

Voids	**HS-469/17-c**	**HS-387/15-c**	**HS-267/14-c**
Octahedral	194 nm	160 nm	110 nm
Tetrahedral	105 nm	87 nm	60 nm
Exchange sites	72 nm	60 nm	41 nm

Corresponding to Chapter 2.2.1.: Thermal Diffusivity of Silica Hollow Sphere Colloidal Crystals

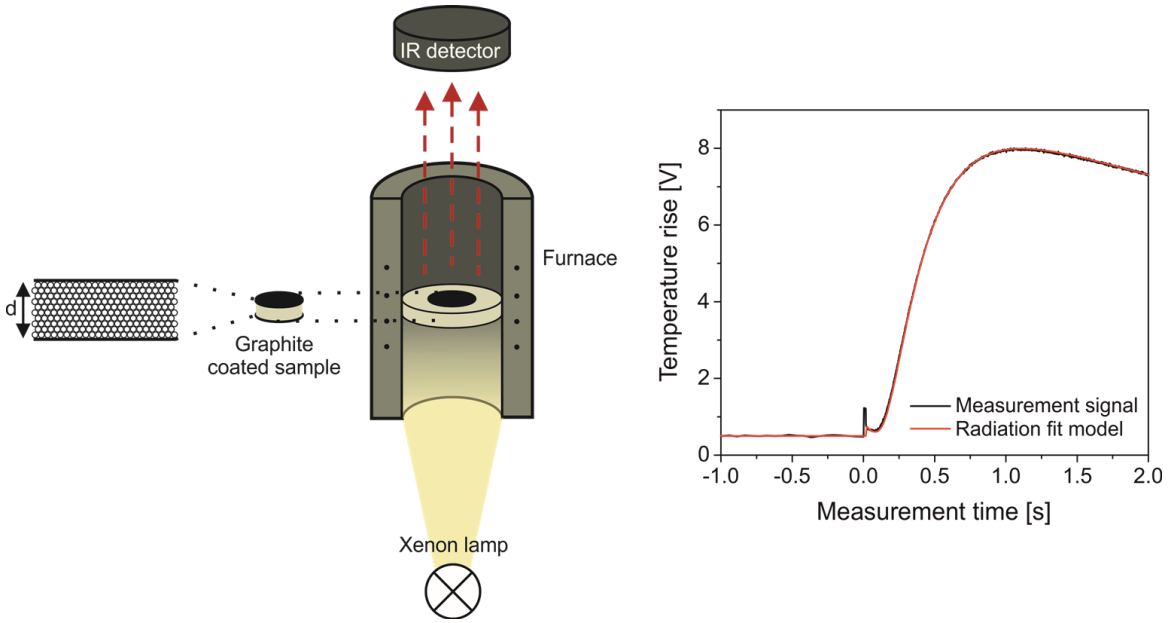

Figure S4. a) Schematic setup of the xenon flash analysis (XFA), modified from Ruckdeschel *et al.*[17]. The setup allows controlling the surrounding atmosphere in a precise manner. The measurement chamber is closed during the measurement and holds vacuum conditions of about 0.05 mbar, which is limited by the gas-tightness of the sample chamber. We define this as "vacuum" measurement. Furthermore, we are able to supply air, nitrogen, or helium to the sample chamber. By using controlled ventilation valves and two pressure gauges (coarse and fine vacuum), we can control the respective gas pressure between 1 mbar and 1000 mbar. b) Typical measurement signal of a hollow silica colloidal crystal modeled with a radiation fit. The radiation fit model represents an extension to the finite-pulse and heat loss corrections given by the Combined fit model from Dusza (L. Dusza, *High Temperatures – High Pressures*, **1995**, 27, 467-473). However, it allows for an amount of the Xenon flash to be directly transmitted to the rear sample surface, leading to an instantaneous temperature jump analogous to Blumm *et al.* (J. Blumm, J. Henderson, O. Nilsson and J. Fricke, *High Temperatures-High Pressures*, **1997**, 29, 555-560).

Corresponding to Chapter 2.2.2.: Thermal Conductivity of Silica Hollow Sphere Colloidal Crystals

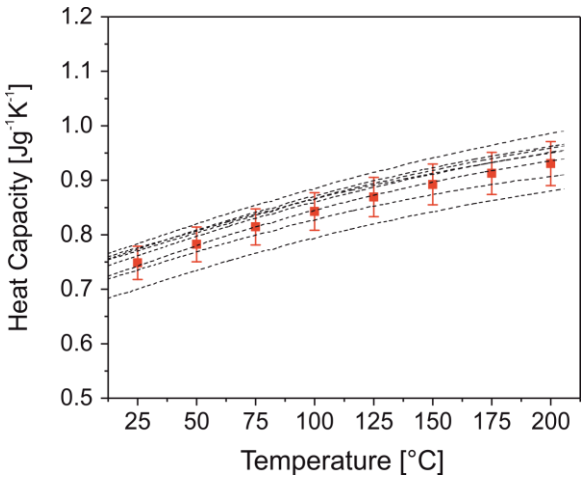

Figure S5. Differential scanning calorimetry (DSC) measurements of silica hollow spheres with different sizes and shell thicknesses (dotted lines) and the corresponding mean values calculated from the individual measurements (red squares). The mean heat capacity at 25 °C was found to be (0.748 ± 0.031) $Jg^{-1}K^{-1}$.

Corresponding to Chapter 2.2.3.: Finite Element Modeling of the Thermal Transport in HS Colloidal Crystals

The FEM software COMSOL Multiphysics (version 5.2.1.262) is used for modeling the thermal transport in silica hollow sphere colloidal crystals. For this, hollow spheres are arranged in a face-centered cubic (*fcc*) unit cell packing. The outer radius of the sphere is constant for all systems, while the shell thickness is varied to get the same shell thickness-to-radius ratios as for the synthesized systems (HS-469/17: 0.0704, HS-387/15: 0.0750, HS-267/14: 0.105, HS-267/27: 0.202, HS-266/40: 0.301). The unit cell edge length is chosen such that the contact (or overlap) area per particle is 0.6 % of the particle surface area, and therefore comparable to the experimental systems. For all simulations (except the data in Figure S9), the overlapping particles are fused into one object. Thus, no thermal resistance between the particles is considered. For the data plotted in Figure S9b, the thermal contact conductance between adjacent particles is varied between 10 and 10^6 $Wm^{-2}K^{-1}$. To study the influence of surrounding gas (helium or air) on the

total heat conduction, the inverse hollow sphere volume is added. The geometry of the colloidal crystal HS-469/17-c is exemplarily shown in Figure S6.

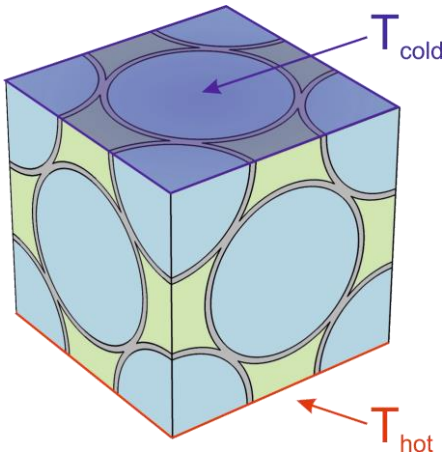

Figure S6. The unit cell of the silica hollow sphere colloidal crystal HS-469/17-c. The different colors show the different phases (gray: silica shell, blue: internal pore volume, green: outer pore volume). A constant hot (T_{hot}) and cold (T_{cold}) temperature is applied to the entire upper and lower face. The residual boundaries are thermally insulated. Thus, a temperature gradient forms, with a heat flux in the direction of the cold face.

Three materials, each with its own thermal conductivity, are assigned to the hollow silica colloidal crystal: silica, gas in open-pores, and gas in closed-pores. The properties of the materials are listed in Table S4 – Table S6. We used bulk material values, except for the gas thermal conductivity. This is justified by the amorphous microstructure of our material, where the thermal transport is governed by diffusive transport. The thermal contact between silica and gas is defined either as a union (no thermal resistance) or with a certain thermal contact conductance h_c (0, 40, and 200 $Wm^{-2}K^{-1}$). For the simulation, a constant temperature is applied to the lower (T_{hot}) and upper (T_{cold}) face of the unit cell. This defines the temperature gradient across the hollow sphere structure and serves at the same time as heat source and heat sink, respectively. Thermal insulation boundary conditions are imposed on all other surfaces of the unit cell. To obtain the effective thermal conductivity κ_{eff}, the integrated heat flux normal to the upper surface is evaluated. Then, the effective thermal conductivity is calculated using Fourier's equation of heat conduction:

$$\kappa_{\text{eff}} = \frac{Q/A}{\Delta T/h}, \tag{S1}$$

where Q is the heat flow rate normal to the cross-sectional area A of the unit cell, ΔT the temperature difference ($T_{\text{hot}} - T_{\text{cold}}$), and h the unit cell edge length.

The mesh is chosen fine enough to ensure mesh size independent thermal conductivity values. Detailed information on the FEM simulations is given in the respective figure and table captions.

Table S4. Specific heat capacity, density, and thermal conductivity used in FEM simulations.

	COMSOL input values		
	Specific heat [$Jg^{-1}K^{-1}$]	**Density [kgm^{-3}]**	**Thermal conductivity [$mWm^{-1}K^{-1}$]**
Silica	0.748	2203	331[a)]
Helium	5.195[b)]	0.1615[b)]	Table S5 and Table S6
Air	1.005[c)]	1.1845[c)]	Table S5

The thermal conductivity of silica is chosen such that for HS-469/17-c (without gas) the same effective thermal conductivity is obtained as experimentally in vacuum, [b)] The specific heat capacity and density of helium at 1000 mbar and 25 °C was calculated according to Petersen (H. Petersen, *The Properties of Helium: Density, Specific Heats, Viscosity, and Thermal Conductivity at Pressures from 1 to 100 Bar and from Room Temperature to about 1800 K*, Jul. Gjellerup, **1970**), [c)] The specific heat capacity and density of air at 1000 mbar and 25 °C was calculated according to Dixon (J. C. Dixon, in *The Shock Absorber Handbook*, DOI: 10.1002/9780470516430.app2, John Wiley & Sons, Ltd **2007**, p. 375ff.).

Table S5. Pore size-dependent thermal conductivity κ of helium and air in the closed- and open-pores used in the FEM simulations for the determination of the effective thermal conductivity of silica hollow spheres colloidal crystals (see Figure 4a and b) as well as for the plot of the heat flux density and streamlines (see Figure 4c and Figure S7b).[a)]

	Helium		***Air***	
	$\kappa_{He(ClosedPores)}$ [$mWm^{-1}K^{-1}$]	**$\kappa_{He(OpenPores)}$ [$mWm^{-1}K^{-1}$]**	**$\kappa_{Air(ClosedPores)}$ [$mWm^{-1}K^{-1}$]**	**$\kappa_{Air(OpenPores)}$ [$mWm^{-1}K^{-1}$]**
HS-469/17-c	94.9	50.2	20.9	14.8
HS-387/15-c	87.6	44.1	20.2	13.6
HS-267/14-c	72.2	33.7	18.3	13.7
HS-267/27-c	67.9	33.7	17.7	13.7
HS-266/40-c	62.8	33.6	17.0	13.7

[a)] The pore size-dependent thermal conductivity for a pressure of 1000 mbar and a temperature of 25 °C is calculated according to Schiffres *et al*. (S. N. Schiffres, K. H. Kim, L. Hu, A. J. H. McGaughey, M. F. Islam, J. A. Malen, *Adv. Funct. Mater.* **2012**, 22, 5251). The pore size of the closed-pores is the inner diameter of the hollow spheres. An average thermal conductivity for the open-pores is calculated from the averaged size of the tetrahedral and octahedral voids (see Table S3).

Table S6. Thermal conductivity of helium used in FEM simulations for the plot of heat flux density and streamlines of particle system HS-469/17-c (see Figure S7a). Here, the same thermal conductivity of helium is used for the closed- and open-pores.[a)]

	Helium		
	$\kappa_{He(bulk)}$ [$mWm^{-1}K^{-1}$]	$\kappa_{He(436nm)}$ [$mWm^{-1}K^{-1}$]	$\kappa_{He(135nm)}$ [$mWm^{-1}K^{-1}$]
HS-469/17-c	153.2	94.9	50.2

[a)] The pore size-dependent thermal conductivity for a pressure of 1000 mbar and a temperature of 25 °C is calculated according to Schiffres *et al*. (S. N. Schiffres, K. H. Kim, L. Hu, A. J. H. McGaughey, M. F. Islam, J. A. Malen, *Adv. Funct. Mater.* **2012**, 22, 5251).

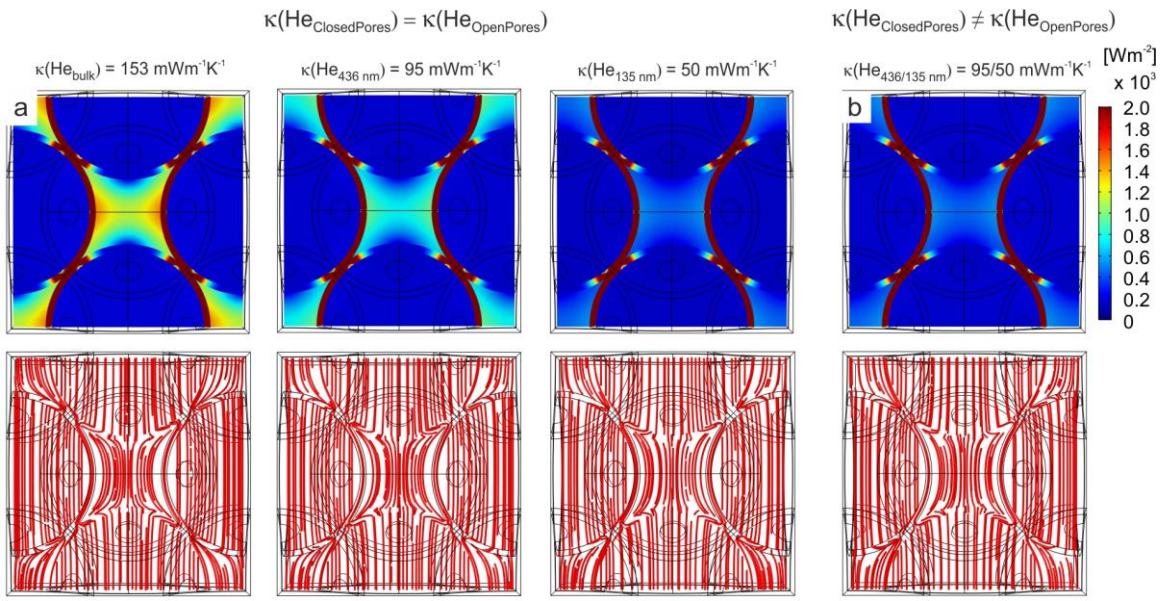

Figure S7. Finite element method modeling: Heat flux density (top) and streamlines (bottom) of particle assembly HS-469/17-c with a thermal contact conductance h_c of 40 $Wm^{-2}K^{-1}$ between the silica network and helium. a) The thermal conductivity of helium is varied (see Table S6), with the same thermal conductivity of helium being assumed for the closed- and open-pores. b) Different thermal conductivity values of helium are applied for the closed- and open-pores (see Table S5), taking into account the different helium thermal conductivities in the closed- and open-pore volume due to the Knudsen effect. The integrated heat flux densities of the different phases are listed in Table S7.

Table S7. Integrated heat flux densities of silica, open-pore, and closed-pore volume of particle assembly HS-469/17-c. For the simulation, a thermal contact conductance h_c of 40 $Wm^{-2}K^{-1}$ between the silica network and helium is used. The thermal conductivity of helium is varied to obtain the same (row 1-3) or different (row 4) helium thermal conductivities for the open- and closed-pore volume (see Table S6 and Table S5). The assumption of different thermal conductivities is the more realistic case due to different confinements, and thus Knudsen effects, present in a hollow sphere colloidal crystal.

	Silica		*Open-pores*		*Closed-pores*	
	Heat flux		**Heat flux**		**Heat flux**	
	[MWm^{-1}]	**[%]**	**[MWm^{-1}]**	**[%]**	**[MWm^{-1}]**	**[%]**
$\kappa(He_{ClosedPores}) = \kappa(He_{OpenPores})$ $\kappa(He_{bulk}) = 153\ mWm^{-1}K^{-1}$	1.302	**49.4**	1.012	**38.4**	0.322	**12.2**
$\kappa(He_{ClosedPores}) = \kappa(He_{OpenPores})$ $\kappa(He_{436\ nm}) = 95\ mWm^{-1}K^{-1}$	1.303	**58.2**	0.635	**28.3**	0.303	**13.5**
$\kappa(He_{ClosedPores}) = \kappa(He_{OpenPores})$ $\kappa(He_{135\ nm}) = 50\ mWm^{-1}K^{-1}$	1.303	**68.1**	0.345	**18.0**	0.266	**13.9**
$\kappa(He_{ClosedPores}) \neq \kappa(He_{OpenPores})$ $\kappa(He_{436/135\ nm}) = 95/50\ mWm^{-}$	1.302	**66.8**	0.345	**17.7**	0.302	**15.5**

Corresponding to Chapter 2.2.4.: Lower Limit of Thermal Transport of Silica Hollow Sphere Colloidal Assemblies

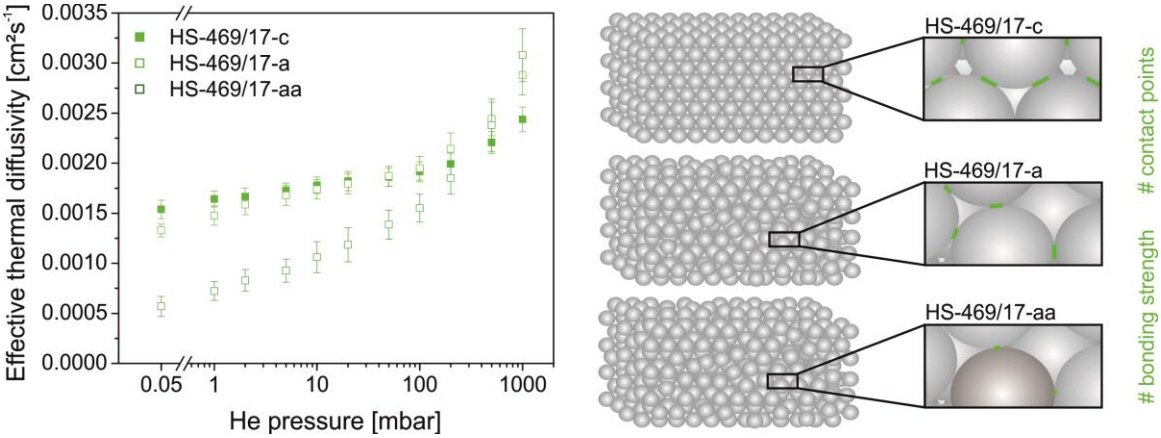

Figure S8. Thermal diffusivity of the colloidal assemblies HS-469/17-c/a with different amount of contact points and bonding strength.

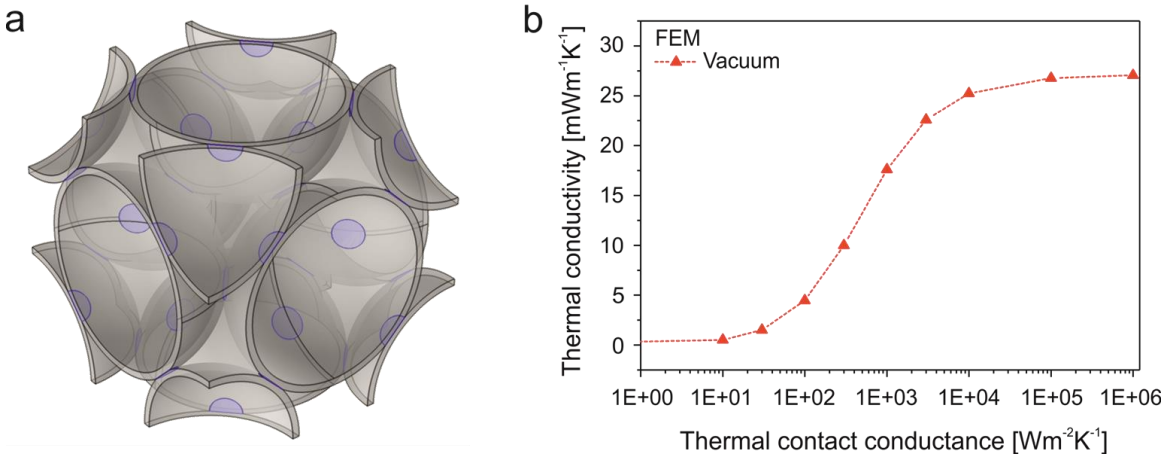

Figure S9. Finite element method modeling: a) Unit cell of a face-centered cubic hollow silica sphere colloidal crystal (HS-469/17-c, without gas). The particles are not fused into one object. The blue circular areas mark the contact area between adjacent spheres. b) Influence of the thermal contact conductance between the particles on the thermal conductivity.

8. Thermal Transport in Binary Colloidal Glasses: Composition Dependence and Percolation Assessment

Pia Ruckdeschel[1,‡], Alexandra Philipp[1,‡], Bernd A. F. Kopera[1], Flora Bitterlich[1], Martin Dulle[2], Nelson W. Pech-May[1], and Markus Retsch[1,*]

[‡] *These authors contributed equally to the work.*

[1]Department of Chemistry, University of Bayreuth, Universitätsstraße 30, 95447 Bayreuth, Germany

[2]JCNS-1/ICS-1: Neutron Scattering, Forschungszentrum Jülich GmbH, Wilhelm-Johnen-Straße 52428, Jülich, Germany

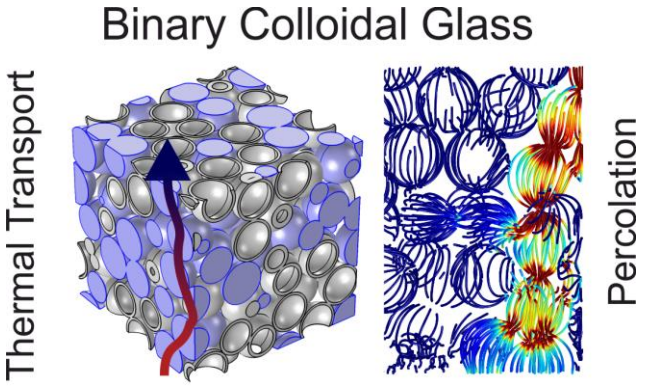

Abstract

The combination of various types of materials is often used to create superior composites that outperform the pure phase components. For any rational design, the thermal conductivity of the composite as a function of the volume fraction of the filler component needs to be known. When approaching the nanoscale, the homogeneous mixture of various components poses an additional challenge. Here, we investigate binary nanocomposite materials based on polymer latex beads and hollow silica nanoparticles. These form randomly mixed colloidal glasses on a sub-μm scale. We focus on the heat transport properties through such binary assembly structures. The thermal conductivity can be well described by the effective medium theory. However, film formation of the soft polymer component leads to phase segregation and a mismatch between existing mixing models. We confirm our experimental data by finite element modeling. This additionally allowed us to assess the onset of thermal transport percolation in such random particulate structures. Our study contributes to a better understanding of thermal transport through heterostructured particulate assemblies.

1. Introduction

Nanostructured materials have been the driving force for the tremendous development of many modern technologies, such as high-performance processors and data storage devices, sensors, or telecommunication equipment. (Opto)electronic devices have benefited from the ongoing miniaturization, which allowed device density to increase according to Moore's law. However, this miniaturization is also accompanied by an increased energy density and, consequently, by much higher, much more localized temperatures. Thus, it becomes increasingly important to control the way heat flows through these structures; one particular challenge is the dissipation of heat in electronic elements[1]. Therefore, electrically insulating heat spreading materials are used to prevent the

formation of hot spots, which reduce the lifetime and reliability of electronic materials.[23] These materials are commonly polymers filled with a highly thermally conductive micro- or nanomaterial.[4-5] The thermal properties of these polymer composites depend mainly on the geometry of the filler (*i.e.*, shape and size)[6], the volume fraction and distribution of the filler material in the matrix (lattice type)[7], the contact between the filler particles[8], and the thermal properties of the components[8]. Advantages of polymer filled materials are easy processing and good mechanical properties.

For the application as a heat spreading material, a composite material needs to enhance the effective thermal conductivity greatly compared to that of its neat matrix. The filler material is typically much more expensive and/or less available than the matrix component. Consequently, low loading fractions of the filler material are highly desirable. An important quantity to characterize the minimum amount of necessary filler is given by its percolation threshold. Percolation describes the formation of long-range connectivity in randomly ordered systems. Expectedly, the threshold shifts to lower filler volume fractions in composites by using small particles with a large aspect ratio (like rods or fibers)[9], a lattice type with a large number of neighbors (such as a face-centered cubic structure)[7], and a low contact resistance between the filler particles.[10]

Percolation theory analytically describes the composition dependence of a binary mixture of isotropic objects.[7] The relationship between the effective thermal conductivity of the composite κ_{eff} and the volume fraction of the filler V_{filler} is given by

$$\kappa_{\text{eff}} \propto \kappa_{\text{filler}}(V_{\text{filler}} - V_{\text{c}})^{n} \quad (1)$$

where κ_{filler} is the thermal conductivity of the filler, V_{c} the percolation threshold, and n the percolation exponent [typically 2 in a three-dimensional (3D) experiment]. Based on this equation, Mamunya *et al.*[11] developed an analytic

expression for the electrical conductivity in composites, which can also be assigned to the effective thermal conductivity (κ_{eff}),[8]

$$\kappa_{\text{eff}} = \left(\frac{\Phi_1 - \Phi_c}{F - \Phi_c}\right)^t (\kappa_1 - \kappa_2) + \kappa_2 \qquad (2)$$

where κ_1, κ_2 are the thermal conductivities of the two components 1 and 2 ($\kappa_1 \gg \kappa_2$), F is the maximum filling packing factor (here $F = 1$), Φ_c is the percolation threshold ($\Phi_c = \chi_c F$), which depends on the lattice structure (χ_c is the critical percolation probability, $\chi_c = 0.27$ for random close-packed structures)[12], Φ_1 is the volume concentration of component 1, and t is a critical exponent which depends on the dimension of the structure (3D structures: $t = 2$)[7]. However, the percolation theory cannot be applied to mixing ratios lower than the percolation threshold. Therefore, the thermal conductivity of a composite material is often predicted by binary mixing models. These can be applied to the entire mixing phase diagram. The most common ones are the series and parallel model, the Maxwell-Eucken (ME) model 1 and 2 and the effective medium theory (EMT).[13-14] These are summarized with their corresponding formulas in Figure 1.

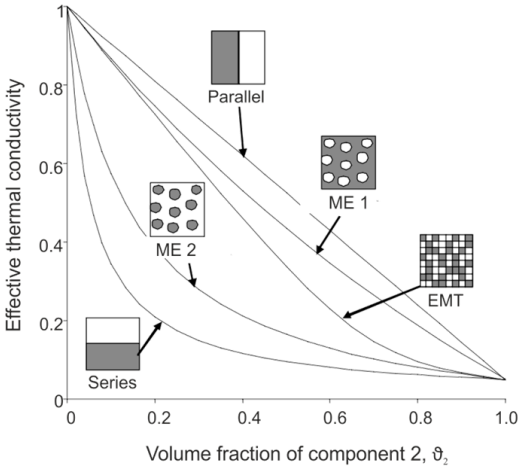

Series model	$\kappa_e = \frac{1}{\frac{1-\vartheta_2}{\kappa_1} + \frac{\vartheta_2}{\kappa_2}}$
Parallel model	$\kappa_e = (1-\vartheta_2)\kappa_1 + \vartheta_2\kappa_2$
Maxwell-Eucken 1	$\kappa_e = \kappa_1 \frac{2\kappa_1 + \kappa_2 - 2(\kappa_1 - \kappa_2)\vartheta_2}{2\kappa_1 + \kappa_2 + (\kappa_1 - \kappa_2)\vartheta_2}$
Maxwell-Eucken 2	$\kappa_e = \kappa_2 \frac{2\kappa_2 + \kappa_1 - 2(\kappa_2 - \kappa_1)(1-\vartheta_2)}{2\kappa_2 + \kappa_1 + (\kappa_2 - \kappa_1)(1-\vartheta_2)}$
Effective medium theory (EMT)	$\kappa_e = 1/4((3\vartheta_2 - 1)\kappa_2 + [3(1-\vartheta_2) - 1]\kappa_1 + \sqrt{[(3\vartheta_2 - 1)\kappa_1 + (3\{1-\vartheta_2\} - 1)\kappa_1]^2 + 8\kappa_1\kappa_2}$

Figure 1. Relative effective thermal conductivities κ_{eff} for the series, the parallel, the Maxwell-Eucken (ME), and the effective medium theory (EMT) model and the corresponding equations. In the ME1 model, 1 is the continuous phase, whereas, in the ME2 model, 1 is the dispersed phase. Adapted with permission from Carson *et al*.[13]

The upper and lower bounds are given by the parallel and series model, respectively, in which the layers are aligned parallel or perpendicular to the heat

flow direction. The ME model 1 and 2 assume separated inclusions in a dispersed phase.[15] Thus, materials with percolating pathways cannot be described by the Maxwell-Eucken models. A better description is given by the EMT model. It considers a structure in which two components are randomly distributed with neither phase being dispersed or continuous. Thus, continuous heat conduction pathways can be formed by either particle type depending on the respective volume fraction. Our contribution addresses two important aspects of composite materials. First, choosing a colloidal approach, we can fabricate nanostructured colloidal materials with any mixing ratio, which otherwise often suffer from macroscopic demixing or clustering. This allows us to investigate the applicability of the existing mixing models. Second, we shed light on thermal transport percolation in an isotropic particle ensemble. We compare our experimental results with finite element method (FEM) simulation, which provides a deeper understanding of the percolation evolution. We base our study on two types of electrically insulating building blocks: polymer latex beads and hollow silica nanoparticles. These are self-assembled into randomly close-packed colloidal ensembles.

2. Experimental Section

2.1. Fabrication of Binary Colloidal Glasses

Two types of nanoparticles were synthesized: hollow silica spheres and poly(methyl methacrylate-*co*-*n*-butyl acrylate) [P(MMA-*co*-nBA)] particles. For the synthesis of hollow silica nanoparticles, first, monodisperse polystyrene particles were prepared by emulsifier-free emulsion polymerization.[16] Subsequently, the particles were coated with a thin silica shell by a modified Stoeber condensation process.[17] Finally, the polystyrene core was removed by calcination. Monodisperse P(MMA-*co*-nBA) particles were synthesized by emulsifier-free emulsion polymerization. Colloidal assemblies were prepared by a vacuum filtration system.

Detailed information on the synthesis of the particles and the assembly process can be found in the Appendix.

2.2. Characterization Methods

Scanning electron microscopy (SEM) was used to image the colloidal assemblies. Differential scanning calorimetry measurements were performed to determine the specific heat capacity. Thermal diffusivity of the colloidal assemblies was measured using a xenon flash apparatus. These measurements were done in vacuum at room temperature and in helium (1000 mbar) in the temperature range from 25 °C to 150 °C. The densities of the hollow sphere assemblies and the unmolten colloidal glasses were determined using a 3D digital surface profiler. The densities of the molten colloidal assemblies were measured using Archimedes' principle (buoyancy method). Further details about the characterization methods are summarized in the Appendix.

2.3. Finite Element Modeling

An amorphous particle assembly was obtained from molecular dynamics simulation. This particle structure was used for the finite element method (FEM) simulations of the effective thermal transport properties using COMSOL MULTIPHYSICS. A random selection process assigned the two types of particles to the colloidal glass. An exemplary structure used for FEM is shown in Figure 2c. For the simulation, a temperature difference was applied to opposite faces of the cube. This defines the temperature gradient across the colloidal structure and serves at the same time as a heat source and a heat sink, respectively. Thermal insulation boundary conditions are imposed on all other faces of the cube. The computed heat flux normal to the isothermal faces was used to calculate the effective thermal conductivity using Fourier's law. More details on the finite element modeling can be found in the Appendix.

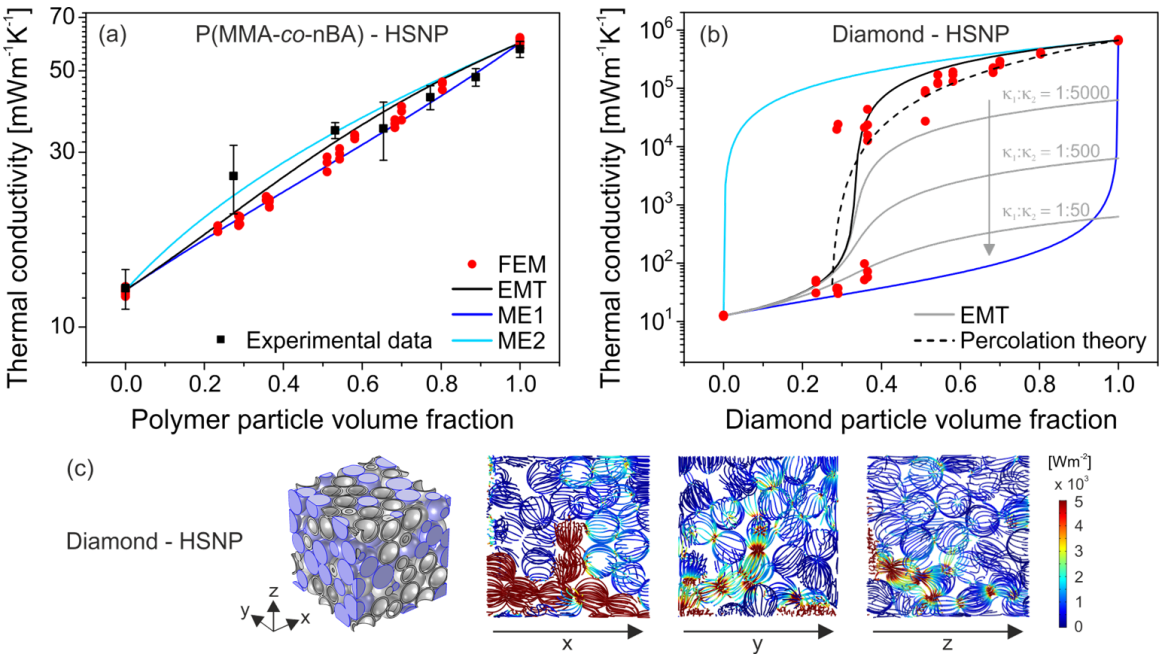

Figure 2. Finite element modeling (FEM) of binary colloidal assemblies with hollow silica spheres. a) Thermal conductivity data of the binary particle mixtures, the EMT, ME1, and ME2 models in comparison to simulated data obtained from FEM. b) Thermal conductivity data from FEM of binary colloidal glasses consisting of hollow spheres and diamond particles and the corresponding EMT (black line), ME1 (dark blue line), and ME2 (light blue line) models. The gray lines show the EMT model for binary particle mixtures with a decreasing thermal conductivity ratio ($\kappa_1:\kappa_2$) between the two types of particles. The black dashed line represents the fit by a percolation model [Equation (2)]. c) The geometry of the binary colloidal glass with a diamond particle volume fraction of 36.5 % (blue particles) used for the FEM simulations and the corresponding heat flux streamlines for the different directions (x, y, and z).

3. Results and Discussion

3.1. Binary Colloidal Assemblies

The binary colloidal assemblies are built from two types of particles with comparable outer diameters and surface charges: copolymer particles P(MMA-*co*-nBA) with a diameter of 441 ± 9 nm (ζ potential of -43 mV) and hollow silica nanoparticles (HSNPs) with a diameter of 423 ± 8 nm, a shell thickness of 25.3 ± 1.2 nm (ζ potential of -27 mV). The electron microscopy images of these particles are shown in Figure 3. Both images highlight the monodispersity of the particles. The polymeric particles feature a shrunk and rough surface due to the sensitivity of the PMMA to the electron beam.

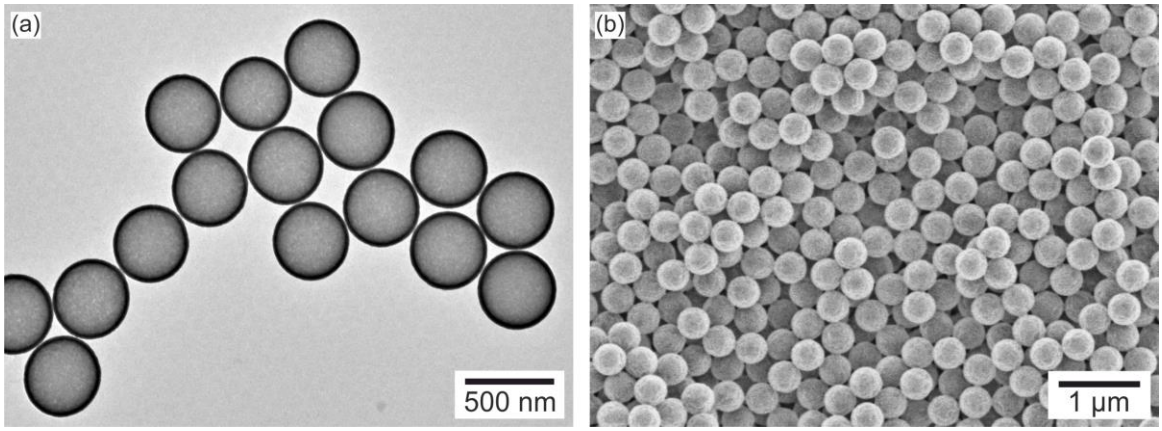

Figure 3. a) Transmission electron microscopy images of the hollow silica nanoparticles. b) Scanning electron microscopy images of the P(MMA-*co*-nBA) particles.

We used vacuum filtration (see Figure 4 and Appendix for more details) for the self-assembly process, since this method enables a fast and facile assembly of the particles into a colloidal glass with a random distribution of the two particle types.

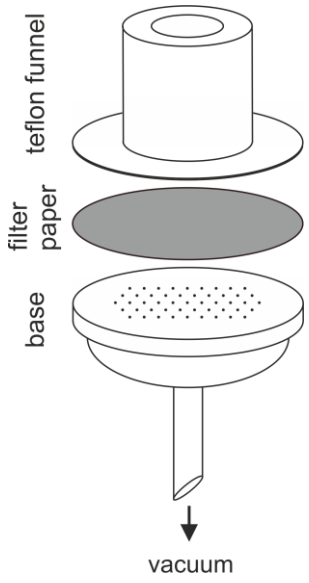

Figure 4. Schematic setup of the vacuum filtration system. The parts were held together by a spring clamp and put on a filter flask.

Particularly, minor density differences do not influence the particle distribution in the colloidal glass using the filtration process.

The number of polymer particles was varied from 100 % to 0 % particles (see Table 1).

Table 1. Designation of the binary colloidal assemblies and the corresponding polymer particle volume fraction.

	100P	**89P**	**77P**	**65P**	**53P**	**27P**	**0P**
Number of polymer particles [%]	100	87.5	75	62.5	50	25	0
Polymer particle volume fraction	1	0.89	0.77	0.65	0.53	0.27	0

The comparable particle size and surface potential lead to a good particle distribution on the sub-μm scale in the composite. This is validated by side-view SEM images. The inset in Figure 5 shows the 50/50 mixture with red-colored hollow spheres for easier identification.

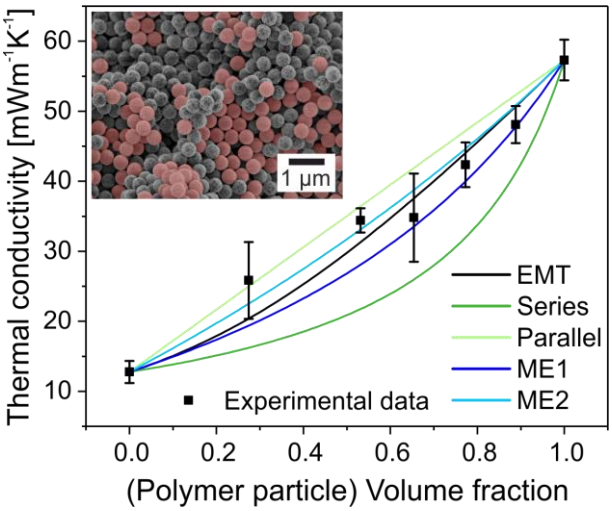

Figure 5. Thermal conductivity data of the binary colloidal glasses measured in vacuum at 25 °C (black squares) in comparison to different mixing models: effective medium theory (EMT), series model, parallel model, and Maxwell-Eucken (ME) model 1 and 2. The inset shows a side-view scanning electron microscopy (SEM) image of the colloidal assembly with a polymer particle volume fraction of 53 % (53P). The hollow silica spheres are red-colored.

Additional SEM images of this 53P particle mixture demonstrate the homogeneous particle distribution throughout the entire colloidal glass (Figure 6).

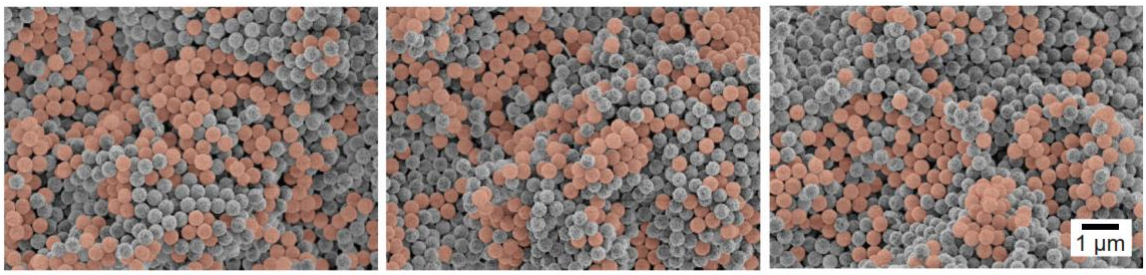

Figure 6. Scanning electron microscopy images of the colloidal assembly with a polymer particle volume fraction of 53 % (53P) taken at different positions of the sample. The hollow silica spheres are red colored.

Only on a local scale, small clusters comprising several particles of the same type can be seen. The other particle composites are shown in Figure 7.

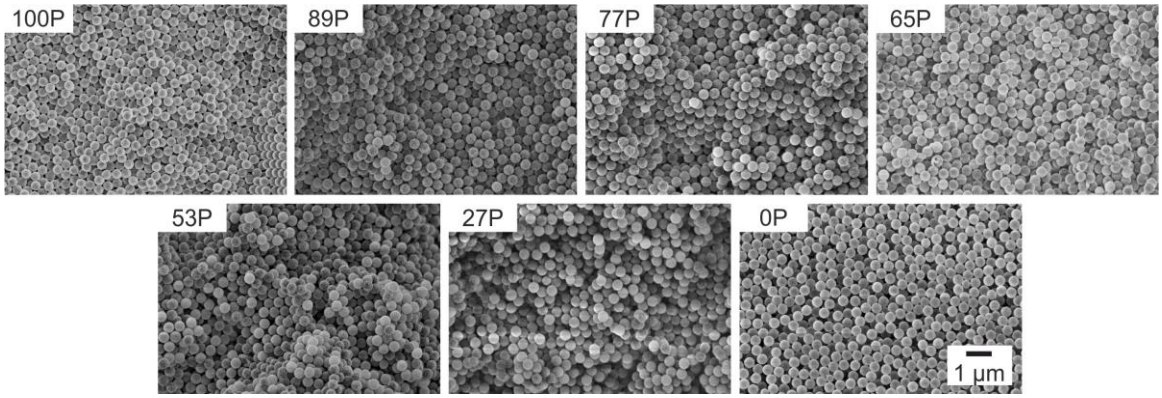

Figure 7. Scanning electron microscopy images of the binary colloidal glasses comprising polymer particle volume fractions between 100 % and 0 % before the heating process.

3.2. Thermal Transport Properties of Binary Colloidal Glasses – Percolation Effect

The thermal transport properties of the colloidal glasses were determined by xenon flash analysis. The method allows the direct determination of the thermal diffusivity α. The thermal conductivity κ can be calculated using the following equation:

$$\kappa = \alpha c_{\mathrm{p}} \rho \tag{3}$$

The specific heat capacity c_{p} and density ρ data are plotted in Figure 8.

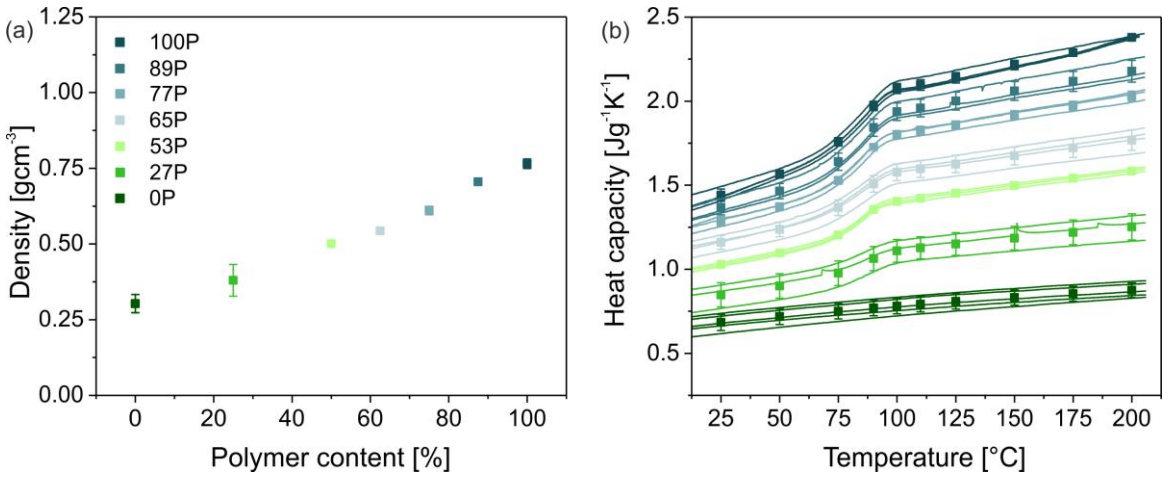

Figure 8. a) The density of the different binary colloidal glasses. b) Differential scanning calorimetry measurements of the particle mixtures.

Figure 5 shows the thermal conductivity data of the binary colloidal glasses for different polymer particle volume fractions. For a colloidal glass consisting of hollow silica spheres (0P), the thermal conductivity is extremely low with a value of only 13 mWm^{-1}K^{-1}. The heat transport is limited in these colloidal glasses due to several structural properties on the nano- and mesoscale.[18-19] These are (i) the hollow structure, which reduces the density to only 0.30 gcm^{-3}, (ii) the large amount of interfaces due to the particulate structure, which increases the thermal resistance by means of interparticle constriction, and (iii) the low packing parameter of the particles to reduce the density and interparticle contact points even further. Thus, silica hollow sphere colloidal glasses represent a highly insulating material class.

The thermal conductivity of the investigated P(MMA-*co*-nBA) particle colloidal glass is about 57 mWm^{-1}K^{-1} at a density of 0.77 gcm^{-3}, which compares well to the value reported for 366 nm polystyrene colloidal crystals.[20] By mixing the two types of particles, the thermal conductivity can be tuned within these bounds. We find that the thermal conductivity increases monotonically with increasing polymer particle ratio within the colloidal assemblies. Thus, we do not find any sign of reduced thermal conductivity caused by mixing unlike particles, *e.g.*, by additional interfacial resistances. We also cannot infer a distinct percolation threshold, which

would be indicative for a preferred energy transport along a specific particle pathway.

We compare now our binary colloidal alloys to the existing set of mixing models.[13] The EMT model describes our system across the whole volume fraction range reasonably well. At low and high volume fractions, the ME models are also in reasonable agreement. For these regions, the separated inclusion assumption of the ME model is valid since the minority particle phase is dispersed in the majority phase. Furthermore, the parallel and the series model are not adequate for our colloidal alloys. The standard deviation of the experimental data and the proximity of the highest and lowest thermal conductivity of the pure phase components does not allow for further discrimination between these models. We prefer the EMT model since it is conceptually applicable over the entire mixing range.

The finite element method is a useful tool to validate and understand the experimental data in greater detail. Figure 2a compares the experimental values (black squares) to the simulation results (red circles) based on a random close-packed particle structure with random binary particle selection. FEM allows the screening of various composition ratios easily. The resulting thermal conductivity data are plotted along with the EMT mixing model (black line), the ME1 (dark blue line), and the ME2 (light blue line) models. The data obtained from finite element modeling fits very well to the experimental data and are well described by the EMT and ME1 models. Thus, the FEM, EMT, and ME1 models are all suitable methods to predict the thermal conductivity of binary colloidal glasses (with comparable thermal conductivities of the two phases, which is discussed below). Furthermore, the assumptions implemented in the FEM simulation, such as diffusive thermal transport and no interfacial thermal contact resistance between adjacent spheres, describe the experimental situation adequately well.

Based on this validation of the applicability of our FEM simulation, we can now use it to investigate the onset of percolation in binary colloidal crystals in greater detail.

Therefore, we selected two types of dielectric particles which possess a large thermal conductivity contrast, which is experimentally hardly accessible: hollow silica nanospheres and diamond particles. The large thermal conductivity contrast should allow for a clear assessment of the percolation through the colloidal assembly. We want to emphasize that the structure of the colloidal glass remains unchanged since we only replace one type of particle species in the simulation volume. The FEM results in comparison to the EMT (black line), ME1 (dark blue line), and ME2 (light blue line) models are shown in Figure 2b. Additionally, we explore the effect of the thermal conductivity difference between the respective components and found that it should at least amount to $\kappa_1 : \kappa_2$ 1:500 in order to experimentally observe a steplike increase in thermal conductivity (gray lines in Figure 2b). The formation of percolation pathways is found at a diamond particle volume fraction of about 30 %. In the range of this mixing ratio, a high degree of variability between the individual simulation points results. As outlined in the Appendix, each simulation was conducted along the x, y, and z axis of the simulation cube. In Figure 2c heat flow streamlines are shown for the different orientations with a diamond particle volume fraction of 36.5 %. While in y and z direction the heat flow is relatively low (thermal conductivity of 60 $mWm^{-1}K^{-1}$), the heat flow in the x direction shows a percolation pathway which increases the thermal conductivity to 24 000 $mWm^{-1}K^{-1}$. This large variability is indicative of a critical mixing ratio close to the percolation threshold. Owing to the hardware limitation of the size of our simulation cube, fully percolated pathways only span across distinct orientations in this regime. Increasing the number of diamond particles (> 50 %) leads to a colloidal glass with robust percolating pathways in all directions. The effective medium theory describes this mechanism also quite well but overestimates the thermal conductivity at high diamond particle ratios. A major difference compared to the data shown in Figure 2a (small differences in thermal conductivity between the two components) is obvious in Figure 2b. Neither

of the ME models describes the FEM data adequately anymore. Both models strongly over- or underestimate the effective thermal conductivity, respectively. The explicit percolation model (Equation 2), however, provides a complementary way to describe the simulated data. In contrast to the EMT model, the percolation theory depends on the underlying particle structure. In Equation 2, κ_1 and κ_2 are the effective thermal conductivities of the pure hollow sphere or diamond particle colloidal assembly. Therefore, the maximum filling packing factor F equals 1. The percolation model is plotted in Figure 2b as a black dashed line and shows a clear consistency with the simulated data above the percolation threshold at a mixing ratio of 27 %. Owing to the random particle packing of our isotropic spheres, both models (EMT and percolation theory) predict a comparable percolation threshold. Furthermore, the percolation model does not overestimate the effective thermal conductivity of the particle mixture, as is the case for the EMT model.

To sum up, the EMT model describes the effective thermal conductivity of binary particle mixtures across the entire mixing range reasonably well. The EMT model is also valid for particle mixtures which possess a significant difference between the individual thermal conductivities. However, the EMT model does not account for the explicit structure of the particle ensemble. The percolation theory, on the other hand, describes the onset of percolation equally well and is explicitly based on a randomly close-packed structure. The percolation theory provides a complementary possibility to describe the effective thermal conductivity beyond the percolation threshold. In contrast to the EMT model, a lower bound of the effective thermal conductivity is given by the percolation theory considering the right particle ordering. Our simulation results thereby validate the analytical solution.

3.3. Thermal Transport Properties of Binary Colloidal Glasses – Temperature Dependency

We followed an additional route to investigate the heat transport through our binary colloidal mixture experimentally by exploiting the known temperature dependence of the thermal conductivity of polymer colloidal crystals.[20] Briefly, upon crossing the glass transition temperature (T_g) of the constituting polymer, the effective thermal conductivity of a pure polymer colloidal crystal increases by 200 % – 300 %. We, therefore, measured the temperature-dependent thermal conductivity. To facilitate a homogeneous temperature distribution in the sample, measurements were performed in helium at 1000 mbar. The thermal conductivity of the different particle ratios is shown in Figure 9. The thermal conductivity of the pure hollow silica nanoparticle colloidal glasses shows a monotonic growth driven by the specific heat capacity and no irreversible increase of the thermal conductivity. At the other extreme, the pure polymer particle glass exhibits the expected sharp step-up of the thermal conductivity after exceeding T_g due to the loss of the particulate structure (see SEM images in Figure 9d).

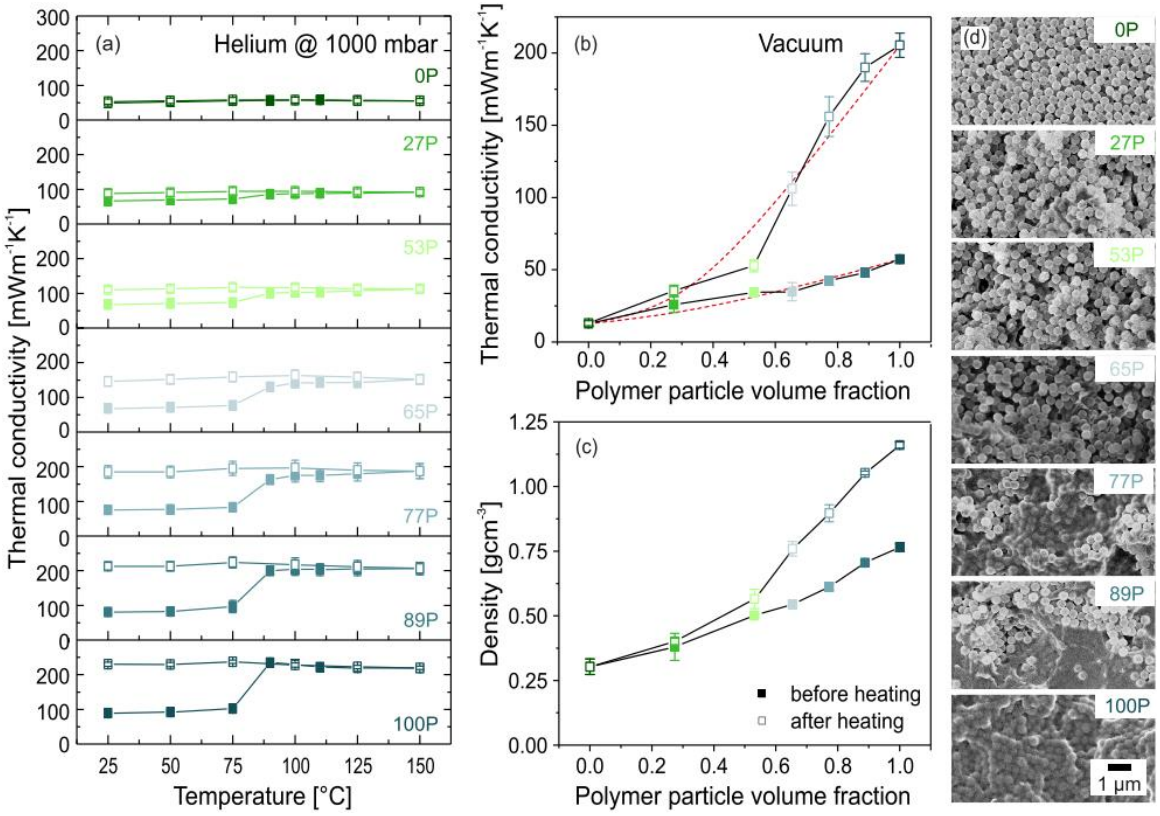

Figure 9. a) Temperature-dependent thermal conductivity of colloidal glasses in helium at 1000 mbar. b) Thermal conductivity of the particle assemblies in vacuum before and after heating to 150 °C. The red dashed line represents the EMT model. c) Density of the colloidal assemblies before and after heating to 150 °C. d) Scanning electron microscopy images of the colloidal assemblies after heating to 150 °C.

The other particle mixtures feature a transient behavior between these two cases, however, with marked differences between the heating and cooling cycle. Figure 9b summarizes the differences before and after heating. In this case, any contribution from gaseous transport can be excluded since these data were measured in vacuum. While the thermal conductivity shows only minor increases of up to 50 % polymer content, the rise is distinct for higher ratios, where the polymer constitutes the majority phase. This can be attributed to the formation of a continuous polymer network due to the loss of interfaces. This is accompanied by an increase of the density shown in Figure 9c. Thus, heat can be conducted faster through the molten polymer phase [compare SEM image in Figure 9d]. It is important to differentiate this loss of structural integrity to the presence of percolating thermal transport pathways across a particular particle type, as discussed in the previous section. A

percolating particle network should form at a polymer particle volume fraction of about 27 %; yet, the temperature- induced film formation becomes significant only at polymer particle volume fractions > 50 %. The structural integrity at elevated temperatures is compromised as soon as the polymer particles constitute the majority phase. The comparison of the molten film to the effective medium model [see Figure 9b] reveals a second severe change to the homogeneity of the nanocomposite. The agreement between the EMT model and the measurement is much worse compared to the initial particle mixture. It now underestimates the thermal conductivity of high polymer mixing ratios and overestimates it at lower ratios. This hints towards a concomitant phase separation upon polymer annealing. The SEM images after the heating cycle qualitatively support this interpretation. Particularly for the case of low hollow sphere contents (89P and 77P), areas with large hollow sphere aggregates, even with a high degree of local order, can be inferred. These could originate from a relocation of the silica hollow spheres upon polymer film formation and confirm the challenge to fabricate homogeneous composite materials on the nanometer scale.

4. Conclusion

We investigated the thermal transport properties of binary colloidal glasses consisting of hollow silica nanoparticles and P(MMA-*co*-nBA) polymer particles. Mixing these two types of particles enables the fabrication of a nanocomposite material with a homogeneous distribution of the two components. The thermal conductivity increases from 13 $mWm^{-1}K^{-1}$ to 57 $mWm^{-1}K^{-1}$ in vacuum, depending on the particle mixture. Established mixing models are suitable to describe the effective thermal conductivity adequately. However, no percolation threshold can be observed for such similar particle mixtures (regarding their thermal conductivity). Using finite element modeling, we validated our experimental results and provided a better understanding of the percolation threshold. We find

that the thermal conductivity ratio (κ_1: κ_2) between two types of particles must be at least 1:500 to observe a distinct step in the mixing ratio dependency. Furthermore, the Maxwell-Eucken mixing models fail to describe such nanocomposites with a large thermal conductivity contrast.

Heating the binary colloidal glasses above the glass transition temperature leads to a melting of the polymer and a loss of the interparticle interfaces. Thus, a continuous polymer network forms with solid particle inclusions for polymer contents > 50 %. This can be understood as a threshold of structural integrity. Concomitantly, the film formation induces a demixing of the hollow silica beads, resulting in a heterogeneous structure. This is less well described by the EMT mixing model. Our study contributes to a thorough understanding of percolation and effective thermal transport properties in particulate nanocomposite materials.

Acknowledgments

P.R. and B.A.F.K. acknowledge support from the Elite Network of Bavaria (ENB). Further support was provided by the SFB840 and the Bavarian Polymer Institute, BPI. This research was funded by the Volkswagen Foundation through a Lichtenberg Professorship. P.R. and A.P. contributed equally to this work.

Appendix: Supporting Information

1. Materials

Styrene (≥ 99 %, Aldrich), 2,2′-azobis(2-methylpropion-amidine) dihydrochloride (AIBA; 97 %, Aldrich), [2-(methacryloxy)ethyl]trimethylammonium chloride (MTC; 70 % solution in water, Polyscience), polyvinylpyrrolidone K30 (PVP, ~Mw 55 kgmol^{-1}, Aldrich), tetraethylorthosilicate (TEOS, ≥ 99 %, Aldrich), ammonium hydroxide solution (30 % - 33 % in water, Aldrich), and potassium peroxodisulfate (KPS; ≥ 99 %, Aldrich) were used as received. Methyl methacrylate (MMA, 99 %, Aldrich) and *n*-butyl acrylate (nBA, ≥ 99 %, Aldrich) were purified by filtration

over an alumina column (activated, basic, Brockmann I, Sigma-Aldrich). Ethanol was used in technical grade, and water was taken from a Millipore Direct Q3UV unit for all the synthesis and purification steps.

2. Synthesis of Hollow Silica Nanoparticles

The synthesis of hollow silica spheres comprises three steps. (i) First, monodisperse polystyrene (PS) particles were prepared by emulsifier-free emulsion polymerization.[16] For the synthesis, 1.8 g PVP were dissolved in 10 mL water and added to a 500-mL three-necked flask equipped with a reflux condenser and a gas inlet. 225 mL water, 26 mL styrene, and 75 μL MTC were added. The emulsion was degassed and heated to the reaction temperature of 70 °C at a stirring speed of 850 rpm for 30 min. For the initiation of the polymerization, 0.6 g AIBA, dissolved in 5 mL water, were added. After the nucleation, the stirring speed was reduced to 450 rpm, and the reaction was carried out overnight under an argon atmosphere. (ii) In the second step, the polystyrene particles were coated with a thin silica shell by a modified Stoeber condensation process to obtain core-shell particles[17]. For the synthesis, 1.9 vol % TEOS were added to an 81.4 vol % ethanol, 10.7 vol % water, 6.0 vol % ammonium hydroxide solution containing 9.73 mgmL^{-1} PS latex particles. (iii) Subsequently, the polystyrene core was removed by calcining the particles at 500 °C for 12 h in air.

3. Synthesis of P(MMA-*co*-nBA) Particles

The polymer particles were prepared by emulsifier-free emulsion polymerization. For the synthesis, 450 mL water and a mixture of 40 mL and 10 mL MMA and nBA were added to a 1000-mL three-necked flask, equipped with a reflux condenser and a gas inlet. The emulsion was degassed and heated to the reaction temperature of 75 °C at a stirring speed of 650 rpm. After 15 minutes, 2 mL of acrylic acid were added to the mixture followed by a further equilibration step for 5 min. The

polymerization was initiated by a rapid injection of 150 mg KPS dissolved in 5 mL water. After the nucleation, the stirring speed was reduced to 400 rpm to avoid the formation of aggregates. The reaction was carried out overnight under an argon atmosphere. Residual reagents were removed by dialysis against water for five days, changing water twice a day.

4. Assembly into Colloidal Glasses

Colloidal assemblies were prepared by a vacuum filtration system from Merck Millipore (see Figure 4). As a filter paper, an MF-Millipore membrane filter with a pore size of 0.2 μm was used. The sample size was reduced by a Teflon inset with a diameter of 2 cm. After the assembly, the samples were dried in vacuum overnight.

5. Characterization Methods

SEM was performed using a Leo 1530 instrument (Zeiss) using acceleration voltages of 2 or 3 kV. The images were taken with an InLens and Everhart-Thornley secondary electron detector.

Differential scanning calorimetry (DSC) measurements were performed on a Discovery Q2500 DSC (TA Instruments). For the determination of the specific heat capacity the ASTM E1269 standard test method was used. Powders of the particles (~10 mg) were scanned in closed aluminum pans under a dry nitrogen flow of 50 $mLmin^{-1}$ over a temperature range from -40 °C to 210 °C with a heating rate of 20 °Cmin^{-1}. Two heating cycles were conducted, whereas only the second cycle was used for evaluation.

Thermal diffusivity measurements of the colloidal assemblies were performed on a xenon flash apparatus (Linseis, XFA500) equipped with an InSb infrared detector. Before the measurements, the samples were coated with a thin graphitic layer (~15 μm) on each side to ensure a good absorbance at the bottom and a high

emissivity at the top side of the sample. The thickness of the graphite layer is negligible compared to the thickness of the colloidal glasses (700–1500 µm). The measurements were performed on at least three samples in vacuum (~0.05 mbar) at room temperature, and in helium (1000 mbar) in the temperature range from 25 °C to 150 °C. The received data were evaluated by the software APROSOFT LASER FLASH Evaluation v1.06 using the radiation fit model. The schematic setup and the corresponding measurement signal, fitted by the radiation model, are shown in Figure 10. The thicknesses of the colloidal glasses were measured using a Litematic VL50 (Mitutoyo) measuring unit.

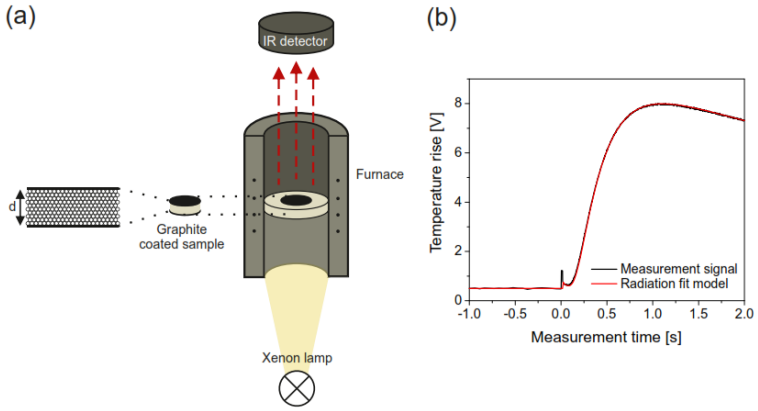

Figure 10. Schematic setup of the xenon flash analysis and the corresponding measurement signal with radiation fit. This fit model represents an extension to the finite-pulse and heat loss corrections given by the combined fit model from Dusza.[21] Moreover, it takes into account that part of the xenon flash is transmitted to the rear sample surface, leading to an instantaneous temperature jump analogous to Blumm *et al.*[22]

The densities of the hollow sphere assemblies and the unmolten colloidal glasses (0P–100P) were determined from the mass and volume of the monoliths. The volume was measured using a 3D digital surface profiler (Keyence V3100), and the mass was determined by weighing the colloidal glasses. The densities of the molten colloidal assemblies (27P–100P) were measured using Archimedes' principle (buoyancy method). The colloidal glasses were hydrophobized by chemical vapor deposition using hexamethyldisilazane (HMDS) to avoid the adsorption of water by the hygroscopic silica network.

6. Finite Element Modeling

An amorphous structure of equally sized particles was compiled using a molecular dynamics simulation. Precisely, we used the gran-hooke pair potential[23-25] in LAMMPS on a set of 20 000 particles that were pulled by a gravitational force to the bottom of a simulation box with periodic boundaries in x and y direction. The $g(r)$ of the resulting structure (Figure 11) shows the distinct features of a random sphere packing as described in the literature[26-30].

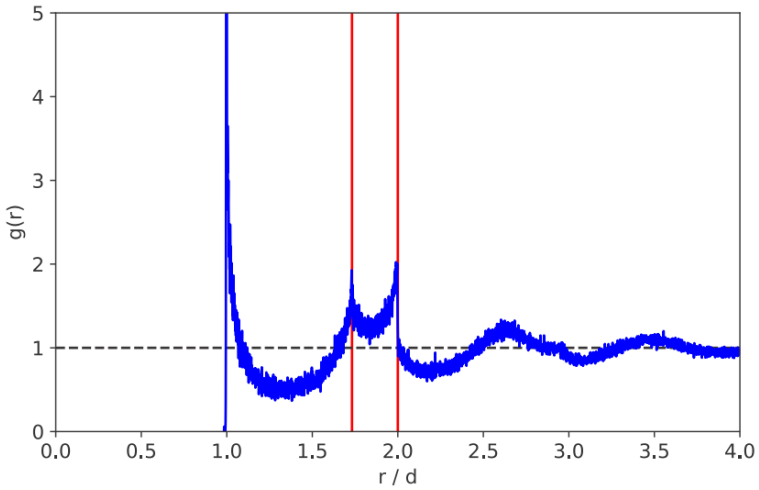

Figure 11. The radial distribution function of a random close- packed particle assembly from molecular dynamics simulation (program LAMPPS). The two red lines are at $\sqrt{3}$ and 2.

This amorphous particle structure was used for the finite element method of the effective thermal transport properties using COMSOL MULTIPHYSICS. A random selection process assigned the two types of particles [hollow silica nanoparticles and P(MMA-*co*-nBA) particles] to the simulated colloidal glass, yielding a binary colloidal assembly with different polymer particle volume fractions. The particle size has been adjusted such that the mutual contact points between the spheres resemble the experiment. There, we find a relative contact area of about 0.6 %-1 % of the total particle surface area per contact point. The absolute value of this contact area is of minor relevance for the discussion, as it will only offset the overall thermal conductivity. For the hollow silica spheres, the experimental shell thickness-to-radius ratio was used. Three cubes per mixture,

each with around 100 particles, were cut out of the amorphous structure. The allowed number of particles in the cube is limited by the physical memory of the simulation computer (128 GB). An exemplary structure used for FEM is shown in Figure 2c. A temperature difference was applied to opposite faces of the cube, while all remaining surfaces were thermally insulating. Therefore, purely one-dimensional thermal transport can occur. Furthermore, no thermal resistance between the particles was considered. The computed heat flux normal to the isothermal faces was used to calculate the effective thermal conductivity using Fourier's law [see Equation A1],

$$\kappa_{\text{eff}} = \frac{Q/A}{\Delta T/h} \qquad \text{A1}$$

where Q is the heat flow rate normal to the isothermal faces, A the cross-sectional area of the cube, ΔT the temperature difference ($T_{\text{hot}} - T_{\text{cold}}$), and h the cube edge length.

The simulation was conducted along all three directions (x, y, and z) of the cube. The same simulations were undertaken using diamond instead of P(MMA-*co*-nBA) to obtain data for a binary colloidal assembly having a higher thermal conductivity contrast. The specific heat capacity, density, and thermal conductivity of all materials used in FEM simulations are listed in Table 2.

Table 2. Specific heat capacity, density, and thermal conductivity of silica, P(MMA-*co*-nBA), and diamond used in FEM simulations.

	Specific heat capacity [$Jg^{-1}K^{-1}$]	**Density [gcm^{-3}]**	**Thermal conductivity [$mWm^{-1}K^{-1}$]**
Silica	0.684	2.20	173[a]
P(MMA-*co*-nBA)	1.441	1.16	205
Diamond[b]	0.507	3.51	2 300 000

[a]Thermal conductivity of silica is chosen such that the same effective thermal conductivity is obtained as experimentally in vacuum. [b]The literature values were obtained from Salazar[31] and Slack[32].

References

1. Tan, F. L.; Tso, C. P., Cooling of mobile electronic devices using phase change materials. *Applied Thermal Engineering* **2004,** *24* (2), 159-169.

2. Moore, A. L.; Shi, L., Emerging challenges and materials for thermal management of electronics. *Materials Today* **2014,** *17* (4), 163-174.

3. Xia, Y.; Gates, B.; Yin, Y.; Lu, Y., Monodispersed colloidal spheres: old materials with new applications. *Advanced Materials* **2000,** *12* (10), 693-713.

4. Lee, G.-W.; Park, M.; Kim, J.; Lee, J. I.; Yoon, H. G., Enhanced thermal conductivity of polymer composites filled with hybrid filler. *Composites Part A: Applied Science and Manufacturing* **2006,** *37* (5), 727-734.

5. Han, Z.; Fina, A., Thermal conductivity of carbon nanotubes and their polymer nanocomposites: A review. *Progress in Polymer Science* **2011,** *36* (7), 914-944.

6. Hasselman, D. P. H.; Johnson, L. F., Effective thermal conductivity of composites with interfacial thermal barrier resistance. *Journal of Composite Materials* **1987,** *21* (6), 508-515.

7. Stauffer, D.; Aharony, A., *Introduction to percolation theory*. Taylor & Francis 1994.

8. Tian, W.; Yang, R., Phonon transport and thermal conductivity percolation in random nanoparticle composites. *Computer Modeling in Engineering and Science* **2008,** *24* (2/3), 123.

9. Xue, Q., The influence of particle shape and size on electric conductivity of metal–polymer composites. *European Polymer Journal* **2004,** *40* (2), 323-327.

10. Kumar, S.; Alam, M. A.; Murthy, J. Y., Effect of percolation on thermal transport in nanotube composites. *Applied Physics Letters* **2007,** *90* (10), 104105.

11. Mamunya, Y. P.; Davydenko, V. V.; Pissis, P.; Lebedev, E. V., Electrical and thermal conductivity of polymers filled with metal powders. *European Polymer Journal* **2002,** *38* (9), 1887-1897.

12. Lux, F., Models proposed to explain the electrical conductivity of mixtures made of conductive and insulating materials. *Journal of Materials Science* **1993,** *28* (2), 285-301.

13. Carson, J. K.; Lovatt, S. J.; Tanner, D. J.; Cleland, A. C., Thermal conductivity bounds for isotropic, porous materials. *International Journal of Heat and Mass Transfer* **2005,** *48* (11), 2150-2158.

14. Wang, J.; Carson, J. K.; North, M. F.; Cleland, D. J., A new approach to modelling the effective thermal conductivity of heterogeneous materials. *International Journal of Heat and Mass Transfer* **2006,** *49* (17–18), 3075-3083.

15. Hashin, Z.; Shtrikman, S., A Variational Approach to the Theory of the Effective Magnetic Permeability of Multiphase Materials. *Journal of Applied Physics* **1962,** *33* (10), 3125-3131.

16. Goodwin, J. W.; Hearn, J.; Ho, C. C.; Ottewill, R. H., Studies on the preparation and characterisation of monodisperse polystyrene latices. *Colloid and Polymer Science* **1974,** *252* (6), 464-471.

17. Graf, C.; Vossen, D. L. J.; Imhof, A.; van Blaaderen, A., A General Method To Coat Colloidal Particles with Silica. *Langmuir* **2003,** *19* (17), 6693-6700.

18. Ruckdeschel, P.; Kemnitzer, T. W.; Nutz, F. A.; Senker, J.; Retsch, M., Hollow silica sphere colloidal crystals: insights into calcination dependent thermal transport. *Nanoscale* **2015,** *7* (22), 10059-10070.

19. Ruckdeschel, P.; Philipp, A.; Retsch, M., Understanding thermal insulation in porous, particulate materials. *Advanced Functional Materials* **2017,** *27*, 1702256.

20. Nutz, F. A.; Ruckdeschel, P.; Retsch, M., Polystyrene colloidal crystals: Interface controlled thermal conductivity in an open-porous mesoparticle superstructure. *Journal of Colloid and Interface Science* **2015,** *457*, 96-101.

21. Dusza, L., Combined solution of the simultaneous heat loss and finite pulse corrections with the laser flash method. *High Temperatures-High Pressures* **1995,** *27/28* (5), 467-473.

22. Blumm, J.; Henderson, J.; Nilsson, O.; Fricke, J., Laser flash measurement of the phononic thermal diffusivity of glasses in the presence of ballistic radiative transfer. *High Temperatures-High Pressures* **1997,** *29*, 555-560.

23. Brilliantov, N. V.; Spahn, F.; Hertzsch, J.-M.; P\"oschel, T., Model for collisions in granular gases. *Physical Review E* **1996,** *53* (5), 5382-5392.

24. Silbert, L. E.; Ertaş, D.; Grest, G. S.; Halsey, T. C.; Levine, D.; Plimpton, S. J., Granular flow down an inclined plane: Bagnold scaling and rheology. *Physical Review E* **2001,** *64* (5), 051302.

25. Zhang, H. P.; Makse, H. A., Jamming transition in emulsions and granular materials. *Physical Review E* **2005,** *72* (1), 011301.

26. Mason, G., Radial distribution functions from small packings of spheres. *Nature* **1968,** *217* (5130), 733-735.

27. Seidler, G. T.; Martinez, G.; Seeley, L. H.; Kim, K. H.; Behne, E. A.; Zaranek, S.; Chapman, B. D.; Heald, S. M.; Brewe, D. L., Granule-by-granule reconstruction of a sandpile from x-ray microtomography data. *Physical Review E* **2000,** *62* (6), 8175-8181.

28. Clarke, A. S.; Jónsson, H., Structural changes accompanying densification of random hard-sphere packings. *Physical Review E* **1993,** *47* (6), 3975-3984.

29. Yang, R. Y.; Zou, R. P.; Yu, A. B., Computer simulation of the packing of fine particles. *Physical Review E* **2000,** *62* (3), 3900-3908.

30. Kansal, A. R.; Torquato, S.; Stillinger, F. H., Diversity of order and densities in jammed hard-particle packings. *Physical Review E* **2002,** *66* (4), 041109.

31. Salazar, A., On thermal diffusivity. *European Journal of Physics* **2003,** *24* (4), 351.

32. Slack, G. A., Thermal Conductivity of pure and impure silicon, silicon carbide, and diamond. *Journal of Applied Physics* **1964,** *35* (12), 3460-3466.

9. Low Thermal Conductivity Through Dense Particle Packings with Optimum Disorder

Fabian A. Nutz[1,‡], Alexandra Philipp[1,‡], Bernd A. F. Kopera[1], Martin Dulle[2], and Markus Retsch[1,*]

[‡] *These authors contributed equally to the work.*

[1]Department of Chemistry, University of Bayreuth, Universitätsstraße 30, 95447 Bayreuth, Germany

[2]JCNS-1/ICS-1: Neutron Scattering, Forschungszentrum Jülich GmbH, Wilhelm-Johnen-Straße 52428, Jülich, Germany

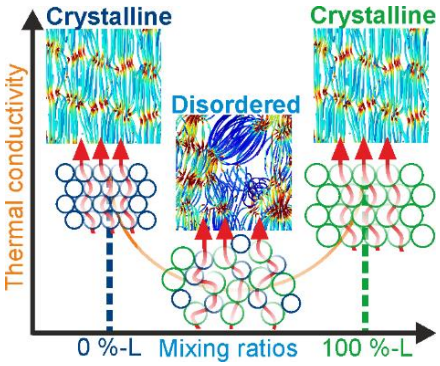

Reprinted with permission from Nutz *et al.*, *Adv. Mater.*, **2018**, *30*(14), 1704910.

Abstract

Heat transport plays a critical role in modern batteries, electrodes, and capacitors. This is caused by the ongoing miniaturization of such nanotechnological devices, which increases the local power density and hence temperature. Even worse, the introduction of heterostructures and interfaces is often accompanied by a reduction in thermal conductivity, which can ultimately lead to the failure of the entire device. Surprisingly, a fundamental understanding of the governing heat transport processes even in simple systems, such as binary particle mixtures is still missing. This contribution closes this gap and elucidates how strongly the polydispersity of a model particulate system influences the effective thermal conductivity across such a heterogeneous system. In a combined experimental and modeling approach, well-defined mixtures of monodisperse particles with varying size ratios are investigated. The transition from order to disorder can reduce the effective thermal conductivity by as much as ≈50 %. This is caused by an increase in the thermal transport path length and is governed by the number of interparticle contact points. These results are of general importance for many particulate and heterostructured materials and will help to conceive improved device layouts with more reliable heat dissipation or conservation properties in the future.

1. Introduction

Materials with low thermal conductivity are employed in many fields such as clothing, refrigeration, building insulation, and thermoelectrics.[1] Concepts to reduce the thermal conductivity of a given material either target the material composition or its nano-, meso-, or microstructure. Generally, for bulk materials, a high thermal conductivity is found in crystalline solids where phonons are able to transport thermal energy over several hundred nanometers based on a well-defined crystal lattice.[2-5] In contrary, low thermal conductivities are mostly found in disordered, amorphous materials. Based on an increased scattering at the

disordered structure, the mean free path of phonons is strongly reduced, resulting in diffusive thermal transport.[6-7] Allen and Feldman[8-9] proposed three different vibrational modes, namely diffusons, propagons, and locons, to describe thermal transport in amorphous matter. Increasing phonon scattering in bulk materials, subsequently leads to a reduction in thermal conductivity. In dense materials this can be achieved by layered structures[10-11], doping[12-13] or the embedding of nanoparticles[14-15], where particularly crystalline solids are strongly affected. Zhang and Minnich investigated how nanoparticle clusters with a particular size distribution can lower the thermal conductivity in crystalline SiGe alloys even below its amorphous limit.[14]

Besides the chemical composition of a certain material, the influence of the overall structure is of high importance, too. The most obvious and well-known structural influence is given by the introduction of porosity. This severely decreases the density of a bulk material and consequently reduces the effective thermal conductivity. Depending on the cell size of the porous material, highly insulating properties are accessible.[16-19] Moreover, classical porous, granular matter becomes increasingly important for a range of applications, which involve heterostructures and interfaces. For instance, thermal management in high-density storage devices such as batteries or supercapacitors is a critical safety concern.[20-22]

Colloidal assembly structures have been proven to be particular suitable to investigate the influence of three-dimensional nanostructuring on the effective thermal transport in granular matter.[23] The thermal conductivity of colloidal crystals is mainly governed by the geometrical constrictions at the interparticle contact points, and the material of the particles itself.[24-26] While most colloidal assembly structures targeted periodically ordered materials, the controlled introduction of disorder also showed to provide fundamental insights, for instance into the physics of phononic bandgaps in the hypersonic regime.[27]

In this work, we provide a conceptual understanding of the influence of structural order on the thermal transport properties in particulate mesostructures. Therefore, binary colloidal assemblies were fabricated from two monodisperse, differently sized polystyrene (PS) particles. These buildings blocks are easily accessible by common polymerization techniques[28-29] and their self-assembly into superstructures is well-established.[30] By mixing two differently sized particles, it is possible to control the structural order of the resulting colloidal assembly. We clarify the underlying effect of the thermal conductivity reduction by finite element modeling combined with molecular dynamic simulations. We further demonstrate how to reduce heat transport in disordered binary assemblies in a rational way.

2. Main Part

Binary colloidal assemblies of PS particles possessing a diameter of 243 nm (S) and 306 nm (L) were fabricated by evaporation-induced self-assembly (size ratio ~0.8). For spectroscopic characterization, binary assemblies were additionally immobilized on a glass slide by dip-coating of a 3 wt% of aqueous particles dispersions. The mixing ratio ranged from 0 vol%-L to 100 vol%-L. Optical microscopy and scanning electron images of the edges of split monoliths are shown in Figure 1a and b and provide a qualitative expression of how the mixing ratio translates into order and disorder.

From optical microscopy (Figure 1a), strong opalescent colors are visible for samples consisting of only one particle type (0 vol%-L and 100 vol%-L) as well as for binary assemblies only containing a small amount of differently sized specimen (9 vol%-L, 95 vol%-L, and 97 vol%-L). This is due to Bragg reflection. The difference in color between 0 vol%-L and 100 vol%-L monoliths arises from the size dependence of the Bragg reflectivity. Different colors within one monolith can be attributed to the angle dependence of the Bragg law, based on different crystal planes exposed to the surface.

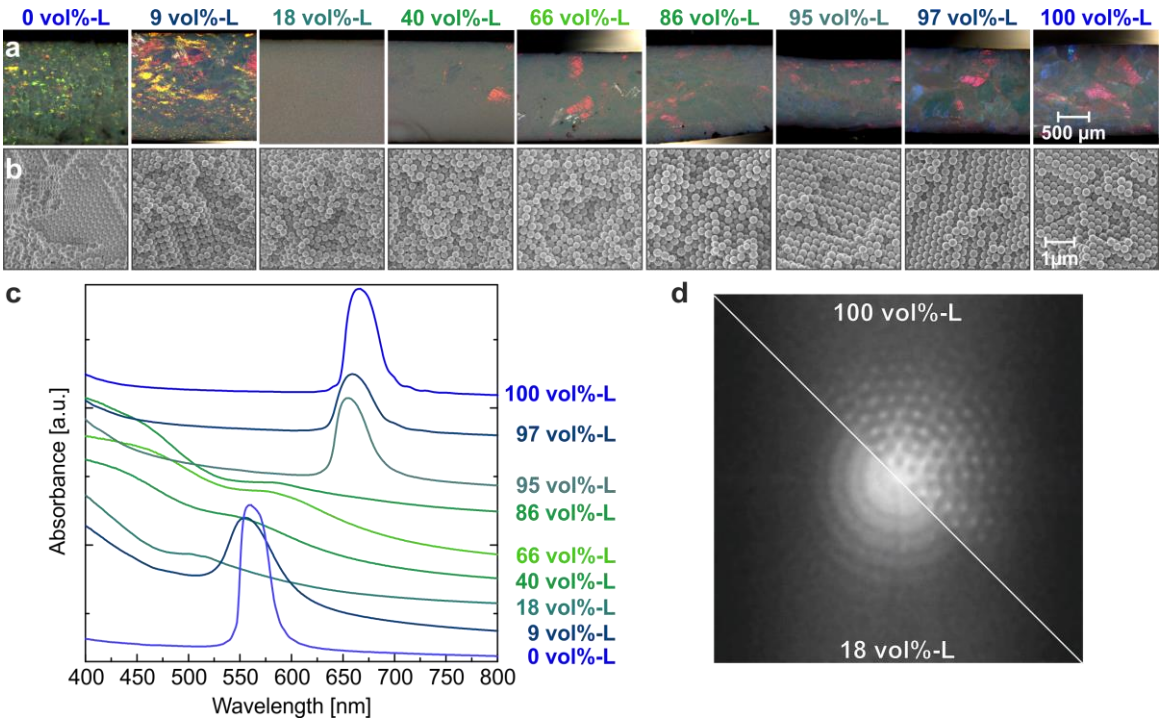

Figure 1. Structural characterization of binary colloidal assemblies. a) Optical and b) scanning electron microscopy side view images of the edges of split colloidal monoliths. c) UV-vis transmission spectra measured on dip-coated assemblies. d) Fast Fourier transformation (FFT) images from scanning electron micrographs with a mixing ratio of 18 vol%-L compared to a FFT image of 100 vol%-L colloidal crystal.

For other mixing ratios, only weak overall Bragg reflection (66 vol%-L and 86 vol%-L) or almost only diffuse scattering (18 vol%-L and 40 vol%-L) is visible. At these mixing ratios, the polydispersity of the binary particle dispersion prevents large area particle crystallization. Noteworthy, some embedded crystalline regions are observable for several intermediate mixing ratios (40 vol%-L, 66 vol%-L, and 86 vol%-L). This can be explained by the strong tendency of demixing in binary colloidal dispersions.[31-33] The slow self-assembly process (several days) of the dispersion enables the formation of phase separated, multicrystalline, and amorphous areas.

Scanning electron microscopy (SEM) images validate the optical impression (Figure 1b). The pure colloidal crystals feature a high degree of crystalline particle ordering. In contrast, for intermediate mixing ratios, only a random packing of the particles is observed. This is additionally highlighted by fast Fourier transformation (FFT) images of the SEM images illustrated in Figure 1d. Whereas

distinct reflexes are visible for 100 vol%-L due to the hexagonal symmetry of the particle lattice, only smeared Debye-Scherrer rings are obtained for 18 vol%-L monoliths. The smearing is based on the disordered mesostructure whereas the observed Debye-Scherrer rings arise from the different particle diameters present within the monoliths.

We further quantify the intrinsic order of the binary colloidal films by UV-vis transmission spectra of dip-coated samples, displayed in Figure 1c. A strong Bragg peak is visible for 0 vol%-L colloidal crystals at a wavelength of 559 nm. At small mixing ratios of 9 vol%-L, the Bragg peak broadens and the maxima is less allocable due to the disturbance of the crystal lattice. A further increase of the large particle volume fraction to 18 vol%-L leads to a vanishing of the Bragg peak. No distinct Bragg peaks are observable for intermediate mixing ratios from 44 vol%-L to 86 vol%-L, indicating a randomly packed structure. The Bragg peak of the larger particle species reoccurs at 95 vol%-L and reaches a maximum intensity for 100 vol%-L at a wavelength 667 nm.

Optical microscopy, SEM, and UV-vis characterization prove the highly crystalline nature of the homo-particle ensembles, which define the edges of the mixture phase diagram. The long-range order is quickly lost, when mixing two particles with a size ratio of 0.8. Depending on the assembly process a complete suppression of crystallinity can be found (dip-coating) or small, multicrystalline regions caused by demixing prevail (dispersion drying).

Laser flash analysis (LFA) was performed on colloidal monoliths obtained from evaporation-induced self-assembly. By determining the sample density and specific heat capacity, it is possible to calculate the specimen's effective thermal conductivity (details see supporting information). The thermal conductivity, normalized to the maximum initial value of the pure colloidal assemblies, as well as the normalized thermal conductivity of intermediate mixing ratios are show in Figure 2a. The color code helps to separate ordered samples (blueish) from

randomly packed assemblies (greenish) and correspond to the mixing ratios given in Figure 1.

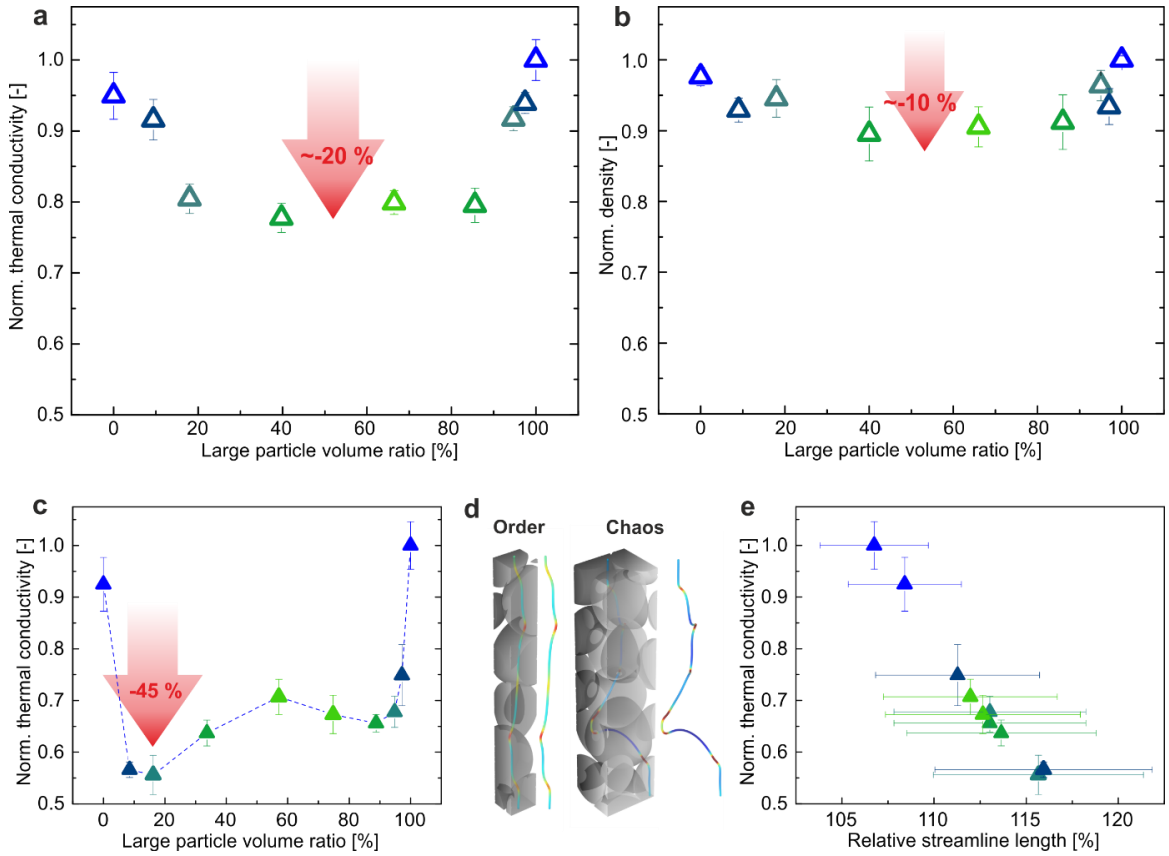

Figure 2. Thermal conductivity of the investigated assemblies with a size ratio of 0.8. Color code indicates ordered (blueish) and disordered assemblies. a) Normalized thermal conductivity of binary PS colloidal assemblies possessing different mixing ratios. The red arrow indicates the reduction of the thermal conductivity due to the introduced disorder. b) Normalized density of the colloidal assemblies. c) Thermal conductivity *vs.* volume fraction of large particles obtained by FEM. Error bars arise from three individual simulations boxes at three different directions in space. d) Exemplary streamlines present within a crystalline and a disordered assembly with a size ratio of 0.8 and 16 vol%-L. e) Thermal conductivity *vs.* relative streamline length of various size ratios. Error bars arise from three individual simulations boxes at three different directions in space.

Homo-particle colloidal assemblies (mixing ratio 0 vol%-L and 100 vol%-L) show a thermal conductivity of 73 $mWm^{-1}K^{-1}$ and 77 $mWm^{-1}K^{-1}$ in absolute numbers, respectively. At small mixing ratios of differently sized particles, the thermal conductivity slightly drops to ~ 93 % of the initial value. For intermediate mixing ratios, the thermal conductivity drops significantly to ~ 80 %. This reduction can only partially be explained by the reduced density of the intermediate assemblies as displayed in Figure 2b. The reduction of the density for intermediate mixing

ratios originates from the prevented close packing of the particles during assembly. This leads to a space filling which deviates from the maximum of 74 %. Still, the density only decreases to ~90 % of its initial value. Therefore, an additional effect is present, which is responsible for the overall reduction of the thermal conductivity to 80 %.

To elucidate this additional contribution, we performed finite element modeling (FEM) on binary particle mixtures possessing a size ratio of 0.8. The required virtual assemblies were obtained by molecular dynamic (MD) simulations of the assembly process. Exemplary particle assemblies obtained from MD simulations are shown in Figure S2a. We found highly crystalline particle assemblies at the edges of the mixing diagram. In contrast to our experimental findings, the crystallization process is already fully prevented at very small mixing ratios (Figure S2a, left). This is caused by the lack of demixing or phase separation of the particles due to the short assembly time-scale used for the MD simulation. FFT images of 0 vol%-L and 9 vol%-L assemblies from MD simulation are compared to the experiment in Figure S2a, right. Thus, the fully amorphous structure obtained from the MD simulation can be regarded as an ideally disordered case. Experimentally, some degree of crystallization will be difficult to exclude owing to the long timescale allowed for the self-assembly process. FEM has been conducted using the software COMSOL Multiphysics®. Details on the modeling are described in the Supporting Information. The calculated thermal conductivity against the volume fraction of large particles is displayed in Figure 2c. Analogous to Figure 2a, the color code indicates ordered (bluish) and disordered assemblies (green). The mixing diagram shows a similar trend for the thermal conductivity as observed for the experiment, with high thermal conductivities for ordered, and a reduced thermal conductivity for disorder assemblies. A minimum thermal conductivity of only 55 % of the initial value is observed at a volume fraction of ~16 vol%-L. This is an almost two-fold enhancement of the insulation capability

caused by the disordered structure, and it is significantly lower compared to the experimental results. We ascribe this deviation to the structural difference between the MD simulation and the experiment. As outlined before, by MD simulation one can observe a more disordered distribution of both particle types within the monolith, leading to a stronger reduction of the thermal conductivity.

To explain the origin of the thermal conductivity reduction beyond the decrease in density, we utilized FEM to analyze the length of the thermal transport pathway through such a particulate assembly structure. This can be done by evaluating the length of heat flux streamlines, which reach from the hot to the cold side of the simulation box. Figure 2d shows two individual cases through an ordered (100 vol%-L) and disordered (~16 vol%-L) particle ensemble. Whereas in the ordered case, a rather straight and unperturbed streamline is obtained, the introduction of disorder strongly bents and perturbes the thermal transport path. The statistic evaluation over the entire simulation box is given in Figure 2e, where we normalized the streamline length on the length of the simulation box. One finds a direct correlation between the streamline length and the thermal conductivity reduction. This finding can be intuitively explained by a sort of effective thermal length, which differs from the plain geometric size of the box. One may draw an analogy to the concept of the diffusive optical path in a particulate powder, which is governed by the scattering cross section of the constituting sphere.[34]

Most interestingly, the FEM simulation finds a strongly asymmetric shape of the thermal conductivity reduction with two minima at moderately high and low mixing ratios, respectively. These are not found in the experiment, presumably due to the presence of mesocrystalline domains, embedded in the amorphous structure. We now want to understand the origin of these minima and how the thermal conductivity could be reduced even further. This question could be rephrased to how the thermal streamline length can be further increased in such colloidal superstructures. We, therefore, return to MD simulation and evaluate the

local structure around one particle more explicitly. We did this in a twofold way: 1) Using the radial distribution function we evaluate the number of particles surrounding a center particle, which are within the local space of about 10 % of the respective particle diameter. 2) Using the individual coordinates of each particle pair, we extracted the number of touching spheres around a central particle. We term the first one "next neighbors", and the second one "contact neighbors". Quite expectedly, when introducing disorder the average number of next and contact neighbors is reduced. For crystalline assemblies, one can find an average number of next neighbors per particles of ~12, based on the face centered-cubic symmetry. For all disordered intermediate mixing ratios, the number of next neighbors is reduced to ~10 (Figure S2b). The next contact neighbor analysis yields ~8 owing to the more rigorous exclusion criterion. One can imagine that this reduction leads to less pathways for heat to travel through the particle structures and therefore reduces the thermal conductivity of the assemblies. However, we find that the mean number of next neighbor particles merely reaches a broad plateau, and does not explain the asymmetric shape shown in Figure 2c. We, therefore, evaluated the next neighbor particle histograms explicitly. This is shown in Figure 3, where we present the next neighbor histograms at selected mixing ratios (bottom row). We chose a special illustration, to highlight the structural heterogeneity, when heat travels through such a system. We, therefore, present a projection of all particles with the same number of next neighbors that can be found within the simulated box. The color code indicates particles possessing the same number of next neighbors from high (blue) to low (red). It therefore provides a direct impression of how many particles are clustered around one central sphere.

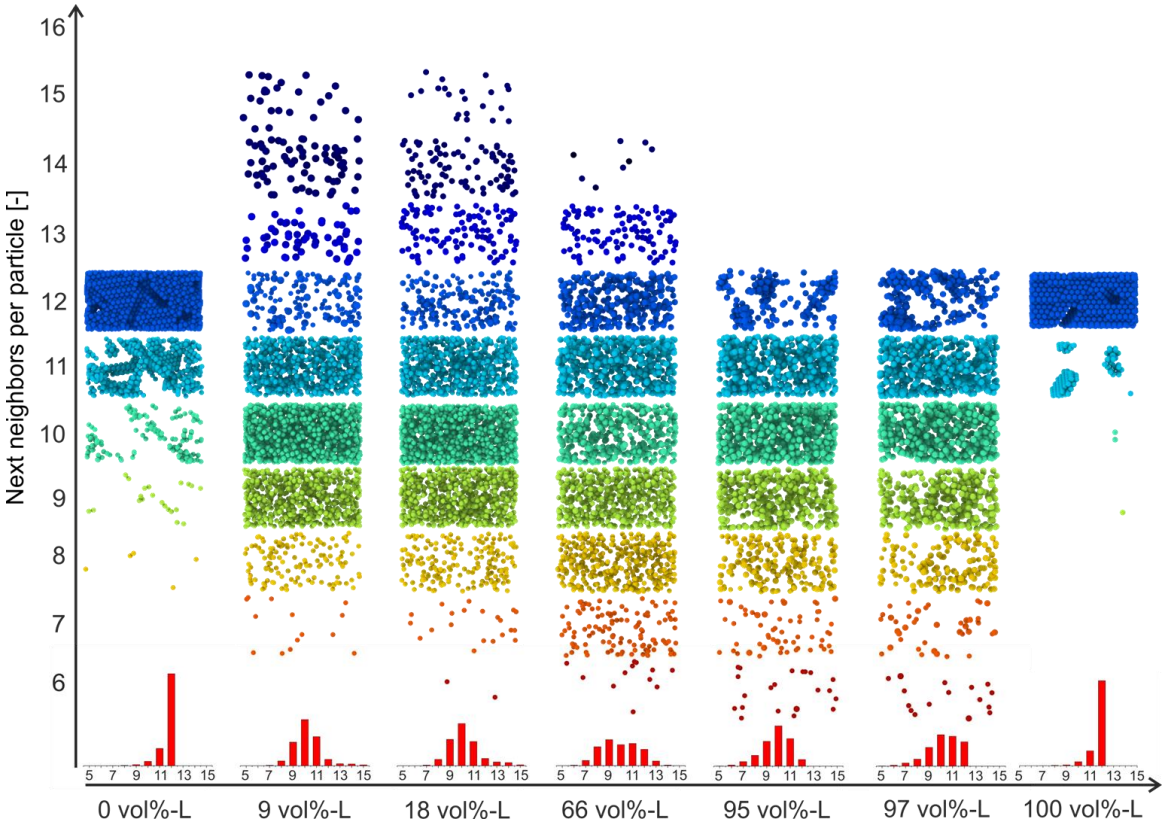

Figure 3. Molecular dynamics simulations of the assembly process of a binary particle mixture. Number of next neighbors per particle against volume fraction of large particles. Size ratio is 0.8. Projection of the assemblies visualize the particles possessing the indicated number of neighbors. Histograms show the relative frequency of particle neighbors per particle present within the different assemblies.

For mixing ratios of 0 vol%-L and 100 vol%-L almost every particle possesses twelve next neighbors. This indicates a nearly fully crystalline face-centered cubic assembly, with few line and point defects being visible. The particle neighbor distribution function quickly broadens at intermediate mixing ratios. Most importantly, this distribution function shows a strongly asymmetric behavior. For mixing ratios of 9 vol%-L to 66 vol%-L, even more than twelve next neighbors per particles are present within the assembly, whereas for high mixing ratios, the number of next neighbors is limited to twelve. For a low number of large particles (small mixing ratios), it is possible that one large particle is decorated by a high number of smaller particles. In contrary, for high mixing ratios of large particles, it is geometrically not possible to decorate a small particle with a high number of large particles, since there is simply not sufficient space. This asymmetry is less

pronounced when considering the contact neighbors (Figure S5). The average contact number stays constant with a tendency towards fewer contact points at the minimum volume fraction ~20 vol%-L. This discrepancy between a constant or reduced number of *contact* neighbor particles compared to the evolution of many *next* neighbor particles hints towards the importance of a jammed particle corona in close vicinity to the central bead.

We also conducted a thorough analysis of the interparticle constriction effect in the Supporting Information (Figure S6-8). We, therefore, analyzed the average interparticle contact area and relate this to the contact neighbor distribution. Using an ideal face-centered cubic reference system we show that a reduction of the interparticle contact area leads to an increase in thermal path length caused by a stronger bending of the heat flux stream lines (Figure S6b). However, the changes of the interparticle contact area play a secondary role compared to the introduction of disorder and consequently to the thermal path length.

The consequence of the asymmetric next neighbor distribution for the effective thermal length is rather surprising. A reduction of the number of next neighbor particles indeed leads to a reduction in thermal conductivity. However, even more efficient is the introduction of a certain amount of many jammed and not necessarily directly contacting particles, since this leads to an even stronger disturbance of the streamline length due to a geometric extension of the predetermined thermal transport path. This is accompanied by a minimum of the total number of interparticle contact points within the simulation volume (Figure S5).

To clarify how this transport pathway is governed by the size mismatch of the two particles, we varied the size ratio of the particles between 0.9 and 0.54 at the mixing ratio around 20 vol%-L, which showed the lowest thermal conductivity. Noteworthy for this data set, the experimental samples were prepared by filtration to speed up the assembly time and therefore obtain particle structures, which are

more comparable to the MD assemblies. Both, experiment and FEM simulation, show a systematic decrease of the thermal conductivity with a decreasing size ratio from 0.9 to 0.54 (Figure 4d). The increase of the thermal conductivity for the smallest size ratio (0.54) for the experiment can be explained by an increasing tendency to demix as outlined above. One also needs to take into account that fully crystalline binary assemblies can be obtained for size ratios of <0.41 owing to the octahedral voids in face-centered cubic structures, which we approach with this small size ratio.[35]

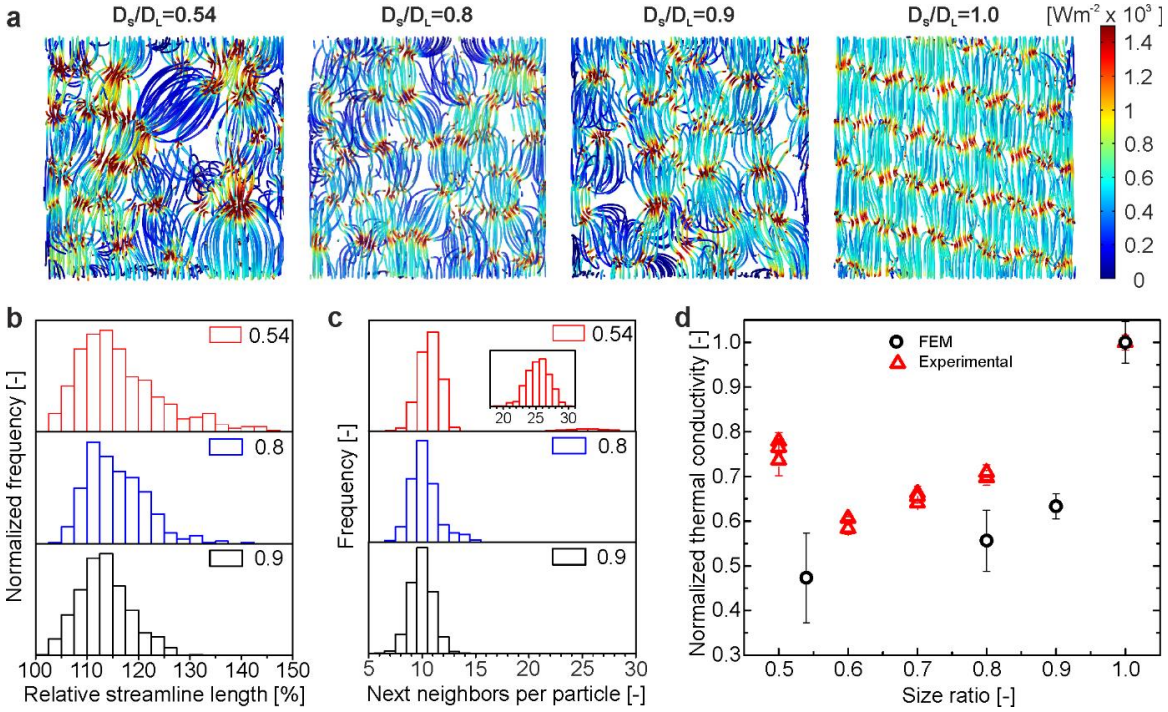

Figure 4. Influence of the size ratio (D_S/D_L) on the thermal conductivity at ~20 vol%-L. a) Comparison of the heat flux densities of particles assemblies possessing different size ratios. b) Histograms of the streamline length and c) next neighbors per particle of the assemblies. d) Resulting thermal conductivity from FEM compared to experimental data.

Figure 4a compares the heat flux density of the particle assemblies from size ratios of 0.54, 0.8, and, 0.9 to the heat flux density of a fully crystalline assembly (size ratio: 1.0). Crystalline assemblies feature uniform and straight streamlines (Figure 4a, 1.0), whereas a decreasing size ratio evokes a high degree of distortion. This is especially obvious for the heat flux density of the size ratio 0.54, where one large particle heavily impedes the heat flux through the entire particle box. The

qualitative impression from the heat flux density images is verified by comparing the relative streamline lengths of the different size ratios (Figure 4b). The smaller the size ratio, the higher the number of long streamlines, which can reach up to 140 % relative to the length of the simulation box. This indicates that the less the particle sizes match, the stronger the heat flux is bent along the particle network, leading to an elongation of the thermal transport path.

The higher fraction of long streamlines coincides with a broadening of the next neighbor distribution function with decreasing size ratio (Figure 4c). The broadening increases the number of >10 next neighbors, indicating an increasing decoration of a large particle with small particles. However, due to the small number of large particles at this volume fraction and size ratio combination (about 4 % number ratio of large particles) this effect is not visible in the average number of neighbors for the whole assembly. Only when looking at the detailed next neighbor histograms the results from the heat flux simulations can be understood (Figure 4c). For a size ratio of 0.54 a second fraction with even 25-30 next neighbors is found. Looking at the contact neighbor distribution for this sample, the number of touching spheres remains rather constant at about 8 (Figure S5). This highlights the evolution of a densely-jammed corona, where a small amount of large particle clusters are decorated with smaller spheres. This constitutes an efficient way to increase the thermal path length. Overall, the higher mismatch between the two particle sizes led to a thermal conductivity reduction by 40 % (size ratio 0.6) in the experiment and 53 % (size ratio 0.54) in the FEM simulation. We finally also checked, whether 19 vol%-L represents the absolute minimum with respect to the mixing ratio. We, indeed, find the highest fraction of >25 next neighbor particles for this mixing ratio (Figure S4). Higher or lower mixing ratios (± 5 vol%-L) lead rapidly to a reduced number of next neighbors. Therefore, a mixing ratio of 19 vol%-L of large particles is sufficient to strongly reduce the effective thermal transport across a binary particle mixture.

We finally compare this disorder derived thermal insulation effect to the thermal conductivity of known polymer materials. The unique properties of colloidal crystals and especially colloidal glasses can be inferred from the Ashby plot in Figure 5 in a straight-forward manner.[36] It shows a direct relation between the thermal conductivity and the polymer density. Using polymer foams, highly insulating materials are accessible, however, at the expense of the materials density. Transitioning from colloidal crystals to colloidal glasses, retains the materials density to a large extent, while the thermal conductivity decreases. This opens the avenue to design highly insulating granular materials at a retained high density.

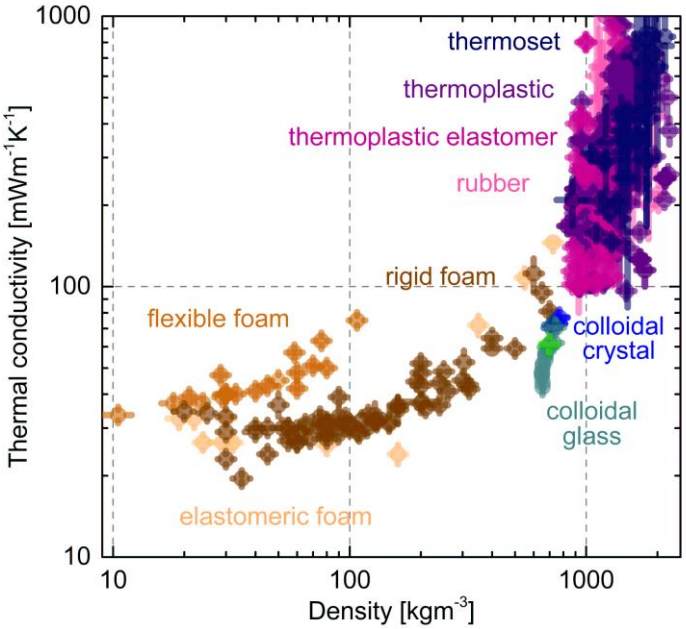

Figure 5. Ashby plot of density *vs.* thermal conductivity of bulk and foam polymer materials. The introduction of disorder to colloidal ensemble reduces the thermal conductivity (measured in vacuum) while retaining a comparatively high density.

3. Conclusion

In summary, we investigated the influence of order and disorder in particle mixtures on their thermal transport properties. We therefore choose a controlled mixture of binary latex particles as a model system. In a combined approach, which comprised experimental characterization, MD simulation as well as FEM, we were

able to relate the observed reduction in thermal conductivity to the local environment of the colloidal particles. Quite surprisingly, the increase of next neighbor contact points at low mixing ratios and at a high size mismatch between the binary spheres, represents the most efficient way to attain a minimum thermal conductivity. This is achieved at a comparatively high density. The decisive concept is the increase in the effective thermal length, across which the thermal energy needs to be transported. Overall, disorder in a binary colloidal glass can reduce the thermal conductivity by as much as ~50 % compared to its single phase, crystalline counterpart. Our findings are of high importance for heterostructured and particulate materials, for applications were a high insulation, but also a good heat dissipation are paramount. Owing to the diffusive thermal transport in our system, our findings are of conceptual nature and applicable to many other nano-, micro- and macrostructured materials, beyond simple latex beads. Most importantly, we want to stress the relevance of the concept of an effective thermal length, which cannot only be increased by constriction but may be even more strongly affected by additional pathways and detours.

4. Experimental Section

Details on the particle synthesis, binary colloidal self-assembly methods, and characterization methods, as wells as a detailed description on thermal transport characterization by laser flash analysis, molecular dynamics simulations, finite element modeling, complementary contact particle analysis and a discussion on the influence of the particle contact area can be found in the Supporting Information.

Supporting Information

Supporting Information is available from the Wiley Online Library or from the author.

Acknowledgements

F.A.N. and A.P. contributed equally to this work. The authors thank Ute Kuhn for help with DSC measurements. Tobias Lauster, Julian Sindram, and Dominik Skrybeck are acknowledged for performing firsts UV-Vis and LFA experiments. B.A.F.K. acknowledges support from the Elite Network of Bavaria (ENB). Additional support was provided by the SFB840 and the Bavarian Polymer Institute, BPI. This work was funded by the Volkswagen foundation through a Lichtenberg professorship.

Conflict of Interest

The authors declare no conflict of interest.

Keywords

colloidal glass, next neighbor correlation, photonic crystal, powder sintering, thermal transport

References

1. Poudel, B.; Hao, Q.; Ma Y.; Lan, Y.; Minnich, A.; Yu, B.; Yan, X.; Wang, D.; Muto, A.; Vashaee, D.; Chen, X.; Liu, J.; Dresselhaus, M. S.; Chen, G.; Ren, Z., High-thermoelectric performance of nanostructured bismuth antimomy telluride bulk alloys. *Science* **2008**, *320* (5876), 634-638.

2. Cahill, D. G.; Braun, P. V.; Chen, G.; Clarke, D. R.; Fan, S. H.; Goodson, K. E.; Keblinski, P.; King, W. P.; Mahan, G. D.; Majumdar, A.; Maris, H. J.; Phillpot, S. R.; Pop, E.; Shi, L., Nanoscale thermal transport. II. 2003 – 2012. *Applied Physics Reviews* **2014**, *1* (1), 011305.

3. Cahill, D. G.; Ford, W. K.; Goodson, K. E.; Mahan, G. D.; Majumdar, A.; Maris, H. J.; Merlin, R.; Phillpot, S. R., Nanoscale thermal transport. *Journal of Applied Physics* **2003**, *93* (2), 793-818.

4. Cahill, D. G.; Pohl, R. O., Lattice vibrations and heat transport in crystals and glasses. *Annual Review of Physical Chemistry* **1988**, 39 (1), 93-121.

5. Maldovan, M., Sound and heat revolutions in phononics. *Nature* **2013**, 503 (7475), 209-217.

6. Einstein, A., Elementare Betrachtungen über die thermische Molekularbewegung in festen Koerpern. *Annalen der Physik (Berlin)* **1911**, *35* (9), 679-694.

7. Cahill, D. G.; Watson, S. K.; Pohl, R. O., Lower limit to the thermal conductivity of disordered crystals. *Physical Review B* **1992**, 46 (10), 6131-6140.

8. Allen, P. B.; Feldman, J. L., Thermal conductivity of disordered harmonic solids. *Physical Review B* **1993**, *48* (17), 12581-12588.

9. Allen, P. B.; Feldman, J. L.; Fabian, J.; Wooten, F., Diffusons, locons and propagons: Character of atomic vibrations in amorphous Si. *Philosphical Magazine B* **1999**, *79* (11-12), 715-1731.

10. Chiritescu, C.; Cahill, D. G.; Nguyen, N.; Johnson, D.; Bodapati, A.; Keblinski, P.; Zschack, P., Ultralow thermal conductivity in disordered, layered WSe2 crystals. *Science* **2007**, *315* (5810), 351-353.

11. Losego, M. D.; Blitz, I. P.; Vaia, R. A.; Cahill, D. G.; Braun, P. V., Ultralow thermal conductivity in organoclay nanolaminates synthesized via simple self-assembly. *Nano Letters* **2013**, *13* (5), 2215-2219.

12. Moon, J.; Minnich, A. J., Sub-amorphous thermal conductivity in amorphous heterogeneous nanocomposites. *RSC Advances* **2016**, *6* (107), 105154-105160.

13. Mizuno, H.; Mossa, S.; Barrat, J. L., Beating the amorphous limit in thermal conductivity by superlattices design. *Scientific Reports* **2015**, *5*, 14116-14116.

14. Zhang, H.; Minnich, A. J., The best nanoparticle size distribution for minimum thermal conductivity. *Scientific Reports* **2015**, *5*, 8995.

15. Kim, W.; Zide, J.; Gossard, A.; Klenov, D.; Stemmer, S.; Shakouri, A.; Majumdar, A., Thermal conductivity reduction and thermoelectric figure of merit increase by embedding nanoparticles in crystalline semiconductors. *Physical Review Letters* **2006**, *96* (4), 045901.

16. Notario, B.; Pinto, J.; Solorzano, E.; de Saja, J. A.; Dumon, M.; Rodríguez-Pérez, M. A., Experimental validation of the Knudsen effect in nanocellular polymeric foams. *Polymer* **2015**, *56*, 57-67.

17. Koebel, M.; Rigacci, A.; Achard, P., Aerogel-based thermal superinsulation: An overview. *Journal of Sol-Gel Science and Technology* **2012**, *63* (3), 315-339.

18. Lu, X.; Arduini-Schuster, M. C.; Kuhn, J.; Nilsson, O.; Fricke, J.; Pekala, R. W., Thermal conductivity of monolithic organic aerogels. *Science* **1992**, *255* (5047), 971-972.

19. Schiffres, S. N.; Kim, K. H.; Hu, L.; McGaughey, A. J. H.; Islam, M. F.; Malen, J. A., Gas diffusion, energy transport, and thermal accommodation in single-walled carbon nanotube aerogels. *Advanced Functional Materials* **2012**, *22* (24), 5251-5258.

20. Chen, Z.; Hsu, P. C.; Lopez, J.; Li, Y. Z.; To, J. W. F.; Liu, N.; Wang, C.; Andrews, S. C.; Liu, J.; Cui, Y.; Bao, Z. N., Fast and reversible thermoresponsive polymer switching materials for safer batteries. *Nature Energy* **2016**, *1* (1), 15009.

21. Sangrós, C.; Schilde, C.; Kwade, A, Effect of microstructure on thermal conduction within lithium-ion battery electrodes using discrete element method simulations. *Energy Technology* **2016**, *4* (12), 1611-1619.

22. Masarapu, C.; Zeng, H. F.; Hung, K. H.; Wei, B., Effect of temperature on the capacitance of carbon nanotube supercapacitors. *ACS Nano* **2009**, *3* (8), 2199-2206.

23. Ruckdeschel, P.; Philipp, A.; Retsch, M., Understanding thermal insulation in porous, particulate materials. *Advanced Functional Materials* **2017**, *27*, 1702256.

24. Nutz, F. A.; Retsch, M., Interfacial and volumetric sensitivity of the dry sintering process of polymer colloidal crystals: a thermal transport and photonic bandgap study. *Physical Chemistry Chemical Physics* **2017**, *19* (24), 16124-16130.

25. Nutz, F. A.; Ruckdeschel, P.; Retsch, M., Polystyrene colloidal crystals: Interface controlled thermal conductivity in an open-porous mesoparticle superstructure. *Journal of Colloid and Interface Science* **2015**, *457*, 96-101.

26. Ruckdeschel, P.; Kemnitzer, T. W., Nutz, F. A.; Senker, J.; Retsch, M., Hollow silica sphere colloidal crystals: insights into calcination dependent thermal transport. *Nanoscale* **2015**, *7* (22), 10059-10070.

27. Still, T.; Cheng, W.; Retsch, M.; Sainidou, R.; Wang, J.; Jonas, U.; Stefanou, N.; Fytas, G., Simultaneous occurrence of structure-directed and particle-resonance-induced phononic gaps in colloidal films. *Physical Review Letters* **2008**, *100* (19), 194301.

28. Goodwin, J. W.; Hearn, J.; Ho, C. C.; Ottewill, R. H., Studies on the preparation and characterisation of monodisperse polystyrene lattices. *Colloid and Polymer Science* **1974**, *252* (6), 464-471.

29. Ottewill, R. H.; Shaw, J. N., Studies on the preparation and characterization of monodisperse polystyrene latices. *Kolloid-Zeitschrift und Zeitschrift für Polymere.* **1967**, *215* (2), 161-166.

30. Vogel, N.; Retsch, M.; Fustin, C. A.; Del Campo, A.; Jonas, U., Advances in colloidal assembly: the design of structure and hierarchy in two and three dimensions. *Chemical Reviews* **2015**, *115* (13), 6265-6311.

31. Pusey, P. N.; van Megen, W., Phase behaviour of concentrated suspensions of nearly hard colloidal spheres. *Nature* **1986**, *320*, 340-342.

32. Dijkstra, M.; van Roij, R.; Evans, R., Phase behavior and structure of binary hard-sphere mixtures. *Physical Review Letters* **1998**, *81* (11), 2268-2271.

33. Kumar, A. V. A., Binary colloidal mixtures in a potential barrier: demixing due to depletion. *Journal of Chemical Physics* **2013**, *138*, 154903.

34. Retsch, M.; Schmelzeisen, M.; Butt, H.-J.; Thomas, E. L., Visible mie scattering in nonabsorbing hollow sphere powders. *Nano Letters* **2011**, *11* (3), 1389-1394.

35. Wang, J.; Ahl, S.; Li, Q.; Kreiter, M.; Neumann, T.; Burkert, K.; Knoll, W.; Jonas, U., Structural and optical characterization of 3D binary colloidal crystal and inverse opal films prepared by direct co-deposition. *Journal of Materials Chemistry* **2008**, *18* (9), 981.

36. Granta design, CES edupack, Cambridge, UK **2015**

Supporting Information

Experimental Section

Materials:

Potassium persulfate (KPS, ≥ 99 %, Aldrich), styrene (≥ 99 %, Aldrich) and acrylic acid (99 %, AA, Aldrich) were used as received. Water was taken from a Millipore Direct Q3UV unit for the entire synthesis and purification steps.

Particle Synthesis: In a typical synthesis, a 500 mL three-neck flask was charged with 245 mL milliQ water and 30 mL of styrene. The mixture was heat to 75 °C at a stirring speed of 650 rpm and allowed to equilibrate under a slight argon flow for ~15 min. Subsequently, 3 mL of acrylic acid were added, and the mixture was allowed to further equilibrate for ~10 min. To initiate the polymerization, 100 mg KPS, dissolved in 5 mL milliQ water were rapidly added to the mixture. The polymerization was carried out overnight under a slight argon flow. To adjust the size of the particles the amount of acrylic acid has been varied.[1-2] The reaction was stop by exposing the mixture to ambient atmosphere. The particles were purified by dialysis against milliQ water for five days, changing water twice a day.

Binary Colloidal Self-Assembly: Binary colloidal assemblies were fabricated by evaporation-induced self-assembly of a given amount of prior mixed binary particle dispersions in a PTFE beaker. The obtained monoliths generally possess a diameter of ~20 mm and a thickness of several hundred micrometers.

Dip-Coating: Samples for UV-vis measurements were prepared on glass slides by dip-coating 3 wt% of binary particle solutions. The glass slides were purified with Hellmanex solution an ethanol prior to use. Furthermore, the dip-coating process the glass slides were treated with oxygen plasma to ensure a constant wetting of the particle solutions.

Methods:

Dynamic Light Scattering: Dynamic light scattering measurements were performed on aqueous particle dispersion at a Malvern Zetasizer with 175° backscattering geometry to determine the hydrodynamic diameter of the particles and their size distribution.

Light Microscopy: Bright field light microscopy side view images of the edges of split of the colloidal assemblies were recorded on a Carl Zeiss Axio Imager.A2m light microscope equipped with an AxioCam Icc 1 camera to get a qualitative impression about the long range ordering of the colloidal particles.

Scanning Electron Microscopy: To determine the hard sphere diameter of the particles, scanning electron microscopy (SEM) was performed on a Zeiss Leo 1530 electron microscope. Therefore, dilute particle dispersions were drop-casted on a silicon wafer and sputtered with 1.3 nm platinum. Furthermore, SEM side-view images of the edges of split of the colloidal monoliths were obtained to gain an impression of the order within the interior of the monoliths. Fast Fourier transformation was applied on the recorded images using the FFT function, implemented in the software ImageJ 146.r.

Differential Scanning Calorimetry: Heat capacity determination was carried out according to ASTM E1269 on a TA Instruments Q1000 differential scanning calorimeter under a nitrogen flow of 50 $mLmin^{-1}$ at a heating rate of 20 $Kmin^{-1}$. Two heating cycles were conducted between -40 °C and 200 °C. The specific heat capacity was evaluated from the second heating cycle. The mean value from all polystyrene particles under investigation has been used for evaluation (Figure S1).

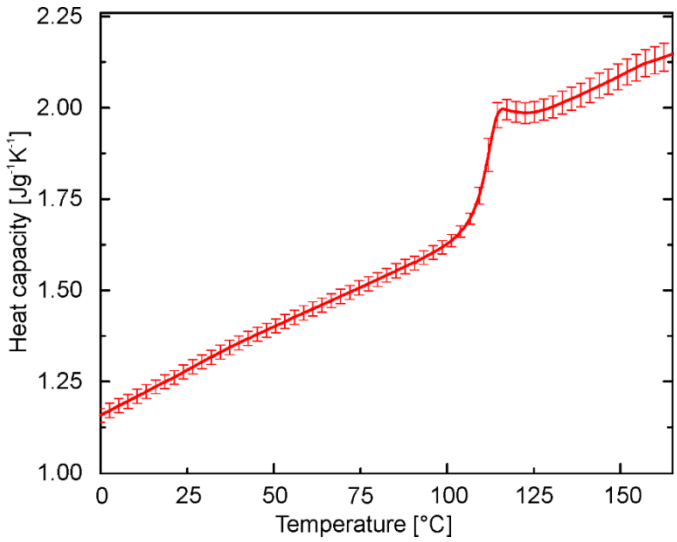

Figure S1. Mean specific heat capacity of the various polystyrene binary assemblies. Error bars represent the standard deviation of the mean value of the specific heat of every mixing ratio.

Density Determination: The density of the colloidal assemblies was determined by the volume and mass of the samples. The volume was obtained from a Keyence V3100 3D digital macroscope.

Laser Flash Analysis: Laser flash analysis was performed on a Linseis XFA 500 XenonFlash apparatus equipped with an InSb infrared detector to obtain the thermal diffusivity of the colloidal assemblies. The thickness of the samples were determined on a Mitotoyo Litematic VL-50. Prior to the measurement, the bottom and top side of the samples were coated with a thin layer of black air-brush color serving as a blocking layer. Furthermore, the samples were coated with a thin graphite layer (< 15 µm). This enables a good absorbance at the bottom, and high emissivity at the top side of the monoliths. Measurements were performed on at least three individual samples. The standard deviation derives from the average of these individual measurements. Experiments were conducted in vacuum atmosphere at a pressure of ~$5 \cdot 10^{-2}$ mbar to exclude any influence of the ambient atmosphere. The raw data was fitted with the radiation fit model provided by the software Aprosoft Laser Flash Evaluation v.1.06. Measurements were performed on at least three samples.

A xenon lamp emits a light pulse onto the sample. The thermal energy of the light pulse is absorbed at the bottom graphite layer and travels through the specimen. The thermal energy is then emitted from the top side. This temperature rise is recorded in dependence of the elapsed time since the light pulse by a fast mid-infrared detector. A numerical fitting procedure provided by the commercial software package Aprosoft Laser Flash Evaluation v1.06 based on the one-dimensional temperature diffusion equation was used to determine the thermal diffusivity α.[3] For this, accurate knowledge of the sample thickness is a prerequisite, as the thickness strongly influences half-rise time as given by:

$$\alpha(T) = \frac{1.38 \cdot d^2}{\pi^2 t_{\frac{1}{2}}} \quad \text{(S1)}$$

$t_{1/2}$ represents the time needed for the half maximum temperature rise at the top surface.[4] The thermal conductivity κ of the sample is calculated by

$$\kappa(T) = \alpha(T) \cdot c_p(T) \cdot \rho(T) \quad \text{(S2)}$$

with the specific heat capacity c_p and the density ρ.

Molecular Dynamics (MD) Simulations: All dense colloidal assemblies used in the finite element modeling were obtained using LAMMPS.[5] Visualization was done with Ovito.[6] Every simulation consisted of 10000 arbitrarily placed spheres of the desired size and number ratio. The simulation box had periodic boundaries and was elongated in the z-direction at the start. This was done to mimic the evaporation of solvent for the real-world system. Using the NPT barostat we compressed the box first along the z-axis up to a pressure where all axes had a comparable length. After that the box was compressed isometrically to a pressure at which no more compression without overlap of the spheres was possible. We used the colloidal Yukawa potential included in the LAMMPS code with a short range repulsive part. Each simulation was run for 60 million steps with a stepsize 0.0001.

We chose the colloidal Yukawa potential in LAMMPS[7] because it treats the spheres as impenetrable bodies with a fixed radius which prevents unwanted overlap even at very high pressures. The Yukawa potential was necessary in order to facilitate the formation of the *fcc* phases at the edges of the phase diagram and the real particles also carry a negative net charge. The pairwise interaction is calculated using the formula:

$$E = \frac{A}{\kappa} e^{-\kappa\left(r-(r_i+r_j)\right)}; \quad r < r_c \tag{S3}$$

With κ being the screening length (inverse distance units), r_i and r_j are the radii of the two interacting spheres. The prefactor A has to be specified for each pair type. It is determined from the relationship of the surface charge to surface potential in the presence of an electrolyte. In our case this prefactor is proportional only to the radius of each particle. All other parameters are the same.

We chose a large screening length of 50 which corresponds to 1/50 of the diameter of the large particles in order to hinder crystallization at higher interparticle distances and ensure good mixing of the differently sized particles. As the particles in the experiments are a few hundred nanometers in size this large screening length also approximates the charge interaction distance relative to the particle size. An example of the interaction parameters is given in Table S1.

Table S1. MD simulation interaction parameters for the size ratio 0.54.

Pair style	Screening length	Interaction cutoff (r_c)	A for 1:1	A for 1:2	A for 2:2
Yukawa/colloid	50	1.5	10000	7500	5000

The analysis of the resulting dense colloidal assemblies was done with a self-written software using C++. The software calculates the radial distribution function (*G(r)*) for the given set of coordinates and uses the first three peaks to determine the three possible next neighbor distances as well as the next neighbor distance cut off. This cut-off was set to 10 % of the particle diameter. In the MD-simulation the type of particle (small or big) is set and the software choses according to this type

the appropriate condition to test whether a particle constitutes a next neighbor or not. This enabled us to obtain very detailed information on the local structure around each particle. This procedure also counts particles as next neighbors that are not touching, which is why introduced the additional term "contact neighbors" to distinguish these two sets of neighbors. It also calculates the density as well as the average number of neighbors.

We used a self-written Python script to evaluate the contact area between particles. The script evaluates the number of contacting particles based on the coordinates of the individual spheres. We defined the contact area as the circle created by the intersection of two spherical particles. The area was normalized to the number averaged particle surface of all particles.

We increased the size of the original spheres from the MD simulation by a factor of 1.04 in order to make the spheres touch (interpenetrating spheres cannot be simulated by MD). The same scaling factor was used for finite element modeling, and was selected such to give comparable interparticle contact areas to our experimental findings. From this we deduced the contact neighbor histogram. The individual contact areas were further correlated to number of contact neighbors.

Finite Element Modeling: We used the finite element method (FEM) software COMSOL Multiphysics® to simulate the heat transport through colloidal assemblies. For this, the crystalline (0 and 100 % large particles) and amorphous particle structures (size ratios: 0.54, 0.8, and 0.9) obtained from the MD simulations were used. The particle sizes were adjusted such that the contact areas between adjacent spheres are comparable to the experimental values. All particles were fused into one object and, thus no thermal resistance between the particles was considered. Due to the limited physical memory (128 GB), the system size has been reduced to a feasible size. Therefore, three cubes with around 100 particles were cut out of each invested colloidal assemblies. The mesh size was as chosen to

ensure mesh size independent results (see Figure 9c). A temperature difference was imposed to two opposite surfaces of the cubes. Since all remaining surfaces were kept thermally insulating, purely one-dimensional thermal transport is obtained. The simulation was conducted along all three directions of the cube (x, y, and z). Using Fourier's law (see Equation S4), the effective thermal conductivity of the assembly is calculated from the computed heat flux, normal to the isothermal faces. Figure S10 demonstrates that three cubes are sufficient to calculate a meaningful average value. Furthermore, heat flux streamlines have been plotted to visualize the heat path length through the different colloidal assemblies. The length of the streamlines (L_{SL}) has been normalized by the total length of the cube (L_C) to calculate the relative streamline length (L_{SL}/L_C in %). Figure S10 demonstrates that three cubes are sufficient to calculate a meaningful average value. Furthermore, heat flux streamlines have been plotted to visualize the heat path length through the different colloidal assemblies. The length of the streamlines (L_{SL}) has been normalized by the total length of the cube (L_C) to calculate the relative streamline length (L_{SL}/L_C in %).

Comparison between MD Simulation and Experimental Colloidal Glass Fabrication

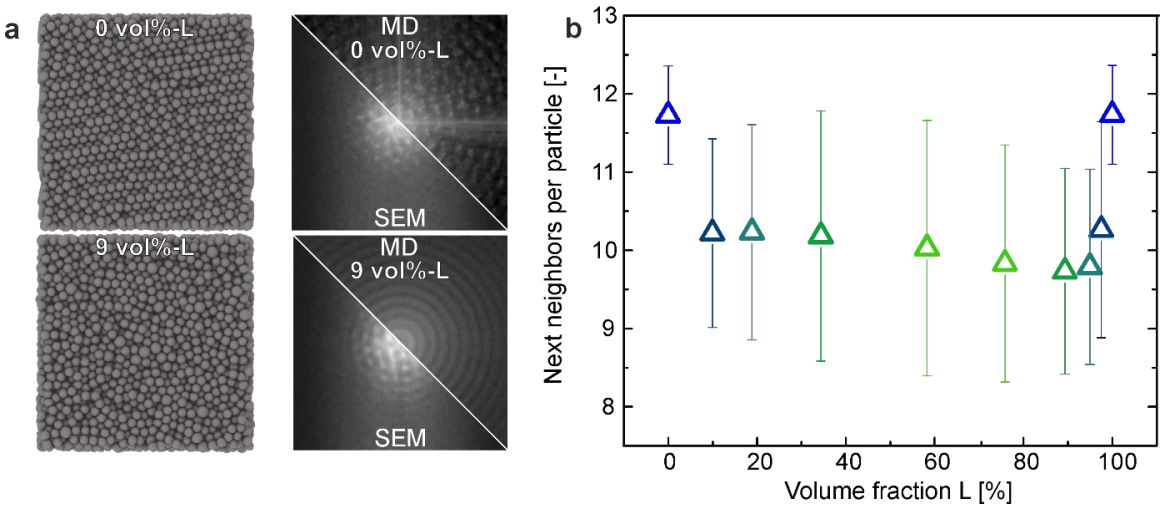

Figure S2. Side views received from MD simulations and number of next neighbors per particles. (a, left) typically obtained particle assemblies from MD studies; (a, right) FFT comparison between experiment and simulation. b) Average next neighbors per particle *vs.* volume fraction of large particles. Color code indicates ordered (blueish) and disordered (greenish) assemblies.

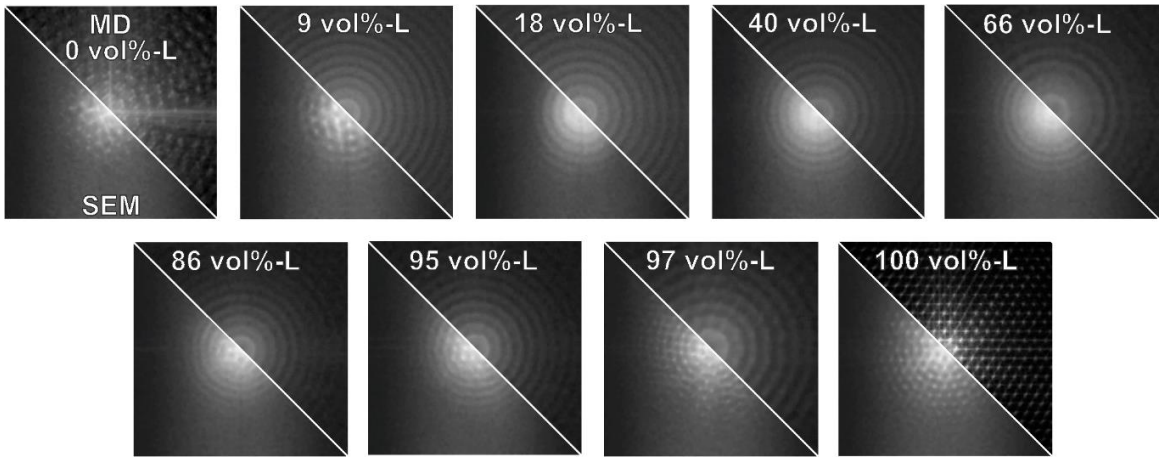

Figure S3. FFT comparison between the particle structures received from MD simulations and SEM side view images. Particularly at low and high mixing ratios a partial crystallinity can be inferred from the experimental SEM images. It indicates an easier colloidal glass formation in the MD simulation compared to the experimental conditions.

Influence of Mixing Ratio on Next Neighbor Distribution Function of a Size Ratio of 0.54

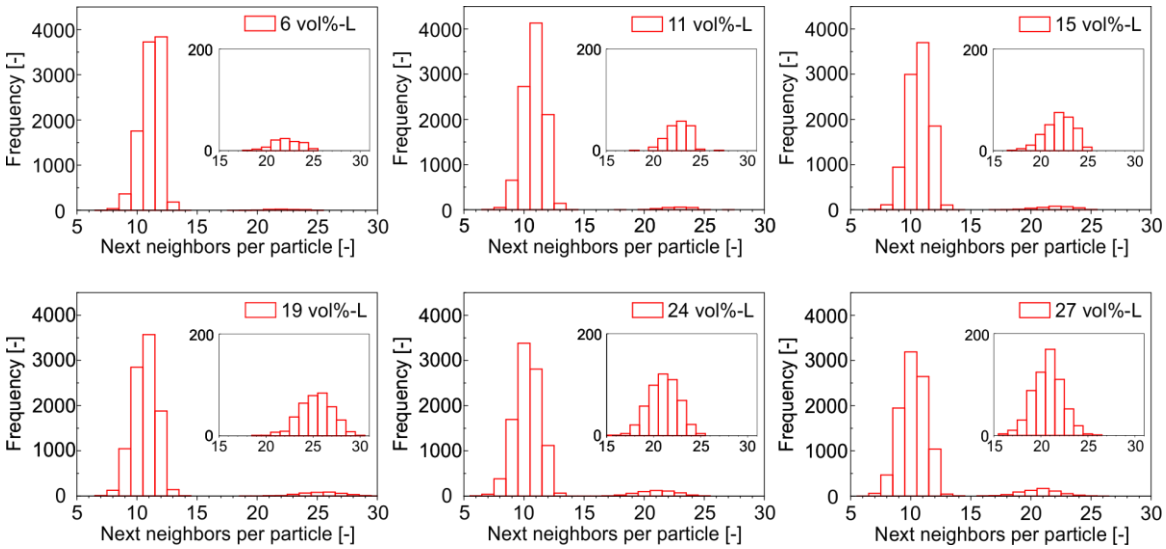

Figure S4. Histograms of the next neighbors per particle for a size ratio of 0.54. Various particle volume ratios close to the minimum thermal conductivity (19 vol%-L) are compared. All assemblies have the same average number of next neighbors (~10-11), but only the assembly with 19 vol%-L shows a second fraction with the highest number of next neighbors (20-30). Thus, this assembly is expected to have the lowest thermal conductivity.

Contact Neighbor Analysis

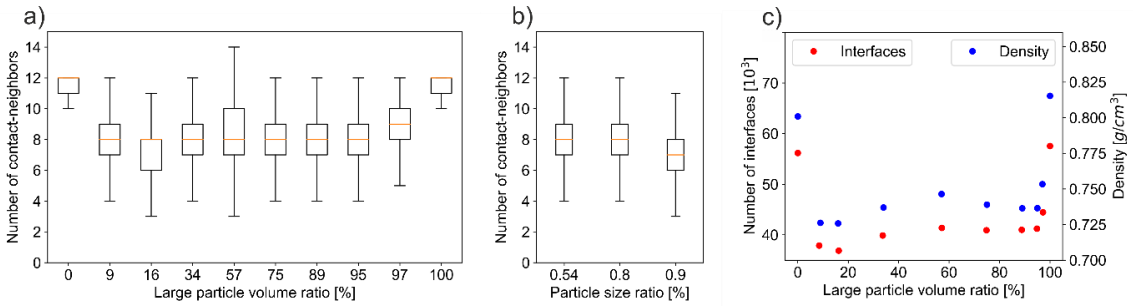

Figure S5. a) Evaluation of the number of contacting next neighbors. An almost constant average number at ~8 is found with a slight tendency towards fewer contact neighbors for 16 vol%-L. b) Contact neighbor analysis for particle mixture of ~ 20 vol%-L with different size ratios. c) Total number of interparticle contact areas and effective density in the entire simulation volume.

Influence of the Interparticle Contact Area on the Thermal Conductivity

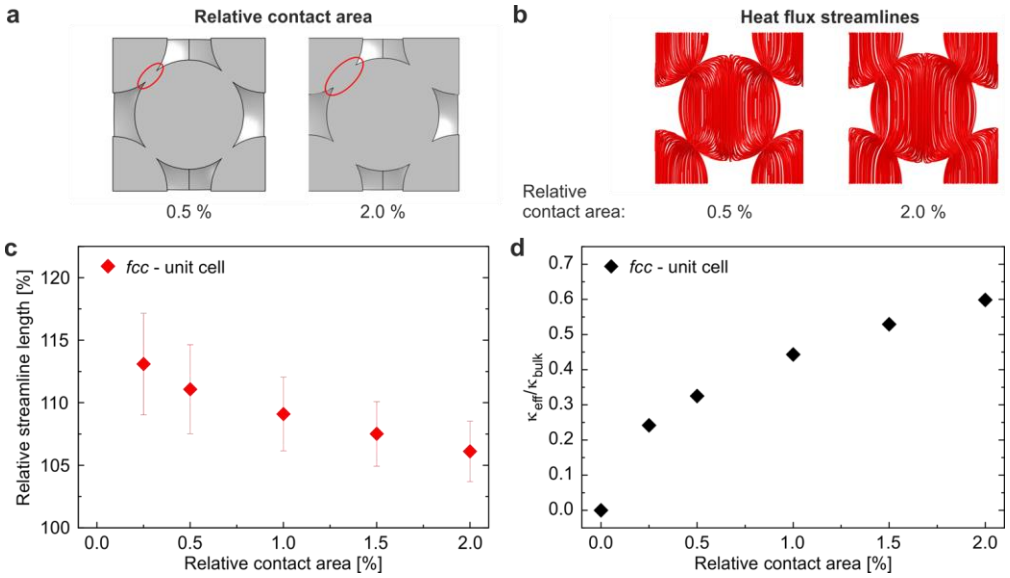

Figure S6. a) Ideal face-centered cubic colloidal crystal with increasing interparticle contact area. b) Heat flux streamlines corresponding to a small (0.5 %) and large (2.0 %) contact area. The streamlines bend more strongly in case of 0.5 % contact area. c) Correlation between the interparticle contact area and the streamline length. The relative contact area is the ratio between the circular connection between adjacent particles and the surface area of the complete particle. The total contact area takes the number of next neighbors into account (here 12 for the *fcc* structure). d) Correlation between the reduced thermal conductivity (relative to the corresponding bulk material) and the relative contact area.

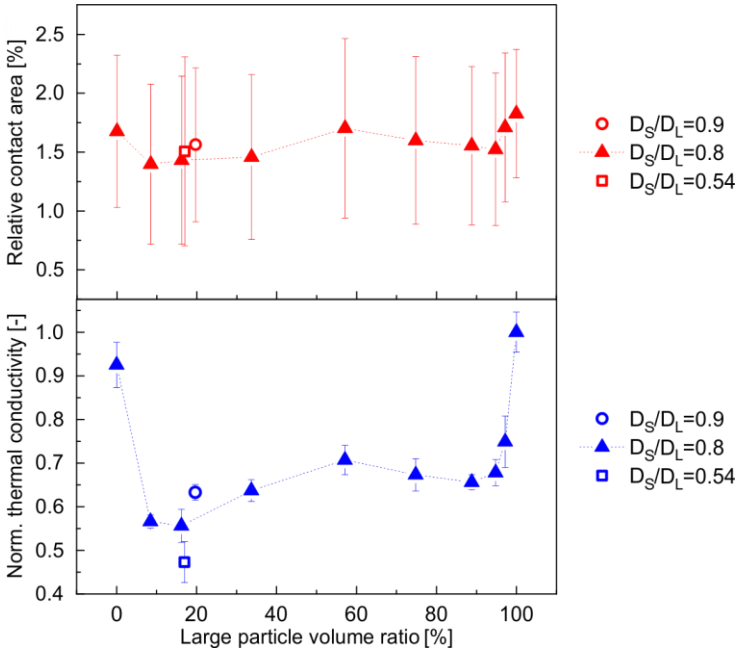

Figure S7. Dependency of normalized thermal conductivity (bottom) and relative contact area (top) on the particle mixing ratio.

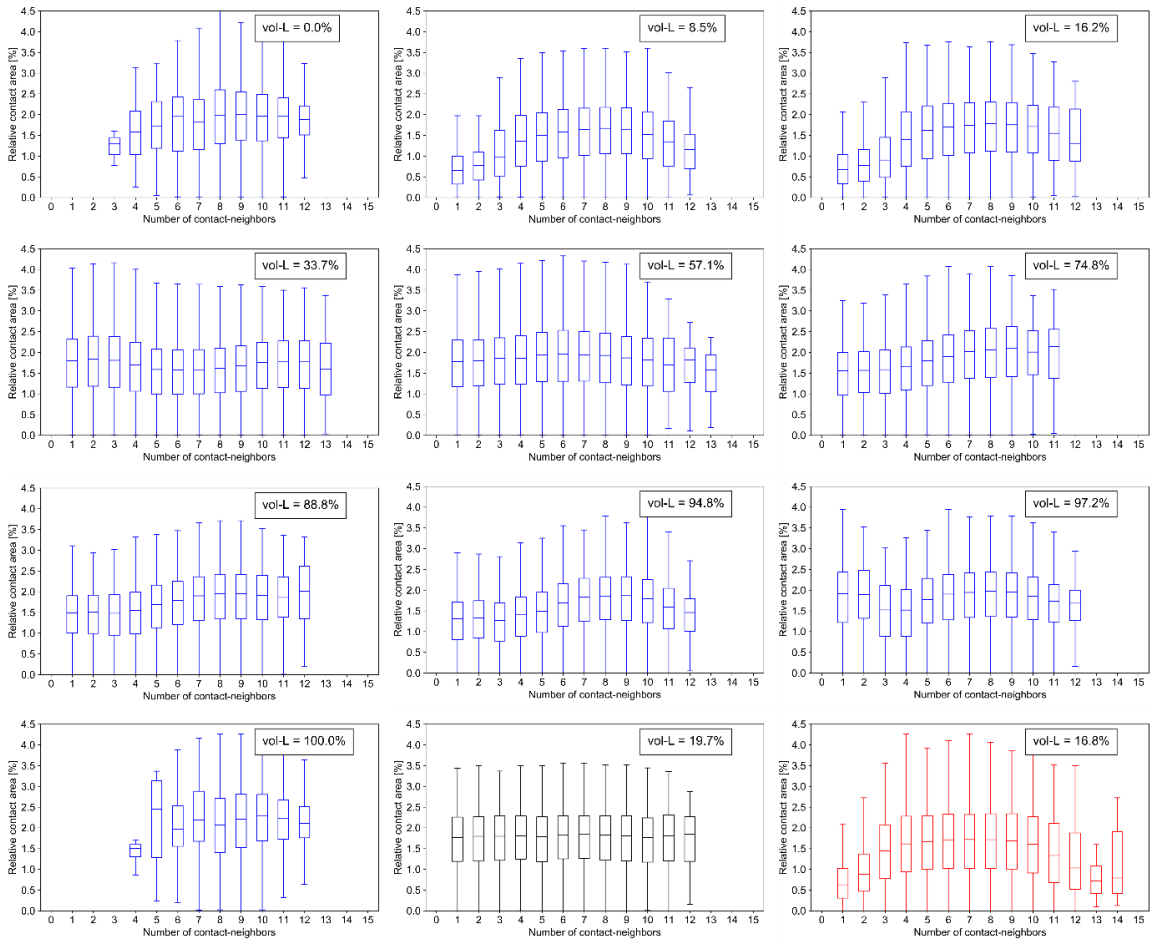

Figure S8. Statistic evaluation of the influence of contacting neighbors on the relative contact area. The box plots give an impression on the average contact are and the width and symmetry of relative contact area distributions. The individual bars at each number of contact neighbors does not include any information on the number of occurrences. The data of size ratio 0.8, 0.9, and 0.54 are colored in blue, black, and red, respectively.

Figure S6 demonstrates the influence of the particle contact area on the streamline length and the effective thermal conductivity for an ideal *fcc* crystal. Figure S7 shows the average contact area in dependence of the mixing ratio and relates it to our experimental findings. Figure S6 shows that contact area and streamline length indeed depend on one another. A strong reduction, however, is only found for relative small contact areas < 0.5 %, which are rarely found in our experiment and simulation. The interparticle constriction adds an additional possibility to increase the thermal path length through the particulate structure. Yet, based on the shown results, we conclude that the changes of the particle contact area play a secondary

role, compared to the increase in thermal path length caused by the disordered structure:

a) The relative contact area in our FEM simulation boxes changes in a range from 1.44 % to 1.83 %, which can account for a maximum of about 10 % thermal conductivity reduction, when comparing to an *fcc* reference system. This is much less compared to our findings, when a disordered structure evolves.

b) When looking at the two shallow minima at about 16 vol%-L and 89 vol%-L mixing ratio, these turn out to possess rather comparable average contact areas of about 1.5 %. The analysis of the contact area distribution (box plots in Figure S8) shows a bell-shaped distribution for the 16 vol%-L case and a decrease towards fewer contact particles for the 89 vol%-L case. The majority of the other mixing ratios exhibit a flat distribution of relative contact areas. (One has to bear in mind that this representation does not give any information on how many particles are present at the respective number of contact neighbors). We assign the more pronounced drop in relative contact area of the 16 vol%-L sample to the presence of large particles jammed in a sphere of smaller particles. Hence, the extension of the thermal path length is not only caused by the disordered structure, but additionally aided by an increased constriction around these defect sites.

c) The effect of small particle jamming around larger central spheres becomes even more obvious, when looking at the influence of the size ratio at comparable volume ratios (16 – 20 vol%-L). The bell-shape of the histogram becomes more pronounced for a decreasing size ratio and shows particularly small relative contact areas for very small and high numbers of contacting neighbors. More similar particle sizes recover a very flat histogram distribution. This is associated with the lack and presence of a high amount of next neighbor spheres, respectively. Consequently, the extension of the thermal path length caused by the introduction of additional next neighbor particles is supported by a stronger constriction around these structures.

Finite Element Modeling

Fourier's law is used to calculate the effective thermal conductivity κ_{eff}:

$$\kappa_{eff} = \frac{Q/A}{\Delta T/h} \tag{S4}$$

Q is the heat flow rate normal to the cross-sectional area A of the cube, ΔT the temperature difference, and h the cube length.

Table S2. Specific heat capacity, density, and thermal conductivity of polystyrene used in FEM simulations.

Specific heat capacity $[Jg^{-1}K^{-1}]$	**Density** $[gcm^{-3}]$	**Thermal conductivity** $[mWm^{-1}K^{-1}]$
1.25	1.05	150

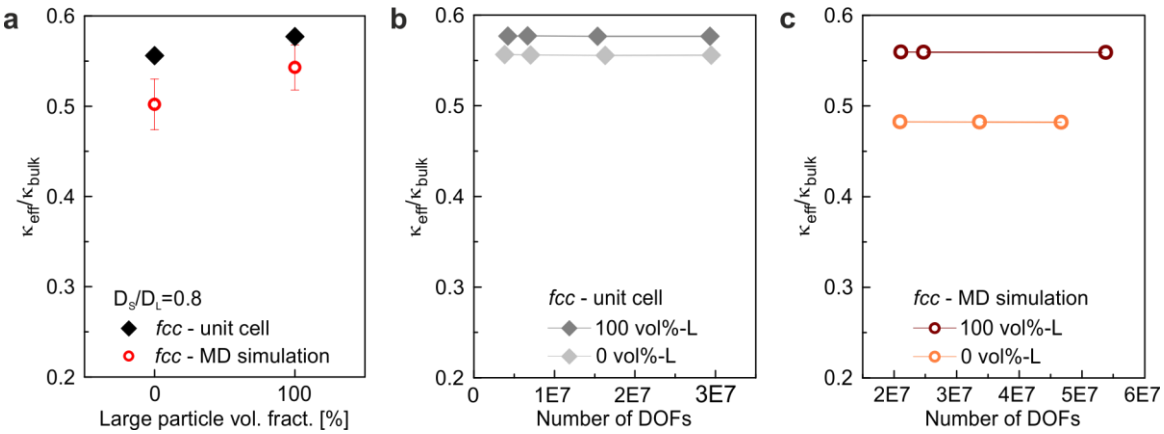

Figure S9. a) Comparison of the effective thermal conductivity divided by the bulk thermal conductivity of polystyrene obtained for an ideal *fcc* unit cell and the *fcc* structure from MD simulation. The average particle contact area of the *fcc* structure from MD simulation was used to create the unit cell. The slight reduction of the MD simulation compared to the ideal unit cell originates from line and point defects, which are not present in the ideal case. b, c) The effective thermal conductivity is independent of the number of DOFs and, thus of the mesh size. c) The data are exemplarily plotted for one position in the *fcc* structure from MD simulation, respectively.

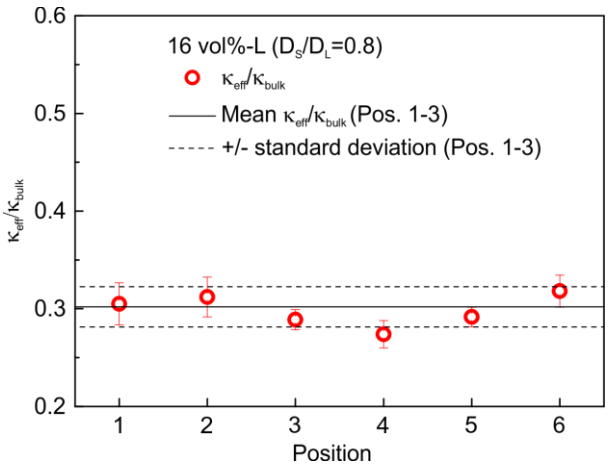

Figure S10. Effective thermal conductivity of the particle assembly with 16 vol% large particles (size ratio 0.8) obtained for six cubes cut out of different positions of the amorphous particle structure (red circles). The error bars arise from the three different simulation directions per cube (x, y, and z). The black solid line represents the mean effective thermal conductivity calculated from the first three values, the dashed line is the corresponding standard deviation. This plot shows that three positions are sufficient to calculate a meaningful average value.

References

1. Goodwin, J. W.; Hearn, J.; Ho, C. C.; Ottewill, R. H., Studies on the preparation and characterisation of monodisperse polystyrene latices, *Colloid. Polym. Sci.* **1974**, *252* (6), 464-471.

2. Ottewill, R. H.; Shaw, J. N., Studies on the preparation and characterization of monodisperse polystyrene latices, *Kolloid Z. Z. Polym.* **1967**, *215* (2), 161-166.

3. Dusza, L., Combined solution of the simultaneous heat loss and finite pulse corrections with the laser flash method, *High Temp. - High Press.* **1995**, *27* (5), 467-473.

4. Parker, W. J.; Jenkins, R. J.; Butler, C. P.; Abbott, G. L., Flash method of determining thermal diffusivity, heat capacity, and thermal conductivity, *J. Appl. Phys.* **1961**, *32* (9), 1679-1684.

5. Plimpton, S., Fast parallel algorithms for short-range molecular dynamics, *J. Comput. Phys.* **1995**, *117* (1), 1-19.

6. Stukowski, A., Visualization and analysis of atomistic simulation data with OVITO – the open visualization tool, *Modell. Simul. Mater. Sci. Eng.* **2010**, *18* (1), 015012.

7. Safran, S. A., *Statistical Thermodynamics of Surfaces, Interfaces, and Membranes*, Westview Press: **2003**, 284.

Part B:

Lock-In Thermography

10. Direct Measurement of the In-Plane Thermal Diffusivity of Semitransparent Thin Films by Lock-In Thermography: An Extension of the Slopes Method

Alexandra Philipp, Nelson W. Pech-May*, Bernd A. F. Kopera, Anna M. Lechner, Sabine Rosenfeldt, and Markus Retsch*

Department of Chemistry, University of Bayreuth, Universitätsstraße 30, 95447 Bayreuth, Germany

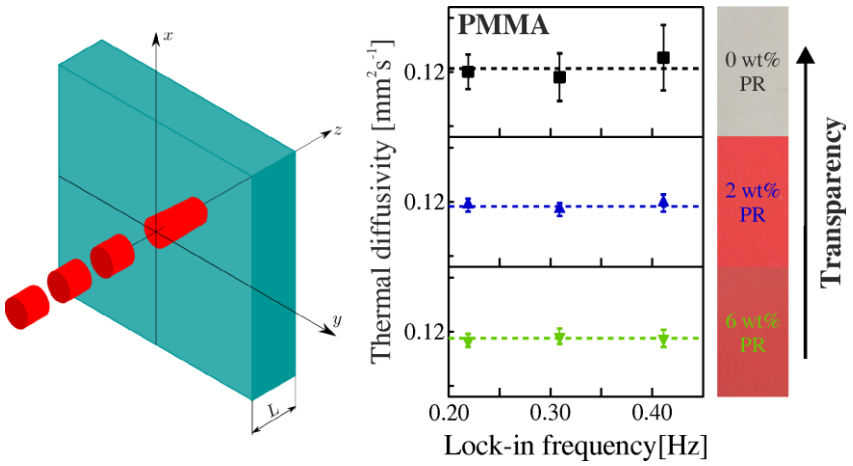

Reprinted with permission from Philipp *et al.*, *Anal. Chem.*, **2019**, *91*(13), 8476-8483 (https://pubs.acs.org/doi/10.1021/acs.analchem.9b01583).

Abstract

We present an extension of the well-known slopes method for characterization of the in-plane thermal diffusivity of semitransparent polymer films. We introduce a theoretical model which considers heat losses due to convection and radiation mechanisms, as well as semitransparency of the material to the exciting laser heat source (visible range) and multiple reflections at the film surfaces. Most importantly, a potential semitransparency of the material in the IR detection range is also considered. We prove by numerical simulations and by an asymptotic expansion of the surface temperature that the slopes method is also valid for any semitransparent film in the thermally thin regime. Measurements of the in-plane thermal diffusivity performed on semitransparent polymer films covering a wide range of absorption coefficients (to the exciting wavelength and in the IR detection range of our IR camera) validate our theoretical findings.

1. Introduction

Lock-in thermography is a well-known technique for accurate determination of the in-plane thermal diffusivity of solids.[1-4] In recent decades, it has attracted the attention of scientists due to its non-contact and non-invasive attributes. Moreover, lock-in thermography has shown versatility for materials characterization, in non-destructive testing and evaluation as well as in biomedical applications.[5-6] In particular, for thermal characterization of isotropic solids, the "slopes method"[2, 7] has been widely used. Therefore, a free-standing sample is periodically heated by a focused optical source. The temperature oscillations as a function of the radial coordinate are detected, typically using an infrared (IR) camera. The thermographic signal (amplitude T and phase Ψ) is either derived from the front-face[2] or the rear-face configuration[1], *i.e.*, from the non-illuminated face. The thermographic signals (ln(amplitude) and phase) far from the heating spot vary linearly with radial distance under the precondition of isotropic opaque thin films

in the thermally thin regime (film thickness << thermal diffusion length). Moreover, the product between the amplitude slope and the phase slope is independent of convective and radiative heat losses. Consequently, it can be used for the determination of the thermal diffusivity of a film if heat conduction to the gas is negligible.[1, 8] Thus, the slopes method is well-suited for measurement of the in-plane thermal diffusivity of high thermal conductors,[4, 9-11] whereas it overestimates the in-plane thermal diffusivity of low thermal conductors.[1] This overestimate is produced by the large conductive heat losses from the low conductor surface to the surrounding gas. However, the overestimation can be avoided by measuring the sample under vacuum conditions.

Even though the characterization of opaque samples using lock-in thermography has been widely explored, there is almost no attempt in literature considering the study of semitransparent samples without coating.[2] Instead, for measuring the in-plane thermal diffusivity of semitransparent films, it is recommended to coat the sample with a thin opaque layer to be able to use the opaque lock-in models. However, there are some cases in which coating the semitransparent material is not an option. For these applications, such as in-situ monitoring of the thermal properties evolution of a polymer film or fiber under stretching, a complete model is required which takes into account the effects of the film semitransparency (to the excitation wavelength and in the infrared range of the IR detector or camera) on the thermographic signal.

In this work, we extend the use of lock-in thermography to the measurement of the in-plane thermal diffusivity of semitransparent thin films of isotropic low thermally conductive materials (such as polymers) without coating. A 2D heat conduction model is considered, which includes heat losses to the surrounding atmosphere, semitransparency of the sample to the exciting wavelength, multiple reflections at the sample surfaces, as well as the effect of its semitransparency through the IR window of the IR camera used.

In addition to our theoretical work, we performed thermal diffusivity measurements with a home-built lock-in thermography set-up. We used three different polymers covering a wide range of absorption properties: poly(methyl methacrylate) (PMMA), low-density polyethylene (LDPE) and polyether ether ketone (PEEK). We chose PMMA as material because of its low absorption to the visible light and high absorption to IR radiation. Thin LDPE films show semitransparency in both the visible and relevant IR wavelength range. We tuned the optical properties of these two materials by the addition of a red dye. The purchased PEEK films are also low absorbers to the visible light. Since their absorption of IR radiation depends on the sample thickness, we measured PEEK films with four different thicknesses.

2. Modeling and Experimental Section

2.1. Modeling

Heat Conduction through a Semitransparent Film

Consider a semitransparent film of thickness L, heated by a focused Gaussian laser of wavelength λ and power P_0 modulated at frequency f. The focused beam has the radius a (measured at $1/e^2$). Besides, this film is thermally isotropic and is in a vacuum. Under this circumstance, heat conduction to the surrounding air can be neglected in the model. Figure 1 shows the described situation.

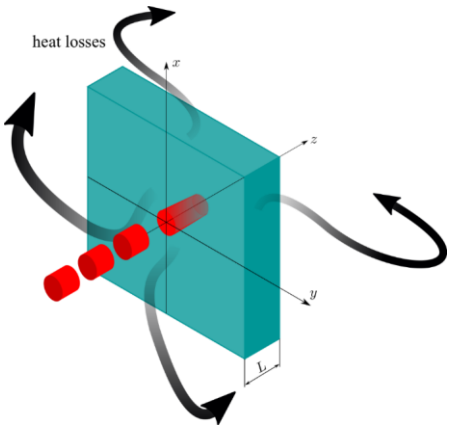

Figure 1. Semitransparent film heated by a focused, modulated Gaussian laser beam. The black arrows indicate heat losses to the environment.

The surface temperature at $z = 0$ (front-face temperature) can be expressed as (a detailed derivation is provided in the Supporting Information):

$$S(r,0,\omega) = F\frac{P_0}{2\pi K}\frac{(1-R)\alpha\gamma}{1-R^2e^{-2\alpha L}}\int_0^\infty \delta\, J_0(\delta r)\frac{e^{-\frac{(\delta a)^2}{8}}}{(\beta^2-\alpha^2)E_0}$$
$$\times\left\{-\frac{A_0}{\beta-\gamma}\left(1-e^{(\beta-\gamma)L}\right)+\frac{B_0}{\beta+\gamma}\left(1-e^{-(\beta+\gamma)L}\right)+\frac{E_0}{\alpha+\gamma}\left(1-e^{-(\alpha+\gamma)L}\right)\right. \quad (1)$$
$$\left.-Re^{-2\alpha L}\left[-\frac{A_1}{\beta-\gamma}\left(1-e^{(\beta-\gamma)L}\right)+\frac{B_1}{\beta+\gamma}\left(1-e^{-(\beta+\gamma)L}\right)-\frac{E_0}{\alpha-\gamma}\left(1-e^{(\alpha-\gamma)L}\right)\right]\right\}d\delta,$$

where $\omega = 2\pi f$, r is the radial coordinate, K is the thermal conductivity of the film. F includes the effect of the IR emissivity, sensor area, IR detection range and the derivative of the Planck distribution at room temperature. R is the reflectance and α is the absorption coefficient of the film, both taken at the laser wavelength. γ is an effective IR absorption coefficient, which averages the IR absorption over the detection range of our IR camera. δ is the Hankel space variable, $J_0(\cdot)$ is the Bessel function of zero order, $\beta^2 = \delta^2 + \frac{i\omega}{D}$. D is the thermal diffusivity of the film. All coefficients A_0, A_1, B_0, B_1, and E_0 are computed explicitly in the Supporting Information, in terms of the thermal diffusivity, modulation frequency, heat convective-radiative losses and optical absorption.

The surface temperature at $z = L$ (rear-face temperature) reads:

$$S(r,L,\omega) = F\frac{P_0}{2\pi K}\frac{(1-R)\alpha\gamma e^{-\gamma L}}{1-R^2e^{-2\alpha L}}\int_0^\infty \delta\, J_0(\delta r)\frac{e^{-\frac{(\delta a)^2}{8}}}{(\beta^2-\alpha^2)E_0}$$
$$\times\left\{-\frac{A_0}{\beta+\gamma}\left(1-e^{(\beta+\gamma)L}\right)+\frac{B_0}{\beta-\gamma}\left(1-e^{-(\beta-\gamma)L}\right)+\frac{E_0}{\alpha-\gamma}\left(1-e^{(\gamma-\alpha)L}\right)\right. \quad (2)$$
$$\left.-Re^{-2\alpha L}\left[-\frac{A_1}{\beta+\gamma}\left(1-e^{(\beta+\gamma)L}\right)+\frac{B_1}{\beta-\gamma}\left(1-e^{-(\beta-\gamma)L}\right)-\frac{E_0}{\alpha+\gamma}\left(1-e^{(\alpha+\gamma)L}\right)\right]\right\}d\delta.$$

The integrals in Equations (1) and (2) cannot be solved in a closed form - not even in the thermally thin regime ($\mu \gg L$), *i.e.*, when the thermal diffusion length $\left(\mu = \sqrt{D/(\pi f)}\right)$ is much larger than the actual thickness of the film (L). Thus, it is

hard to prove the validity of the slopes method for semitransparent films. Up to now, it has been confirmed for the optically opaque case.[1]

However, it is reliable to do numerical simulations to show the validity of the slopes method for semitransparent films in the thermally thin regime. In this work, we perform simulations for the rear-face configuration, which corresponds to our experimental setup. Moreover, in the thermally thin regime, we have shown the numerical equivalence between the front-face and rear-face temperatures (see Figure S1 of the Supporting Information).

Mendioroz *et al*.[1] showed that the radial temperature profile for an optically opaque film in the thermally thin regime far from the punctual heating spot ($a = 0$) can be written as

$$T(r \to \infty, 0, \omega) \approx \sqrt{\frac{\pi}{2}} \frac{e^{-\sigma r}}{\sqrt{\sigma r}}, \tag{3}$$

where $\sigma^2 = \frac{2h}{KL} + \frac{i\omega}{D}$ and h is the combined coefficient due to convection and radiation losses. From Equation (3), it can be shown that the slopes method (product of the amplitude and phase slopes) gives the thermal diffusivity of the film, overcoming the effect of the heat losses. In general, for a given complex number $\sigma^2 = u + \frac{i\omega}{D}$, such that $u \in \mathbb{R}$, ω and D are positive real numbers. It is straightforward to show that the product of its real part $\Re\{\sigma\}$ and its imaginary part $\Im\{\sigma\}$ is independent of u, *i.e.*, $\Re\{\sigma\} \cdot \Im\{\sigma\} = \frac{\omega}{2D}$.

On the other hand, the asymptotic behavior of the Hankel integrals involved in Equations (1) and (2) can be explored.[12-13]

Consider a Hankel integral of zero order:

$$I_0(b) = \int_0^\infty \phi(x) J_0(bx) dx\,, \qquad b \to \infty \tag{4a}$$

an asymptotic expansion when $b \to \infty$ can be expressed as:[12]

$$I_0(b\to\infty)=\frac{1}{b}\sum_{s=0}^{\infty}\frac{(-1)^{1+s}\phi^{(s)}(0)}{s!}\frac{\Gamma\left[\left(\frac{1}{2}\right)(1+s)\right]}{\Gamma\left[\left(\frac{1}{2}\right)(1-s)\right]}\left(\frac{2}{b}\right)^{s}+\Delta_0(b), \tag{4b}$$

where the first term (infinite summation) is the Poincaré Asymptotic Expansion (PAE) of the integral in Equation (4a) and is a series expansion containing integer powers of $1/b$. $\phi^s(0)$ represents the s-th derivative of $\phi(x)$ evaluated at $x=0$ and $\Gamma(\cdot)$ is the Gamma function. The second term takes into account the exponentially small decaying terms of the integral. For odd functions $\phi(-x)=-\phi(x)$, the PAE equals zero, and only the exponentially small terms are relevant for the asymptotic expansion. The $\Delta_0(b)$ term can be obtained using the McClure-Wong distributional method.[13] For meromorphic functions, as is our case, it reads

$$\Delta_0(b)=i\pi\sum_{j=0}^{m}\mathrm{Res}\left\{H_0^{(1)}(bz)\phi(z^2)z;z=a_j\right\}, \tag{5}$$

where $H_0^{(1)}(\cdot)$ is the Hankel function of first class and zero order. $\mathrm{Res}\{f(z);z=a_j\}$ stands for the residues of $f(z)$ evaluated at $z=a_j$ and a_j is the j-th pole of $\phi(z^2)$ located in the upper half complex plane.

Considering a semitransparent film, in the thermally thin regime, illuminated by a punctual laser source ($a=0$). The asymptotic expansion of the front-face thermographic signal $S(r\to\infty,0,\omega)$ can be obtained by computation of the residues appearing the integral in Equation (1). The terms which contain poles in Equation (1) are linear combinations of:

$$S(r\to\infty,0;\omega)\sim\int_0^{\infty}\frac{\delta J_0(\delta r)}{\left(\delta^2-\alpha^2+i\frac{\omega}{D}\right)\left(\delta^2-\gamma^2+i\frac{\omega}{D}\right)\left(\delta^2+\frac{2h}{KL}+i\frac{\omega}{D}\right)}d\delta. \tag{6}$$

Following Equation (5) we obtain

$$S(r\to\infty,0;\omega)\sim\frac{e^{-\sigma_\alpha r}}{\sqrt{\sigma_\alpha r}}+\frac{e^{-\sigma_\gamma r}}{\sqrt{\sigma_\gamma r}}+\frac{e^{-\sigma_h r}}{\sqrt{\sigma_h r}}, \tag{7}$$

where $\sigma_\alpha^2 = -\alpha^2 + \frac{i\omega}{D}$, $\sigma_\gamma^2 = -\gamma^2 + \frac{i\omega}{D}$ and $\sigma_h^2 = \frac{2h}{KL} + \frac{i\omega}{D}$. Note that if the three real parts are of the same order of magnitude, then the expression in Equation (7) reduces to a single exponential decaying term

$$S(r \to \infty, 0; \omega) \sim \frac{e^{-\sigma r}}{\sqrt{\sigma r}}, \tag{8}$$

where $\sigma^2 = u + \frac{i\omega}{D}$ and u is a combination of α, γ, and $2h/(KL)$. This means that the slopes method holds for this particular case. On the other hand, if any of the real parts are larger than the others, the corresponding term in Equation (7) can be dropped, because its amplitude is exponentially small with respect to the others. Accordingly, Equation (7) always can be reduced to Equation (8) for a suitable value of u. As mentioned before, the value of u does not influence the product of the real and imaginary parts of σ. Thus, we have shown that the slopes method $m_{\ln(|T\sqrt{r}|)} \cdot m_\Psi = \frac{\pi f}{D}$ is also applicable for semitransparent films in the thermally thin regime, using a punctual excitation source.

2.2. Experimental Section

Materials

Poly(methyl methacrylate) Plexiglas® 7N (PMMA; Evonik), low-density polyethylene Purell PE 1840H (LDPE; LyondellBasell), tetrahydrofuran (THF; > 99.9 %; Sigma Aldrich), and phenol red (PR; Alfa Aesar) were used as received. Amorphous polyether ether ketone (PEEK) films with a thickness of 25 μm, 50 μm, 75 μm, and 250 μm were purchased from www.goodfellow.com, potassium bromide (KBr) round cell windows were ordered from Sigma Aldrich.

Preparation of Thin, Free-Standing Films for Lock-In Thermography

Free-standing PMMA films were prepared from solution. Therefore, 30 wt% PMMA was dissolved in THF under magnetic stirring. To obtain red-colored PMMA films 2 wt% and 6 wt% PR (with regard to the amount of PMMA), respectively, were added to PMMA before dissolving in THF. Then, the PMMA solution was cast on a glass substrate using the doctor-blade method. After drying for 48 h, the film was removed from the glass substrate and cut into pieces of appropriate sizes. The thickness of the PMMA films was around 200 μm. The fabrication of the free-standing LDPE films is composed of the following steps: compounding, injection molding, and hot pressing. First, LDPE pellets and PR powder were mixed under N_2 flow in a twin-screw compounder with a stirring speed of 40 rpm and at a temperature of 200 °C. Second, the compounded material was directly filled into the injection unit. Disks with a diameter of ~ 27 mm and a thickness of ~ 1 mm were fabricated using an injection force of 6 kN and a tool temperature of 20 °C. Finally, thin, free-standing LDPE films were obtained by hot pressing of the disks at a temperature of 200 °C and subsequent cooling to room temperature. In this way, LDPE film with 0 wt%, 2 wt%, and 6 wt% PR, respectively, were prepared. The thickness of the LDPE films was around 200 μm. Photographs of the PMMA and LDPE thin films with various content of PR are depicted in Figures S3 and S4. PEEK films were cleaned and cut into pieces.

Characterization Methods

In-plane thermal diffusivity measurements on thin, free-standing films (~ 200 μm) were conducted using a home-built lock-in thermography (LIT) set-up (Figure S4). The sample was heated by a laser beam (Genesis MX 488-1000 SLM OPS, Coherent, λ=488.1 nm) focused onto the sample surface by a lens of 150 mm focal length. The amplitude of the laser was modulated in sine waveform using a Rigol Waveform Generator DG1022A. The emitted infrared (IR) radiation of the sample surface is detected by an Infratec VarioCAM HD research IR camera (7.5 – 14 μm). The camera is equipped with a close-up lens. In this configuration, the minimum spatial resolution is 29 μm at a working distance of 33 mm. To avoid heat losses due to conduction and convection into the environment, all samples were measured under vacuum conditions (~$3 \cdot 10^{-3}$ mbar). However, heat losses due to radiation still remain. LIT measurements were performed using Infratec's IRBISactiveonline software. Transparent samples (PMMA and LDPE without phenol red as well as all PEEK films) were coated with a 20 nm carbon layer for enhanced laser absorption. The coating of the sample was facing to the infrared camera. The influence of the carbon coating on the absorption of light in the IR and UV-vis range is shown in Figure S6. In the case of the fabricated polymeric films (PMMA and LDPE), we measured three different films per sample; in case of the purchased PEEK films, we measured only one film per sample.

UV-Vis measurements were conducted on an Agilent Cary 5000 spectrometer in the transmission mode. Absorption spectra were recorded from 380 – 800 nm. The data interval was fixed to 1 nm, averaging for 100 ms. Each measured sample was normalized with a suitable reference (control): For the free-standing polymers the direct lamp spectrum in air was used. For the measurement of the carbon coating an uncoated KBr disc was used. The phenol red powder was measured applying a thin layer on scotch tape and using the same scotch tape as reference. The same polymeric samples as characterized by lock-in thermography were investigated.

A Bruker Vertex 70 FT-IR spectrometer was used for absorption spectra acquisition. The polymeric samples, as well as a carbon-coated KBr window, were measured in transmission mode. To get the IR absorbance of the pure carbon layer, an uncoated KBr window with the same thickness as the uncoated one was used as a reference. Furthermore, an ATR-IR spectrum of phenol red powder was recorded. All samples were measured in the wavenumber range of the spectral range of the infrared camera (data interval: 4 cm^{-1}, averaging: 32 measurements).

3. Results and Discussion

3.1. Numerical Simulations

Here we present numerical simulations of the radial temperature profiles based on Equation (2). A thin polymeric film ($K = 0.15\ Wm^{-1}K^{-1}, D = 0.10\ mm^2s^{-1}$) with thickness $L = 25$ µm is considered. The laser power is set to $P_0 = 50$ mW at a modulation frequency $f = 0.10$ Hz. This gives a thermal diffusion length $\mu = 564$ µm, *i.e.*, the film is in the thermally thin regime ($\mu \gg L$). A typical value is used for the combined heat transfer coefficient $h = 15\ Wm^{-2}K^{-1}$.[8, 14]

Figure 2a shows simulations of a surface temperature radial profile for a semitransparent film, considering a fixed IR absorption coefficient such that $\gamma L = 5$. The absorption coefficient to the incident laser wavelength is varied over a wide range: $0.01 \leq \alpha L \leq 100$. The laser beam is focused on the film surface with a radius $a = 0.1\mu$. The temperature profiles for the 'amplitude' ln ($|T\sqrt{w}|$) and phase Ψ are presented with a vertical shift and in ascending order of αL from top to bottom.

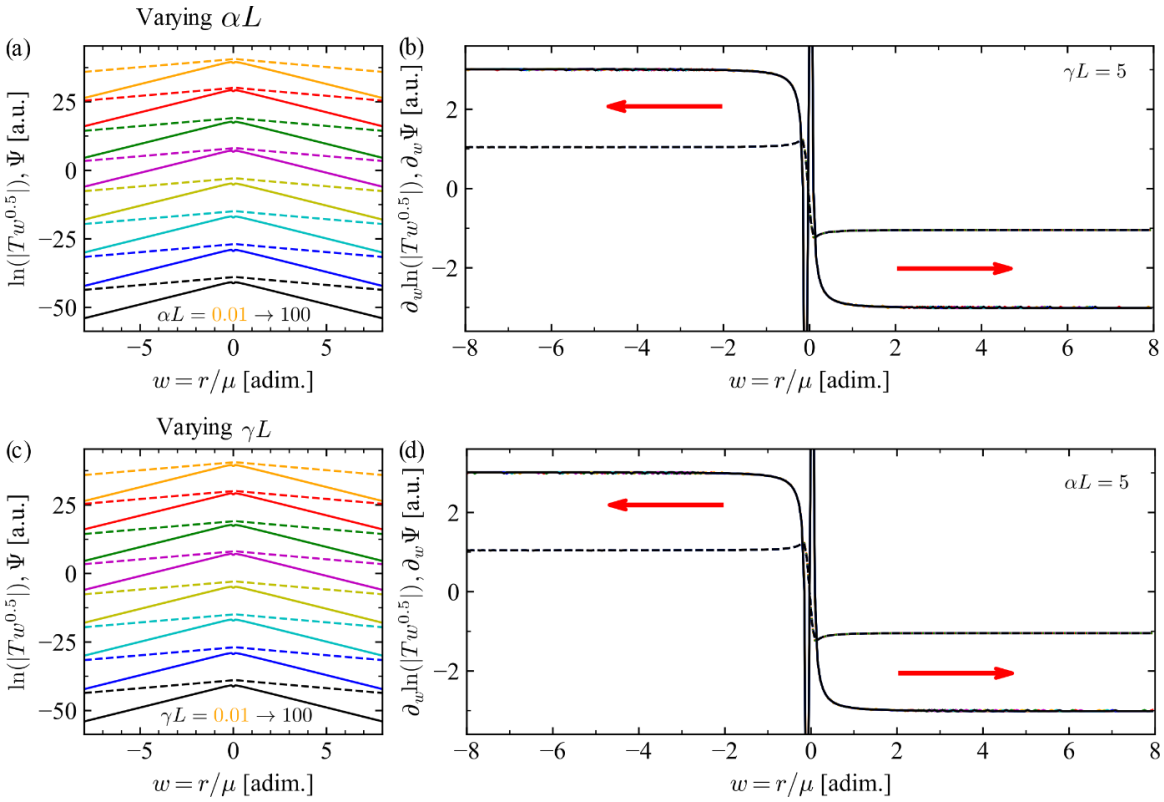

Figure 2. a) Plots of $\ln(|T\sqrt{w}|)$ (continuous lines) and Ψ (dashed lines) as a function of the normalized radial profile $w = r/\mu$. A wide range of absorption coefficients is explored at a fixed IR absorption: $\gamma L = 5$. b) Derivatives of amplitudes (continuous lines) and phases (dashed lines) with respect to w, for different absorption coefficients are explored. Note that results overlap. c) Plots of $\ln(|T\sqrt{w}|)$ (continuous lines) and Ψ (dashed lines) as a function of the normalized radial profile $w = r/\mu$. A wide range of IR absorption coefficients is explored at a fixed optical absorption: $\alpha L = 5$. d) Derivatives of amplitudes (continuous lines) and phases (dashed lines) with respect to w, for the different IR absorption coefficients, are explored. Note that results overlap.

The derivatives of the 'amplitude' $\partial_w \ln(|T\sqrt{w}|)$ and phase $\partial_w \Psi$ with respect to the normalized radial profile are antisymmetric around the beam spot position ($r = 0$), as depicted in Figure 2b. Both derivatives reach a constant value above $r = 2\mu$ (and below $r = -2\mu$), as indicated by the red arrows. Thus, $|r| \geq 2\mu$ corresponds to the linear part of the temperature profiles shown in Figure 2a. Two red arrows mark these intervals. Within the region $0 \leq r \leq 2\mu$, the amplitude derivative shows a concave upwards behavior and is discontinuous at $r = 0$. This discontinuity is due to the logarithmic function. In contrast, the phase derivative is concave downwards away from the beam spot; it shows an abrupt change to concave upwards near $r = 0$ and is continuous at the beam spot position. Moreover, the values of the derivatives for the different absorption coefficients to

the exciting wavelength are equal, as they are all superimposed in Figure 2b. This means that the difference between the slopes of the amplitude $\ln(|T\sqrt{w}|)$ and phase Ψ profiles (for $|r| \geq 2\mu$) is due to the heat losses independent of αL.

Simulations presented in Figure 2c are similar to those in Figure 2a, but in this case, the optical absorption coefficient to the exciting wavelength is fixed ($\alpha L = 5$), and a wide range of IR absorption coefficients are explored: $0.01 \leq \gamma L \leq 100$. The same radius $a = 0.1\mu$ is used for the focused beam. The simulations are vertically shifted in ascending order of γL from top to bottom.

The corresponding 'amplitude' and phase derivatives are shown in Figure 2d. The same characteristics as described in Figure 2b are found. In this case, the values of the derivatives for the different IR absorption coefficients are equal, as they are all superimposed. This means that the difference between the slopes of the amplitude $\ln(|T\sqrt{w}|)$ and phase Ψ profiles is also due to the heat losses, independent of γL. To validate the above results, further simulations for a wide range of both absorption coefficients were performed (see Supporting Information).

We have found that the product between the amplitude derivative $\partial_w \ln(|T\sqrt{w}|)$ and phase derivative $\partial_w \Psi$, for $|r| \geq \mu$, is constant and independent of the optical absorption to the exciting wavelength and to the optical absorption in the IR detection range, *i.e.*, this result is also correct in the optically opaque limit. Consequently, based on the slopes method for optically opaque films in the thermally thin regime,[1] we conclude that for any semitransparent or opaque film in the thermally thin regime and far from the excitation beam spot, $|r| \geq \mu$:

$$\partial_r \ln\left(\left|T\sqrt{r}\right|\right) \cdot \partial_r \Psi = m_{\ln(|T\sqrt{r}|)} \cdot m_{\Psi} = \frac{\pi f}{D}. \tag{9}$$

This confirms our theoretical expectation as outlined above.

3.2. Lock-In Thermography Measurements

To validate our theoretical results experimentally, we measured three different polymers covering a wide range of IR absorption coefficients and optical absorption coefficients to the exciting wavelength: poly(methyl methacrylate) (PMMA), low-density polyethylene (LDPE) and polyether ether ketone (PEEK). To tune the optical properties of PMMA and LDPE, we added 2 and 6 wt% phenol red (PR), respectively (Figure S3). Furthermore, PEEK films with different thicknesses, *i.e.*, 25 µm, 50 µm, 75 µm, and 250 µm, were investigated.

In Figure 3a, a plot of the IR absorption ($A_{IR} = \gamma L/\ln(10)$) as a function of the optical absorption ($A_{Vis} = \alpha L/\ln(10)$) to the exciting wavelength of all samples is shown. In Table 1, the corresponding values are listed. Furthermore, the samples are classified in 'semitransparent' or 'opaque' regarding their optical properties to the exciting laser light and IR radiation.

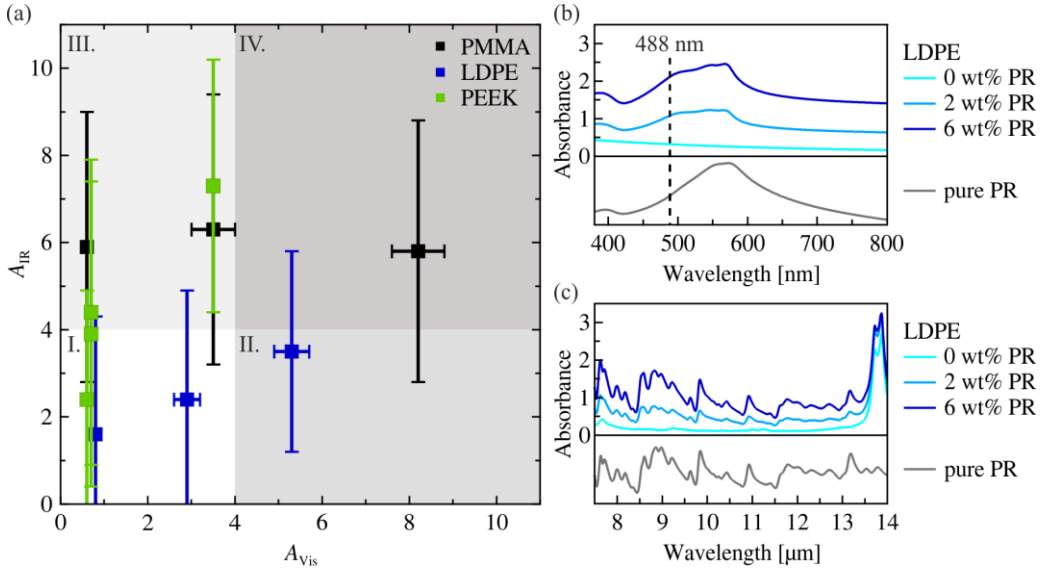

Figure 3. a) Plot of A_{IR} versus A_{Vis} of all polymeric thin films. The error bars of A_{IR} arise from measuring three films per sample (except for PEEK) and from averaging over the spectral wavelength range of the infrared camera (7.5 – 14 µm), the error bars of A_{Vis} arise from measuring three films per sample (except for PEEK). Area I. marks the (semi)transparent A_{Vis} and A_{IR} range, area II. the opaque A_{Vis} range and (semi)transparent A_{IR} range, area III. the (semi)transparent A_{Vis} range and opaque A_{IR} range, and area IV. the opaque A_{Vis} and A_{IR} range. Exemplary IR (b) and UV-vis (c) absorbance spectra of LDPE with 0, 2, and 6 wt% phenol red (PR) as well as the spectra of pure PR powder are shown. The dashed line at 488 nm marks the wavelength of the incident laser used in lock-in measurements.

Figure 3a is divided into four areas dependent on the optical properties of the material:

I. (semi)transparent to both IR radiation in the wavelength range of the IR camera (7.5 – 14 μm) and the exciting wavelength of the laser (488 nm),
II. (semi)transparent to the IR radiation and opaque to the exciting wavelength,
III. opaque to the IR radiation and (semi)transparent to the exciting wavelength, and
IV. opaque to both IR radiation and exciting wavelength.

As can be seen from this plot, PMMA is opaque to IR radiation and semitransparent (III.) or opaque (IV.) to the exciting laser light depending on the dye concentration. LDPE, on the other hand, is semitransparent to IR radiation and semitransparent (I.) or opaque, due to a higher PR content, (II.) to the exciting laser light. Here, the addition of PR enhances not only the absorbance of visible light (Figure 3b) but also the absorbance of IR light (Figure 3c). All PEEK films are semitransparent to the exciting laser light, but either semitransparent (I.) or opaque (III.) to the IR radiation depending on the sample thickness. IR and UV-vis absorbance spectra of all samples are summarized in Figure S7.

Table 1. Summary of A_{Vis} and A_{IR} values of PMMA and LDPE films with various PR content, and PEEK samples with different film thicknesses. Classification of the optical properties regarding the exciting laser light and IR radiation in 'semitransparent' or 'opaque'.

		A_{Vis}[b]	A_{IR}[c]	Exciting laser light	IR radiation
PMMA	**0 wt% PR**[a]	0.6 ± 0.1	> 3.5[d]	semitransparent	opaque
	2 wt% PR	3.5 ± 0.5	> 3.5[d]	semitransparent	opaque
	6 wt% PR	8.2 ± 0.6	> 3.5[d]	opaque	opaque
LDPE	**0 wt% PR**[a]	0.8 ± 0.1	1.6 ± 2.7	semitransparent	semitransparent
	2 wt% PR	2.9 ± 0.3	2.4 ± 2.5	semitransparent	semitransparent
	6 wt% PR	5.3 ± 0.4	3.5 ± 2.3	opaque	semitransparent
PEEK	**25 µm film**[a]	0.6	2.4 ± 2.5	semitransparent	semitransparent
	50 µm film[a]	0.7	> 3.5[d]	semitransparent	opaque
	75 µm film[a]	0.7	> 3.5[d]	semitransparent	opaque
	250 µm film[a]	3.5	> 3.5[d]	semitransparent	opaque

[a]: with 20 nm carbon coating, [b]: value at 488 nm, [c]: average value for 7.5 – 14 µm, error is the standard deviation of the average value, [d]: above the detection limit. In the case of the PMMA and LDPE samples three films were measured, and an average value of A_{Vis} and A_{IR} was calculated.

Exemplary lock-in thermography (LIT) measurement data of PMMA with various PR content (0, 2, 6 wt% PR) are depicted in Figure 4a. Here, temperature profiles for the 'amplitude' ln ($|T\sqrt{w}|$) and phase Ψ are shown for a lock-in frequency f of 0.219 Hz. To be independent of the optical properties of the thin films, we extracted the phase and 'amplitude' slopes above a radial distance of 2µ (vertical dashed lines in Figure 4a). Subsequently, we calculated the thermal diffusivity D for each frequency using the equation $m_{\ln(|T\sqrt{r}|)} \cdot m_{\Psi} = \frac{\pi f}{D}$. Fits were done on radial averaged profiles for each phase and amplitude image. In this way, the whole phase and amplitude distribution are evaluated rather than single lines. Figure 4b shows the individual thermal diffusivities in dependence on the used lock-in frequency. The error bars arise from the fitting of the radial profiles. From this data, an average thermal diffusivity is calculated (dashed line). The data in Figure 4b indicates that the PMMA films have similar thermal diffusivities independent of the PR content. Therefore, the slopes method is valid independent of the optical

absorption at the exciting wavelength. However, the standard error of the individual thermal diffusivities is larger for the sample without PR due to the lower signal-to-noise ratio of the radial profiles.

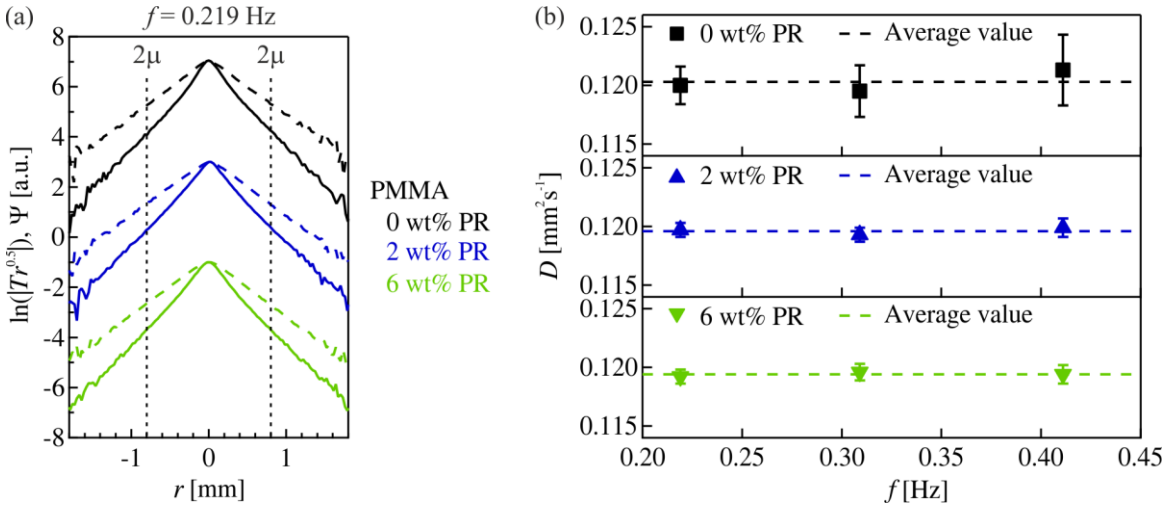

Figure 4. Exemplary measurement data of a PMMA film with 0, 2, and 6 wt% phenol red (PR), respectively: a) Plots of $ln\ (|T\sqrt{w}|)$ (continuous lines) and Ψ (dashed lines) as a function of the radial profile r. The vertical dashed lines at 2μ (~ 800 μm) represent the lower fitting boundary used for evaluation of the phase and amplitude profiles. b) Plots of the thermal diffusivity D against the lock-in frequency f. Error bars are the standard error arising from the fitting of the radial profiles. The dashed lines represent the respective average value.

The thermal diffusivities determined by LIT are shown in Figure 5. We measured PMMA and LDPE films with 0, 2 and 6 wt% of PR content. Additionally, four PEEK samples with different thicknesses were measured. For all samples, we obtained rather small standard deviations of the thermal diffusivity. In Figure 5, we plot an uncertainty of 5 % as error bars.[1, 15]

From our lock-in measurements, we determined an in-plane thermal diffusivity of ~ 0.12 mm^2s^{-1} for PMMA independent of the PR content. Thus, the result does not depend on the optical absorption coefficient to the exciting wavelength that changes from semitransparent to opaque with an increasing amount of red dye (Table 1). Similarly, for LDPE with 0, 2 and 6 wt% PR, we found a thermal diffusivity of ~ 0.19 mm^2s^{-1}. Here, too, we observe no dependence on the optical absorption coefficient to the exciting laser light (Table 1).

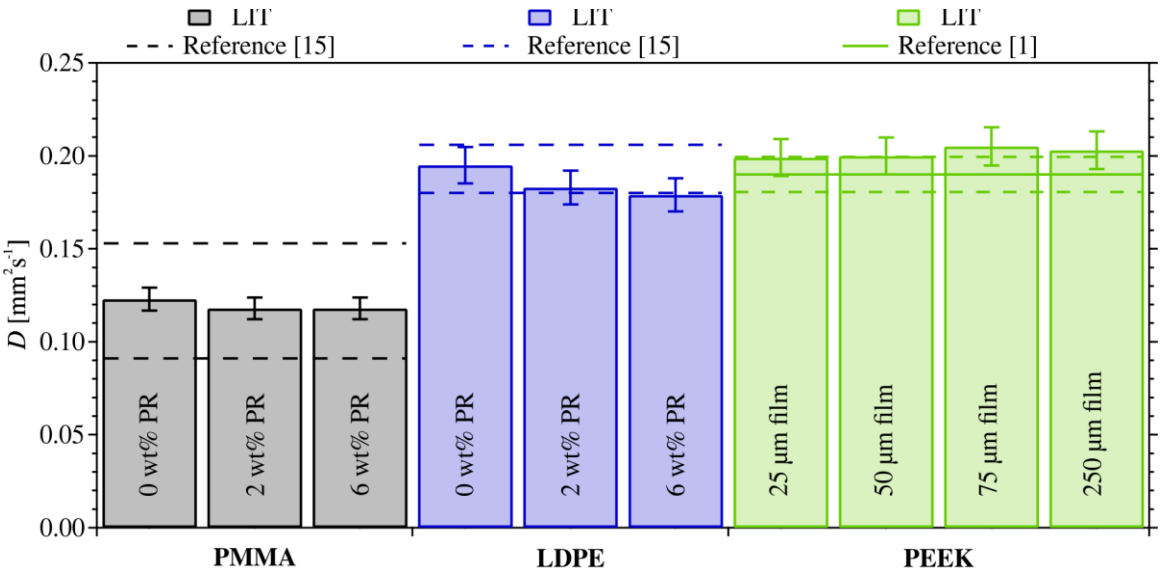

Figure 5. Thermal diffusivity *D* of PMMA (black bars) and LDPE (blue bars) with 0, 2, and 6 wt% phenol red (PR), respectively. Error bars are 5 % uncertainty. The dashed lines represent the lower and upper limit of the reference values for unmodified PMMA and LDPE.[15] The thermal diffusivity of PEEK films with a thickness of 25 µm, 50 µm, 75 µm, and 250 µm are plotted as green bars. Error bars are 5 % uncertainty. The corresponding solid line represents the literature value also measured with lock-in thermography. The dashed lines are the 5 % uncertainty range given by Mendioroz *et al.*[1]

We obtained an average thermal diffusivity value of ~ 0.20 mm^2s^{-1} for all PEEK samples independent of the film thickness. Consequently, the result is not affected by the IR absorption coefficients that change from semitransparent to opaque with increasing film thickness (Table 1). The PEEK films also serve as reference material for our LIT set-up, since literature values are available that were also measured with thermographic methods.[1, 16] The literature value of 0.19 mm^2s^{-1} from Mendioroz *et al.*[1] is plotted as solid green line in Figure 5, the dashed green lines represent 5 % uncertainty range of this value. We found a low relative deviation of ~ 5 % between our average value and the literature value. This good agreement proves that correct thermal diffusivity values are obtained even for samples with low optical absorption coefficients to the exciting wavelength.

We note the fundamental difficulty to quantitatively compare the thermal conductivity of polymer samples reported from different groups. This is an inherent problem owing to the variability of the sample microstructure, which can

be strongly altered based on the fabrication and processing conditions. This is particularly true for semi-crystalline samples because not only the polymer chain orientation but also the degree of crystallinity can vary significantly. Furthermore, a quantitative characterization of the exact polymer microstructure is difficult to achieve and often not reported along the measured thermal conductivity values. In addition to the microstructure, the thermal transport characterization technique may also result in systematically differing thermal conductivity values. Consequently, a broad range of typical thermal conductivities are generally accepted for many polymer materials, which lead to the dashed lines for PMMA and LDPE in Figure 5.[15] We report the influence of both issues (sample microstructure and measurement method) on the thermal conductivity value for our samples to provide a more reasonable classification of the absolute thermal conductivity values that we offer (see Supporting Information for further information). We, therefore, compare LIT to Xenon flash analysis (XFA) for polymer samples stemming from various preparation conditions. We found for the amorphous PMMA samples no signs of polymer crystallinity (Figure S8) and a comparable polymer microstructure. This led to a good agreement between LIT and XFA (which measure the cross-plane thermal diffusivity) measurements. For the semi-crystalline LDPE samples, we did not observe any influence of the PR dye on the degree of crystallinity (see Supporting Information). Yet, the orientation of the crystalline domains is strongly anisotropic and depends on the processing conditions such as hot-pressing and thermal annealing (Figure S10). The XFA measurement results in lower cross-plane thermal diffusivities compared to LIT, which may be caused by the in-plane orientation of the LDPE crystallites. Thermal annealing further alters the LDPE microstructure, as can be seen for the thick XFA samples, which leads to a concomitant increase in thermal diffusivity. Due to the much lower degree of anisotropy upon hot pressing, the thin samples for LIT are

less sensitive to the thermal annealing step and, consequently, do not change significantly.

Considering these uncertainties, it becomes clear that we obtained accurate values of thermal diffusivity for uncoated semitransparent samples using the slopes method. These experimental results validate our theoretical expectations discussed in Chapter 3.1. Lock-in thermography is, consequently, a powerful and versatile characterization technique to measure thermal transport in thin, free-standing films and fibers, independent on their optical properties.

4. Conclusion

In this paper, we developed a two-dimensional heat conduction model which includes besides heat losses to the surrounding atmosphere also semitransparency of the sample to the exciting wavelength, multiple reflections at the sample surfaces, as well as the effect of its semitransparency through the infrared (IR) sensitivity of the IR camera used. Based on this model, we conducted numerical simulations to investigate separately the effect of semitransparency to the exciting laser light and to the IR wavelength of the IR camera. We found that the well-known slope method, which does not consider semitransparency is still valid as long as the phase and amplitude slopes are extracted far from the heating spot center ($\gtrsim 2\mu$). We translate our theoretical findings into the measurement of three different polymers, poly(methyl methacrylate) (PMMA), low-density polyethylene (LDPE) and polyether ether ketone (PEEK). The optical properties in the visible and IR wavelength range of these polymers were varied by their film thickness (PEEK) or by the addition of a red dye (PMMA and LDPE). We obtained thermal diffusivity values which are in good agreement with literature values and independent on the optical absorption properties of the samples. We could, therefore, show that in the thermally thin regime, the slopes method holds (far from the heating spot center) independent of semitransparency (to the exciting

wavelength and in the IR range of the camera). Consequently, the in-plane thermal diffusivity can be measured accurately.

Supporting Information

Details of the analytical model for a semitransparent film are presented. Photographs of polymer samples, UV-vis and IR spectra of all samples as well as the influence of carbon coating, XRD and SAXS data, and reference thermal diffusivity measurements using XFA.

Acknowledgments

The authors thank Rainer Giesa and Sandra Ganzleben for help with injection molding and hot-pressing. Argyrios Georgiadis is acknowledged for XFA measurements of the LDPE samples after thermal annealing. B.A.F.K. acknowledges support from the Elite Network of Bavaria (ENB). The Bavarian Polymer Institute is acknowledged for access to polymer processing and small angle scattering facilities. The Volkswagen foundation funded this work through a Lichtenberg professorship. Further support was provided through ERC StG VISIRday #714968.

References

1. Mendioroz, A.; Fuente-Dacal, R.; Apinaniz, E.; Salazar, A., Thermal diffusivity measurements of thin plates and filaments using lock-in thermography. *Review of Scientific Instruments* **2009,** *80* (7), 074904.

2. Zhang, B.; Imhof, R. E., Theoretical analysis of the surface thermal wave technique for measuring the thermal diffusivity of thin slabs. *Applied Physics A* **1996,** *62* (4), 323-334.

3. Salazar, A.; Mendioroz, A.; Fuente, R.; Celorrio, R., Accurate measurements of the thermal diffusivity of thin filaments by lock-in thermography. *Journal of Applied Physics* **2010,** *107* (4), 043508.

4. Wolf, A.; Pohl, P.; Brendel, R., Thermophysical analysis of thin films by lock-in thermography. *Journal of Applied Physics* **2004,** *96* (11), 6306-6312.

5. Boué, C.; Cassagne, F.; Massoud, C.; Fournier, D., Thermal imaging of a vein of the forearm: Analysis and thermal modelling. *Infrared Phyics and Technology* **2007,** *51* (1), 13-20.

6. Rantala, J.; Wu, D.; Busse, G., Amplitude-modulated lock-in vibrothermography for NDE of polymers and composites. *Research in Nondestructive Evaluation* **1996,** *7* (4), 215-228.

7. Fabbri, L.; Fenici, P., Three-dimensional photothermal radiometry for the determination of the thermal diffusivity of solids. *Review of Scientific Instruments* **1995,** *66* (6), 3593-3600.

8. Salazar, A.; Mendioroz, A.; Fuente, R., The strong influence of heat losses on the accurate measurement of thermal diffusivity using lock-in thermography. *Applied Physics Letters* **2009,** *95* (12).

9. Muscio, A.; Bison, P. G.; Marinetti, S.; Grinzato, E., Thermal diffusivity measurement in slabs using harmonic and one-dimensional propagation of thermal waves. *International Journal of Thermal Science* **2004,** *43* (5), 453-463.

10. Pradère, C.; Goyhénèche, J. M.; Batsale, J. C.; Dilhaire, S.; Pailler, R., Thermal diffusivity measurements on a single fiber with microscale diameter at very high temperature. *International Journal of Thermal Science* **2006,** *45* (5), 443-451.

11. Oksanen, M.; Scholz, R.; Fabbri, L., On the longitudinal thermal diffusivity of SiC-based fibres. *Journal of Material Science Letters* **1997,** *16* (13), 1092-1094.

12. Galapon, E. A.; Martinez, K. M., Exactification of the Poincare asymptotic expansion of the Hankel integral: spectacularly accurate asymptotic expansions and non-asymptotic scales. *Proceedings of the Royal Society A: Mathematical, Physical and* Engineering *Sciences* **2014,** *470* (2162), 20130529.

13. Frenzen, C. L.; Wong, R., A Note on Asymptotic Evaluation of Some Hankel Transforms. *Mathematics of Computations* **1985,** *45* (172).

14. Kanstad, S. O.; Nordal, P.-E., Experimental aspects of photothermal radiometry. *Canadian Journal of Physics* **1986,** *64* (9), 1155-1164.

15. *Granta Design, CES edupack*, Cambridge, UK, 2015.

16. Pech-May, N. W.; Mendioroz, A.; Salazar, A., Simultaneous measurement of the in-plane and in-depth thermal diffusivity of solids using pulsed infrared thermography with focused illumination. *Independent nondestructive testing and evaluation* **2016,** *77*, 28-34.

Supporting Information

1. Modeling

Consider the geometry shown in Figure 1 of the main text. The power distribution $P(z)$ inside the semitransparent thin film can be calculated using the Beer-Lambert law taking into account multiple reflections of the laser beam at the film surfaces,[1]

$$P(z) = \frac{P_0(1-R)(e^{-\alpha z} + Re^{-2\alpha L}e^{\alpha z})}{1 - R^2e^{-2\alpha L}}, \tag{S1}$$

where R is the reflectance and α is the absorption coefficient of the film, both taken at the laser wavelength. A fraction of this power is converted into heat $Q(z) = \chi P(z)$ and is the heating source of the film. Where χ is the efficiency of the light to heat conversion. We consider heat conduction by diffusion in the film. Accordingly, the heat diffusion equation for the presented configuration reads

$$\nabla^2 T - \frac{i\omega}{D}T = -\frac{\chi P_0}{2K}\frac{e^{-\frac{2r^2}{a^2}}}{\pi a^2}\frac{(1-R)\alpha(e^{-\alpha z} - Re^{-2\alpha L}e^{\alpha z})}{(1 - R^2e^{-2\alpha L})}, \tag{S2}$$

where $T = T(\vec{r}, \omega)$ is the temperature field inside the sample at the angular frequency $\omega = 2\pi f$, D and K is the thermal diffusivity and thermal conductivity of the film, respectively.

Because the film is thermally isotropic, Equation (S2) has cylindrical symmetry. Thus, we can express the temperature field as a Hankel transform:

$$T(r, z, \omega) = \int_0^\infty \delta J_0(\delta r)\left[Ae^{\beta z} + Be^{-\beta z} + Ce^{-\alpha z} + Ee^{\alpha z}\right]d\delta, \tag{S3}$$

where δ is the Hankel space variable, $J_0(\cdot)$ is the Bessel function of zero order, $\beta^2 = \delta^2 + \frac{i\omega}{D}$ and the coefficients C and E are obtained from a particular solution of Equation (S2):[1]

$$T(r, z, \omega) = \int_0^\infty \delta J_0(\delta r)\left[Ae^{\beta z} + Be^{-\beta z} + Ce^{-\alpha z} + Ee^{\alpha z}\right]d\delta, \tag{S3}$$

$$C = \frac{\chi P_0}{2\pi K}\frac{(1-R)\alpha}{(\beta^2 - \alpha^2)}\frac{e^{-\frac{(\delta a)^2}{8}}}{1 - R^2e^{-2\alpha L}}, \tag{S4a}$$

$$E = -\frac{\chi P_0}{2\pi K}\frac{(1-R)\alpha R e^{-2\alpha L}}{(\beta^2-\alpha^2)}\frac{e^{-\frac{(\delta a)^2}{8}}}{1-R^2e^{-2\alpha L}}. \quad \text{(S4b)}$$

The solution of the homogeneous part of Equation (S2) gives the other two coefficients in Equation (S3) by considering the following boundary conditions:

$$K\frac{dT}{dz}\Big|_{z=0} = hT(z=0), \quad \text{(S5a)}$$

$$K\frac{dT}{dz}\Big|_{z=L} = -hT(z=L), \quad \text{(S5b)}$$

where h is the linearized combined coefficient of convective and radiative heat transfer.[2-3] Accordingly, the temperature field given in Equation (S3) can be written as

$$T(r,z,\omega) = \frac{\chi P_0}{2\pi K}\frac{(1-R)\alpha}{1-R^2e^{-2\alpha L}}\int_0^\infty \delta J_0(\delta r)\frac{e^{-\frac{(\delta a)^2}{8}}}{(\beta^2-\alpha^2)}\left[\frac{A_0e^{\beta z}+B_0e^{-\beta z}}{E_0} + e^{-\alpha z} - Re^{-\alpha L}\left(\frac{A_1e^{\beta z}+B_1e^{-\beta z}}{E_0}+e^{\alpha z}\right)\right]d\delta. \quad \text{(S6)}$$

Where

$$A_0 = e^{-\beta L}(\beta-h')(\alpha+h') + e^{-\alpha L}(\beta+h')(-\alpha+h'), \quad \text{(S7a)}$$

$$B_0 = e^{\beta L}(\beta+h')(\alpha+h') + e^{-\alpha L}(\beta-h')(-\alpha+h'), \quad \text{(S7b)}$$

$$A_1 = e^{-\beta L}(\beta-h')(-\alpha+h') + e^{\alpha L}(\beta+h')(\alpha+h'), \quad \text{(S7c)}$$

$$B_1 = e^{\beta L}(\beta+h')(-\alpha+h') + e^{\alpha L}(\beta-h')(\alpha+h'), \quad \text{(S7d)}$$

$$E_0 = e^{-\beta L}(\beta-h')^2 - e^{\beta L}(\beta+h')^2, \quad \text{(S7e)}$$

and $h' = h/K$.

The semi-transparency of the film in the infrared (IR) region is also considered. In particular, for the detection range of our IR camera (7.5 – 14 μm), the signal is collected not only from the sample surface but also from the inside.

Let us consider an effective IR absorption coefficient γ, which averages the IR absorption over the detection range of our IR camera. This effective coefficient is a good approximation for materials with smoothly varying IR absorption spectra in

the corresponding detection range.[4] Accordingly, the signal recorded by the IR camera can be written as,

$$S(r, z_0, \omega) = F \int_0^L \gamma e^{-\gamma|z-z_0|} T(r, z, \omega) dz, \tag{S8}$$

where $z_0 = \{0, L\}$ for the IR camera placed in the same side (front-face configuration) or in the backside (rear-face configuration) of the illuminated surface, respectively. The proportionality constant F includes the effect of the IR emissivity, sensor area, IR detection range and the derivative of the Planck distribution at room temperature.

Setting $z_0 = 0$ in Equation (S8) allows us to evaluate the resulting integral and obtain an expression for the signal recorded by the IR camera, in the front-face configuration (see Equation (1) in main text). Similarly, to the previous case, we set $z_0 = L$ and evaluate the integral in Equation (S8). We obtain the following expression for the signal recorded by the IR camera, in the rear-face configuration (see Equation (2) in the main text).

In order to show the equivalence of front-face and rear-face signals for the thermally thin case, we performed simulations using Equations (1) and (2) of the main text and we plot the difference in 'amplitude' and phase. The results are shown in Figures S1a and S1b, respectively. For these simulations, we have used the same parameters as in Figure 2a of the main text.

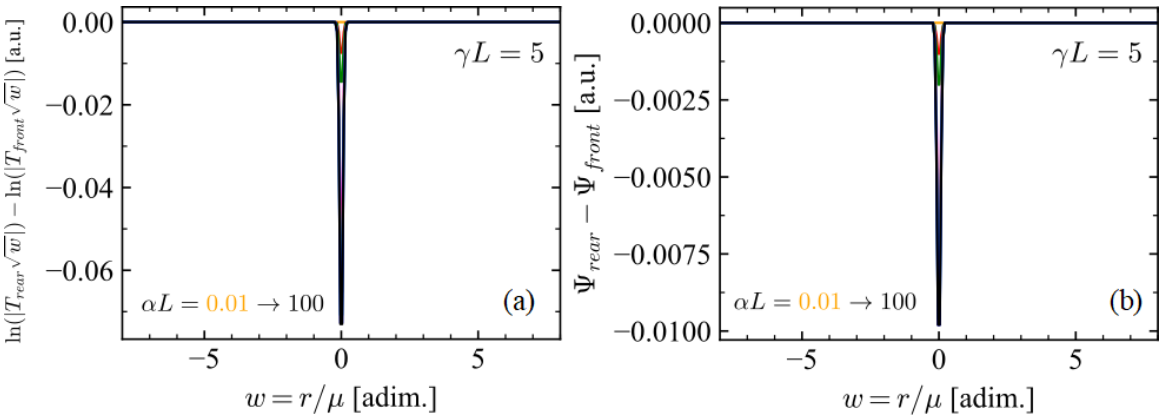

Figure S1. Difference in a) amplitude and b) phase between the surface temperature at $z = L$ (rear-face) and the front surface temperature at $z = 0$. Note that differences appear only near to the excitation spot, but for $|r| \gtrsim \mu$ both temperatures are equal.

To validate our simulations in Chapter 3.1, for a wide range of both absorption coefficients, we perform simulations at three different values of the IR absorption coefficient ($\gamma L = 0.10, 5$ and 50). For each case, the optical absorption coefficient to the exciting wavelength was varied over a wide range: $0.01 \leq \alpha L \leq 100$. The product between the amplitude derivative and phase derivative is depicted in Figure S2a-c. Note that for $|r| \geq \mu$, the product of the derivatives is constant, independent of the optical absorption at the exciting wavelength and for each of the three different values of γL. This is analogous to the product of the slopes $m_{\ln(|T\sqrt{r}|)} \cdot m_{\Psi} = \pi f / D$ for the optically opaque case.[5] Actually, the optically opaque case is covered in our simulations, as represented in Figure S2c for large values of αL.

Figure S2d-f show the product of derivatives for three different values of the optical absorption to the exciting wavelength ($\alpha L = 0.10, 5$ and 50), covering a wide range of IR absorption coefficients $0.01 \leq \gamma L \leq 100$. Once again, for $|r| \geq \mu$, the product of the derivatives is constant, independent of the IR optical absorption and for each of the three different values of αL. The optically opaque case is covered in Figure S2f for large values of γL.

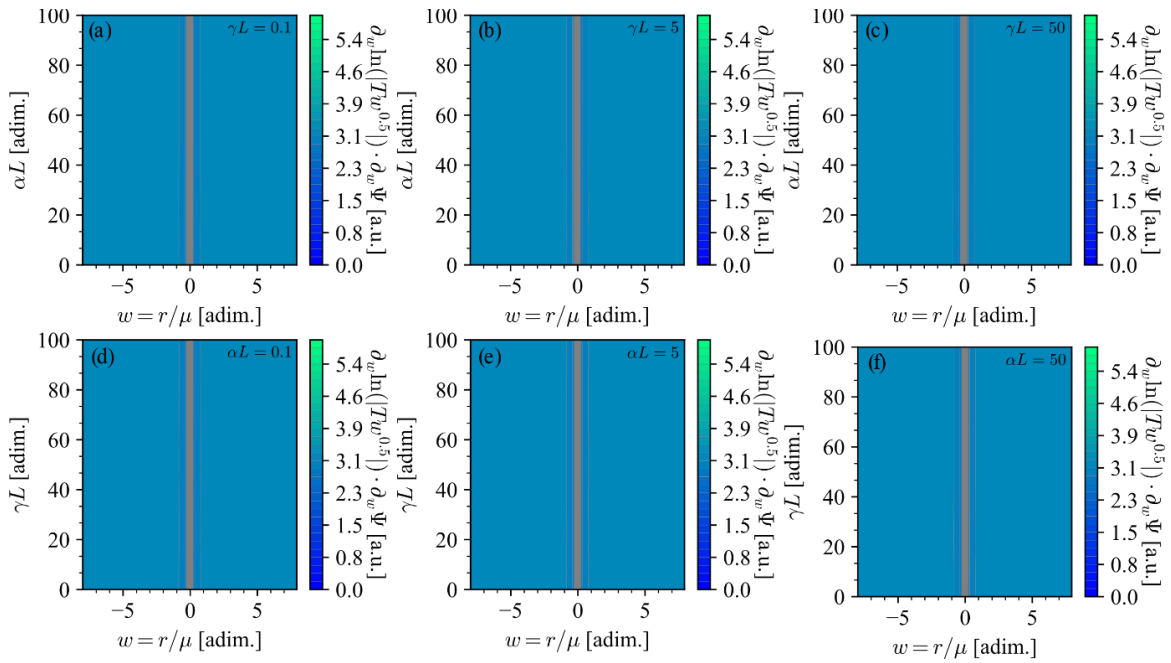

Figure S2. Product between amplitude and phase derivatives. Upper row (a-c): three different values of the IR absorption coefficient ($\gamma L = 0.10, 5$ and 50), covering a wide range of optical absorption coefficients to the exciting wavelength $0.01 \leq \alpha L \leq 100$. Lower row (d-f): three different values of the optical absorption to the exciting wavelength ($\alpha L = 0.10, 5$ and 50), covering a wide range of IR absorption coefficients $0.01 \leq \gamma L \leq 100$.

2. Experimental Section

Photographs of PMMA and LDPE Samples for LIT Measurements

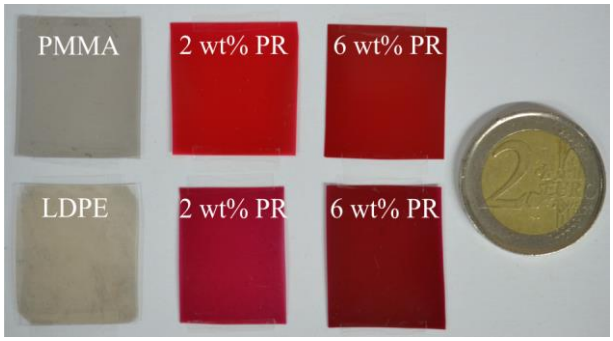

Figure S3. Photographs of LIT samples. Upper row: PMMA film with 20 nm carbon, PMMA film with 2 and 6 wt% PR, respectively. Lower row: LDPE film with 20 nm carbon, LDPE film 2 and 6 wt% PR, respectively.

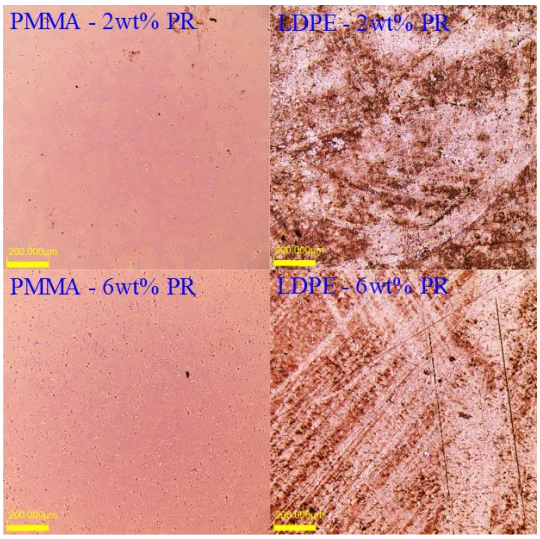

Figure S4. Micrographs of LIT samples with PR. Upper row: PMMA and LDPE films with 2 wt% PR. Lower row: PMMA and LDPE films with 6 wt% PR.

Lock-In Thermography Set-Up

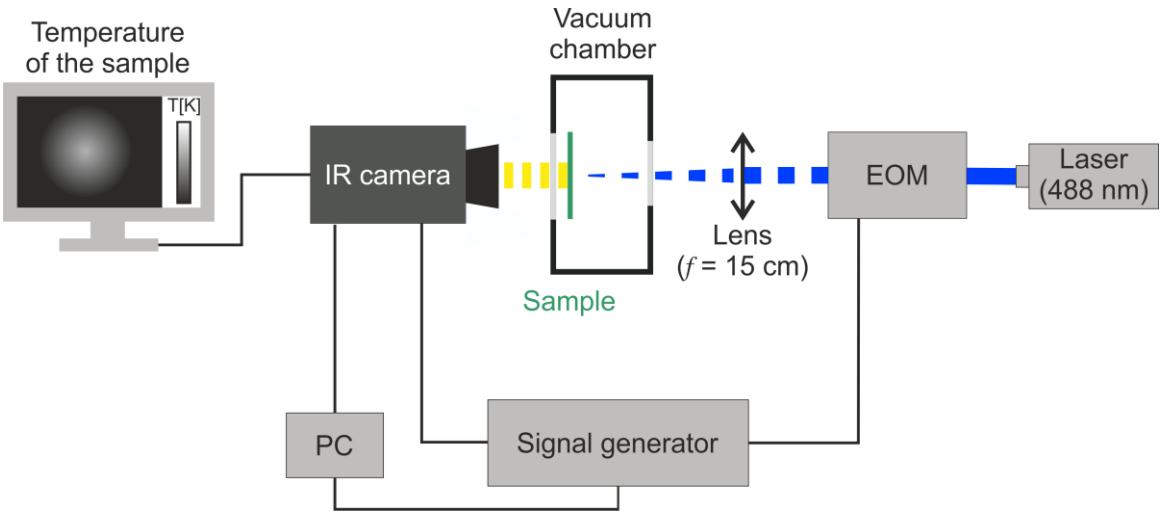

Figure S5. Schematic set-up used for lock-in thermography measurements. PC and EOM stand for personal computer and electro optic modulator, respectively.

IR and UV-Vis Spectra of PMMA and LDPE Samples for LIT Measurements

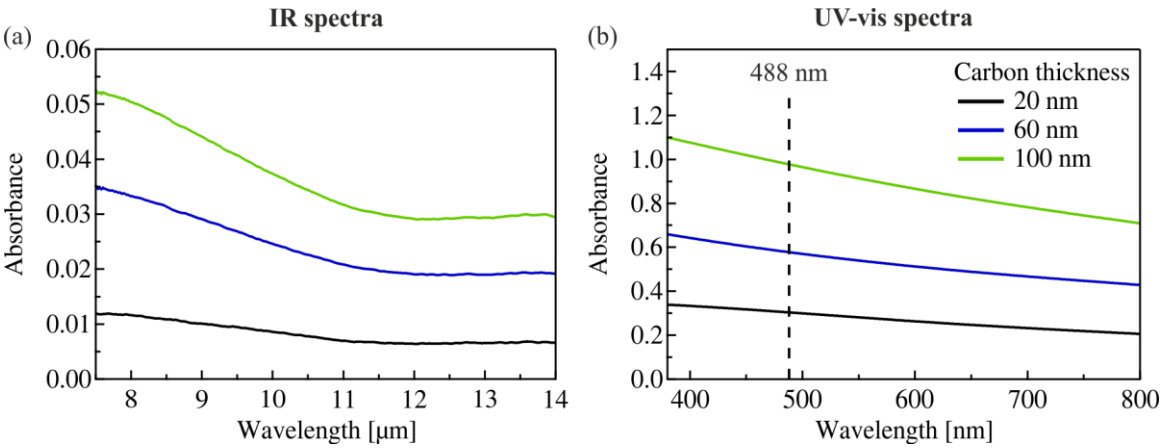

Figure S6. Influence of carbon coating on the optical properties: a) IR spectra and b) UV-vis spectra of 20 nm, 60 nm, and 100 nm carbon (The spectra are represented relative to an uncoated KBr disc as control). The dashed line at 488 nm marks the wavelength of the incident laser used in lock-in measurements. The absorbance of IR and UV-vis light increases with an increasing carbon layer. The coating leads to a higher absorbance of light in the UV-vis range compared to IR light.

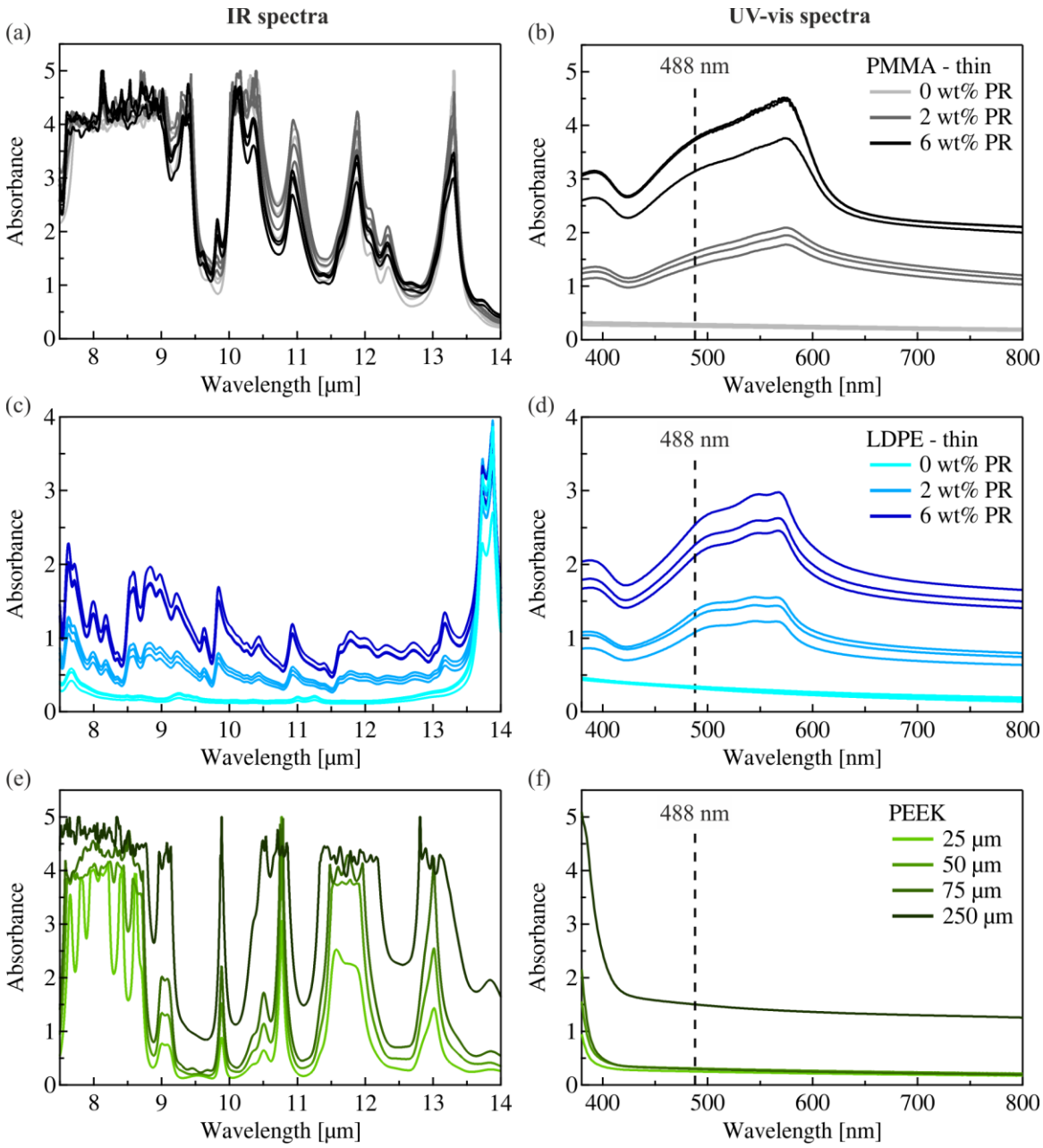

Figure S7. Optical properties of the thin, free-standing polymeric films measured with lock-in thermography. a) IR spectra and b) UV-vis spectra of PMMA films with 0 wt%, 2 wt%, and 6 wt% PR, respectively. c) IR spectra and d) UV-vis spectra of LDPE films with 0 wt%, 2 wt%, and 6 wt% PR, respectively. e) IR spectra and f) UV-vis spectra of a 25 μm, 50 μm, 75 μm, and 250 μm PEEK film, respectively. The dashed line at 488 nm marks the wavelength of the incident laser used in lock-in measurements. Absorbance values higher than 4 units are difficult to resolve accurately with our detector. Therefore, we set the opaqueness threshold to $A_{Vis}>4$ (for the excitation wavelength) and $A_{IR}>4$ (in the IR range).

Reference Thermal Diffusivity Measurements of Thick PMMA and LDPE Samples

1) Preparation of Thick Reference Samples for Xenon Flash Analysis

1 mm thick PMMA samples were fabricated by compounding and injection molding. PMMA pellets and PR powder were mixed under N_2 flow in a twin-screw compounder with a stirring speed of 40 rpm and at a temperature of 240 °C. Then, the compounded material was directly filled into the injection unit. Disks with a diameter of ~27 mm and a thickness of ~1 mm were fabricated using an injection force of 6 kN and a tool temperature of 20 °C. In this way, PMMA disks with 0 wt%, 2 wt%, and 6 wt% PR, respectively, were prepared. LDPE samples were taken from the remaining LDPE disks which were already prepared using injection molding (see Experimental section in the main text).

2) Cross-Plane Thermal Diffusivity Measurements using Xenon Flash Analysis (XFA)

Xenon flash analysis (XFA) was used to obtain reference thermal diffusivity values for the fabricated PMMA and LDPE samples. We performed cross-plane thermal diffusivity measurements on an XFA500 Xenon flash apparatus (Linseis), equipped with an InSb infrared (IR) detector. The upper and lower sample surfaces were coated with a thin graphitic layer (each ~10 μm). Since the thickness of the coating is significantly thinner than the sample thickness (20 μm ≪ 1000 μm), it does not affect the measurement result. The coating ensures a good absorbance of the Xenon flash and a high IR emissivity. The sample thickness which is needed to obtain the thermal diffusivity was measured with a Litematic VL-50 (Mitutoyo). All XFA measurements were performed in air at room temperature (295 K). The obtained data were evaluated using our own fitting framework, which will be published separately. This fitting procedure accounts for the pulse shape correction, radial and facial losses and yields reliably the thermal diffusivity. The

LDPE samples were measured before and after thermal annealing (90 °C, one week).

3) X-Ray Diffraction (XRD) and Small Angle X-Ray Scattering (SAXS)

To demonstrate the amorphous nature of the PMMA samples and the semi-crystallinity of the LDPE samples we performed X-ray diffraction (XRD). The measurements were conducted in Bragg-Brentano geometry on an Empyrean system with a PIXEL solid-state detector (PANalytical, Almelo, Netherlands) using Cu-radiation.

Small-angle X-ray scattering (SAXS) was performed on the PMMA and LDPE samples using the lab-based system Ganesha Air (SAXSLAB, Denmark), equipped with a rotating anode (copper, MicroMax 007HF, Rigaku Corporation, Japan) and a position sensitive detector (Pilatus 300K, Dectris). The samples (and air as background) were measured as obtained in parallel and perpendicular beam geometry. Different detector positions were used to cover a larger scattering range q ($q = \frac{4\pi}{\lambda}\sin\left(\frac{2\theta}{2}\right)$).

4) Discussion of Polymer Microstructure

The pure PMMA samples show broad oscillations without prominent Bragg reflections in the XRD regime proving their amorphous nature (Figure S8, black curve). The broad oscillations around 13.5°, 30° and 42° result from the packing and defined backbone sequence of the polymeric chains. These characteristic patterns are also obtained for the dye-doped PMMA samples (Figure S8, red curve, and Figure S9a,b), which additionally show small reflections due to tiny crystallites of phenol red. The combination of XRD and SAXS of a pure PMMA sample (Figure S8, inset) indicates a rough surface of the films ($I(q) \propto q^{-2.8}$). In that context, one may imagine the texture of the sample area as a dense fractal-like object.

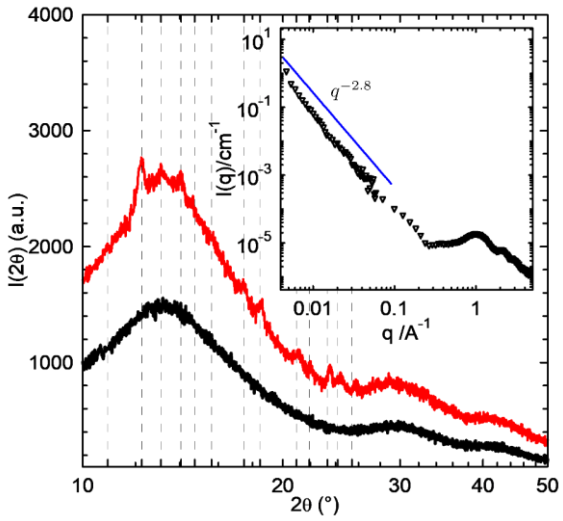

Figure S8. XRD pattern of thick PMMA samples without PR (black line) and with 6 wt% PR (red line) as well as the expected pattern of phenol red (gray vertical dashed lines). The inset shows the X-ray intensity of the pure PMMA sample over a wider q range (triangles, SAXS and XRD) and a theoretical intensity calculated for a mass fractal (blue line).

As can be seen in Figure S9a and b, the XRD patterns reveal no significant differences in the polymeric structure between the thin and thick PMMA samples prepared for lock-in thermography and Xenon flash analysis, respectively. In both cases, the small Bragg reflections base on the incorporated PR dye and increase slightly with increasing concentration of the dye. This shows that all samples exhibit a similar polymeric microstructure independent of the PR content, sample thickness, and preparation method (injection molding *vs.* doctor-blading).

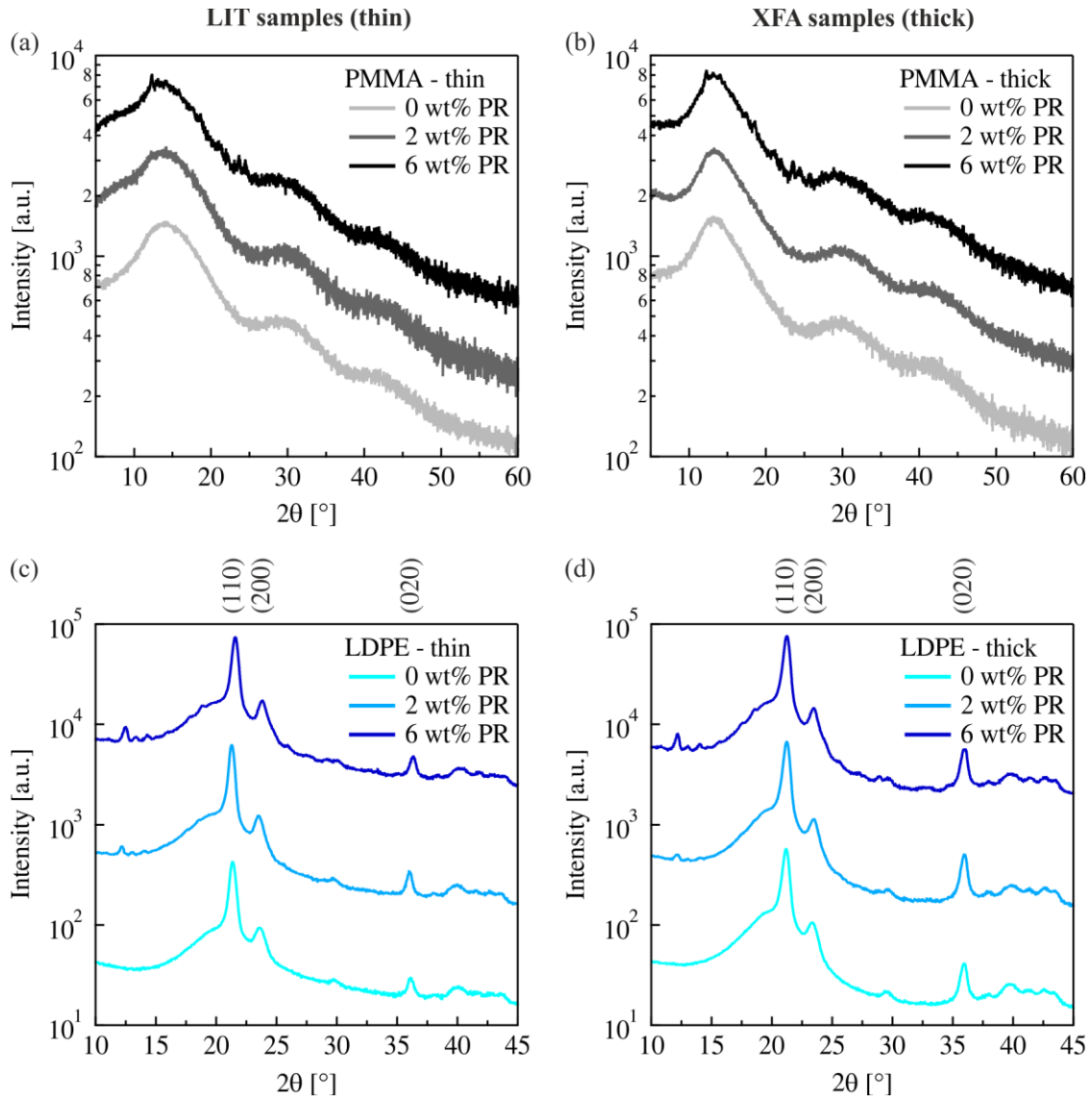

Figure S9. XRD curves of amorphous PMMA and semi-crystalline LDPE: a) thin PMMA used for lock-in thermography (LIT) measurements, and b) thick PMMA for Xenon flash analysis (XFA), c) thin LDPE for LIT measurements, and d) thick LDPE for XFA. Curves are presented with a vertical shift.

LDPE is a low-density, semi-crystalline polymer. The semi-crystallinity of the LDPE films is visible by the pronounced Bragg reflexes at 21.2° (100 % peak), 23.3° and 36.0° (Figure S9c and d). The reflections correspond to [110], [200], and [020] of space group Pnam. As expected, the PR doped films show additionally small Bragg spots due to the dye.

We found comparable degrees of crystallinity (~ 45%) for all LDPE samples. Consequently, the addition of phenol red does not affect the degree of crystallinity

of the LDPE samples. Furthermore, also the subsequent hot-pressing of the injection molded LDPE disks does not change the degree of crystallinity.

Usually, one expects for a semi-crystalline film that (i) the amorphous and crystalline regions are randomly distributed over the solid material (isotropy) and that (ii) the small crystallites are polydisperse. Nevertheless, due to external forces like shear stress or elevated temperatures phase segregation between the amorphous phase and the crystallites cannot be ruled out.

Consequently, we performed SAXS experiments in parallel and perpendicular beam geometries to study the in-plane and cross-plane polymeric microstructures, respectively. Figure S10 shows an example of such a study for the LDPE samples with 6 wt% PR. Astonishing, the SAXS patterns taken perpendicular exhibit a broad reflection at $q \approx 0.04$ Å^{-1}, which corresponds to a correlation length of about 15 nm and hints to a two-phase LDPE system (segregation of crystallites and amorphous LDPE). This feature is anisotropic spot-like for the thick sample (Figure S10a) and isotropic for the thin film (Figure S10b). As a consequence, the crystallites of the thick samples have a stronger tendency to align lamellar-like parallel to the sample surface (*i.e.*, in in-plane direction) compared to the thin samples.

In the mesoscopic scattering signals observed for the thick and thin samples in parallel beam geometry (Figure S10c and S10d), the oscillation at $q \approx 0.04$ Å^{-1} is attenuated, and the patterns appear more isotropic.

Thus, the thick samples (prepared for XFA) and thin films (prepared for LIT) exhibit a different microstructure despite their comparable degree of crystallinity. Both samples show a preferred orientation of the crystallites in the in-plane direction and more random orientation in the cross-plane direction. However, the anisotropy is much more pronounced for the thick samples. This difference in the microstructure may be associated with the different fabrication processes and the

applied temperature gradients (injection molding *vs.* injection molding and subsequent hot-pressing).

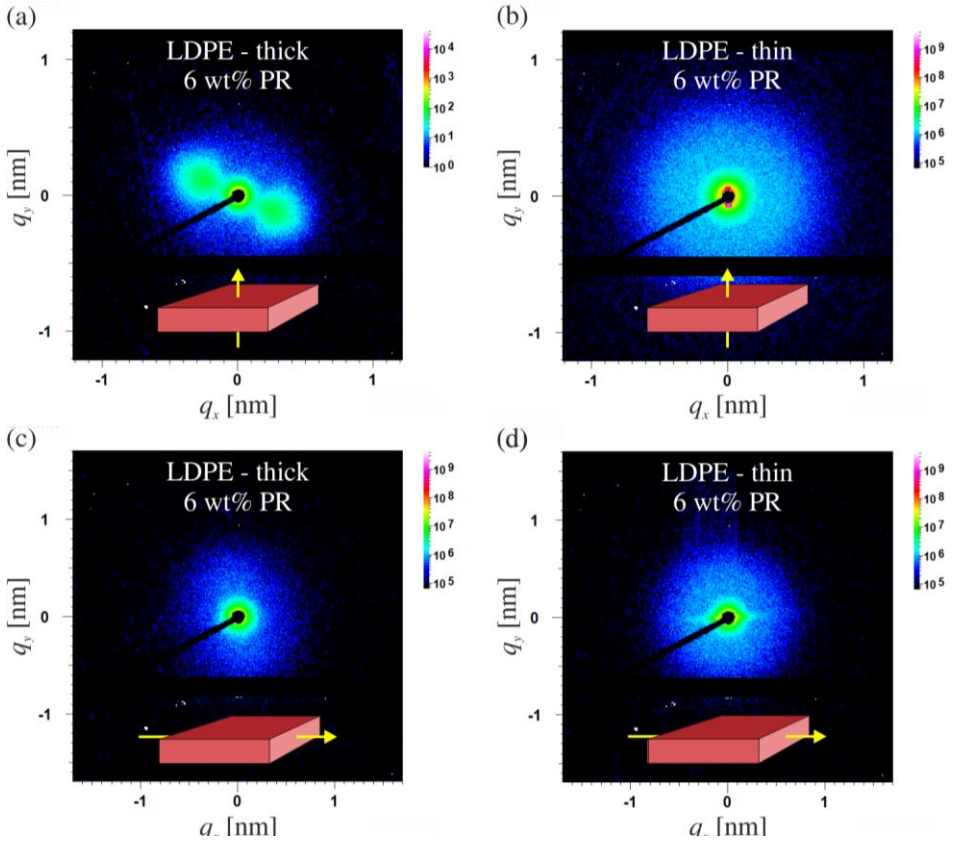

Figure S10. 2D SAXS patterns of LDPE films with 6 wt% PR in perpendicular (a, b) and parallel (c, d) beam geometry (see sketch: sample with beam direction).

In Figure S11 the two-dimensional SAXS data of a thick LDPE sample as used for XFA and after additional annealing at 90 °C for one week are compared to illuminate the effect of the temperature/fabrication method on the orientation of the crystallites. All annealed samples show a significantly more preferred orientation of the crystallites compared to the non-annealed state. Note, that the spots appear even triangular for the data of the annealed film in perpendicular geometry and at the same time, the amorphous halo is less pronounced. We conclude that a direction dependent crystal growth is introduced by thermal annealing. The same trend is observed in case of the thin films, but much less pronounced.

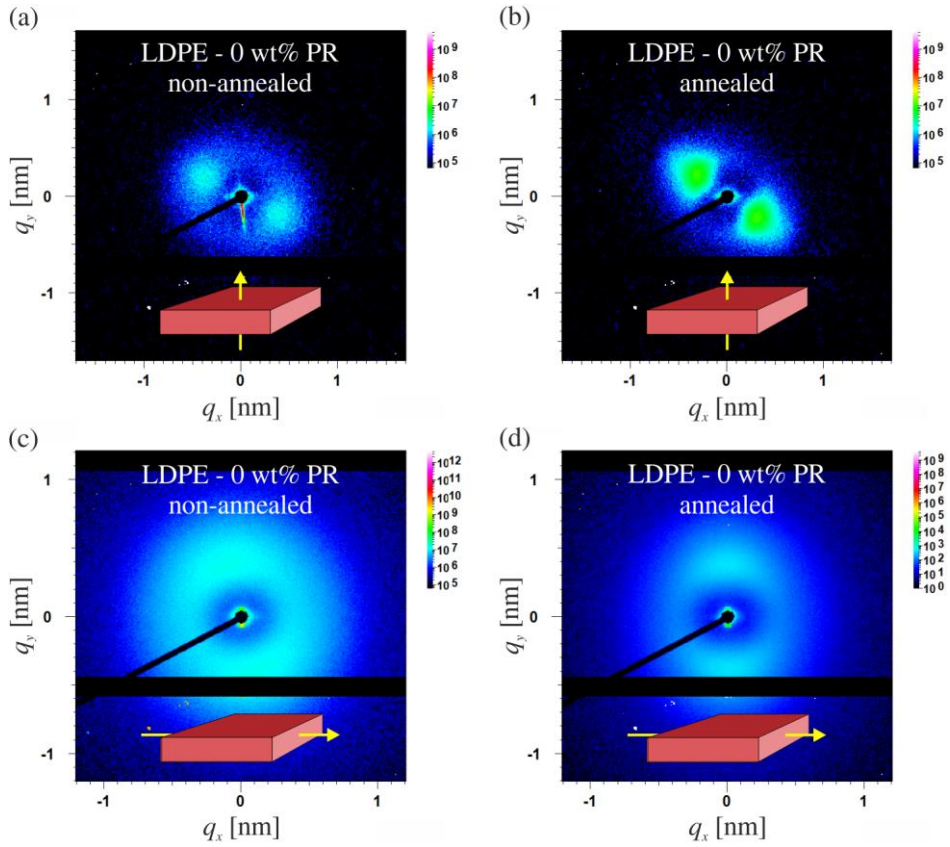

Figure S11. 2D SAXS patterns of thick LDPE samples (for XFA) with 0 wt% PR in perpendicular (a, b) and parallel (c, d) beam geometry (see sketch: sample with beam direction).

5) Comparison of Thermal Diffusivity Data (LIT vs. XFA)

Figure S12 summarizes the thermal diffusivity values obtained for the fabricated PMMA and LDPE samples with 0, 2, and 6 wt% PR, respectively. The *in-plane* thermal diffusivity of the thin, free-standing samples was determined using lock-in thermography (LIT). The 1 mm thick reference samples were characterized using Xenon flash analysis (XFA). It is to be noted that this measurement technique gives the *cross-plane* thermal diffusivity.

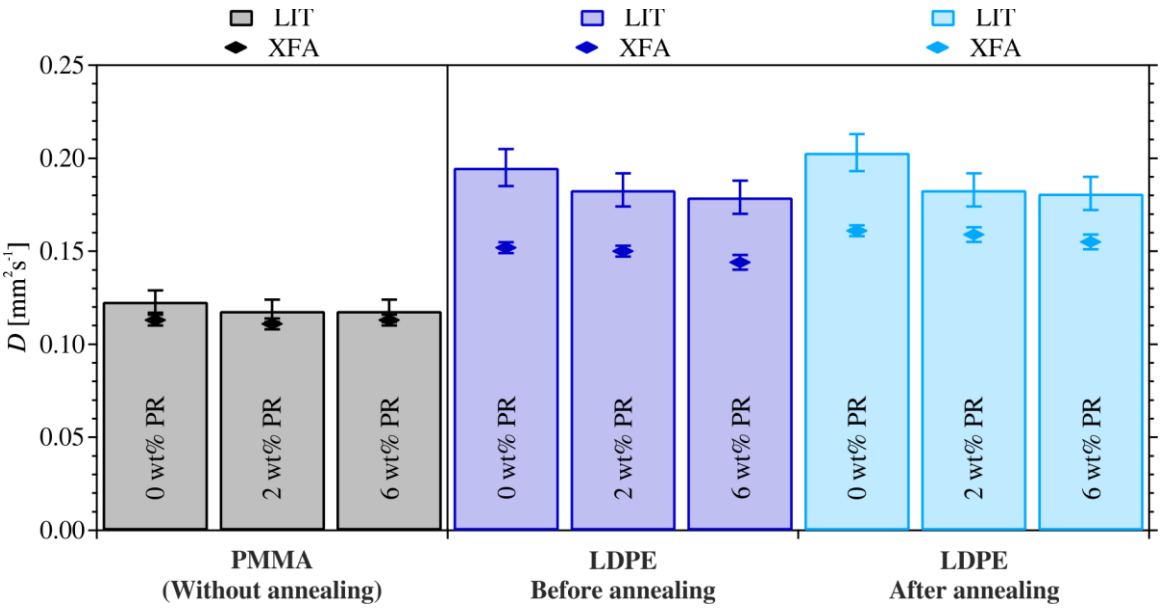

Figure S12. Thermal diffusivity *D* of PMMA and LDPE with 0, 2, and 6 wt% phenol red (PR), respectively. The thin samples (~ 200 µm) were measured with lock-in thermography ((LIT), bars) that determines the in-plane thermal diffusivity; the thick samples (~ 1 mm) were analyzed with Xenon flash analysis ((XFA), markers) that gives the cross-plane thermal diffusivity. LDPE samples were measured before and after thermal annealing (90 °C, one week). The error bars arise from 5 % uncertainty (LIT) and from the standard deviation of the averaged value (XFA). Two to three samples were measured in each case.

As discussed in the main text, we obtain an in-plane thermal diffusivity of ~ 0.12 mm^2s^{-1} for all PMMA samples independent of the PR content. The cross-plane values obtained from XFA are ~ 0.11 mm^2s^{-1}, and thus close to the data obtained from LIT. This good agreement confirms that the microstructure of the amorphous polymer is similar (see XRD curves in Figure S8, Figure S9a and S9b) leading to isotropic thermal diffusivity values.

However, in the case of LDPE (before annealing), we extracted significantly lower cross-plane thermal diffusivities from XFA (~ 20 %). We relate this discrepancy to the difference in the underlying microstructure as discussed above. Since the degree of crystallinity of all samples is the same, the preferred in-plane orientation leads apparently to a reduced cross-plane thermal diffusivity as measured by XFA. Thermal annealing at 90 °C for one week led to a more pronounced anisotropy within the thick films. In comparison to the values before thermal annealing, we

obtained similar in-plane thermal diffusivity values from LIT and slightly higher cross-plane thermal diffusivity values from XFA after annealing.

In summary, we found that comparable in-plane and cross-plane thermal diffusivity values are obtained for an amorphous polymer independent of the fabrication method. In case of a semi-crystalline polymer, the fabrication method has a strong influence on the polymer microstructure, and thus on the in-plane and cross-plane thermal diffusivity, which renders a quantitative comparison difficult.

References

1. Pech-May, N. W.; Mendioroz, A.; Salazar, A., Simultaneous measurement of the in-plane and in-depth thermal diffusivity of solids using pulsed infrared thermography with focused illumination. *Independent nondestructive testing and evaluation* **2016,** *77*, 28-34.

2. Kanstad, S. O.; Nordal, P.-E., Experimental aspects of photothermal radiometry. *Canadian Journal of Physics* **1986,** *64* (9), 1155-1164.

3. Salazar, A.; Mendioroz, A.; Fuente, R., The strong influence of heat losses on the accurate measurement of thermal diffusivity using lock-in thermography. *Applied Physics Letter* **2009,** *95* (12).

4. Walther, H. G.; Seidel, U.; Karpen, W.; Busse, G., Application of modulated photothermal radiometry to infrared transparent samples. *Review of Scientific Instruments* **1992,** *63* (11), 5479-5480.

5. Mendioroz, A.; Fuente-Dacal, R.; Apinaniz, E.; Salazar, A., Thermal diffusivity measurements of thin plates and filaments using lock-in thermography. *Review of Scientific Instruments* **2009,** *80* (7), 074904.

11. Anisotropic Thermal Transport in Spray-Coated Single-Phase Two-Dimensional Materials: Synthetic Clay vs. Graphene Oxide

Alexandra Philipp[1,2,‡], Patrick Hummel[1,2,‡], Theresa Schilling[1,2], Patrick Feicht[1,2], Sabine Rosenfeldt[1,2], Michael Ertl[1,2], Anna M. Lechner[1,2], Zhen Xu[3], Chao Gao[3], Josef Breu[1,2,*], and Markus Retsch[1,2*]

[‡] *These authors contributed equally to the work.*

[1]Department of Chemistry, University of Bayreuth, Universitätsstraße 30, 95447 Bayreuth, Germany

[2]Bavarian Polymer Institute, University of Bayreuth, Universitätsstraße 30, 95447 Bayreuth, Germany

[3]Department of Polymer Science and Engineering, Zhejiang University, 38 Zheda Road Hangzouh, Zhejiang 310027, China

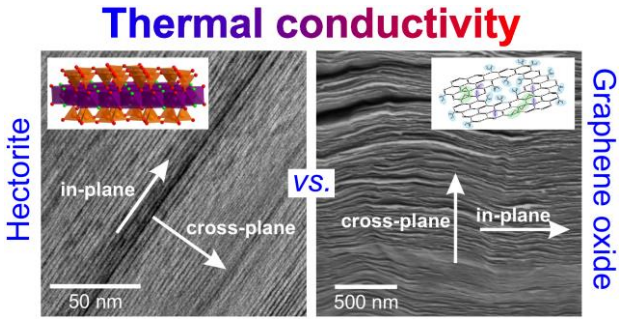

Reprinted with permission from Philipp *et al.*, *ACS Appl. Mater. Interf.*, **2020**, 12, 18785-18791.

Abstract

Directional control on material properties such as mechanical moduli or thermal conductivity are of paramount importance for the development of nanostructured next generation devices. Two-dimensional materials are particularly interesting in this context owing to their inherent structural anisotropy. Here, we compare graphene oxide (GO) and synthetic clay sodium fluorohectorite (Hec) with respect to their thermal transport properties. The unique sheet structure of both allows preparing highly ordered Bragg stacks of these pure materials. The thermal conductivity parallel to the platelets strongly exceeds the thermal conductivity perpendicular to them. We find a significant difference in the performance between GO and synthetic clay. Our analysis of the textured structure, size of the platelets and chemical composition shows that Hec is a superior two-dimensional component compared to GO. Consequently, synthetic clay is a promising material for thermal management applications in electronic devices, where electrically insulating materials are prerequisite.

1. Introduction

Modern electronics crucially depend on materials and structures that are capable of dissipating their ever-increasing thermal energy density. Materials with a high thermal conductivity manage to divert heat away from hot spots efficiently. At the same time, the thermal management in the entire device needs to be considered, where areas of high and low-temperature tolerance may be located in close vicinity.[1] Consequently, materials that are capable of directing the flow of heat are required. Two-dimensional (2D) materials with an anisotropic thermal conductivity match this requirement.[2] Well-known representatives of such materials are graphite[3] and graphene[4]. Both exhibit a high in-plane thermal conductivity, while the cross-plane thermal conductivity is much lower. However, they are both also electrically conductive and consequently not suitable in most

electronic applications. To prevent shortcuts the use of nonconductive materials is mandatory. This demand is represented in the field of thermal interface materials.[5-6] The right selection of matrix and filler, as well as the processing and structure formation are essential for achieving an optimum performance.[7-8]

Two materials have been widely used to prepare electrically nonconductive composites with anisotropic thermal conductivity, namely graphene oxide (GO) and the graphene analog hexagonal boron nitride (hBN). Strong oxidation of graphite allows for the water processability of GO, but significantly reduces the in-plane thermal conductivity compared to graphite/graphene. The degree of oxidation relates to the in-plane thermal conductivity.[9] In most cases GO is reduced (rGO) to restore the high in-plane thermal conductivity partially. Concomitantly, the electrical conductivity increases.[10-13] Consequently, the anisotropy ratios (*i.e.*, the ratio between in-plane and cross-plane thermal conductivity) in GO-based materials depend on the oxidation state and can reach values of 19 for GO[9] and up to 675 for rGO[10]. An additional drawback of this reduction step is the necessity to apply either reducing chemicals (such as hydrazine) or high thermal temperatures, which both needed to be tolerated by the entire devices or composite.

The structure and properties of hBN are comparable to graphite/graphene. The most significant difference exists in the electrical conductivity. In comparison to graphene, hBN is not electrically conductive. The thermal transport properties, however, are comparable. Meaning a high in-plane thermal transport and, therefore, a high anisotropic thermal conductivity. A fundamental study of bulk single crystalline hBN demonstrated a promising anisotropy ratio of 87.5.[14] However, the sample was a 1-mm-sized flake, and it is, yet, not possible to produce large-area samples of single-crystalline hBN. Nevertheless, hBN can be mixed with polymers to achieve composite materials. In contrast to GO, hydrophobic hBN is still challenging to fully exfoliate, especially in water. A simple sonication assisted hydrolyzation process in water leads only to a mixture of monolayers and

multilayers.[15] Therefore, studies about the anisotropic thermal conductivity of hBN/polymer composites lack structural control and cannot reach the value of the single crystal.[16-20] A maximum ratio up to 39 could be realized by stretching the composite, which improves the alignment and therefore demonstrates the difficulty in controlling the composite structure during processing.[19]

Synthetic clays are less known materials in the context of thermal interface materials. Nevertheless, this material class offers a range of advantages particularly regarding the structural control of the assembled composite structure. Due to superior control over the aspect ratio and the delamination process, highly ordered composites with outstanding mechanical,[21-23] gas barrier[24-25], and fire resistance[22-23] properties have already been realized. Additionally, the high phase purity of Hec leads to optically clear and transparent films, which is relevant for optical applications. Furthermore, ultralow cross-plane thermal conductivity was demonstrated in organoclays[26] and hybrid Bragg stacks[27]. Although this hints towards the high potential of this material class for high anisotropic thermal conductivity, little is known about the direction-dependent heat spreading in the pure filler components.

Our contribution aims to close this knowledge gap. We focus on pure, single-phase components to elaborate the fundamental filler properties without introducing additional complications originating from filler/matrix interactions. Our study bases on a synthetic clay sodium fluorohectorite of different platelet diameter. For a better classification of this unnoticed material in the context of anisotropic thermal conductivity, we compare our results to two types of GO samples stemming from different sources.

2. Results and Discussion

Our investigation bases on four samples: synthetic sodium fluorohectorite (Hec, $[Na_{0.5}]^{inter}[Mg_{2.5}Li_{0.5}]^{oct}[Si_4]^{tet}O_{10}F_2$) in its native form termed Hec-L, consisting of large platelets (tens of μm in lateral size) and Hec-S, consisting of small platelets (sub-μm) received after sonication of Hec-L. We compare the Hec samples to GO, which was synthesized following a modified Hummers/Offeman procedure[28] termed GO-syn, and a commercially available GO, termed GO-com. In all samples, we focus on the contribution of the platelet dimension, platelet defect concentration and chemical composition on the thermal transport anisotropy. All materials were processed by spray coating of a dilute aqueous dispersion (0.5 wt%) onto a substrate (polyethylene terephthalate (PET) film or glass). Thereby, the Hec and GO sheets align parallel to the substrate introducing a macroscopic orientation to the individual nanosheets. After drying for 5 h at 100 °C, free-standing samples were obtained by peeling off the films from PET. These films were used to determine the in-plane thermal conductivity by lock-in thermography. The cross-plane thermal conductivity was measured using the photoacoustic method with thin films immobilized on a glass substrate. The obtained thermal conductivity values are summarized in Figure 1a. We found comparable in-plane and cross-plane thermal conductivities for Hec-L (in-plane: 5.7±0.1 $Wm^{-1}K^{-1}$, cross-plane: 0.21±0.03 $Wm^{-1}K^{-1}$) and for Hec-S (in-plane: 5.6±0.2 $Wm^{-1}K^{-1}$, cross-plane: 0.18±0.02 $Wm^{-1}K^{-1}$). Compared to literature values of related structures, the in-plane thermal transport of our pure Hec samples is exceptionally high. Muscovite and biotite single crystals show in-plane thermal conductivities of 3.89 $Wm^{-1}K^{-1}$ and 3.14 $Wm^{-1}K^{-1}$, respectively.[29] The thermal conductivity of a montmorillonite sample, which was prepared from a suspension of delaminated platelets showed an in-plane conductivity of only 1.92 $Wm^{-1}K^{-1}$.[30] The high in-plane thermal conductivity of pure Hec is very promising in the context of heat spreading, particularly since this high value is obtained without any further processing of the

spray-coated film. By contrast the cross-plane thermal conductivity of muscovite and biotite are 0.62 $Wm^{-1}K^{-1}$ and 0.52 $Wm^{-1}K^{-1}$, respectively,[29] and therefore more than twice as high as in our synthetic Hec samples. The montmorillonite sample, by contrast, has a cross-plane thermal conductivity of 0.2 $Wm^{-1}K^{-1}$,[30] which is comparable to our samples.

The in-plane and cross-plane thermal conductivities of the as-prepared GO samples are both lower compared to the clay samples. The in-plane values are 1.7±0.1 $Wm^{-1}K^{-1}$ for GO-syn and 1.0±0.1 $Wm^{-1}K^{-1}$ for GO-com, while the cross-plane values are 0.12±0.01 $Wm^{-1}K^{-1}$ and 0.13±0.01 $Wm^{-1}K^{-1}$, respectively. The values of the cross-plane thermal conductivity are comparable to reports in literature of 0.18 $Wm^{-1}K^{-1}$ [10] and 0.15 $Wm^{-1}K^{-1}$.[9] The in-plane thermal conductivities show a much higher degree of variability. Renteria *et al.* reported a value of 2.94 $Wm^{-1}K^{-1}$,[10] which is almost twice as high as the value for GO-syn. Meng *et al.* measured a value of 1.6 $Wm^{-1}K^{-1}$,[9] which is in good agreement with our value for GO-syn. The variation of the GO results indicates that the in-plane thermal conductivity is strongly sensitive to the exact synthesis and preparation of the GO samples. This result is in line with reported large spreads of in-plane moduli ranging from 170 GPa to 530 GPa[28], which was attributed to holes formed in the GO sheets due to overoxidation as proposed by Hofmann et al.[31] This variation is also visible in the specific heat capacity (Figure 1b). Both Hec samples have comparable heat capacity, whereas GO-com has a higher heat capacity than GO-syn.

The Hec films exhibit a two – threefold higher anisotropy ratio ($\kappa_{in\text{-}plane}/\kappa_{cross\text{-}plane}$) of thermal conductivity compared to the GO samples (grey numbers in Figure 1a). The anisotropy ratio of the GO-syn sample of 14 is in good agreement with other studies[10], which reported a ratio of 16, while the anisotropy of GO-com (8) is even lower. The anisotropy values of the synthetic Hec (~30) exceed the anisotropy ratios of natural clays, like boom clay[32] (~1.7). Even the literature values of well-

oriented samples like muscovite (6.3)[29], biotite (6.0)[29], and montmorillonite (9.6)[30] hardly compare to the anisotropy in our synthetic structure. The superior anisotropy underlines the very high textured orientation of our structure.

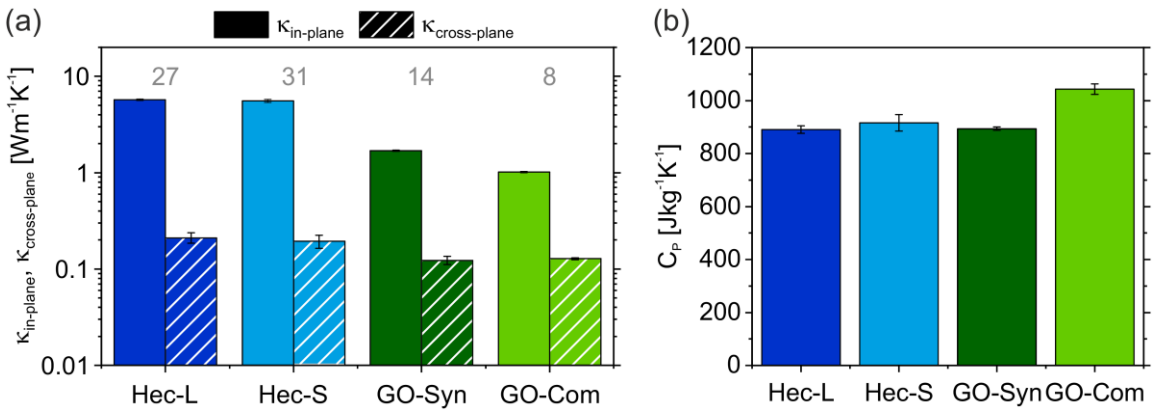

Figure 1. Thermal properties: a) In-plane ($\kappa_{in\text{-}plane}$) and cross-plane ($\kappa_{cross\text{-}plane}$) thermal conductivity. The numbers in the graph represent the anisotropy ratio of the thermal conductivity ($\kappa_{in\text{-}plane}/\kappa_{cross\text{-}plane}$). b) Specific heat capacity (C_p).

We next focus on the structure and composition of the samples under investigation to work out any potential influence on the thermal conductivity. Hec belongs to the trioctahedral 2:1 smectite family and shows a sandwich-like structure comprising two tetrahedral and one octahedral layer (Figure 2a) with the nominal composition of $[Na_{0.5}]^{inter}[Mg_{2.5}Li_{0.5}]^{oct}[Si_4]^{tet}O_{10}F_2$. The thickness of an individual Hec platelet is ≈10 Å (Figure 2b). The synthetic Hec applied here, has been shown to delaminate into individual single layers by repulsive osmotic swelling when immersed in deionized water.[33] For well-controlled delamination, a uniform intracrystalline reactivity is prerequisite, which comes along with phase purity and a homogeneous charge density. For synthetic Hec, this is achieved by a melt synthesis followed by long-term annealing. The delamination was studied by small-angle X-ray scattering (SAXS). The high orientational lamellar order in liquid crystals leads typically to (a) anisotropic 2D scattering patterns and (b) a rational series of *00l*-reflections due to the defined interlayer spacing d at $d=2\pi/q$. Further, in that case the swelling behavior of 2D lamellae with volume fraction Φ and thickness t is expected to be $d=t/\Phi$.[34] The homogeneous intracrystalline reactivity

assures a rational *00l*-series with adjacent Hec nanosheets being separated in suspension to 53 ± 6 nm (3 wt%) and 38 ± 4 nm (5 wt%) for Hec-L and Hec-S, respectively (Figure 2c). Due to the hindered polar rotation of Hec nanosheets in suspension, these Hec suspensions represent nematic phases. The observable rational series up to six higher-order reflections emphasize the superior positional order of adjacent individual nanosheets. The high positional order is further proved by an anisotropic 2D scattering pattern (Figure S1). Spray coating these nematic phases of dilute Hec suspensions led to homogeneous, one-dimensional (1D) crystalline structures (smectic films) comprised of largely overlapping individual sheets forming quasi-single crystalline band-like films.[27]

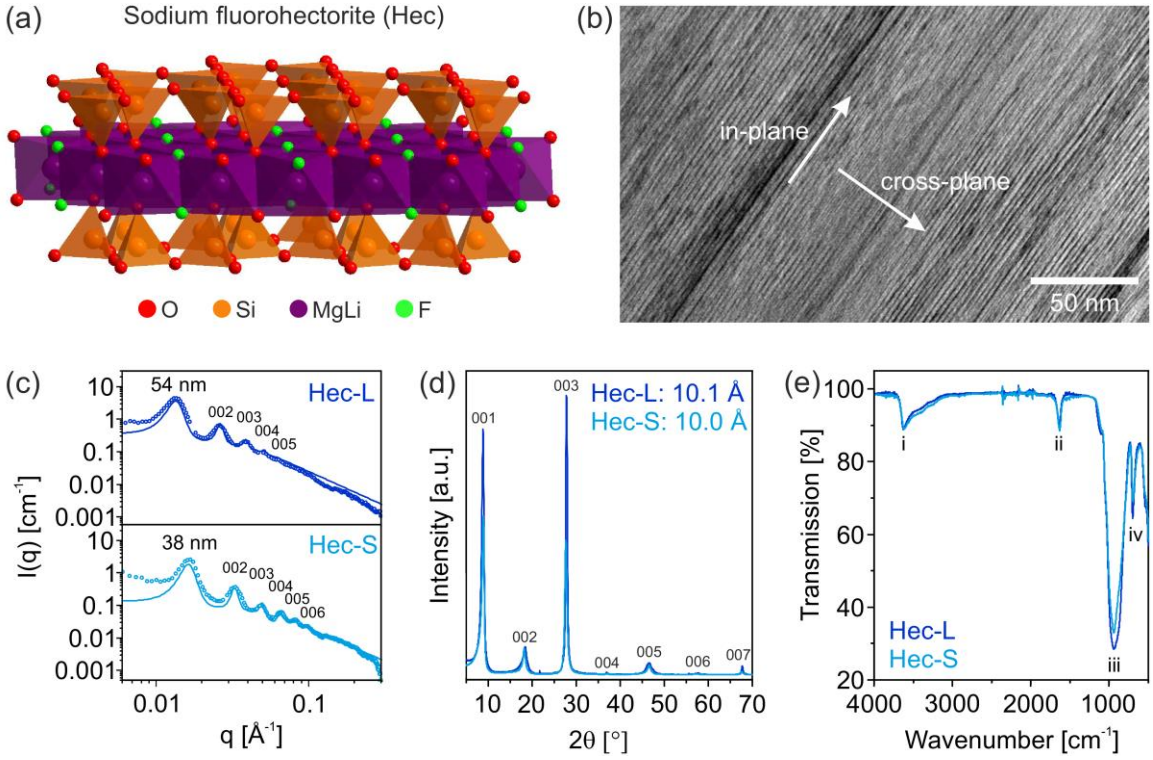

Figure 2. a) Structure of a sodium fluorohectorite (Hec) platelet. Sodium counter ions are located between two Hec platelets. b) A cross-sectional TEM image of an aligned smectic Hec film. White arrows illustrate the in-plane and cross-plane direction. c) SAXS results of aqueous Hec suspensions showing a rational series of 00l reflections. d) XRD patterns of the free-standing Hec films showing intense 00l-reflections. Both samples have a basal spacing around 10 Å. e) IR spectra prove the same chemical composition of both samples.

The exceptional periodic homogeneity can be seen from the cross-sectional transmission electron microscopy (TEM) image (Figure 2b). The white arrows

highlight the directions of the in-plane and cross-plane thermal conductivity measurements, respectively. X-ray diffraction (XRD) patterns (Figure 2d) of both samples show a rational *00l*- series up to the seventh order with sharp and intense basal reflections after spray-coating. The quality of the 1D crystalline order is further confirmed by a low coefficient of variation of the *00l*- series (Table S1) and a small full width at half maximum. Furthermore, both Hec-L and Hec-S samples have a comparable basal spacing of ≈ 10 Å in the dry state, which represents the periodicity along the stacking direction. In Figure S2 the platelet area, measured by scanning electron microscopy (SEM) followed by evaluating the area with ImageJ, are compared for samples Hec-L and Hec-S. Sample Hec-L (Figure S3), which was used as received from the synthesis, consists of large platelets with areas up to 800 μm^2. We fabricated Hec-S from Hec-L by ultrasound treatment, which reduced the platelet area by more than three orders of magnitude (< 0.4 μm^2, Figure S2 and Figure S3). Due to the ultrathin platelet thickness of 1 nm, both samples still have a high aspect ratio (20000 and 300, respectively). The sonication procedure for platelet-size reduction leaves the structure and chemical composition of Hec unaltered. Infrared (IR) spectroscopy (Figure 2e) and X-ray photoelectron spectroscopy (XPS) spectra (Figure S5) of both samples were measured to demonstrate this. In case of IR spectroscopy four main signals are visible which correspond to (i) OH stretching vibrations of water or cation-OH stretching vibrations at platelet edges, (ii) OH-bending vibrations of water, (iii) stretching vibration of SiO-groups in tetrahedral sheets, and (iv) bending vibration of SiO-groups and stretching vibration of MgF-groups in octahedral sheets.[35-37] Hec-L and Hec-S show good quantitative agreement of all these characteristic absorption peaks. Similarly, fitting of the element-specific bands in the XPS measurement results in comparable atomic ratios. Overall, sonication of Hec-L only reduced the size of the Hec platelets and did not affect the self-assembly, *i.e.*, the basal spacing and order, as well as the chemical composition.

Counterintuitively, we found that small Hec sheets are still great in-plane conductors. This can be explained by an in-plane mean free path that is still orders of magnitude smaller than the average platelet diameter. Consequently, boundary effects become negligible, which would typically lead to reduced thermal conductivity.[27]

For GO, it is not possible to provide a chemical formula. Its chemical structure is based on graphene, but GO is ill-defined, and the number of defects, *i.e.*, vacancies/holes in the 2D structure and functional groups, strongly depend on the synthesis route.[28] Figure 3a shows an exemplary structure of GO having various functional defects (epoxide, hydroxyl, and carboxylic groups) as well as a hole.[31, 38] SAXS was used to further investigate the graphene oxide dispersions of about 3.5 wt%. Diluted graphene oxide dispersions are expected to form nematic liquid crystalline phase in water via ordering of the sheets.[39] The scattering intensity $I(q)$ of the two GO suspensions decrease with the scattering vector q, following a q^{-2} power law (Figure 3c). This scaling law is typically obtained for platelet-shaped scattering objects and proves the 2D morphology of the dispersed graphene oxide layers. The graphene oxide dispersions exhibit an anisotropic 2D SAXS pattern (Figure S1), indicating a nematic orientation. In contrast, Hec in a similar concentration shows additionally a series of *00l* reflection.[34] The absence of these reflections in case of GO is mainly attributed to a much more pronounced dislocation of the lamellar order by slipping or tilting of the individual GO layers. This strongly hints to a more heterogeneous charge distribution of the graphene oxide sheets. Similar to the Hec samples, spray coating of dilute GO dispersions led to aligned stacks of overlapping individual sheets, as can be seen from the SEM image (Figure 3b). The white arrows highlight the directions of the in-plane and cross-plane thermal conductivity measurements, respectively. The XRD patterns in Figure 3d show one weak, a rather broad peak at 6 Å[40] and no higher-order peaks as typical for randomly interstratified structures with varying layer

separation. Thus, the stacking of the spray-coated GO sheets is less well-defined compared to the Hec platelets. Furthermore, the GO layers (~ 6 Å) are thinner than the Hec platelets (~ 10 Å). The analysis of the sheet area (Figure S2) revealed that GO-syn is much smaller than Hec-L, whereas GO-com is comparable to Hec-L, but very broadly distributed (Figures S3 and S4). Both GO samples are, however, much larger compared to Hec-S. Additionally, we measured Raman spectra (Figure S7) and XPS (Figure 3e and Figure S6) to analyze the degree of functional defects of the GO samples. The intensity ratios of the D and G band (I_D/I_G) of both samples are around 1, which is a measure for a high number of defects within the graphene-based structure. The overview XPS spectra (Figure S6) reveal the presence of carbon (C), oxygen (O), and sulfur (S). The latter stems from sulfate groups and is typical for GO made by Hummers/Offeman protocols.[28] Integrating over the various C-1s species revealed that the main difference between the GO samples is the ratio of pristine sp^2 *vs.* oxygenated C atoms. Figure 3e shows the C1s XPS spectra of GO-syn and GO-com. Three main peaks are visible, which are assigned to double-bonded carbon-oxygen (C=O; ≈ 288.3 eV), single-bonded carbon-oxygen (C-O; ≈ 286.8 eV), and sp^2 and sp^3 carbon (C=C/C-C; ≈ 284.7 eV).[10] GO-com has a higher amount of oxygen-containing functional groups such as hydroxyl, epoxide, carbonyl, and carboxyl groups compared to GO-syn.

Since we found a two times lower in-plane thermal diffusivity for GO-com in comparison to GO-syn, we conclude that the difference in the degree of oxidation has a high impact on the in-plane thermal transport. These findings also support the results of Meng *et al*.[9] They investigated GO samples with different degrees of oxidation. In agreement with our findings, the sample with a higher degree of oxidation showed a lower thermal conductivity. The reason is the decrease in sp^2 cluster size with an increasing amount of oxygen in the structure and holes in the 2D structure produced by overoxidation.[31] Consequently, phonon scattering is enhanced by the likewise increased sp^2/sp^3 boundaries.[9]

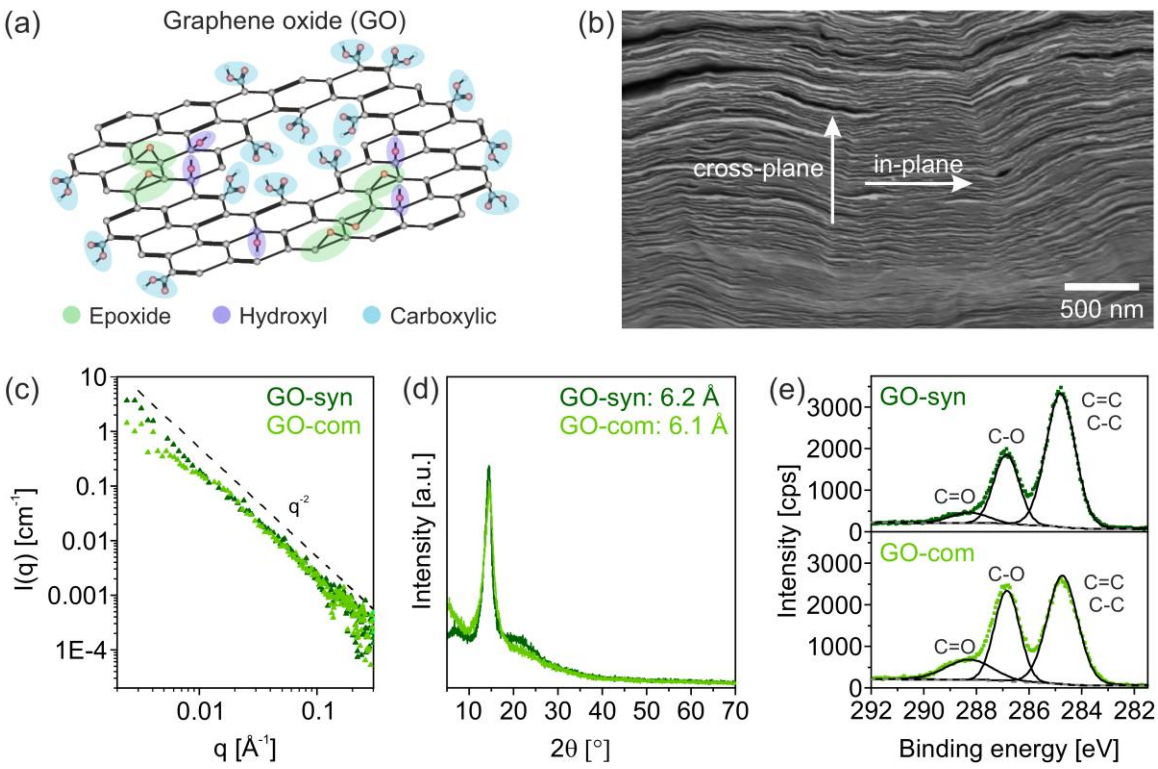

Figure 3. a) Exemplary structure of graphene oxide (GO). b) SEM image of an aligned GO film. White arrows illustrate the in-plane and cross-plane direction. c) SAXS results of GO suspensions showing a q^{-2} scaling of the scattering intensity. d) XRD patterns show no long-range order. Both samples have a spacing of approximately 6 Å. e) XPS data of the carbon signatures.

3. Conclusion

In this study, we investigated the anisotropic thermal transport properties of thin films of synthetic clay sodium fluorohectorite (Hec) films and graphene oxide (GO). Whereas these materials are often used in the context of nanocomposite materials, we focused on the pure phase components and their thermal transport properties. The properties of such 2D materials are strongly governed by the chemical composition, vacancy defects in the layer structure, and the platelet size. We, therefore, determined the thermal transport properties of four different samples. All of them were fabricated into (free-standing) thin films via spray coating of diluted dispersions of Hec and GO, respectively. The superior long-range order in Hec films results in a significantly higher anisotropy ratio compared to the GO samples. Quite remarkably, the in-plane thermal conductivity reaches

very high values of up to 5.7 $Wm^{-1}K^{-1}$, which makes Hec an attractive material for heat spreading applications. GO in its oxidized form as received directly after spray coating features in-plane thermal conductivities on the order of only 1 $Wm^{-1}K^{-1}$. The thermal transport properties are strongly affected by the chemical composition of the GO samples. In particular, the in-plane thermal conductivity is reduced with an increasing degree of functional groups containing oxygen. The cross-plane thermal conductivity is hardly affected and remains at a low value of ~ 0.12 $Wm^{-1}K^{-1}$. Surprisingly, the platelet size does not influence the in-plane thermal conductivity, which can be concluded from comparing Hec-L and Hec-S films. The chemical composition remained unaltered between large and small platelets of Hec. However, even though the platelet diameters were drastically reduced by approximately two orders of magnitude, the superior in-plane heat spreading properties were retained.

Overall, anisotropic heat transport is gaining increased attention in applications of thermal interface materials or heat management in light-emitting diodes or batteries. Our contribution provides a better understanding of the interplay between platelet size and chemical composition on the direction-dependent thermal conductivity. Furthermore, synthetic hectorite is an up-and-coming alternative to the more established GO and hBN heat spreading materials.

4. Materials and Methods

Sample Preparation and Characterization

The synthetic clay sodium fluorohectorite (Hec, $[Na_{0.5}]^{inter}[Mg_{2.5}Li_{0.5}]^{oct}[Si_4]^{tet}O_{10}F_2$) was delaminated by immersing it into Millipore water (0.5 wt%). For the synthesis of the small Hec platelets (Hec-S), a 0.5 wt% suspension of Hec-L was sonicated in an ice bath with the ultrasonic device UIP 1000hd. GO-syn, based on Hummers/Offeman's method, was synthesized according to an established procedure.[28] GO-com was provided by Hangzhou Gaoxi Technology Co. Ltd.

(China). The self-supporting films and the thinner films sprayed on a glass substrate were prepared with a fully automatic spray coating system. Every spraying cycle is followed by a drying cycle of 90 s at a temperature of 55 °C. The films were characterized by X-ray diffraction, transmission electron microscopy, scanning electron microscopy, X-ray photoelectron, infrared, and Raman spectroscopy. Additional information about the sample preparation and characterization methods can be found in Section S1 (Supporting Information).

Thermal Conductivity Measurements

In-Plane Thermal Conductivity Measurements

Lock-in thermography measures the temperature spreading within thin, free-standing samples upon thermal excitation by an intensity-modulated, focused laser beam. Measurements are conducted in a vacuum to prevent heat losses due to conduction and convection. The amplitude and phase data are obtained from the temperature oscillations. The slope method for thermally thin films is used to calculate the in-plane thermal diffusivity from the linear profiles of the radial phase and amplitude profiles.[41] In combination with the density, determined by helium pycnometry, and the specific heat capacity, determined by differential scanning calorimetry, the in-plane thermal conductivity can be calculated. More details are provided in Section S2 (Supporting Information).

Cross-Plane Thermal Conductivity Measurements

The photoacoustic method exploits the photoacoustic effect to determine the thermal properties of a sample.[42-43] The sample is fixed to a gas-tight glass cell, filled with 20 psi helium. A modulated laser beam runs through the cell volume and periodically heats the transducer layer on top of the sample. The induced pressure change on the surface of the sample leads to an acoustic wave propagating into the gas. A microphone, coupled to a lock-in amplifier, detects the phase shift between

the acoustic signal and the modulated laser dependent on the frequency. By comparing the data to a multilayer model, describing the temperature distribution in the sample, the total layer resistance of the sample is obtained. Together with the film thickness determined by atomic force microscopy, the effective thermal conductivity is calculated. Details about the photoacoustic characterization can be found in Section S2 (Supporting Information).

Supporting Information

Detailed information on the material fabrication and characterization, Section S1. Material synthesis, film preparation, SAXS, XRD, TEM, SEM, XPS, RAMAN, IR analysis and instruments used. Detailed information on the thermal conductivity characterization, Section S2. He-pycnometry, DSC, lock-in thermography and photoacoustic characterization.

Acknowledgements

The Volkswagen Foundation funded this project through a Lichtenberg professorship. Additional support was provided by the German Research Foundation through DFG RE3550/2-1. Kai Herrmann is acknowledged for discussions on the PA method.

References

1. Barako, M. T.; Gambin, V.; Tice, J., Integrated nanomaterials for extreme thermal management: a perspective for aerospace applications. *Nanotechnology* **2018,** *29* (15), 154003.

2. Song, H.; Liu, J.; Liu, B.; Wu, J.; Cheng, H.-M.; Kang, F., Two-dimensional materials for thermal management applications. *Joule* **2018,** *2* (3), 442-463.

3. Xiang, J.; Drzal, L. T., Thermal conductivity of exfoliated graphite nanoplatelet paper. *Carbon* **2011,** *49* (3), 773-778.

4. Zhang, Y.; Edwards, M.; Samani, M. K.; Logothetis, N.; Ye, L.; Fu, Y.; Jeppson, K.; Liu, J., Characterization and simulation of liquid phase exfoliated graphene-based films for heat spreading applications. *Carbon* **2016,** *106*, 195-201.

5. Razeeb, K. M.; Dalton, E.; Cross, G. L. W.; Robinson, A. J., Present and future thermal interface materials for electronic devices. *Int. Mater. Rev.* **2018,** *63* (1), 1-21.

6. Swamy, M. C. K.; Satyanarayan, A review of the performance and characterization of conventional and promising thermal interface materials for electronic package applications. *J. Electron. Mater.* **2019,** *48* (12), 7623-7634.

7. Prasher, R., Thermal interface materials: historical perspective, status, and future directions. *Proceedings of the IEEE* **2006,** *94* (8), 1571-1586.

8. McNamara, A. J.; Joshi, Y.; Zhang, Z. M., Characterization of nanostructured thermal interface materials – A review. *International Journal of Thermal Sciences* **2012,** *62*, 2-11.

9. Meng, Q.-L.; Liu, H.; Huang, Z.; Kong, S.; Jiang, P.; Bao, X., Tailoring thermal conductivity of bulk graphene oxide by tuning the oxidation degree. *Chin. Chem. Lett.* **2018,** *29* (5), 711-715.

10. Renteria, J. D.; Ramirez, S.; Malekpour, H.; Alonso, B.; Centeno, A.; Zurutuza, A.; Cocemasov, A. I.; Nika, D. L.; Balandin, A. A., Strongly anisotropic thermal conductivity of free-standing reduced graphene oxide films annealed at high temperature. *Adv. Funct. Mater.* **2015,** *25* (29), 4664-4672.

11. Song, N.; Jiao, D.; Ding, P.; Cui, S.; Tang, S.; Shi, L., Anisotropic thermally conductive flexible films based on nanofibrillated cellulose and aligned graphene nanosheets. *Journal of Materials Chemistry C* **2016,** *4* (2), 305-314.

12. Song, N.; Jiao, D.; Cui, S.; Hou, X.; Ding, P.; Shi, L., Highly Anisotropic thermal conductivity of layer-by-layer assembled nanofibrillated cellulose/graphene nanosheets hybrid films for thermal management. *ACS Appl Mater Interfaces* **2017,** *9* (3), 2924-2932.

13. Peng, L.; Xu, Z.; Liu, Z.; Guo, Y.; Li, P.; Gao, C., Ultrahigh thermal conductive yet superflexible graphene films. *Adv. Mater.* **2017,** *29* (27), 1700589.

14. Jiang, P.; Qian, X.; Yang, R.; Lindsay, L., Anisotropic thermal transport in bulk hexagonal boron nitride. *Physical Review Materials* **2018,** *2* (6), 064005.

15. Lin, Y.; Williams, T. V.; Xu, T.-B.; Cao, W.; Elsayed-Ali, H. E.; Connell, J. W., Aqueous dispersions of few-layered and monolayered hexagonal boron nitride nanosheets from sonication-assisted hydrolysis: critical role of water. *The Journal of Physical Chemistry C* **2011,** *115* (6), 2679-2685.

16. Xie, B.-H.; Huang, X.; Zhang, G.-J., High thermal conductive polyvinyl alcohol composites with hexagonal boron nitride microplatelets as fillers. *Compos. Sci. Technol.* **2013,** *85*, 98-103.

17. Zeng, X.; Ye, L.; Yu, S.; Li, H.; Sun, R.; Xu, J.; Wong, C.-P., Artificial nacre-like papers based on noncovalent functionalized boron nitride nanosheets with excellent mechanical and thermally conductive properties. *Nanoscale* **2015,** *7* (15), 6774-6781.

18. Huang, Y.-F.; Wang, Z.-G.; Yin, H.-M.; Xu, J.-Z.; Chen, Y.; Lei, J.; Zhu, L.; Gong, F.; Li, Z.-M., Highly anisotropic, thermally conductive, and mechanically strong polymer composites with nacre-like structure for thermal management applications. *ACS Applied Nano Materials* **2018,** *1* (7), 3312-3320.

19. Kwon, O. H.; Ha, T.; Kim, D.-G.; Kim, B. G.; Kim, Y. S.; Shin, T. J.; Koh, W.-G.; Lim, H. S.; Yoo, Y., Anisotropy-driven high thermal conductivity in stretchable poly(vinyl alcohol)/hexagonal boron nitride nanohybrid films. *ACS Appl Mater Interfaces* **2018,** *10* (40), 34625-34633.

20. Han, J.; Du, G.; Gao, W.; Bai, H., An anisotropically high thermal conductive boron nitride/epoxy composite based on nacre-mimetic 3D network. *Adv. Funct. Mater.* **2019,** *29* (13), 1900412.

21. Fischer, B.; Ziadeh, M.; Pfaff, A.; Breu, J.; Altstädt, V., Impact of large aspect ratio, shear-stiff, mica-like clay on mechanical behaviour of PMMA/clay nanocomposites. *Polymer* **2012,** *53* (15), 3230-3237.

22. Schütz, M. R.; Kalo, H.; Lunkenbein, T.; Breu, J.; Wilkie, C. A., Intumescent-like behavior of polystyrene synthetic clay nanocomposites. *Polymer* **2011,** *52* (15), 3288-3294.

23. Schütz, M. R.; Kalo, H.; Lunkenbein, T.; Gröschel, A. H.; Müller, A. H. E.; Wilkie, C. A.; Breu, J., Shear stiff, surface modified, mica-like nanoplatelets: a novel filler for polymer nanocomposites. *J. Mater. Chem.* **2011,** *21* (32), 12110-12116.

24. Tsurko, E. S.; Feicht, P.; Nehm, F.; Ament, K.; Rosenfeldt, S.; Pietsch, I.; Roschmann, K.; Kalo, H.; Breu, J., Large scale self-assembly of smectic nanocomposite films by doctor blading versus spray coating: Impact of crystal quality on barrier properties. *Macromolecules* **2017,** *50* (11), 4344-4350.

25. Tsurko, E. S.; Feicht, P.; Habel, C.; Schilling, T.; Daab, M.; Rosenfeldt, S.; Breu, J., Can high oxygen and water vapor barrier nanocomposite coatings be obtained with a waterborne formulation? *Journal of Membrane Science* **2017,** *540*, 212-218.

26. Losego, M. D.; Blitz, I. P.; Vaia, R. A.; Cahill, D. G.; Braun, P. V., Ultralow thermal conductivity in organoclay nanolaminates synthesized via simple self-assembly. *Nano Lett.* **2013,** *13* (5), 2215-9.

27. Wang, Z.; Rolle, K.; Schilling, T.; Hummel, P.; Philipp, A.; Kopera, B. A. F.; Lechner, A. M.; Retsch, M.; Breu, J.; Fytas, G., Tunable thermoelastic anisotropy in hybrid Bragg stacks with extreme polymer confinement. *Angew. Chem. Int. Ed. Engl.* **2019,** *10.1002/anie.201911546*.

28. Feicht, P.; Siegel, R.; Thurn, H.; Neubauer, J. W.; Seuss, M.; Szabó, T.; Talyzin, A. V.; Halbig, C. E.; Eigler, S.; Kunz, D. A.; Fery, A.; Papastavrou, G.; Senker, J.; Breu, J., Systematic evaluation of different types of graphene oxide in respect to variations in their in-plane modulus. *Carbon* **2017,** *114*, 700-705.

29. Clauser, C.; Huenges, E., Thermal conductivity of rocks and minerals. In *Rock Physics & Phase Relations*, 2013; pp 105-126.

30. Tiwari, A.; Boussois, K.; Nait-Ali, B.; Smith, D. S.; Blanchart, P., Anisotropic thermal conductivity of thin polycrystalline oxide samples. *AIP Advances* **2013,** *3* (11), 112129.

31. Hofmann, U.; König, E., Untersuchungen über Graphitoxyd. *Z. Anorg. Allg. Chem.* **1937,** *234* (4), 311-336.

32. Dao, L.-Q.; Delage, P.; Tang, A.-M.; Cui, Y.-J.; Pereira, J.-M.; Li, X.-L.; Sillen, X., Anisotropic thermal conductivity of natural Boom Clay. *Applied Clay Science* **2014,** *101*, 282-287.

33. Stöter, M.; Kunz, D. A.; Schmidt, M.; Hirsemann, D.; Kalo, H.; Putz, B.; Senker, J.; Breu, J., Nanoplatelets of sodium hectorite showing aspect ratios of ≈20 000 and superior purity. *Langmuir* **2013,** *29* (4), 1280-1285.

34. Rosenfeldt, S.; Stöter, M.; Schlenk, M.; Martin, T.; Albuquerque, R. Q.; Förster, S.; Breu, J., In-depth insights into the key steps of delamination of charged 2D nanomaterials. *Langmuir* **2016,** *32* (41), 10582-10588.

35. Prescott, H. A.; Li, Z.-J.; Kemnitz, E.; Deutsch, J.; Lieske, H., New magnesium oxide fluorides with hydroxy groups as catalysts for Michael additions. *J. Mater. Chem.* **2005,** *15* (43), 4616-4628.

36. Wojciechowska, M.; Czajka, B.; Pietrowski, M.; Zieliński, M., MgF2 as a non-conventional catalytic support. Surface and structure characterization. *Catal. Lett.* **2000,** *66* (3), 147-153.

37. Rywak, A. A.; Burlitch, J. M., Sol−Gel synthesis of nanocrystalline magnesium fluoride: Its use in the preparation of MgF2 films and MgF2−SiO2 composites. *Chem. Mater.* **1996,** *8* (1), 60-67.

38. Lerf, A.; He, H.; Forster, M.; Klinowski, J., Structure of graphite oxide revisited. *The Journal of Physical Chemistry B* **1998,** *102* (23), 4477-4482.

39. Xu, Z.; Gao, C., Graphene chiral liquid crystals and macroscopic assembled fibres. *Nature Communications* **2011,** *2* (1), 571.

40. Hofmann, U.; Frenzel, A.; Csalán, E., Die Konstitution der Graphitsäure und ihre Reaktionen. *Justus Liebigs Annalen der Chemie* **1934,** *510* (1), 1-41.

41. Mendioroz, A.; Fuente-Dacal, R.; Apiñaniz, E.; Salazar, A., Thermal diffusivity measurements of thin plates and filaments using lock-in thermography. *Rev. Sci. Instrum.* **2009,** *80* (7), 074904.

42. Hu, H. P.; Wang, X. W.; Xu, X. F., Generalized theory of the photoacoustic effect in a multilayer material. *J. Appl. Phys.* **1999,** *86* (7), 3953-3958.

43. Wang, X.; Hu, H.; Xu, X., Photo-acoustic measurement of thermal conductivity of thin films and bulk materials. *J. Heat Transfer* **2001,** *123* (1), 138-144.

Supporting Information

S1. Sample Preparation and Characterization

Materials

The synthetic clay sodium fluorohectorite (Hec, $[Na_{0.5}]^{inter}[Mg_{2.5}Li_{0.5}]^{oct}[Si_4]^{tet}O_{10}F_2$) was synthesized with high-purity reagents of SiO_2, LiF, MgF_2, MgO and NaF in a gastight molybdenum crucible via melt synthesis according to an already published procedure.[1] To improve the charge density of the clay platelets and relating thereto the intracrystalline reactivity, the melt synthesis is followed by long-term annealing at 1045 °C for 6 weeks.[2] The material featured a cation exchange capacity of 1.27 mmol g^{-1}.[1-2] This sample is called Hec-L. For the fabrication of the small Hec platelets (Hec-S), a 0.5 wt% suspension of Hec-L was sonicated for 15 minutes in an ice bath with the ultrasonic device UIP 1000hd (Hielscher Ultrasonic GmbH, Germany), equipped with an ultrasonic horn BS2d22 and a booster B2-1.2, at 20 kHz with a maximal output power of 1000 W. GO-syn, based on Hummers/Offeman's method, was synthesized according to an established procedure.[3] GO-com was provided by Hangzhou Gaoxi Technology Co. Ltd. (China).

Film Preparation

For the delamination, the synthetic Hec was immersed into Millipore water (0.5 wt%). The complete delamination was studied by small-angle X-ray scattering (SAXS).[4] The self-supporting films of Hec and GO were prepared by spray coating of 0.5 wt% suspensions of the respective material. The fully automatic spray coating system was equipped with a SATA 4000 LAB HVLP 1.0 mm spray gun (SATA GmbH & Co. KG, Germany). Suspensions were sprayed on a corona-treated polyethylene terephthalate (PET) foil (optimont 501, bleher Folientechnik, Germany). The spraying and nozzle pressure were set constant at values of 2 and 4 bar, respectively. The round per flat fan control was set to 6 with a flow speed of

3 mL s^{-1}. The distance between the spraying gun and the substrate was 17 cm. The thickness of the suspension layer applied in one spraying step is about 2 μm which corresponds to about 20 nm dry film thickness. For drying the suspension layer, the sample is stopped under infrared lamps until evaporation of the solvent is complete. After every spraying cycle, a drying cycle of 90 s with a temperature of 55 °C took place. The spraying/drying cycle is repeated until the desired barrier film thickness of 50 μm is obtained. Afterward, the film was dried at 100 °C for 3 days and peeled off from the PET foil for achieving self-supporting films. For characterization by photoacoustic analysis thinner films on the order of a few μm were spray-coated onto clean 1 mm microscope glass slides. In total, we prepared four different samples: Hec-L, Hec-S, GO-syn, and GO-com.

Small-Angle X-Ray Scattering (SAXS)

All SAXS data were measured using the small-angle X-ray system "Double Ganesha AIR" (SAXSLAB, Denmark). The X-ray source of this laboratory-based system is a rotating anode (copper, MicroMax 007HF, Rigaku Corporation, Japan), providing a micro-focused beam. The data were recorded by a position-sensitive detector (PILATUS 300 K, Dectris). To cover the range of scattering vectors different detector positions were used. The measurements of the suspensions were done in 1 mm glass capillaries (Hilgenberg, code 4007610, Germany) at room temperature. To improve the detection limit of the in-house machine, the suspensions were first concentrated by centrifugation at 10,000 rpm for 1 hour. The data were radially averaged and background corrected. As background, a water-filled capillary was used.

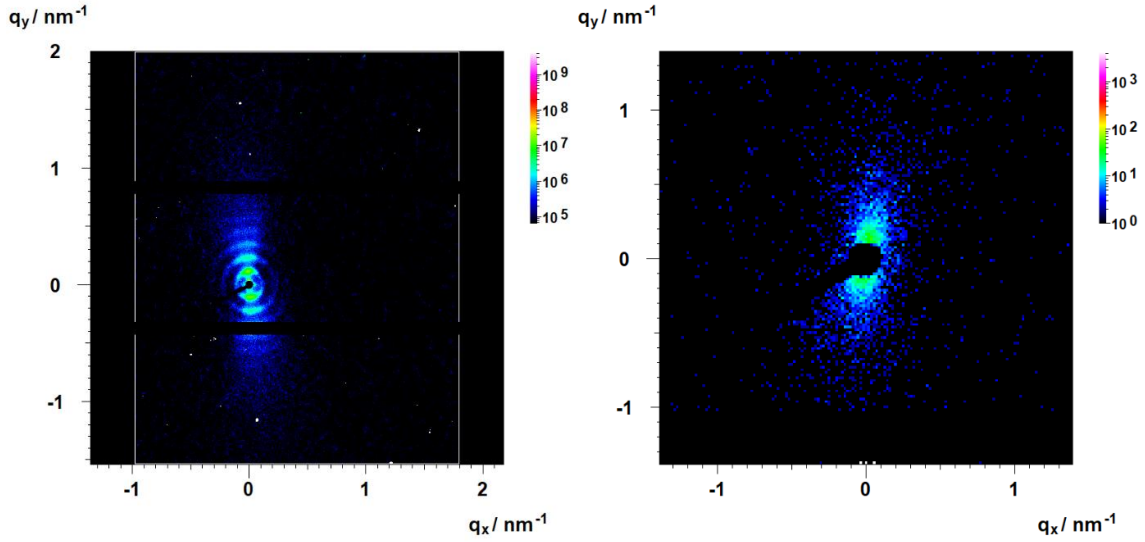

Figure S1. 2D SAXS patterns of an aqueous Hec suspension (left) and an aqueous GO suspension (right).

X-Ray Diffraction (XRD) Analysis

XRD patterns for the films were recorded in Bragg-Brentano-geometry on an Empyrean diffractometer (PANalytical B.V.; the Netherlands) using Cu Kα radiation (λ = 1.54187 Å). The self-supporting films were placed on glass slides (Menzel-Gläser; Thermo Scientific). Before the measurements, samples were dried at 100 °C for one week in a vacuum chamber.

As a measure of the quality of the one-dimensional crystallinity of the films, the coefficient of variation (CV) and the full width at half maximum (FWHM) were determined (Table S1). Large CV-values (~3%[4]) and large FWHM indicate non-rationality of the diffraction pattern as caused by a random interstratification of different interlayer heights.

Table S1. Overview of the structural characterization by XRD.

Sample	Description	dXRD [Å]	CV [%]	FWHM [°2θ]
Hec-L	Large Hec platelets	10.1	1.6	0.7
Hec-S	Small Hec platelets	10.0	1.1	0.6
GO-syn	Synthetic GO	6.2	-	3.1
GO-com	Commercial GO	6.1	-	3.5

Transmission Electron Microscopy (TEM)

TEM images of the samples Hec-L and Hec-S were taken on a JEOL JEM-2200FS (JEOL GmbH, Germany) at an acceleration voltage of 200 kV. Cross-section pictures of the self-supporting films were prepared with a Cryo Ion Slicer IB-09060CIS (JEOL, Germany).

Scanning Electron Microscopy (SEM)

SEM images were taken with a Zeiss Ultra plus (Carl Zeiss AG, Germany) at an operating voltage of 3 kV. Samples were prepared by drop coating a 0.001 wt% solution on a plasma-treated silicon wafer. The samples with Hec were sputtered with 10 nm carbon. For analyzing the area of the platelets, ImageJ was used, and at least 100 platelets were evaluated. Figure S2 shows the histograms of the platelet areas of Hec (a) and GO (b) samples. Figures S3 and S4 show exemplary SEM pictures of Hec and GO, respectively.

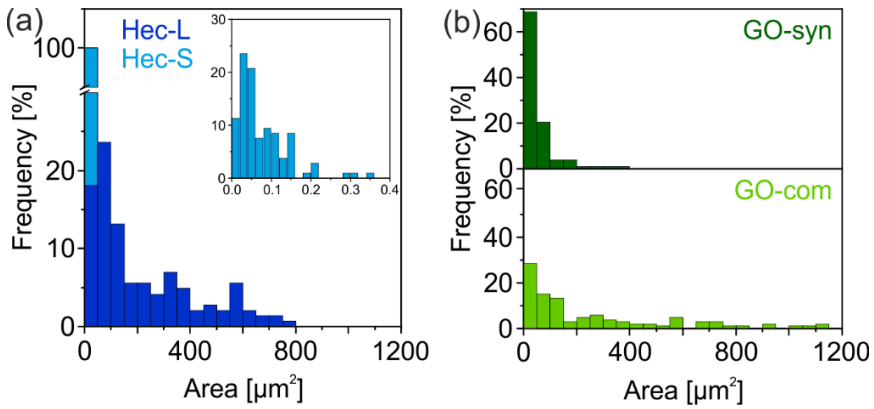

Figure S2. Histograms of platelet areas of Hec (a) and GO (b) samples evaluated from SEM images.

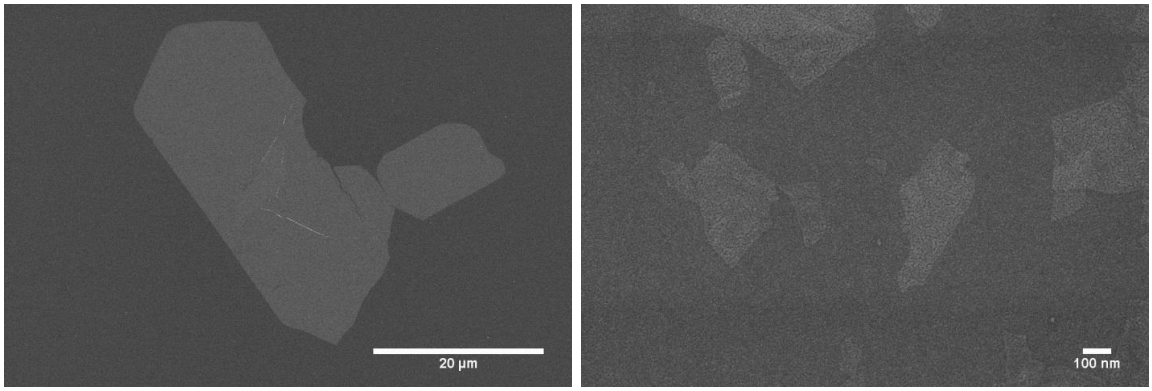

Figure S3. SEM pictures of Hec-L (left) and Hec-S (right).

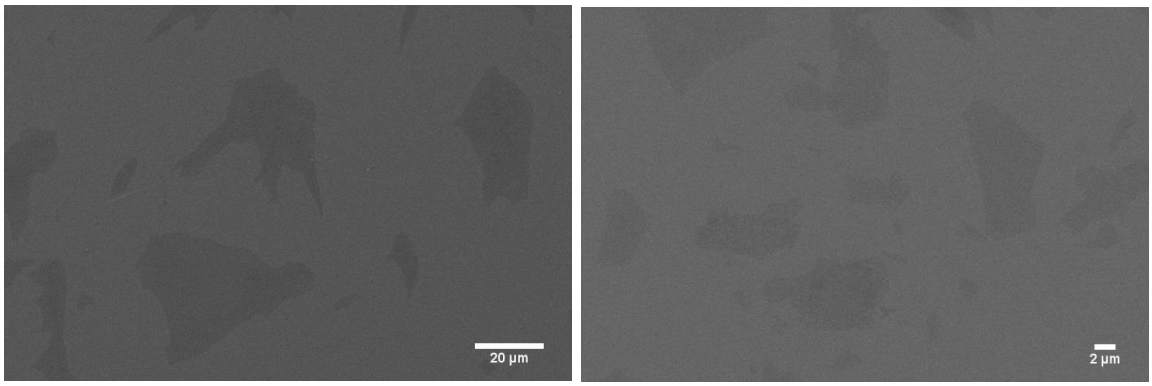

Figure S4. SEM pictures of GO-com (left) and GO-syn (right).

Cross-sections of the films were prepared by cutting the self-supporting films with a razor blade and sputtering with 10 nm carbon.

X-Ray Photoelectron Spectroscopy (XPS)

XPS measurements were carried out using a Versa Probe III from Physical electronics. Cu and Au were used for calibration. Shirley-type background-subtracted data is presented. Scotch tape was used to fixate the sample films on the measurement stage. The samples were sputtered with Argon after being introduced into the XPS chamber to remove adsorbed hydrocarbons. To minimize charging effects, a charge neutralization system was used. Figures S5 and S6 show the XPS spectra of Hec and GO samples. Peaks used for calculation of the elemental composition (Tables S2 and S3) are marked.

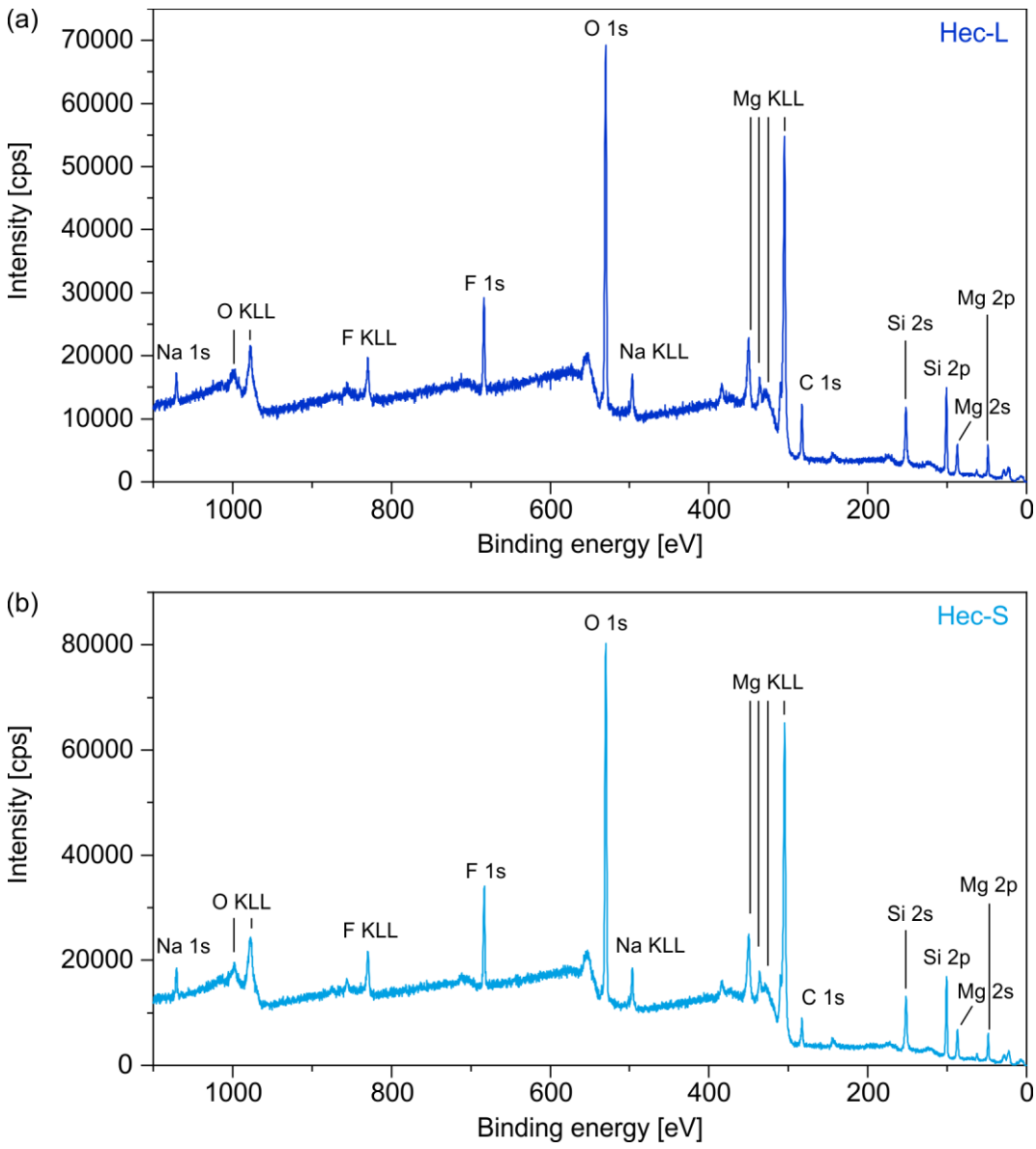

Figure S5. Overview XPS spectra of Hec-L (a) and Hec-S (b). Both spectra show the same chemical composition (see Table S2).

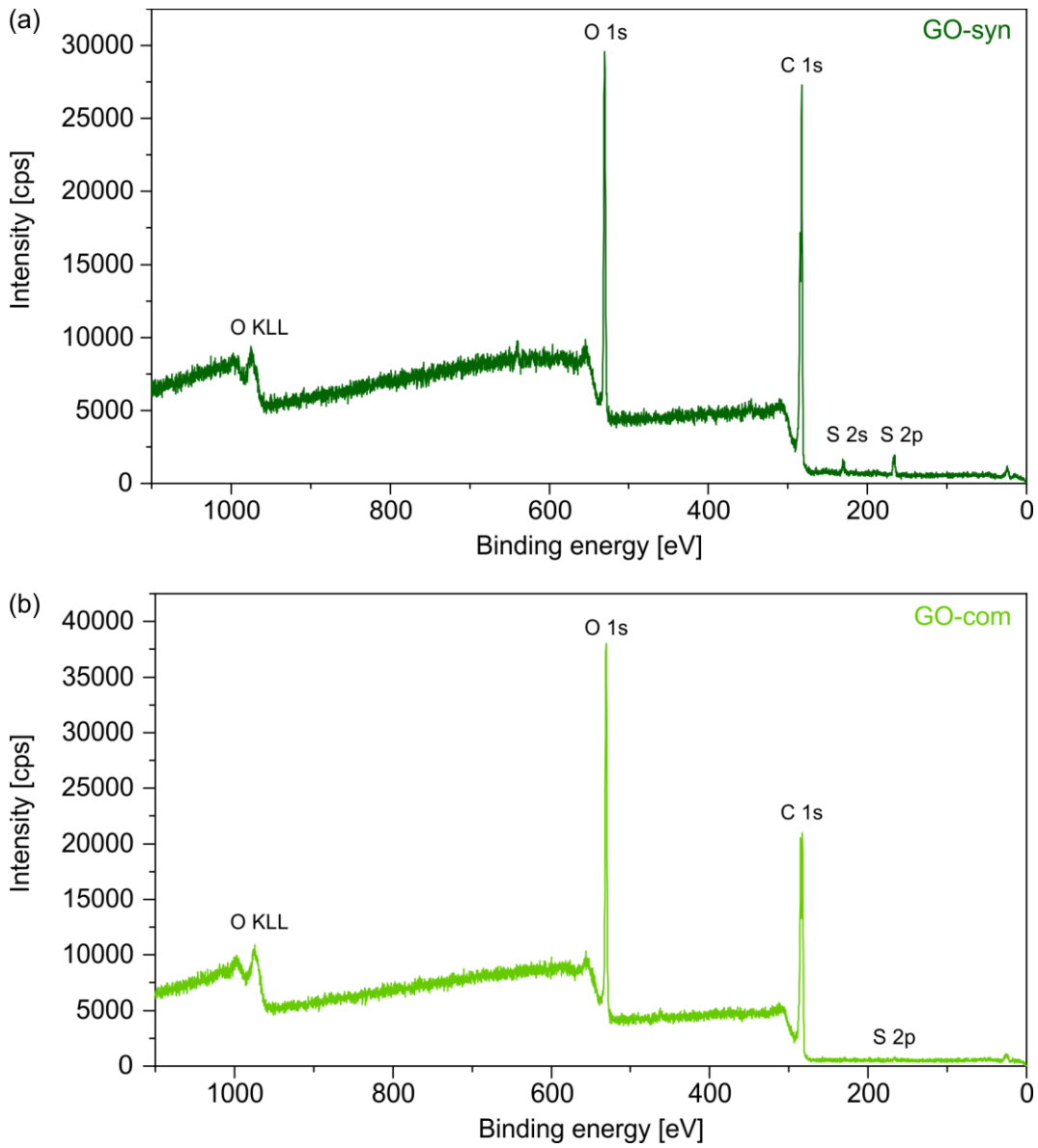

Figure S6. Overview XPS spectra of GO-syn (a) and GO-com (b). Two main differences are visible: GO-com contains more oxygen (O) than GO-syn, and GO-syn contains a little amount of sulfur (S), whereas GO-com contains almost no sulfur (see Table S3).

Table S2. Elemental composition of Hec samples extracted from XPS data.

Sample	Na	Mg	Li	Si	O	F
Hec-L	2.95 %	10.67 %	3.79 %	18.26 %	54.06 %	10.27 %
Hec-S	2.58 %	10.72 %	1.89 %	18.90 %	54.33 %	11.57 %

Table S3. Elemental composition of GO samples extracted from XPS data.

Sample	C	O	S
GO-syn	72.06 %	26.70 %	1.25 %
GO-com	68.74 %	30.94 %	0.31 %

Raman Spectroscopy

Raman spectroscopy was performed with a Raman microscope (Horiba Scientific, Olympus Ex41, λ_{Laser} =635 nm) equipped with a Synapse CCD camera.

The obtained Raman spectra are shown in Figure S7. The intensity ratios of the D and G band (I_D/I_G) of both samples are around 1, which is a measure for a high number of defects (functional groups and holes) within the GO structure.

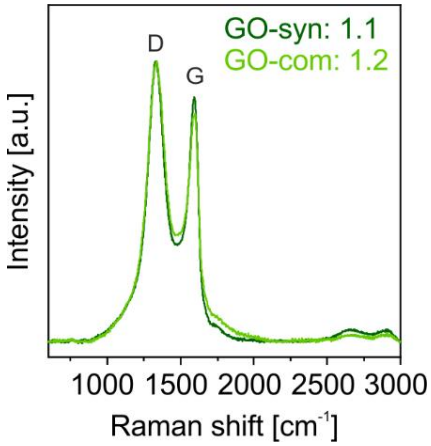

Figure S7. Raman spectra reveal a comparable degree of defects of both samples (the ratio I_D/I_G for both samples is around 1).

Infrared (IR) Spectroscopy

For IR spectra, a JASCO FT/IR-6100 Fourier transform IR spectrometer (JASCO Corporation, Japan) with an attenuated total reflectance (ATR) unit was used.

S2. Thermal Measurements

Two different methods were used to characterize the thermal transport properties of the Hec and GO samples: lock-in thermography for the in-plane thermal diffusivity and the photoacoustic method for the cross-plane thermal conductivity. For the calculation of the in-plane thermal conductivity and the determination of the cross-plane thermal conductivity, the density and the specific heat capacity are needed. Therefore, Helium pycnometry and differential scanning calorimetry have been used. Before all measurements, the samples have been dried for seven days at 100 °C in a vacuum oven.

Helium Pycnometry

The density of the samples was obtained from helium pycnometry using an Ultrapyc 1200e (Quantachrome Instruments). First of all, the volume of the (empty) measurement cell was measured. Then, small pieces of the free-standing films were weighed into the sample cell with a nominal volume of 1.8 cm^3. One hundred runs were conducted to measure the volume of the films at room temperature. By knowing the mass (weighed on a fine balance) and the volume, the density of the samples was calculated. The obtained densities are summarized in Table S4.

Table S4. Densities of Hec and GO films (measured at room temperature).

Sample	Density [gcm^{-3}]
Hec-L	2.73 ± 0.01
Hec-S	2.57 ± 0.02
GO-syn	1.53 ± 0.01
GO-com	1.54 ± 0.01

Differential Scanning Calorimetry (DSC)

The specific heat capacity was determined by DSC measurements on a TA instruments Discovery DSC 2500, according to the ASTM E1269 standard. All samples were freeze ground for better processability and contact with the DSC pans. Before the measurement, an isothermal step (1 h, 100 °C) was conducted to

ensure dry conditions. Subsequently, two heating cycles were performed, whereas only the second cycle was evaluated. The temperature profile ranged in the case of the Hec samples from -40 °C to 250 °C and in case of the GO samples from -40 °C to 100 °C using a heating rate of 20 K min^{-1} with a nitrogen flow of 50 mL min^{-1}. Triplicates of each sample were measured (Figure S8).

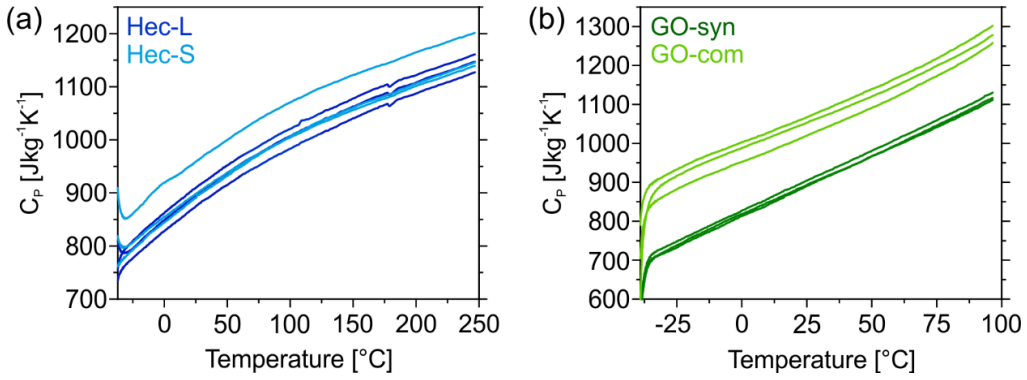

Figure S8. Specific heat capacity C_P versus temperature: a) Hec-L and Hec-S. b) GO-syn and GO-com. The C_P at 25 °C was used for the determination of the thermal conductivity.

Lock-In Thermography (LIT)

The in-plane thermal diffusivity of free-standing Hec and GO films was obtained by lock-in thermography (LIT). Figure S9 shows the self-built LIT set-up.

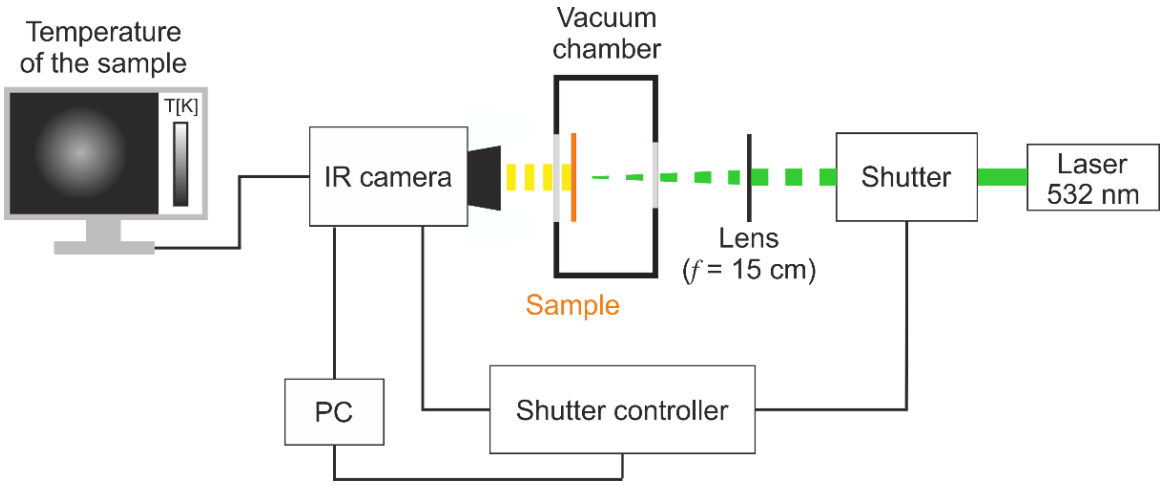

Figure S9. Scheme of the lock-in thermography set-up. The samples were measured in a vacuum chamber to avoid heat losses (convection and conduction) to the environment.

A laser beam periodically heats the free-standing sample (Genesis MX 532-1000 SLM OPS, Coherent, $\lambda = 532$ nm) focused onto the sample surface by a lens of 150 mm focal length. For the modulation of the laser a shutter (SH05/M, Thorlabs) controlled by a shutter controller (SC10, Thorlabs) is used. The emitted infrared (IR) radiation of the sample surface is detected in rear-face configuration (*i.e.*, from the non-illuminated side) by an Infratec VarioCAM HD research IR camera (spectral window: 7.5-14 μm). The IR camera is equipped with a close-up lens which enables a spatial resolution of around 29 μm.Since heat conduction to the gas and convection lead to an overestimation of the thermal diffusivity[5-6] all samples were measured in a vacuum (~$3 \cdot 10^{-3}$ mbar).

Furthermore, the Hec samples were coated with a 20 nm carbon layer for enhanced laser absorption. The coating of the sample was facing to the IR camera. Due to the blackish color of GO, the GO samples possess a proper laser absorption, and therefore a coating was not necessary.

LIT measurements were performed using Infratec's IRBISactiveonline software. Measurements were conducted at several lock-in frequencies between 0.309 and 1.765 Hz. Furthermore, each measurement was averaged over several (800-2000) lock-in periods to enhance the signal to noise ratio, with the first 100 periods being discarded. The software calculates the amplitude and phase of the sample's temperature oscillations automatically. Exemplary phase images are depicted in Figure S10. The red point marks the focal point of the laser excitation and thus the midpoint of the radial distribution.

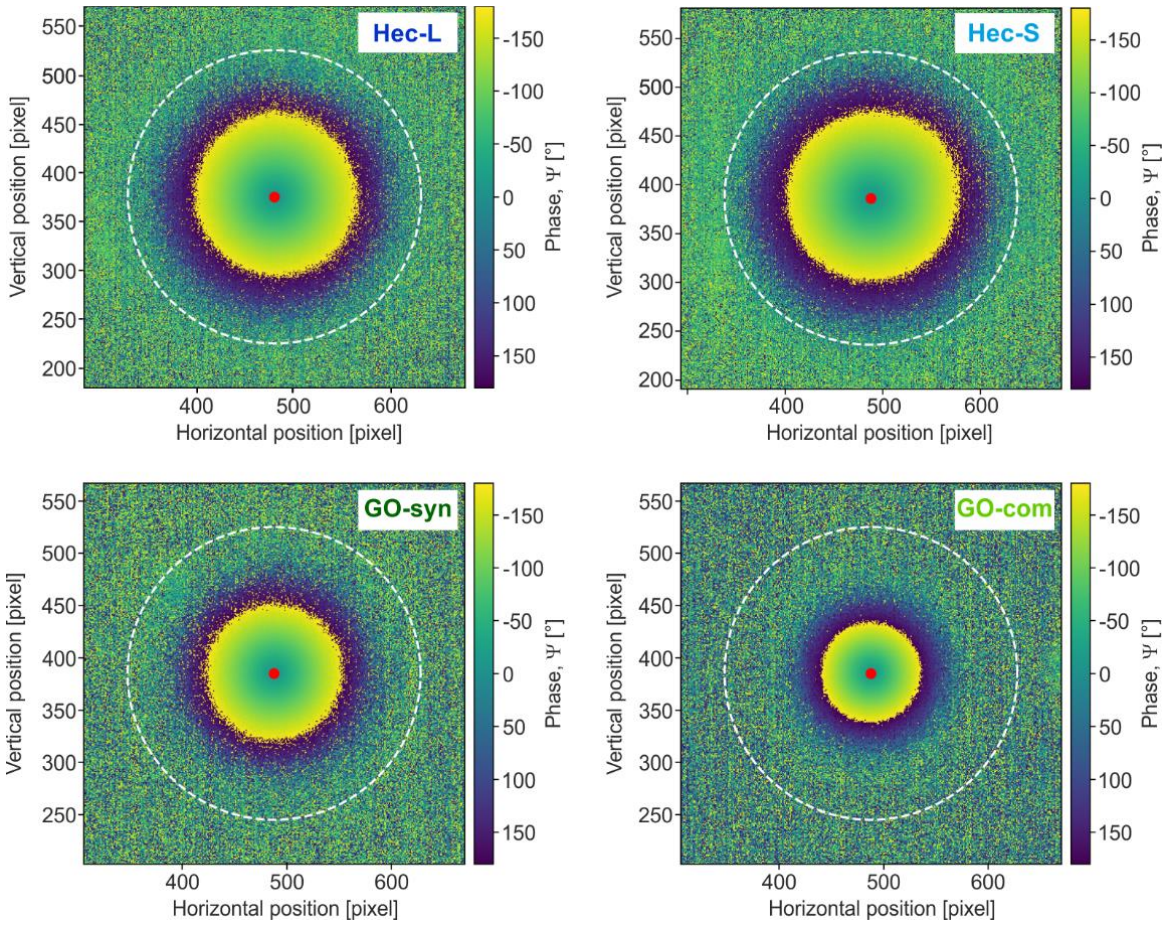

Figure S10. Exemplary two-dimensional phase images measured at a frequency of 1.111 Hz. The penetration depth of the temperature oscillations depends on the material's properties and decreases with decreasing thermal diffusivity. The red point in the center of the phase image marks the focal point of the laser.

Radial profiles for the phase and amplitude images (Figure S11) are extracted using a self-written Python script. The in-plane thermal diffusivity is calculated from the phase and amplitude slopes according to the slope method of a thermally thin film:

$$m_{\Psi} \cdot m_{\ln(T \cdot r^{0.5})} = \frac{\pi \cdot f_{\mathrm{lock-in}}}{\alpha_{\mathrm{in-plane}}} \tag{S1}$$

Here, m_{Ψ} is the slope of the linear relation of the phase and the radial distance r, $m_{\ln(T \cdot r^{0.5})}$ is the slope of the linear relation of the natural logarithm of the amplitude T multiplied by the square root of the radial distance r, $f_{\mathrm{lock-in}}$ is the lock-in frequency, and $\alpha_{\mathrm{in-plane}}$ is the in-plane thermal diffusivity.

Three films have been measured for each sample type. An average in-plane thermal diffusivity value with a standard deviation was calculated from this data (Table S5).

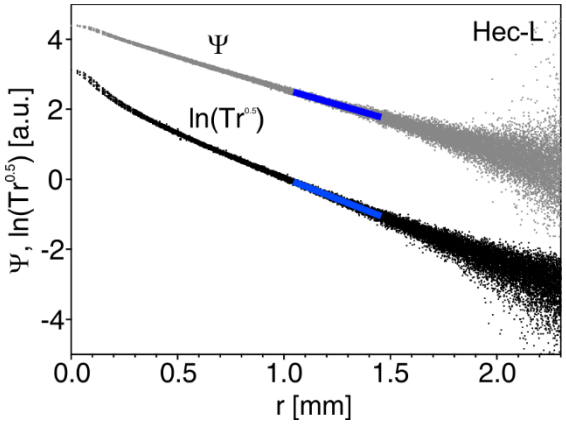

Figure S11. Exemplary phase Ψ and amplitude profiles of Hec-L. The blue lines indicate the regions where the linear fit was evaluated. This position is sufficiently far away from the central excitation spot.[7]

Table S5. In-plane thermal diffusivity values of Hec and GO films. Three films per sample type were measured, and an average thermal diffusivity with a standard deviation was calculated.

Sample	In-plane thermal diffusivity [mm² s⁻¹]
Hec-L	2.35 ± 0.03
Hec-S	2.36 ± 0.01
GO-syn	1.24 ± 0.02
GO-com	0.63 ± 0.01

Finally, the in-plane thermal conductivity was calculated from the in-plane thermal diffusivity $\alpha_{\mathrm{in-plane}}$, the density ρ, and the specific heat capacity C_{P}:

$$\kappa_{\mathrm{in-plane}} = \alpha_{\mathrm{in-plane}} \cdot \rho \cdot C_{\mathrm{P}} \quad \text{(S2)}$$

Photoacoustic Method

The samples for the cross-plane thermal conductivity characterization were spray-coated on glass substrates. A gold transducer layer (~ 150 nm) was evaporated on top of the samples. In the photoacoustic measurement, a modulated laser beam (λ = 488 nm) periodically heats the sample. Due to the photoacoustic effect an acoustic response is induced, which relies on the thermal properties of the sample. The schematic layout of the measurement cell is shown in Figure S12a. The gas-tight cell is filled with a helium pressure of 20 psi. The microphone (Bruel&Kjaer, 4398-A-011) connected to the cell detects the acoustic wave, which is induced by the periodic heat conduction from the sample surface to the gas phase. The

microphone is linked to a lock-in amplifier with integrated signal generator (Zurich instruments, HF2LI), as shown in Figure S12b. The signal generator targets the modulation frequency for the electro-optic modulator (EOM, Conoptics, M25A) and therefore controls the frequency of the laser beam. The lock-in amplifier then transfers the acoustic signal into amplitude and phase shift concerning the modulation of the incident laser beam.

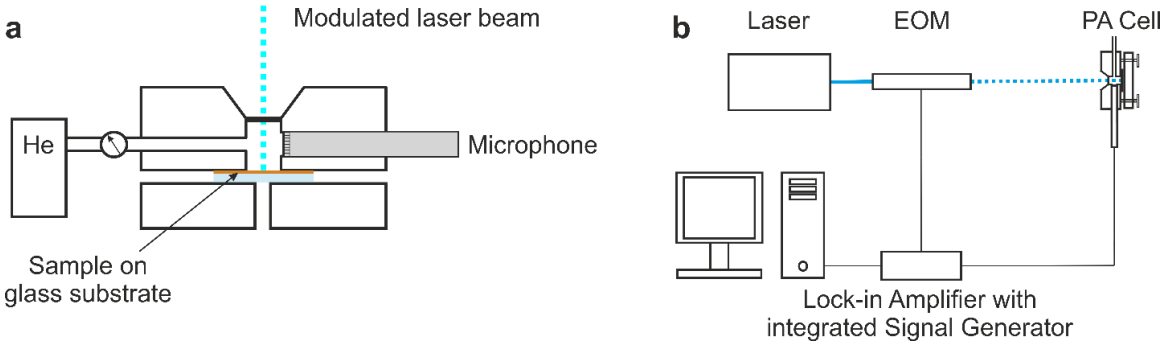

Figure S12. Scheme of (a) the photoacoustic cell and (b) the whole setup.

For measurement, we performed a frequency sweep in a range from 110 Hz to 4000 Hz. The phase shift signal is then normalized with the signal of a thermally thick glass sample (1 mm) of known thermal properties. Figure S13 shows a representative measurement curve together with the best fit. The fitting procedure was realized according to Singh *et al.*[8] Therefore, the generalized multilayer model of Hu *et al.*[9] is used. The model described the temperature distribution in the sample, assuming a one-dimensional heat transfer. The unknown parameters contact resistance between the gold layer and the sample, the thermal diffusivity of the sample, and the contact resistance between sample and substrate are fitted to match the experimental data. When fitting three parameters at the same time, the results for the individual parameters may not accurately be predicted. However, it was found that the total layer resistance (consisting of all three parameters) can be estimated with high accuracy. The reason is the difference in sensitivity of the model on the individual parameters.[10] Hence, we report only the total layer resistance. In addition to that, we calculate the effective thermal

conductivity of our samples. We estimated based on literature data[11-12] that the thermal interface resistance between the gold transducer layer and sample is on the order or less than 10^{-8} K m^2 W^{-1}. We, consequently, do not expect a significant influence of this interface on our calculation of the effective thermal conductivity. The thermal conductivity is obtained by dividing the total layer resistance by the sample thickness. AFM measurements determined the sample thickness. We summarized the values of the total layer resistance, the sample thickness and the resulting effective thermal conductivity in Table S6.

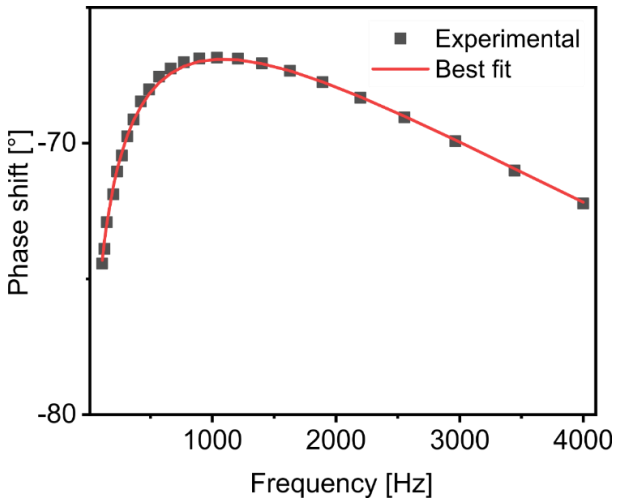

Figure S13. Representative photoacoustic measurement of the GO-syn sample with a thickness of 446 nm. Normalized photoacoustic phase signal is dependent on the frequency. The red line indicates the best fit.

Table S6. Summary of the photoacoustic measurements. The total layer resistance, the thickness, and the resulting effective cross-plane thermal conductivity are given for each sample.

Sample	Total layer resistance [mm^2 K W^{-1}]	Thickness [μm]	Effective thermal conductivity [W m^{-1} K^{-1}]
Hec-L	1.58	0.28	0.177
Hec-L	2.55	0.595	0.234
Hec-L	4.34	0.94	0.217
Hec-S	5.39	0.972	0.180
Hec-S	4.62	0.972	0.210
Hec-S	5.86	0.972	0.166
GO-syn	1.92	0.233	0.121
GO-syn	3.99	0.446	0.117
GO-syn	5.52	0.746	0.135
GO-com	1.43	0.179	0.125
GO-com	2.65	1.382	0.128
GO-com	4.50	1.979	0.131

References

1. Breu, J.; Seidl, W.; Stoll, A. J.; Lange, K. G.; Probst, T. U., Charge homogeneity in synthetic fluorohectorite. Chem. Mater. 2001, 13 (11), 4213-4220.

2. Stöter, M.; Kunz, D. A.; Schmidt, M.; Hirsemann, D.; Kalo, H.; Putz, B.; Senker, J.; Breu, J., Nanoplatelets of sodium hectorite showing aspect ratios of ≈20 000 and superior purity. Langmuir 2013, 29 (4), 1280-1285.

3. Feicht, P.; Siegel, R.; Thurn, H.; Neubauer, J. W.; Seuss, M.; Szabó, T.; Talyzin, A. V.; Halbig, C. E.; Eigler, S.; Kunz, D. A.; Fery, A.; Papastavrou, G.; Senker, J.; Breu, J., Systematic evaluation of different types of graphene oxide in respect to variations in their in-plane modulus. Carbon 2017, 114, 700-705.

4. Rosenfeldt, S.; Stöter, M.; Schlenk, M.; Martin, T.; Albuquerque, R. Q.; Förster, S.; Breu, J., In-depth insights into the key steps of delamination of charged 2D nanomaterials. Langmuir 2016, 32 (41), 10582-10588.

5. Salazar, A.; Mendioroz, A.; Fuente, R., The strong influence of heat losses on the accurate measurement of thermal diffusivity using lock-in thermography. Appl. Phys. Lett. 2009, 95 (12), 121905.

6. Mendioroz, A.; Fuente-Dacal, R.; Apiñaniz, E.; Salazar, A., Thermal diffusivity measurements of thin plates and filaments using lock-in thermography. Rev. Sci. Instrum. 2009, 80 (7), 074904.

7. Philipp, A.; Pech-May, N. W.; Kopera, B. A. F.; Lechner, A. M.; Rosenfeldt, S.; Retsch, M., Direct measurement of the in-plane thermal diffusivity of semitransparent thin films by lock-in thermography: an extension of the slopes method. Anal. Chem. 2019.

8. Singh, V.; Bougher, T. L.; Weathers, A.; Cai, Y.; Bi, K.; Pettes, M. T.; McMenamin, S. A.; Lv, W.; Resler, D. P.; Gattuso, T. R.; Altman, D. H.; Sandhage, K. H.; Shi, L.; Henry, A.; Cola, B. A., High thermal conductivity of chain-oriented amorphous polythiophene. Nat Nanotechnol 2014, 9 (5), 384-90.

9. Hu, H. P.; Wang, X. W.; Xu, X. F., Generalized theory of the photoacoustic effect in a multilayer material. J. Appl. Phys. 1999, 86 (7), 3953-3958.

10. Wang, X.; Cola, B. A.; Bougher, T. L.; Hodson, S. L.; Fisher, T. S.; Xu, X., Photoacoustic technique for thermal conductivity and thermal interface measurements. In Annual Review of Heat Transfer, 2013; pp 135-157.

11. Losego, M. D.; Grady, M. E.; Sottos, N. R.; Cahill, D. G.; Braun, P. V., Effects of chemical bonding on heat transport across interfaces. Nat. Mater. 2012, 11 (6), 502-6.

12. Juvé, V.; Scardamaglia, M.; Maioli, P.; Crut, A.; Merabia, S.; Joly, L.; Del Fatti, N.; Vallée, F., Cooling dynamics and thermal interface resistance of glass-embedded metal nanoparticles. Phys. Rev. B 2009, 80 (19), 195406.

12. Tunable Thermoelastic Anisotropy in Hybrid Bragg Stacks with Extreme Polymer Confinement

Zuyuan Wang[1], Konrad Rolle[1,‡], Theresa Schilling[2,3,‡], Patrick Hummel[2,3,‡], Alexandra Philipp[2,3,‡], Bernd A. F. Kopera[2,3], Anna M. Lechner[2,3], Markus Retsch[2,3,*], Josef Breu[2,3,*], and George Fytas[1,4,*]

[‡] *These authors contributed equally to the work.*

[1]Max Planck Institute for Polymer Research, Ackermannweg 10, 55128 Mainz, Germany

[2]Bavarian Polymer Institute, University of Bayreuth, Universitätsstraße 30, 95447 Bayreuth, Germany

[3]Department of Chemistry, University of Bayreuth, Universitätsstraße 30, 95447 Bayreuth, Germany

[4]Institute of Electronic Structure and Laser, F.O.R.T.H, 70013 Heraklion, Greece

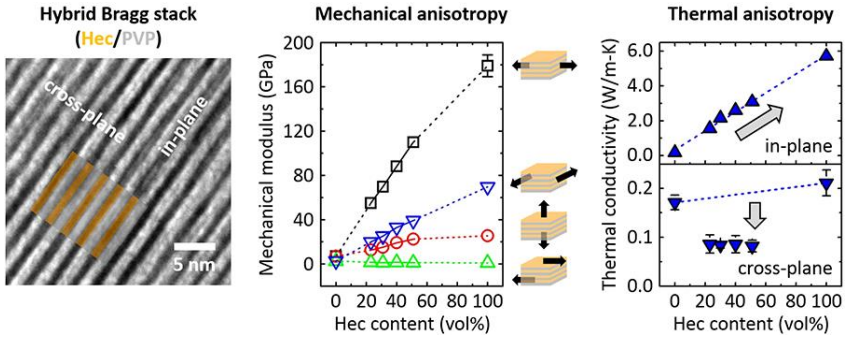

Reprinted with permission from Wang *et al.*, *Angew. Chem. Int. Ed.*, **2019**, 59(3), 1286-1294.

Abstract

Controlling thermomechanical anisotropy is important for emerging heat management applications such as thermal interface and electronic packaging materials. Whereas many studies report on thermal transport in anisotropic nanocomposite materials, a fundamental understanding of the interplay between mechanical and thermal properties is missing, due to the lack of measurements of direction-dependent mechanical properties. In this work, exceptionally coherent and transparent hybrid Bragg stacks made of strictly alternating mica-type nanosheets (synthetic hectorite) and polymer layers (polyvinylpyrrolidone) were fabricated at large scale. Distinct from ordinary nanocomposites, these stacks display long-range periodicity, which is tunable down to angstrom precision. A large thermal transport anisotropy (up to 38) is consequently observed, with the high in-plane thermal conductivity (up to 5.7 $Wm^{-1}K^{-1}$) exhibiting an effective medium behavior. The unique hybrid material combined with advanced characterization techniques allows correlating the full elastic tensors to the direction-dependent thermal conductivities. We, therefore, provide a first analysis on how the direction-dependent Young's and shear moduli influence the flow of heat.

1. Introduction

Heat management is crucial in many applications important for fueling the growth of our technology-driven society. It needs to address not only very small length scales to dissipate the heat produced, for example, by electronic circuits, but also very large length scales to realize air conditioning, for instance, for commercial buildings. The ubiquity of heat makes it obvious that heat management is a key-technology to realize international long-term goals regarding global warming. Controlling the elusive flow of heat is a complex challenge across multiple materials, length scales, and ultimately devices. This results in stringent

requirements for directional control over the heat flux based on advanced material design. Whereas heat transport represents an effective, far-field phenomenon, it is decisively governed by the material structure[1] and chemistry[2] on the microscale. Extreme phenomena of both heat dissipation and thermal insulation have been demonstrated in nanostructured and hybrid materials. For heat dissipation, surprisingly high thermal conductivities have been reported for one-dimensional (1D) fibers comprising synthetic[3] and natural polymers[4]. For thermal insulation, unusually low thermal conductivities have been shown for (disordered) stacks of two-dimensional (2D) materials.[5] Extremely efficient anisotropic thermal insulation materials have been demonstrated with various mixtures of polymers and nanoparticles or 2D materials.[6]

The combination of inherently different materials, such as soft and hard matter, is attractive, as new properties, deviating from those based on the simple linear interpolation, could emerge. This is often accompanied by improved processability, which is aided by the complementary properties of the constituent components. For instance, the soft component can serve as a binder to enable fabrication of large-area, thin films of an otherwise brittle, hard component. On the contrary, the expected effective material properties, such as mechanical reinforcement, optical transparency, and electrical or thermal conductivity, have been often found inferior to the high expectations. The reason for such shortcomings is that the nanocomposite structure, particularly the soft-hard interface, is poorly controlled. Furthermore, although many characterization techniques, such as tensile testing, indentation, and abrasion tests, are capable of assessing engineering properties, they are unsuitable for directly identifying and quantifying anisotropies or microscopic contributions to the effective properties.

Nevertheless, hybrid systems have been reported to drastically alter the materials' thermal transport properties,[3-6] depending on the geometry, dimensionality, crystallographic symmetry, and confinement. Interestingly, layered structures

inherently exhibit structural anisotropy, a feature that can be detrimental or desirable depending on the application.[7] In particular, when polymer films are filled with nanosheets of huge aspect ratio, the resulting nanocomposite properties ought to be exceedingly anisotropic. Yet, only effective material properties such as electrical or thermal conductivity have been reported in a direction-dependent manner. Direction-dependent mechanical properties, which fundamentally translate into thermal transport properties are still missing. Strong anisotropies in hybrid materials are preferentially achieved at small stacking periodicities[5b] or by combining components with a large property contrast.[8]

For a thorough characterization of such nanosheet/polymer stacks (also known as "nacre-mimics"[9]), macroscopically oriented and homogeneous systems are paramount. Such ideal model system should also exhibit translational crystallographic symmetry, tunability, and strong anisotropy. Direction-dependent studies benefit significantly from the availability of various light-scattering methods, rendering a transparent filler such as the synthetic clay hectorite with a mica-type structure desirable. For fundamental investigations of elastic properties, Brillouin light spectroscopy (BLS) has established itself as a technique of choice, as it allows for microscopic observations of high frequency (GHz) dynamics, at which viscoelasticity effects are usually negligible.[10] On the other hand, lock-in thermography and photoacoustic techniques have been proven reliable in accessing the in-plane and cross-plane thermal conductivities of thin films.[11]

Here, we show for the first time the complete mechanical properties of clay/polymer Bragg stacks that are fabricated using a uniquely defined, scalable spray-coating process meeting all aforementioned specifications of a suitable model system. We, therefore, introduce 1D hybrid Bragg stacks based on nacre-mimetic clay/polymer with small stacking periods and large property contrast. These Bragg stacks are scalable in both lateral extension and thickness, and they

are macroscopically oriented. The fully controlled microstructure allows a detailed orientation dependent characterization of the thermal and mechanical properties. We couple the thermal and mechanical analyses to achieve an in-depth understanding of the interplay between the thermal conductivities and mechanical moduli in a direction-dependent manner. The extreme confinement of polymer between the clay sheets further prompts a question regarding the validity of continuum mechanics that we also address. The combination of unique hybrid materials and advanced characterization techniques provides an unprecedented insight into the physics of direction-dependent nanomechanical and thermal transport properties in strongly anisotropic materials with polymer confinement.

2. Results and Discussion

Hybrid Bragg Stacks with Extreme Polymer Confinement.

The Bragg stacks comprise synthetic clay sodium fluorohectorite (Hec, $[Na_{0.5}]^{inter}[Mg_{2.5}Li_{0.5}]^{oct}[Si_4]^{tet}O_{10}F_2$) and polyvinylpyrrolidone (PVP, Mw = 40000 $gmol^{-1}$). Like layered titanates[12] and antimony phosphates[13], Hec belongs to a handful of compounds showing a rare phenomenon of osmotic swelling.[14] In contrast to mechanical exfoliation by, *e.g.*, sonication in the liquid phase[15], osmotic swelling is a thermodynamically favored, repulsive process[16], allowing for complete and gentle delamination that preserves the diameter of the parent crystals. In general, exfoliation describes the process of slicing tactoids into thinner stacks, whereas by delamination, the layered material is exfoliated to the level of individual single nanosheets.[17] For Hec, nanosheets with a thickness of 10 Å and a median diameter of 20 μm (Figure S1) are obtained by simply immersing the material into deionized water.[18] Phase purity and a homogeneous charge density guaranteeing a uniform intracrystalline reactivity are prerequisite for such a well-controlled delamination. For Hec this is achieved by long-term annealing, while

less uniform natural or other synthetic clays commonly applied for nacre-mimics comprise mixtures of auxiliary minerals, mono-, few- and multilayer stacks.[18] Because of the large aspect (diameter to thickness) ratio, polar rotation of the nanosheets in suspension is hindered, leading to parallel nanosheets after osmotic swelling. Even dilute (< 1 vol%) suspensions of Hec represent nematic phases.[19] The parallel pre-orientation of adjacent nanosheets in the highly swollen dispersion is indispensable for the fabrication of homogenous and periodic Bragg stacks via spray coating. Similar to titanate nanosheets[20], Hec nanosheets adopt this cofacial arrangement due to strong electrostatic repulsion with inter-nanosheet distances exceeding 50 nm. Polymers can easily diffuse into these spacious galleries. By mixing Hec suspensions with varying aliquots of an aqueous PVP solution, we obtained perfectly homogeneous, nematic dispersions, as evidenced by small-angle X-ray scattering (SAXS) measurements (Figure S2).

Through spray coating of dilute nematic mixtures of high-aspect-ratio Hec nanosheets with PVP (1-2 wt% total solid content, see Section S1) highly coherent Bragg stack films with tunable gallery spacings are fabricated.[21] The transverse flexibility of clay monolayers[22] and their large aspect ratio are essentials assuring the high degree of precision obtained in the self-assembly.[23] Both, all nanosheets and the macroscopic film are aligned parallel to a polyethylene terephthalate substrate. The microscopic orientation of the Hec nanosheets prescribes the macroscopic film orientation, which is prerequisite for the direction-dependent measurements. The macroscopic film orientation is, consequently, equivalent to the microscopic polymer/clay direction and allows using far-field and integrating characterization techniques to reveal direction-dependent properties. After drying, self-supporting hybrid films with lateral extensions of several square centimeters are peeled off the substrate and used in the BLS and thermal conductivity measurements. Only by generating a nematic phase consisting of a homogeneous mixture of large aspect ratio and flexible nanosheets allows for

fabrication of large area, self-standing 1D single crystals referred to in literature as Bragg stacks or smectic films.[23] Furthermore, appropriate processing like spray coating fostering the thermodynamic equilibration of the hybrid structure during drying has to be employed.

In total, we prepared six samples: pure polymer, pure Hec, and four hybrid Bragg stacks, which are denoted as Hec0/PVP100, Hec100/PVP0, Hec23/PVP77, Hec31/PVP69, Hec40/PVP60, and Hec51/PVP49, respectively. Here, the numbers indicate the volume fractions (vol%) of Hec and PVP, as confirmed by thermogravimetric analysis (Table S1 and Figure S3).

The Hec surface is corrugated (Figure 1a) allowing for interdigitation and anchoring of PVP chains. Such interdigitation has been documented for intercalated molecular moieties, where structures based on single crystal data refinement are available.[24] An in-scale impression of the ultra-high aspect ratio provided by the Hec nanosheet gallery is shown in Figure 1b, where the length of the line corresponds to the typical lateral size of a clay nanosheet, and the thickness of the line to the height of a Hec/PVP/Hec layer. The magnifying lens highlights the extreme polymer confinement in the cross-plane direction. The perfect homogeneous arrangement of Hec nanosheets and PVP is demonstrated by TEM and SEM images over different dimensions (Figure 1c-e, Figure S7). Note that the lateral dimensions of the Hec nanosheets are much larger than the typical persistence and even contour lengths of the PVP chains. While for the polymer chains the Hec nanosheet confinement appears infinite, at the length scale of the Bragg stack films extending over tens of centimeters, they are of course finite. At the magnification where single 1 nm thick nanosheets are observable (Figure 1c-e, Figure S5), the occurrence of nanosheet edges is very rare (fewer than one per 2500 nm^2). Careful inspection, however, reveals few (Figure S6) of these nanosheet edges. The clay nanosheets show in-plane crystalline order resembling the structure of mica. While mica possesses 3D crystalline order, our nanocomposite

films belong to the transversely isotropic symmetry class, because the adjacent Hec nanosheets are positioned randomly in the lateral direction. However, all hybrid films show translational crystallographic symmetry along 001 (the cross-plane direction), as indicated by several orders of Bragg reflections (Figure 1c-e and Figure S5). By varying the PVP content, the basal spacing was tuned in the range from 19 to 38 Å, leading to PVP layer thicknesses ranging from 9 to 28 Å. For all samples, the gallery height is, therefore, significantly smaller than the PVP chains' radius of gyration (Rg, PVP ≈ 15 nm[25]), implying strong polymer confinement.

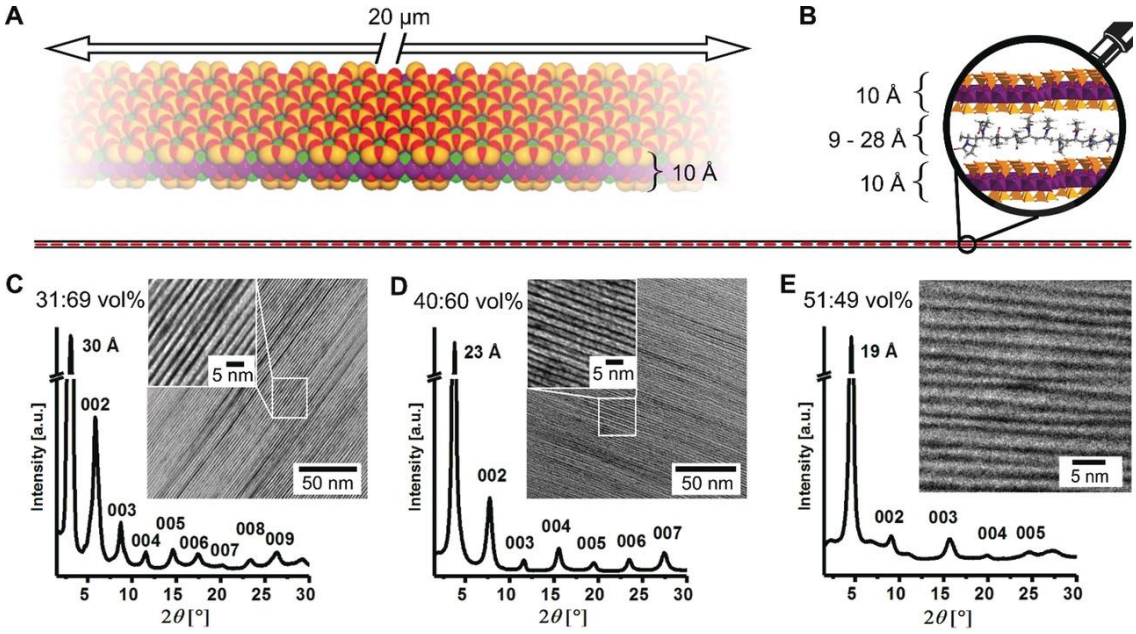

Figure 1. Schematic and microscopic images of ultra-anisotropic and extremely confined Hec/PVP Bragg stacks. a) Space-filling model of one single Hec nanosheet emphasizing the anisotropy of the nanosheet and the corrugation of the clay nanosheet allowing for interdigitation with PVP. b) True to scale schematic of the pronounced structural anisotropy. The ultra-high-aspect-ratio nanosheets stretch from left to right and have lateral dimensions much larger than the length of the PVP polymer chains. The gallery height is on the order of magnitude of the molecular dimensions. c-d) XRD patterns of Hec31/PVP69 and Hec40/PVP60 (defect-free materials) showing intense *001*-reflections and a rational series of basal reflections up to the ninth order. The cross-sectional TEM images show exceptionally periodic homogeneity of these hybrid films over large length scales. e) XRD patterns and cross-sectional TEM image of Hec51/PVP49 displaying a random stacking of two gallery heights.

In contrast to known nanocomposite films[9b, 26], Hec and PVP are thermodynamically miscible over a wide range of compositions. This miscibility is a prerequisite for tuning the basal spacing over a wide range with angstrom

precision, which typically is only observed when vapour-phase deposition techniques are applied.[5a] The miscibility is also reflected in an agreement of the basal spacing observed by X-ray diffraction (d_{XRD}) with the nominal values calculated based on the Hec and PVP volume fractions (d_{nominal}, Table S1). To the best of our knowledge, our Hec/PVP Bragg stack films are the first of its kind showing such an agreement. Because the polymer confinement, however, is getting to the point where the gallery height is on the order of the size of an individual polymer chain, it is not possible to vary the gallery height continuously but only in incremental steps that relate to the diameter of the polymer chain. Consequently, only discrete polymer volume fractions lead to essentially defect-free Bragg stacks, as seen in Hec40/PVP60 and Hec31/PVP69. XRD patterns reflect this with a rational 001-series, where the average basal spacing (d_{XRD}) calculated from individual reflections shows a low coefficient of variation with the reflection peaks being sharp and intense (Table S1). The two gallery heights of the two defect-free hybrid materials (1.3 nm for Hec40/PVP60 and 2.0 nm for Hec31/PVP69) might be attributed to the elliptical nature of PVP chains with principle axes of 1.0 nm and 1.3 nm (Figure S4a). The observed gallery heights correspond to a monolayer with the longer principal axis (Figure S4b) oriented perpendicular to the Hec nanosheets and a bilayer with the longer principle axis (Figure S4c) lying in the plan of the Hec nanosheets, respectively.

In the two cases where the volume ratios do not happen to match (Hec23/PVP77 and Hec51/PVP49), the miscibility is nevertheless assured at small length scale by random interstratification of two gallery heights (Figure 1e; transmission electron microscopy (TEM) close-up), and the coefficient of variation of the 001-series increases[27] (Table S1) with the reflection peaks being less intense (Figure 1e and Figure S5).

In-Plane and Cross-Plane Thermal Conductivities.

The in-plane and cross-plane thermal conductivities of the Hec/PVP hybrid Bragg stacks were characterized by lock-in thermography and photoacoustic measurements,[11,28] respectively. Since the density, ρ, and specific heat, C_P, are prerequisites for the thermal conductivity analysis, they were also determined experimentally by using helium pycnometry and differential scanning calorimetry (DSC) (Section S2), respectively. As the Hec volume fraction increases from 0 to 100 %, the density increases from 1190 to 2730 kgm^{-3} (Figure 2a). This is well captured by a volume-fraction-based mixing model (dashed line in Figure 2a). Correspondingly, the specific heat decreases from 1140 to 890 $Jkg^{-1}K^{-1}$ (Figure 2b), which also follows the prediction by an effective medium model (Figure S8b). Both analyses indicate that despite the extreme polymer confinement the properties of the hybrid stacks could be described by linearly interpolating the properties of the two bulk constituents. The polymer confinement, however, leads to a significant increase in the glass transition temperature (T_g) of PVP, with no discernable T_g below 250 °C even at the lowest Hec composition (Figure S8a). Expectedly, the thermal conductivity of the Bragg stacks strongly depends on the direction. The in-plane thermal conductivity achieves its maximum, $k_{\parallel,\mathrm{max}}$= 5.71 $Wm^{-1}K^{-1}$, in Hec100/PVP0, which is even higher than typical in-plane thermal conductivities of natural micas (Figure 4a).[29] The lower end is given by the isotropic thermal conductivity of Hec0/PVP100, *i.e.*, $k_{\perp,\mathrm{min}}$ = 0.17 $mWm^{-1}K^{-1}$ (only determined by photoacoustic characterization). The four hybrid Bragg stacks have in-plane thermal conductivities between these limiting values following a parallel mixing model (Figure 2c).[30] This is again surprising, as it implies that the confinement of PVP has no effect on the in-plane thermal conductivity of the Hec/PVP hybrid stacks compared to bulk PVP. The cross-plane thermal conductivity exhibits a broad minimum at $k_\perp$ ≈ 0.09 W $mWm^{-1}K^{-1}$, which is comparable to previously reported data for organoclay laminates.[5b] The deviation of the cross-plane thermal

conductivities from an effective medium behavior (Figure 2d, dashed line) could be attributed to the Hec/PVP interfaces, which are the dominating contributors to the cross-plane thermal resistance, as discussed below. The thermal conductivity anisotropy, $k_{\parallel}/k_{\perp}$, depends strongly on the hybrid composition, attaining a maximum of 38 in Hec51/PVP49 (Figure 2e). We note that this anisotropy is exceptionally high for electrically insulating hybrid materials[31] and outperforms natural nacre by a factor of ~20.[32] All in all, the structural perfection of the pure components and hybrid Bragg stacks translate into a record-high in-plane thermal conductivity and thermal transport anisotropy.

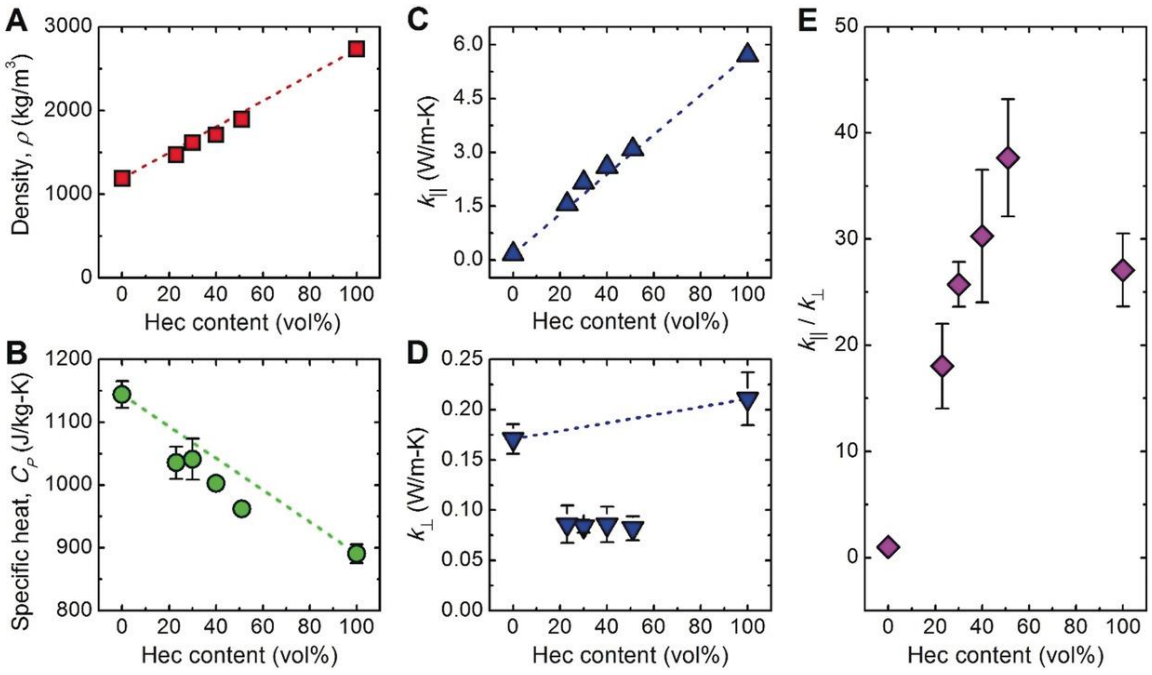

Figure 2. Direction-dependent thermal conductivities of Hec/PVP hybrid Bragg stacks. a) Film density, b) specific heat, and effective c) in-plane and d) cross-plane thermal conductivities, as a function of the Hec volume fraction. The red, green, and blue dashed lines in a-d) show linear trends based on a simple mixing model, *A(x) = (1-x)A(0%)+xA(100%)*, where *A* represents ρ, C_P, $k_{\parallel}$, or $k_{\perp}$, and x denotes the Hec volume fraction. e) Ratio of the in-plane to cross-plane thermal conductivities *vs*. the Hec volume fraction. For clarity, error bars smaller than the symbol size are not shown.

Anisotropic Mechanical Properties.

The unique macroscopic orientation in the hybrid Bragg stacks allows us to track down the origin of their high thermal conductivity anisotropy by measuring their full mechanical tensors. The measurements were conducted by using BLS, which

probes the phonon wave vector, q, dependent sound velocity, v, through inelastic light scattering by thermally excited, high frequency (GHz) phonons.[10] Since the hybrid Bragg stacks are transversely isotropic, only q vectors in a single plane containing the symmetry axis have to be considered. For such a q vector, the direction can be denoted by α, the angle between q and the normal to the sample film, and because of symmetry α can be restricted in the range from 0° to 90°. The measurements corresponding to $\alpha = 0°$, $0° < \alpha < 90°$, and $\alpha = 90°$ were conducted in the reflection, backscattering, and transmission scattering geometries, respectively, while the polarization of the phonon mode was selected using different incident and scattered light polarization configurations (*e.g.*, VV for quasi-longitudinal (Q-L) and quasi-transverse (Q-T) modes, and VH for a pure-transverse (P-T) mode).[33] This flexibility of accessible parameters makes BLS particularly suitable for characterizing anisotropic or crystalline structures, as demonstrated in previous experiments on mica crystals.[34] Since this work is the first one to apply the BLS technique to a hybrid Bragg stack material, we briefly outline the BLS measurement and data analysis.

Consider Hec31/PVP69 as an example. A typical BLS spectrum from the reflection geometry (inset to Figure S14a) displays a cross-plane longitudinal ($L_\perp$) mode in the VV polarization configuration (Figure S14b). A typical BLS spectrum from the backscattering geometry (Figure 3a, top-right inset) depicts a Q-L and a Q-T mode in the VV polarization configuration (Figure 2a) and a weak P-T mode in the VH polarization configuration (Figure 3a, top-left inset). Comparatively richer information exists in a typical BLS spectrum from the transmission geometry (Figure 3b, top-right inset). In the VV polarization configuration, the BLS spectrum features an in-plane longitudinal ($L_\parallel$) and a Q-L mode at a small laser incident angle, β, and an additional Q-T mode at a large β (Figure 3b). In the VH polarization configuration, a weak P-T mode at all β (Figure 3b, top-left inset) is clearly resolved. In the transmission BLS spectra, the intensity ratio of the Q-L and

Q-T peaks yields additional information (Figure S15b) and the Q-T mode intensity increases noticeably at higher Hec contents. By comparing the backscattering and transmission spectra, it becomes clear that the appearance of the Q-L and Q-T peaks in the latter (Figure 3b) results from the scattering of the laser beam internally reflected on the sample's backside.[35]

Based on the frequency shift, f, from the BLS spectrum and the phonon wave vector, q, from the momentum conservation analysis, we calculated the sound velocity along a certain q as $v = 2\pi f/|q|$. Whereas the reflection measurements give the v_{Q-L} at α = 0° and the transmission measurements result in the v_{Q-L}) and v_{P-T} at α = 90°, the backscattering measurements provide sound velocities for all the Q-L, Q-T, and P-T modes at intermediate α angles, as limited by the sample's refractive index. These direction-dependent sound velocities are reported in Figure 3c for Hec31/PVP69; additional data for the other samples are shown in Figure S16, A-D. Since sound velocities are intimately related to the elastic stiffness tensor in the framework of the Christoffel equation,[36] the availability of the former together with the measured sample densities (Figure 2a and Table S4) enables unique determination of the latter. For a transversely isotropic material, the elastic stiffness tensor contains five independent elastic constants (*e.g.*, C_{11}, C_{12}, C_{13}, C_{33}, and C_{44}).[37] Through χ^2 fitting[38], we obtained the elastic stiffness constants (Figure S16e and Table S4), which allow theoretical representation of the direction-dependent sound velocities (solid lines in Figure 3c and Figure S16, a-d) as well as determination of the engineering mechanical properties (Figure 3d and Table S5). In addition, we analyzed the error bars (standard deviations) of the quantities according to principles of uncertainty propagation (Section S5).

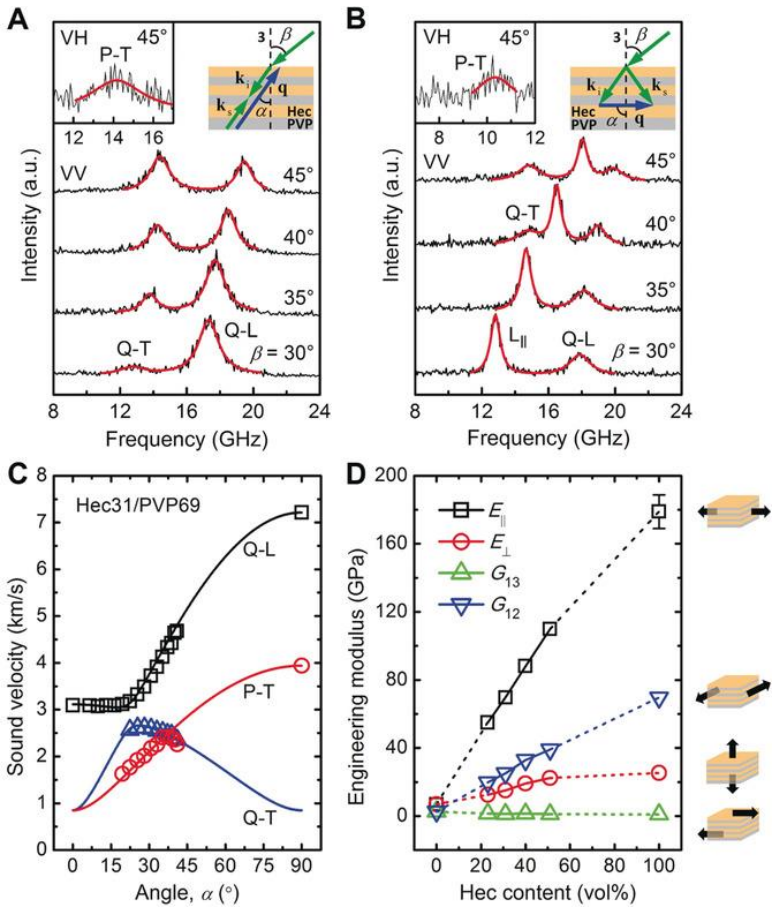

Figure 3. BLS measurements and strong mechanical anisotropy of Hec/PVP hybrid Bragg stacks. a,b) Polarized BLS spectra (anti-Stokes side) of the Hec31/PVP69 hybrid stack film recorded in a) the backscattering geometry with q forming a variable angle, α, with the normal to the sample film (top-right inset to a)) and b) the transmission geometry with the phonon wave vector, q, directed in-plane ($\alpha = 90°$; top-right inset to b)). k_i and k_s are the wave vectors of the incident and scattered light beams, respectively. β is the incident angle of the laser beam. The quasi-longitudinal (Q-L), quasi-transverse (Q-T), and in-plane longitudinal ($L_{\parallel}$) phonon modes are indicated in a) and b). The much weaker depolarized VH spectra of the pure transverse modes are shown in the top-left insets. Notice the correspondence between the Q-L and Q-T modes in a) and those in b). c) Direction-dependent sound velocities of the observed acoustic phonons in the BLS spectra of Hec31/PVP69. The three solid lines indicate theoretical representations (Equations (S6)-(S8)) of the experimental sound velocities of the three modes. d) Composition dependence of four engineering moduli. The moduli of the anisotropic hybrid films are extrapolated to those of the pure PVP and pure Hec films, as shown by the dashed lines. The four schematics beside d) visualize the physical meanings of the corresponding moduli.

This analysis provides the first direction-dependent insights into the mechanical properties of hybrid Bragg stacks in general and of clay/polymer nanocomposites in particular. The Young's moduli, $E_{\parallel}$ and $E_{\perp}$, and torsional shear modulus, G_{12}, all increase with increasing Hec volume fraction. The sliding shear modulus, G_{13}, however, decreases from 2.6 GPa in Hec0/PVP100 to 1.0 GPa in Hec100/PVP0. A

reduction in polymer chain entanglement upon confinement could be the cause of the decrease in G_{13}[39] Since the elastic moduli of polymer nanocomposites depend on the specific filler-polymer and polymer-polymer interactions, a rationalization of the increase ($E_{\parallel}$, $E_{\perp}$, G_{12}) or decrease (for G_{13}) with Hec content would require computer simulations.[39] All the mechanical moduli of the Bragg stacks display an effective medium behavior, assuming values between those of the two bulk components. We point out that even though the PVP chains are strongly confined between the adjacent Hec nanosheets (note R_{g}, PVP > 5(d_{XRD} - d_{Hec})), bulk properties (*e.g.*, ρ_{PVP}, ρ_{Hec}) are sufficient to fully capture the BLS measurements. As expected from the structural anisotropy, the Young's moduli exhibit large differences between the in-plane and cross-plane directions (Figure 3d). As the Hec volume fraction increases from 0 to 100 %, the mechanical anisotropy ratio, $E_{\parallel}/E_{\perp}$, increases from 1 to 7. Concomitantly, the two characteristic Poisson's ratios, υ_{13} and υ_{12}, vary in ranges of 0.02-0.05 (nearly zero or cork-like values) and 0.34-0.41 (typical polymer values), respectively (Table S5). The reasonable values of the mechanical properties corroborate the validity of continuum mechanics at length scales of a few nanometers and in the presence of extreme polymer confinement.

In the last section, we summarize the new insights onto the anisotropic thermoelasticity that can be gained from this wholistic analysis. We firstly exploit the directly measured direction-dependent sound velocities, and secondly correlate the derived mechanical moduli to the direction-dependent thermal conductivities. We first apply a kinetic theory model, $k = C_{\mathrm{V}}\bar{v}_{\mathrm{g}}\overline{\Lambda}/3$ to estimate the average phonon mean free path $\overline{\Lambda}$ along different directions in the Bragg stacks.[40] We use $C_{\mathrm{V}} = C_{\mathrm{P}}\mathrm{P}$ and $\bar{v}_{\mathrm{g}} = \bar{v}_{\mathrm{s},\parallel} = (v_{\mathrm{Q-L},\parallel} + v_{\mathrm{Q-T},\parallel} + v_{\mathrm{P-T},\parallel})/3$; a similar analysis is done for $k_{\perp}$ The in-plane $\overline{\Lambda}$ strongly depends on the hybrid composition, ranging from 14 Å for Hec100/PVP0 to 2 Å for Hec0/PVP100 (Figure 4a). We note that these $\overline{\Lambda}$ values significantly underestimate the presence of longer ranged phonons, which are typically better described by a phonon mean free path accumulation

function.[40,41] It is well known that thermal transport involves phonons over a wide range of frequencies which have different specific heat capacities, group velocities, and mean free paths. The underestimated $\overline{\Lambda}$ in our analysis could be attributed to the overestimated $\bar{v}_g$ from the BLS measurements, which mainly characterizes the propagation speed of a small fraction of the low frequency (long wavelength) phonons. These low frequency phonons carry only a negligible fraction of the overall heat. For the in-plane direction, the lateral size of the Hec nanosheets by far exceeds the average phonon mean free path. Hence, the high in-plane thermal conductivities are governed by the intrinsic material properties, not by the presence of grain boundaries between the aligned Hec nanosheets. The complementary analysis for $k_\perp$ demonstrates a strong reduction of $\overline{\Lambda}$ down to less than 1 Å (Figure 4b) with no discernible composition dependence along the cross-plane direction. Interfacial effects apparently dominate the thermal transport in this direction, which is better analyzed using a series resistance model (SRM, Figure 4c and f) as outlined by Losego *et al*.[5b] The fitted value of the interfacial conductance, $G_{\mathrm{Hec/PVP}}$ = 89 ± 8 MWm^{-2}K^{-1} (see Section S4), falls well into the range of reported values for other inorganic/organic interfaces.[21, 42] The intercalation of PVP between the clay sheets leads to a strong reduction of the interfacial conductance, which is $G_{\mathrm{Hec/PVP}}$ = 219 ± 28 MWm^{-2}K^{-1} for the pure hectorite.

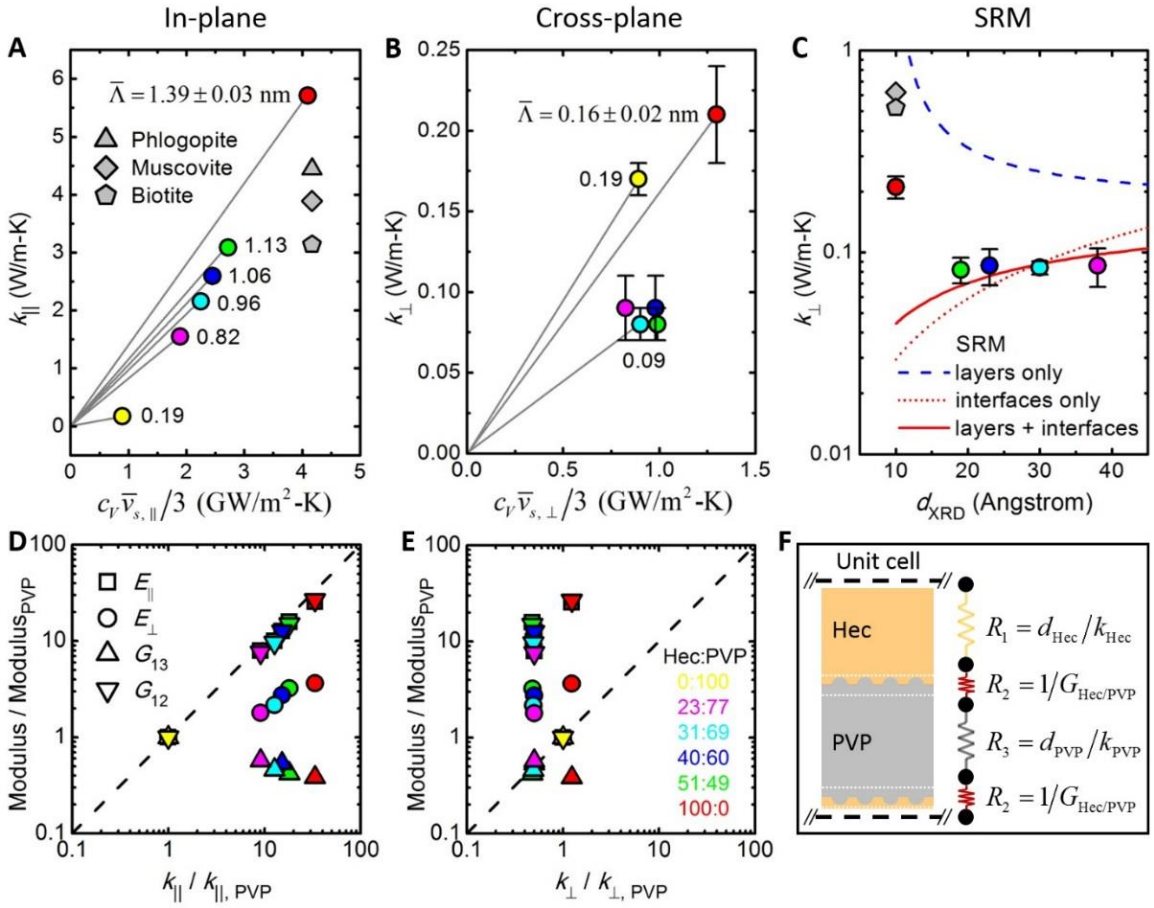

Figure 4. Analysis of anisotropic thermomechanical coupling in Hec/PVP hybrid Bragg stacks. a) Effective in-plane thermal conductivity, $k_{\parallel}$, *vs.* $C_V \bar{v}_{s,\parallel}/3$. The yellow, purple, cyan, blue, green, and red colored symbols represent the Hec0/PVP100, Hec23/PVP77, Hec31/PVP69, Hec40/PVP60, Hec51/PVP49, and Hec100/PVP0 samples, respectively. The phlogopite data point is from our additional measurements; muscovite and biotite data points are from reference.[29] b) Effective cross-plane thermal conductivity, $k_{\perp}$, *vs.* $C_V \bar{v}_{s,\perp}/3$. In a) and b), the numbers beside the data points indicate the average phonon mean free paths, $\bar{\Lambda}$ (*i.e.*, the slope of the gray lines). c) Effective cross-plane thermal conductivity, $k_{\perp}$ *vs.* the basal spacing of the Bragg stacks. The red solid line is a fit to the experimental data based on the series resistance model (SRM) shown in f). As a comparison, the blue dashed line considers only the thermal resistances of the Hec and PVP layers, and the red dotted line considers only the thermal resistances of the Hec/PVP interfaces. d) Normalized mechanical moduli *vs.* normalized effective in-plane thermal conductivity, $k_{\parallel}$. The dashed line shows a direct correlation between the two axes with a power of one. e) Normalized mechanical moduli *vs.* normalized effective cross-plane thermal conductivity, $k_{\perp}$. In d) and e), the following values of the pure PVP film, $E_{\parallel} = E_{\perp} = 7.0$ GPa, $G_{13} = G_{12}$ = 2.6 GPa, and $k_{\parallel} = k_{\perp}$k|| = 0.17 Wm^{-1}K^{-1}, are used as references in the normalization. f) A schematic of the SRM used to analyze the Hec/PVP interfacial thermal conductance.

We next address the correlation between the anisotropic mechanical moduli and thermal conductivities. Two distinct conclusions can be drawn. (i) In the direction parallel to the Hec nanosheets, a correlation between the thermal conductivity and all mechanical moduli is found. Along this direction the phonon mean free path is

considerably shorter than the typical lateral size of a Hec nanosheet, rendering grain boundary effects insignificant. The influence of $E_{\parallel}$, $E_{\perp}$, and G_{12} on the thermal transport dominates over G_{13} since the former moduli show a direct relation to the in-plane thermal conductivity. $E_{\parallel}$ and G_{12} show a power scaling law close to one (0.93) between in-plane thermal conductivity and modulus ($E_{\perp}$ scales with 0.38). Whereas we find a clear correlation between the moduli and the thermal conductivity, we cannot deduce which change in mechanical modulus causes which effect to the thermal transport. The applicability of a simple mixing model along the parallel direction as outlined in Figure 2a-c is certainly surprising in view of the strong polymer confinement effect on the glass transition (Figure S8). (ii) In the direction perpendicular to the Hec nanosheets, the phonon mean free path is comparable to the periodicity of the Bragg stacks. Here, the composition dependence of the mechanical properties does not influence the reduction of the cross-plane thermal conductivity (vertical spread of the data points in Figure 4e). Thus, changes to the gallery height are insignificant, which indicates the overwhelming contribution of the interfacial conductance. Considering changes to the pure components we find that reducing the sliding shear modulus G_{13} decreases the cross-plane thermal transport properties of the polymer component. The reduction in $k_{\perp}$ of the hybrid stacks relative to pure hectorite correlates to losses in $E_{\parallel}$, $E_{\perp}$, and G_{12} that apparently counteract the increase in G_{13}. Overall, the mechanical and thermal properties are uncorrelated along the perpendicular direction, and the thermal transport is governed by the Hec/PVP interfaces.

3. Conclusion

In conclusion, fully delaminated hectorite platelets can be processed into hybrid Bragg stacks with unique properties, with the polymer polyvinylpyrrolidone being the intercalated second component. Such long-range 1D ordered materials become accessible by simply spray coating the desired nematic dispersions of

adjusted volume fractions, which at the same time controls the periodicity of the hybrid stacks down to the angstrom level. The macroscopic lattice alignment enables the determination of direction-dependent thermoelastic properties, which we assessed by thermal transport characterization techniques and Brillouin light spectroscopy. We found a record-high anisotropy between the in-plane and cross-plane thermal conductivities in clay/polymer hybrid materials. This is corroborated by the first report of direction-dependent Young's and shear moduli that are also strongly anisotropic. The effective gallery spacing, density, specific heat, and in-plane thermal conductivity were found to conform to composition-dependent simple mixing models. Despite the nanometer-level lattice periodicity and angstrom-level polymer confinement, the Christoffel-equation-based model, derived in the framework of continuum mechanics, remains applicable for determining the anisotropic elasticity. Of general relevance is the direction dependency of the way that the mechanical moduli and thermal conductivities correlate. In the in-plane direction, where grain boundaries are negligible relative to the phonon mean free path, $E_{\parallel}$, $E_{\perp}$, and G_{12} directly correlate with the in-plane thermal conductivity. In the cross-plane direction, where the phonon mean free path is comparable to the lattice periodicity, the thermal transport is governed by the clay/polymer interfaces. We are convinced that a wholistic understanding of direction-dependent thermoelastic properties will have a broad impact on important applications such as electronic packaging and thermoelectrics. This contribution is only a first step towards this goal. More work needs to be done for the deterministic - maybe even independent - design of mechanical and thermal properties. Future studies should also address the role of enthalpic interaction at the clay/polymer interface, interdigitation of the confined polymer, size effects of the platelets, and other nanosheet materials.

4. Experimental Section

Sample Preparation.

The synthetic clay sodium fluorohectorite (Hec, $[Na_{0.5}]^{inter}[Mg_{2.5}Li_{0.5}]^{oct}[Si_4]^{tet}O_{10}F_2$) was delaminated by immersing it into Millipore water (0.5 wt%). The aqueous PVP solution (1 wt%) was added in the desired weight ratio. The suspension was mixed for at least one day in an overhead shaker. The homogeneity of the suspension was crosschecked by SAXS measurements. Self-supporting films were prepared using a fully automatic spray coating system. Every spraying cycle is followed by a drying cycle of 90 s at a temperature of 55 °C. We prepared pure PVP, pure Hec, and four hybrid Hec/PVP films. The self-supporting films were characterized by thermogravimetric analysis, XRD, and TEM. Additional information about the sample preparation can be found in Section S1.

In-Plane Thermal Conductivity Measurements.

Lock-in thermography measures the temperature spreading across the free-standing samples upon thermal excitation by a focused laser beam with a modulated intensity. To prevent convective heat losses, the experiments are conducted in a vacuum chamber. The amplitude and phase data are extracted from the radial temperature distribution. The thermal diffusivity is then fitted by the slope method for thermally thin films. With the density, determined by helium pycnometry, and the specific heat, determined by differential scanning calorimetry (DSC), the thermal conductivity can be calculated. More details are provided in Section S2.

Cross-Plane Thermal Conductivity Measurements.

The photoacoustic method uses a modulated laser beam to periodically heat a transducer layer in intimate contact with the sample. The heat is converted into an acoustic wave propagating into a gas tight cell above the sample, which is filled

with helium at 20 psi. A sensitive microphone detects the phase shift between the acoustic signal and the modulated laser by a lock-in amplifier. The frequency-dependent phase shift is then compared to a multilayer model, assuming one-dimensional heat transfer. Therefrom, the total layer resistance is obtained. With the film thickness determined by AFM, the effective thermal conductivity is calculated. More details are provided in Section S2.

Brillouin Light Spectroscopy (BLS).

BLS measures the phonon dispersion, $\omega(q)$, by detecting the Doppler frequency shift, ω, of the inelastically scattered light by sound waves ("phonons") with a wave vector, q. We recorded BLS spectra utilizing three scattering geometries (transmission, reflection, and backscattering) and two polarization configurations of the incident (λ = 532 nm) and scattered light (polarized VV, depolarized VH), which allowed us to establish the nature of the observed phonons. We varied the incident angle to obtain the direction-dependent sound velocities necessary for the determination of the anisotropic elasticity. The elastic stiffness tensors were obtained from the representation of the direction-dependent sound velocities by the Christoffel equation assuming transverse isotropy. The characteristic Young's moduli, shear moduli, and Poisson's ratios of the Bragg stacks were subsequently calculated. More details can be found in Section S3.

Acknowledgements

We thank Sabine Rosenfeldt for conducting SAXS measurements on the gel samples. We also thank Marco Schwarzmann for preparing TEM samples and taking TEM micrographs. The Volkswagen Foundation funded this project through a Lichtenberg professorship. DFG RE 3550/2-1 provided additional support. Z.W., K.R., and G.F. acknowledge the financial support by ERC AdG SmartPhon (Grant No. 694977).

Conflict of Interest

The authors declare no conflict of interest.

Keywords

Brillouin light scattering, mechanical properties, thermal conductivity, anisotropy,

Organic-inorganic hybrid composites

References

1. a) B. Graczykowski, A. El Sachat, J. S. Reparaz, M. Sledzinska, M. R. Wagner, E. Chavez-Angel, Y. Wu, S. Volz, Y. Wu, F. Alzina, C. M. Sotomayor Torres, Nat. Commun. 2017, 8, 415; b) M. E. Siemens, Q. Li, R. Yang, K. A. Nelson, E. H. Anderson, M. M. Murnane, H. C. Kapteyn, Nat. Mater. 2010, 9, 26-30; c) J. A. Tomko, A. Pena-Francesch, H. Jung, M. Tyagi, B. D. Allen, M. C. Demirel, P. E. Hopkins, Nat. Nanotechnol. 2018, 13, 959-964.

2. a) M. D. Losego, M. E. Grady, N. R. Sottos, D. G. Cahill, P. V. Braun, Nat. Mater. 2012, 11, 502-506; b) G. H. Kim, D. Lee, A. Shanker, L. Shao, M. S. Kwon, D. Gidley, J. Kim, K. P. Pipe, Nat. Mater. 2015, 14, 295-300.

3. S. Shen, A. Henry, J. Tong, R. Zheng, G. Chen, Nat. Nanotechnol. 2010, 5, 251-255.

4. a) X. Huang, G. Liu, X. Wang, Adv. Mater. 2012, 24, 1482-1486; b) R. Fuente, A. Mendioroz, A. Salazar, Mater. Lett. 2014, 114, 1-3.

5. a) C. Chiritescu, D. G. Cahill, N. Nguyen, D. Johnson, A. Bodapati, P. Keblinski, P. Zschack, Science 2007, 315, 351-353; b) M. D. Losego, I. P. Blitz, R. A. Vaia, D. G. Cahill, P. V. Braun, Nano Lett. 2013, 13, 2215-2219.

6. a) B. Wicklein, A. Kocjan, G. Salazar-Alvarez, F. Carosio, G. Camino, M. Antonietti, L. Bergström, Nat. Nanotechnol. 2015, 10, 277-283; b) T. Li, J. Song, X. Zhao, Z. Yang, G. Pastel, S. Xu, C. Jia, J. Dai, C. Chen, A. Gong, F. Jiang, Y. Yao, T. Fan, B. Yang, L. Wagberg, R. Yang, L. Hu, Sci. Adv. 2018, 4, eaar3724; c) M. Chau, B. A. F. Kopera, V. R. Machado, S. M. Tehrani, M. A. Winnik, E. Kumacheva, M. Retsch, Mater. Horiz. 2017, 4, 236-241.

7. X. Tian, M. E. Itkis, E. B. Bekyarova, R. C. Haddon, Sci. Rep. 2013, 3, 1710-1715.

8. N. Song, D. Jiao, S. Cui, X. Hou, P. Ding, L. Shi, ACS Appl. Mater. Interfaces 2017, 9, 2924-2932.

9. a) A. Eckert, T. Rudolph, J. Guo, T. Mang, A. Walther, Adv Mater 2018, 30, e1802477; b) T. Verho, M. Karesoja, P. Das, L. Martikainen, R. Lund, A. Alegría, A. Walther, O. Ikkala, Adv. Mater. 2013, 25, 5055-5059; c) T. Szabó, M. Szekeres, I. Dékány, C. Jackers, S. De Feyter, C. T. Johnston, R. A. Schoonheydt, J. Phys. Chem. C 2007, 111, 12730-12740; d) Z. Tang, N. A. Kotov, B. Magonov, B. Ozturk, Nat. Mater. 2003, 2, 413-418.

10. a) T. Still, High frequency acoustics in colloid-based meso- and nanostructures by spontaneous Brillouin light scattering, 1 ed., Springer-Verlag Berlin Heidelberg, 2010; b) E. Alonso-Redondo, M. Schmitt, Z. Urbach, C. M. Hui, R. Sainidou, P. Rembert, K. Matyjaszewski, M. R. Bockstaller, G. Fytas, Nat. Commun. 2015, 6, 8309.

11. a) V. Singh, T. L. Bougher, A. Weathers, Y. Cai, K. Bi, M. T. Pettes, S. A. McMenamin, W. Lv, D. P. Resler, T. R. Gattuso, D. H. Altman, K. H. Sandhage, L. Shi, A. Henry, B. A. Cola, Nat. Nanotechnol. 2014, 9, 384-390; b) A. Mendioroz, R. Fuente-Dacal, E. Apinaniz, A. Salazar, Rev. Sci. Instrum. 2009, 80, 074904.

12. L. Wang, T. Sasaki, Chem. Rev. 2014, 114, 9455-9486.

13. P. Davidson, C. Penisson, D. Constantin, J.-C. P. Gabriel, PNAS 2018, 115, 6662-6667.

14. A. Lerf, Dalton Trans. 2014, 43, 10276-10291.

15. V. Nicolosi, M. Chhowalla, M. G. Kanatzidis, M. S. Strano, J. N. Coleman, Science 2013, 340, 1226419.

16. M. Daab, N. J. Eichstaedt, A. Edenharter, S. Rosenfeldt, J. Breu, RSC Adv. 2018, 8, 28797-28803.

17. J. E. F. C. Gardolinski, G. Lagaly, Clay Miner. 2018, 40, 547-556.

18. M. Stöter, D. A. Kunz, M. Schmidt, D. Hirsemann, H. Kalo, B. Putz, J. Senker, J. Breu, Langmuir 2013, 29, 1280-1285.

19. S. Rosenfeldt, M. Stöter, M. Schlenk, T. Martin, R. Q. Albuquerque, S. Förster, J. Breu, Langmuir 2016, 32, 10582-10588.

20. K. Sano, Y. S. Kim, Y. Ishida, Y. Ebina, T. Sasaki, T. Hikima, T. Aida, Nat. Commun. 2016, 7, 12559.

21. H. Kalo, W. Milius, J. Breu, RSC Adv. 2012, 2, 8452-8459.

22. D. A. Kunz, J. Erath, D. Kluge, H. Thurn, B. Putz, A. Fery, J. Breu, ACS Appl. Mater. Interfaces 2013, 5, 5851-5855.

23. M. Wong, R. Ishige, K. L. White, P. Li, D. Kim, R. Krishnamoorti, R. Gunther, T. Higuchi, H. Jinnai, A. Takahara, R. Nishimura, H. J. Sue, Nat. Commun. 2014, 5, 3589.

24. a) W. Seidl, J. Breu, Z. Kristallogr.- Cryst. Mater. 2005, 220, 169-176; b) A. Baumgartner, K. Sattler, J. Thun, J. Breu, Angew. Chem. Int. Ed. 2008, 47, 1640-1644.

25. N. L. McFarlane, N. J. Wagner, E. W. Kaler, M. L. Lynch, Langmuir 2010, 26, 13823-13830.

26. E. S. Tsurko, P. Feicht, F. Nehm, K. Ament, S. Rosenfeldt, I. Pietsch, K. Roschmann, H. Kalo, J. Breu, Macromolecules 2017, 50, 4344-4350.

27. D. M. Moore, R. C. Reynolds, D. M., X-ray Diffraction and the Identification and Analysis of Clay Minerals, Oxford University Press, Oxford, U.K., 1997.

28. A. Philipp, N. W. Pech-May, B. A. F. Kopera, A. M. Lechner, S. Rosenfeldt, M. Retsch, Anal. Chem. 2019, 91, 8476-8483.

29. C. Clauser, E. Huenges, in Rock Physics & Phase Relations: A Handbook of Physical Constants (Ed.: T. J. Ahrens), American Geophysical Union, Washington DC, 2013, pp. 105-126.

30. J. K. Carson, S. J. Lovatt, D. J. Tanner, A. C. Cleland, Int. J. Heat and Mass Transfer 2005, 48, 2150-2158.

31. Y.-F. Huang, Z.-G. Wang, H.-M. Yin, J.-Z. Xu, Y. Chen, J. Lei, L. Zhu, F. Gong, Z.-M. Li, ACS Appl. Nano Mater. 2018, 1, 3312-3320.

32. L. P. Tremblay, M. B. Johnson, U. Werner-Zwanziger, M. A. White, J. Mater. Res. 2011, 26, 1216-1224.

33. R. W. Gammon, Brillouin scattering experiments in the ferroelectric crystal triglycine sulfate, PhD thesis, John Hopkins University, 1967.

34. L. E. McNeil, M. Grimsditch, J. Phys. Cond. Mat. 1993, 5, 1681.

35. J. Krüger, L. Peetz, M. Pietralla, Polymer 1978, 19, 1397-1404.

36. a) S. P. Cheadle, R. J. Brown, D. C. Lawton, Geophysics 1991, 56, 1603-1613; b) M. Mah, D. R. Schmitt, Geophysics 2001, 66, 1217-1225.

37. a) S. Cusack, A. Miller, J. Mol. Biol. 1979, 135, 39-51; b) Y. C. Chu, S. I. Rokhlin, J. Acoust. Soc. Am. 1994, 96, 342-352.

38. M. Zgonik, P. Bernasconi, M. Duelli, R. Schlesser, P. Günter, M. H. Garrett, D. Rytz, Y. Zhu, X. Wu, Phys. Rev. B 1994, 50, 5941-5949.

39. J. Midya, Y. Cang, S. A. Egorov, K. Matyjaszewski, M. R. Bockstaller, A. Nikoubashman, G. Fytas, Nano Lett. 2019, 19, 2715-2722.

40. G. A. Elbaz, W. L. Ong, E. A. Doud, P. Kim, D. W. Paley, X. Roy, J. A. Malen, Nano Lett. 2017, 17, 5734-5739.

41. A. S. Henry, G. Chen, J. Comput. Theor. Nanosci. 2008, 5, 1-12.

42. W. L. Ong, S. M. Rupich, D. V. Talapin, A. J. McGaughey, J. A. Malen, Nat. Mater. 2013, 12, 410-415.

Supporting Information

Section S1. Sample Preparation

Materials

The synthetic clay sodium fluorohectorite (Hec, $[Na_{0.5}]^{inter}[Mg_{2.5}Li_{0.5}]^{oct}[Si_4]^{tet}O_{10}F_2$) was synthesized via melt synthesis followed by long-term annealing, according to an established procedure. The material featured a cation exchange capacity of 1.27 $mmolg^{-1}$ (References[1]). Polyvinylpyrrolidone (PVP; Mw = 40.000 $gmol^{-1}$) was provided by Sigma Aldrich.

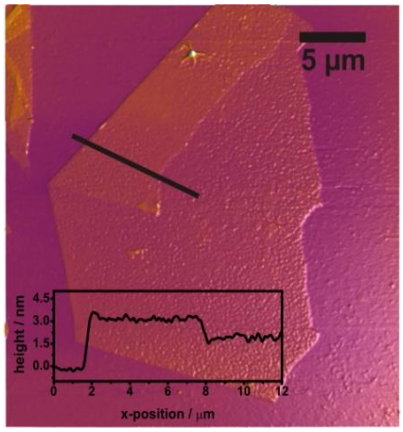

Figure S1. Atomic force microscopy image of a single delaminated Hec nanosheet. Reprinted with permission from Langmuir [1b] Copyright 2019 American Chemical Society.

Film Preparation

For the delamination, the synthetic Hec was immersed into Millipore water (0.5 wt%). The complete delamination was studied by small angle X-ray scattering (SAXS).[2] The aqueous PVP solution (1 wt%) was added in the desired weight ratio. The suspension was mixed for at least 1 day in the overhead shaker. Homogeneity of the suspensions was cross-checked by SAXS measurements. All SAXS data were measured using the small-angle X-ray system "Double Ganesha AIR" (SAXSLAB, Denmark). The X-ray source of this laboratory-based system is a rotating anode (copper, MicroMax 007HF, Rigaku Corporation, Japan) providing a micro-focused beam. The data were recorded by a position sensitive detector (PILATUS 300 K, Dectris). To cover the range of scattering vectors between 0.004-1.0 $Å^{-1}$, different

detector positions were used. The measurements of the suspensions were done in 1 mm glass capillaries (Hilgenberg, code 4007610, Germany) at room temperature. To improve the detection limit of the in-house machine, the suspensions were first concentrated to ≈ 10 wt% by centrifugation at 10000 rpm for 1 hour. A rational basal series was found for all suspensions, indicating that all clay nanosheets were separated to exactly the same distance by water and PVP (Figure S2). Within experimental errors reaggregation to stacks of Hec can be excluded by the absence of a reflection typical for crystalline hydrated Hec phases at q = 0.65-0.41 Å^{-1}.

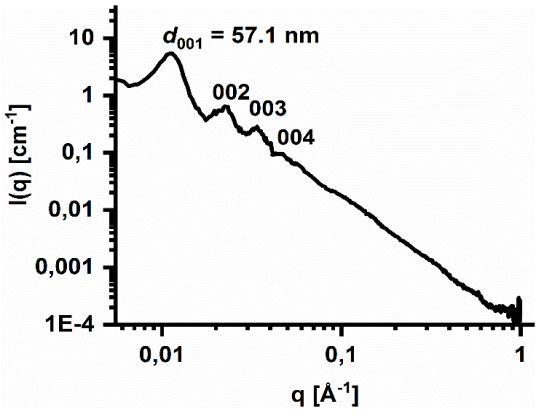

Figure S2. 1D SAXS pattern of the concentrated gel sample Hec40/PVP60.

The self-supporting films were prepared by spray coating. The fully automatic spray coating system was equipped with a SATA 4000 LAB HVLP 1.0 mm spray gun (SATA GmbH & Co. KG, Germany). Suspensions were sprayed on a corona-treated polyethylene terephthalate (PET) foil (optimont 501, bleher Folientechnik, Germany). The spraying and nozzle pressure were set constant at values of 2 and 4 bar, respectively. The round per flat fan control was set to 6 with a flow speed of 3 mLs^{-1}. The distance between the spraying gun and the substrate was 17 cm. The thickness of the suspension layer applied in one spraying step is ≈ 2 µm which corresponds to ≈ 20 nm dry nanocomposite film thickness. For drying the suspension layer, the sample is stopped under infrared lamps until evaporation of the solvent is complete. After every spraying cycle, a drying cycle of 90 s with a temperature of 55 °C took place. The spraying/drying cycle is repeated until the

desired barrier film thickness of 50 μm is obtained. Afterwards, the film was dried at 100 °C for 3 days and peeled off from the PET foil to achieve self-supporting films. For characterization by photoacoustic analysis thinner films on the order of a few μm were spray coated onto clean 1 mm thick microscopy glass slides.

In total, we prepared six samples, which are denoted as Hec0/PVP100, Hec23/PVP77, Hec31/PVP69, Hec40/PVP60, Hec51/PVP49, and Hec100/PVP0, respectively (Table S1). Throughout the manuscript, all samples are referred to by the nominal volume fractions (vol%) of Hec and PVP, respectively. To rule out compositional changes during spray coating, these ratios were cross-checked (Table S1) by thermogravimetric analysis (TGA), using a Linseis STA PT 1600 (Linseis Messgeräte GmbH, Germany). Changes in mass observed upon heating in synthetic air up to 800 °C were attributed to the combustion of PVP.

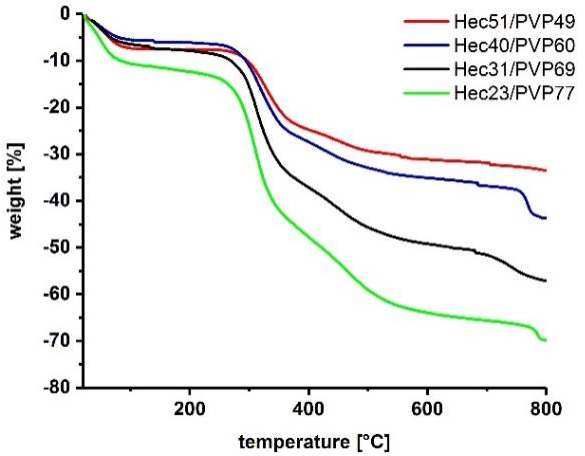

Figure S3. TGA curves of four hybrid Bragg stacks. The weight loss below 200 °C corresponds to the water.

X-ray diffraction (XRD) patterns for the films were recorded in Bragg-Brentano-geometry on an Empyrean diffractometer (PANalytical B.V.; the Netherlands) using Cu Kα radiation (λ = 1.54187 Å). The self-supporting films were placed on glass slides (Menzel-Gläser; Thermo Scientific). Prior to the XRD measurements, the samples were dried at 100 °C in a vacuum chamber for one week.

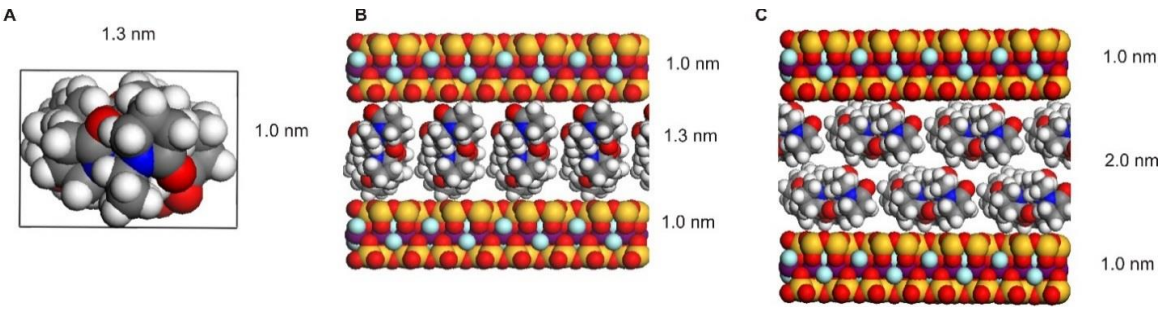

Figure S4. Space filling models. a) PVP viewed along the polymer backbone chain. b) Monolayer of PVP oriented with the longer principal axis perpendicular to the Hec nanosheet. c) Bilayer of PVP lying in the plane of the Hec nanosheets.

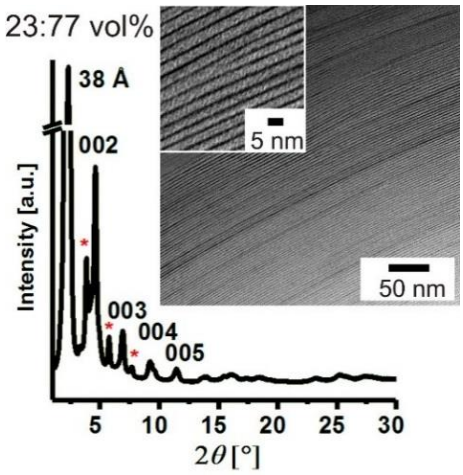

Figure S5. XRD pattern and TEM image of the nanocomposite film Hec23/PVP77. The red asterisks denote a second series of basal reflections of a minority phase (d = 2.3 nm).

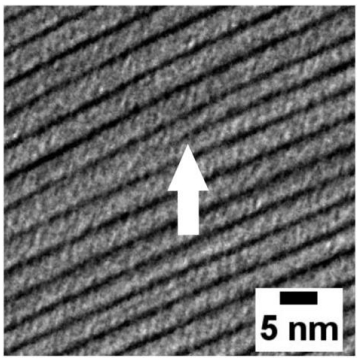

Figure S6. Lattice plane termination of a single Hec nanosheet.

As a measure of the quality of the one-dimensional crystallinity of the films, the coefficient of variation (CV) and the full width at half maximum (FWHM) were determined (Table S1). Large CV-values (≈ 3%)[3] and large FWHM indicate non-rationality of the diffraction pattern as caused by a random interstratification of different interlayer heights.

Assuming PVP and Hec densities of 1.2 gcm^{-3} and 2.7 gcm^{-3}, respectively, nominal d-spacings can be calculated for the various volume ratios (d_{nominal} in Table S1).[4] They agree reasonably with those obtained from XRD measurements (d_{XRD} in Table S1). In analyzing the cross-plane thermal conductivity using the series resistance model, we used the d_{XRD} values.

Table S1. Overview of the structural and chemical characterization.

	nominal Hec:PVP ratio [wt%]	nominal Hec:PVP ratio [vol%]	PVP content [a] [wt%]	PVP content [b] [vol%]	d_{nominal} [Å]	d_{XRD} [Å]	gallery height (PVP) [c] [nm]	CV [%]	FWHM [°2θ]
Hec100/PVP0	100:0	100:0	-	-	10	10	-	-	-
Hec51/PVP49	70:30	51:49	27	45	18	19	0.9	5.9	0.4
Hec40/PVP60	60:40	40:60	38	58	23	23	1.3	1.3	0.3
Hec31/PVP69	50:50	31:69	49	68	30	30	2.0	1.0	0.3
Hec23/PVP77	40:60	23:77	59	76	41	38	2.8	2.8	0.3
Hec0/PVP100	0:100	0:100	100	100	-	-	-	-	-

[a] determined by TGA; [b] calculated with the PVP content determined by TGA; [c] gallery height corresponds to the *d*-spacing minus the Hec platelet height of 1 nm.

Scanning electron microscopy (SEM) images were taken with a Zeiss LEO 1530 (Carl Zeiss AG, Germany) at an operating voltage of 3 kV. Cross sections were prepared by cutting with a razor blade. The samples with Hec were sputtered with 10 nm carbon.

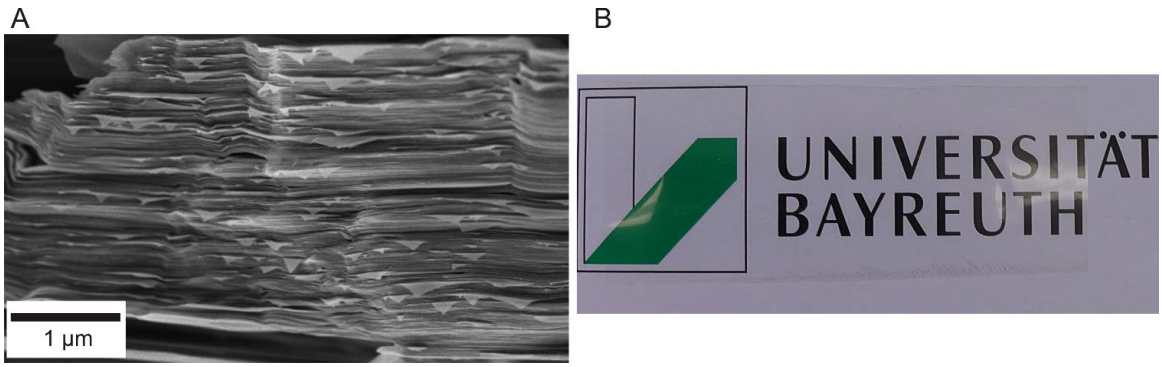

Figure S7. SEM image and photograph of the hybrid film. a) The SEM image displays the ordered arrangement of hectorite sheets at the macro-scale. b) As the hectorite platelets arrange highly ordered, light scattering is prevented and the films is transparent.

Transmission electron microscopy (TEM) images were taken on a JEOL JEM-2200FS (JEOL GmbH, Germany) at an acceleration voltage of 200 kV. Cross-section pictures of the self-supporting films were prepared with a Cryo Ion Slicer IB-09060CIS (JEOL, Germany).

Section S2. Thermal Measurements

For the determination of the in-plane and cross-plane thermal conductivity, the density and the specific heat are needed. Therefore, Helium pycnometry and differential scanning calorimetry (DSC) were used. We determined the in-plane thermal diffusivity by lock-in thermography, and the cross-plane thermal conductivity by the photoacoustic method. Prior to the measurements, the samples were dried at 100 °C in a vacuum chamber for one week.

Helium Pycnometry

The density of the samples was measured by helium pycnometry. Therefore, an Ultrapyc 1200e (Quantachrome Instruments) was used. Prior to each measurement the volume of the empty measurement cell was measured. Afterwards, small pieces of the free-standing films were weighed into the sample cell with a nominal volume of 1.8 cm^3. One hundred runs were performed to determine the volume of the films at room temperature. By knowing the mass (measured on a fine balance) and the volume, the density of the samples was calculated.

Differential Scanning Calorimetry

The specific heat was determined by DSC measurements according to the ASTM E1269 standard. The samples were freeze ground for better processability and contact to the DSC pans. The measurements were performed on a TA instruments Discovery DSC 2500. An isothermal step (1 h, 100 °C) was conducted prior to the measurement to ensure dry conditions. Then two heating cycles were used and

only the second cycle evaluated. The temperature profile ranged from -40 to 250 °C using a heating rate of 20 $Kmin^{-1}$ with a nitrogen flow of 50 $mLmin^{-1}$.

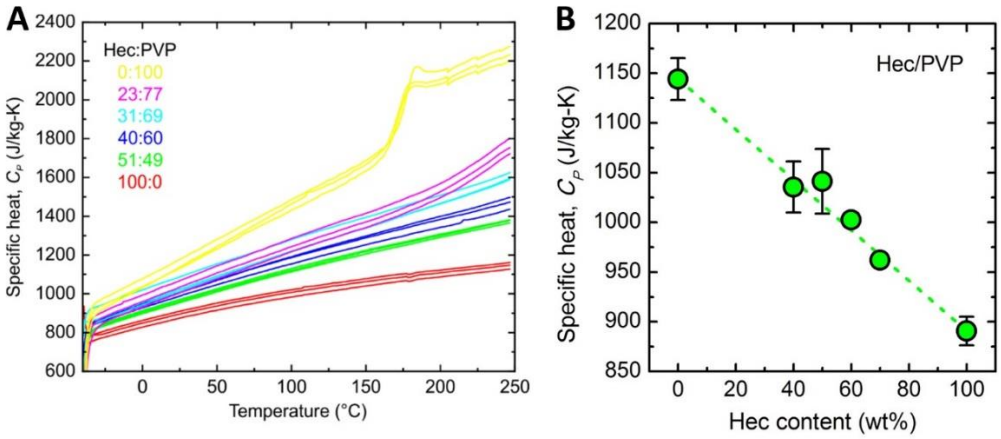

Figure S8. Temperature and composition dependencies of the specific heat. a) Three samples per Hec/PVP composition were measured. The average specific heat at 25 °C was used to calculate the thermal conductivity. b) The green dashed line shows the prediction by a simple mixing model, $C_P(x) = (1-x)C_P(0\%) + xC_P(100\%)$, with x being the hectorite weight fraction.

Lock-In Thermography

The in-plane thermal diffusivity of free-standing Hec/PVP stack films was obtained by lock-in thermography (LIT). The self-built LIT set-up is shown in Figure S9.

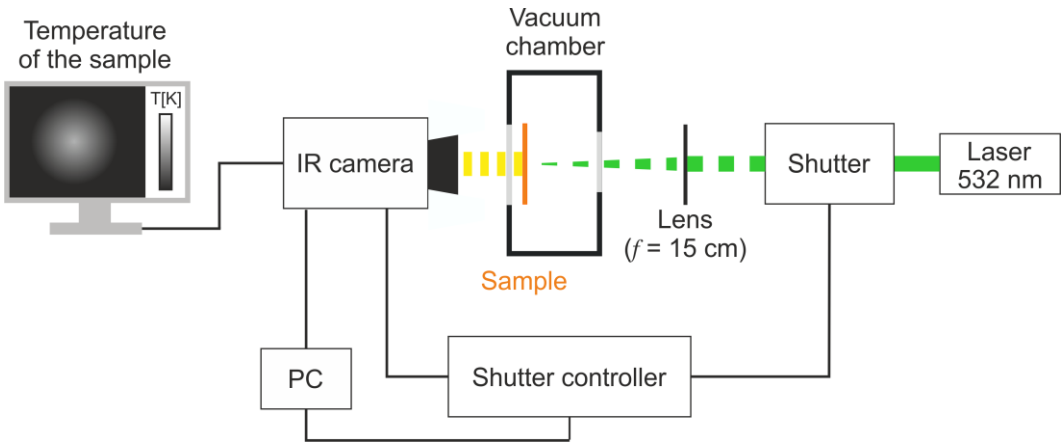

Figure S9. Scheme of the lock-in thermography set-up. The samples were measured in a vacuum chamber to avoid convective heat losses to the environment.

The sample is heated by a laser beam (Genesis MX 532-1000 SLM OPS, Coherent, λ = 532 nm) focused onto the sample surface by a lens of 150 mm focal length. The intensity of the laser is modulated using a shutter (SH05/M, Thorlabs) controlled by a shutter controller (SC10, Thorlabs). The emitted infrared (IR) radiation of the sample surface is detected by an Infratec VarioCAM HD research IR camera (spectral window: 7.5-14 μm). The camera is equipped with a close-up lense. In this configuration, the minimum spatial resolution is 29 μm (working distance: 33 mm). Since heat losses to the environment lead to an overestimation of the thermal diffusivity[5] all samples were measured under vacuum conditions (~$3x10^{-3}$ mbar). Furthermore, all samples were coated with a 20 nm carbon layer for enhanced laser absorption. The coating of the sample was facing to the IR camera. LIT measurements were performed using Infratec's IRBISactiveonline software. Measurements were conducted at several lock-in frequencies between 0.219 and 1.765 Hz (depending on the Hec/PVP composition). Furthermore, each measurement was averaged over several (600-2000) lock-in periods to enhance the signal to noise ratio, with the first 60-100 periods being discarded. The software calculates automatically the amplitude and phase of the temperature oscillations (Figure S10). The red point marks the midpoint of the laser excitation and thus the midpoint of the radial distribution.

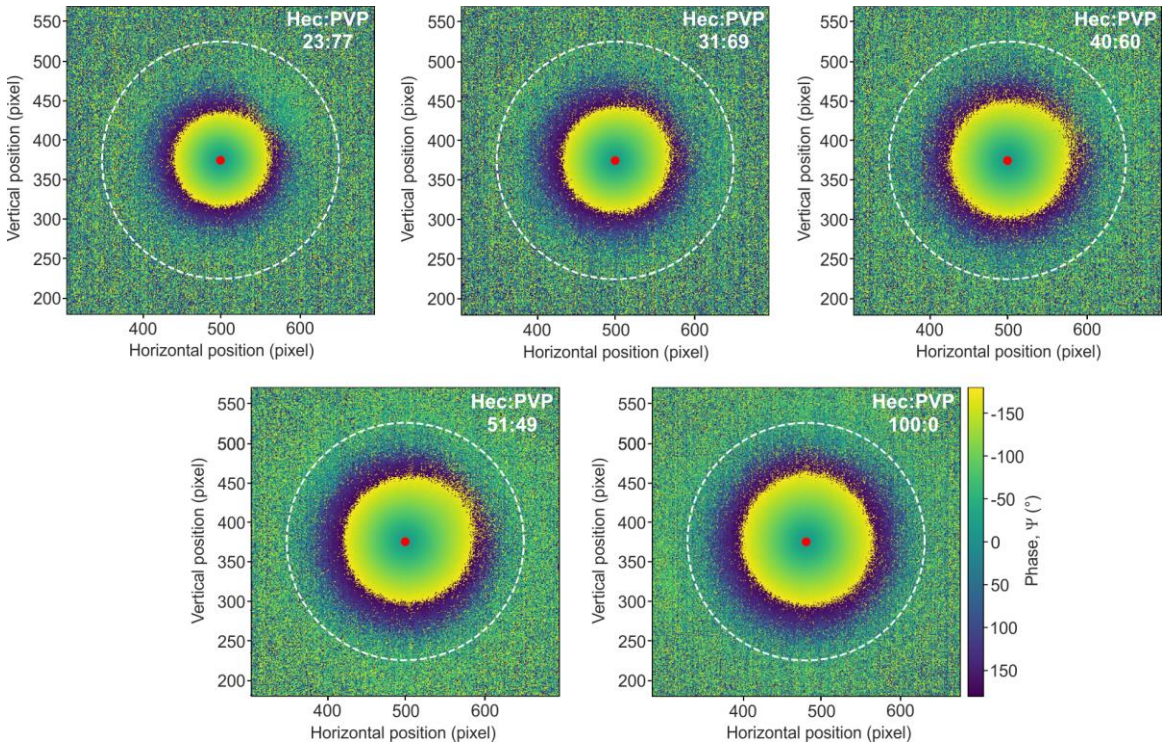

Figure S10. Exemplary two-dimensional phase images measured at a frequency of 1.111 Hz. The penetration depth of the temperature oscillations increases with increasing thermal diffusivity of the Hec/PVP films. The focal point of the laser is marked by a red point in the center of the IR image.

A self-written Python script is used to extract radial profiles for the phase and amplitdue images (Figure S11). The thermal diffusivity is calculated from the phase and amplitude slopes according to the slope method of a thermally thin film[5b]:

$$m_{\Psi} \cdot m_{\ln(Tr^{0.5})} = \frac{\pi \cdot f_{\mathrm{lock-in}}}{\alpha_{\parallel}} \tag{S1}$$

Here, m_{Ψ} is the slope of the linear relation of the phase and the radial distance r, $m_{\ln(Tr^{0.5})}$ is the slope of the linear relation of the natural logarithm of the amplitude T multiplied by the square root of the radial distance r, $f_{\mathrm{lock-in}}$ is the lock-in frequency, and $\alpha_{\parallel}$ is the in-plane thermal diffusivity.

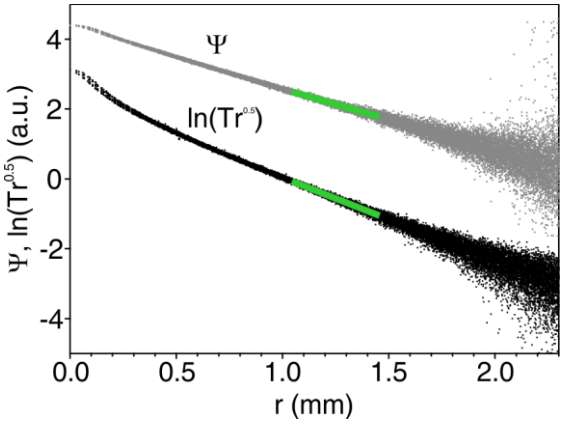

Figure S11. Exemplary phase Ψ and amplitude profiles. The green line indicates the region, where the linear fit was evaluated. This is sufficiently far away from the central excitation spot.

Three films have been measured for each Hec/PVP composition. An average in-plane thermal diffusivity and a standard deviation were calculated for each composition, as summarized in Table S2.

Table S2. In-plane thermal diffusivity values of Hec/PVP stack films. Three films per Hec/PVP composition were measured, based on which an average in-plane thermal diffusivity and a standard deviation were calculated.

Sample	In-plane thermal diffusivity [mm^2s^{-1}]
Hec23/PVP77	1.02 ± 0.04
Hec31/PVP69	1.28 ± 0.02
Hec40/PVP60	1.52 ± 0.04
Hec51/PVP49	1.69 ± 0.03
Hec100/PVP0	2.35 ± 0.03

The in-plane thermal conductivity was calculated from the in-plane thermal diffusivity ($\alpha_\parallel$), density (ρ), and specific heat (C_P) as

$$\kappa_\parallel = \alpha_\parallel \cdot \rho \cdot C\mathrm{p} \tag{S2}$$

Photoacoustic Method

The cross-plane thermal conductivity was determined by the photoacoustic method. It uses the photoacoustic effect to determine the thermal properties of a sample. Therefore, a modulated laser beam (λ = 488 nm) periodically heats the sample. For good absorption of the laser energy a thin Au transducer layer (~150 nm) was coated on the sample surface. For photoacoustic characterization, the samples were spray-coated on a glass substrate. The layout of the measurement cell above the sample is shown in Figure S12a. The gas tight cell is filled with a helium pressure of 20 psi. The microphone (Bruel&Kjaer, 4398-A-011) connected to the cell measures an acoustic wave, which is induced by the periodic heat conduction from the transducer layer surface to the gas phase. As shown in Figure S12b, the microphone is linked to a lock-in amplifier with integrated signal generator (Zurich instruments, HF2LI). The signal generator controls the electro-optic modulator (EOM, Conoptics, M25A) and therefore the frequency of the modulated laser beam. The acoustic signal detected by the microphone is then transferred into a phase and amplitude shift in relation to the modulation of the incident laser beam.

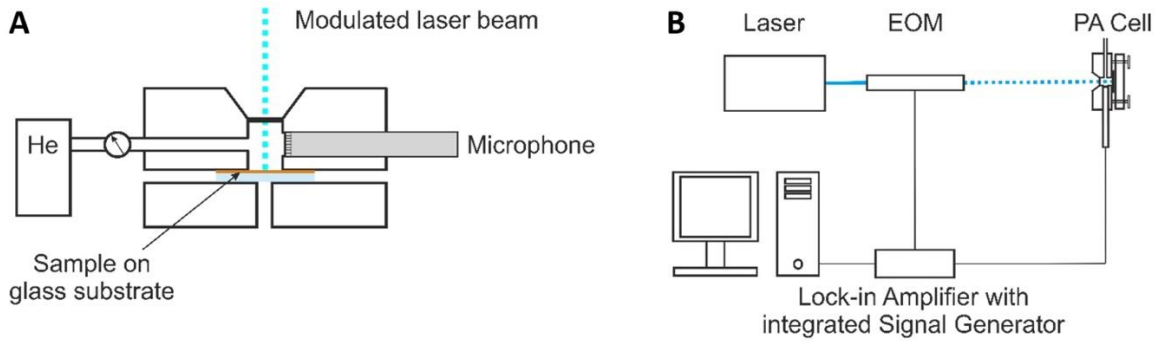

Figure S12. Scheme of photoacoustic measurements. a) The photoacoustic cell. b) The whole setup.

The phase shift is detected as a function of the frequency in a range from 110 Hz to 4000 Hz. The signal is then normalized with the phase shift signal of a thermally thick glass sample (1 mm) with known thermal properties. A representative frequency sweep is shown in Figure S13. The red line indicates the best fit

according to the fitting procedure presented by Singh *et al.*[6] They used the generalized multilayer model of Hu *et al.*[7] assuming one-dimensional heat transfer. The unknown fitting parameters are the contact resistance between the gold layer and the sample, the thermal diffusivity of the sample, and the contact resistance between sample and substrate. For thin films the fit is not very sensitive to the individual parameters, but to the total layer resistance. Therefore, only the total layer resistance is reported. From the total layer resistance it is possible to calculate the effective thermal conductivity by dividing with the thickness. The thickness of the samples was determined by AFM measurements. The values of the total layer resistance and sample thickness are summarized in Table S3. For each Hec/PVP ratio samples with three different thicknesses were measured to exclude influences from the sample thickness.

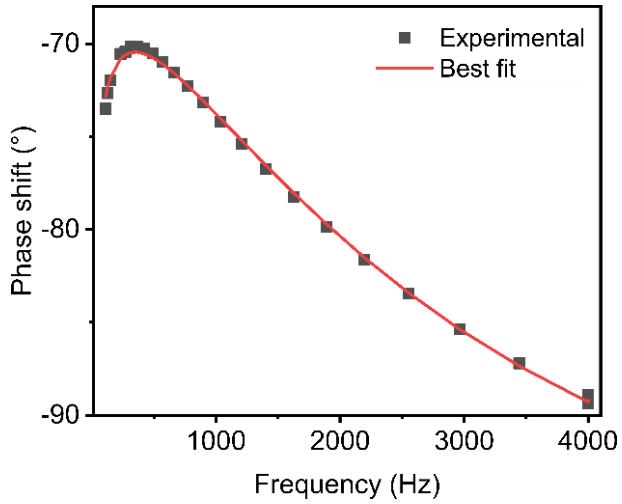

Figure S13. Normalized photoacoustic phase signal. Representative photoacoustic measurement of the Hec31/PVP69 sample with a thickness of 1.979 µm. The red line shows the best fit.

Table S3. Summary of the photoacoustic measurements. The total layer resistance, the thickness, and the resulting effective cross-plane thermal conductivity are given for each sample.

Sample	Total layer resistance [mm^2KW^{-1}]	Thickness [μm]	Effective cross-plane thermal conductivity [$Wm^{-1}K^{-1}$]
Hec100/PVP0	1.58	0.28	0.177
Hec100/PVP0	2.55	0.595	0.234
Hec100/PVP0	4.34	0.94	0.217
Hec51/PVP49	3.69	0.255	0.069
Hec51/PVP49	7.74	0.722	0.093
Hec51/PVP49	11.53	0.957	0.083
Hec40/PVP60	6.54	0.463	0.071
Hec40/PVP60	14.03	1.139	0.081
Hec40/PVP60	18.96	1.987	0.105
Hec31/PVP69	8.20	0.744	0.091
Hec31/PVP69	17.58	1.382	0.079
Hec31/PVP69	24.06	1.979	0.082
Hec23/PVP77	8.81	0.568	0.064
Hec23/PVP77	17.45	1.677	0.096
Hec23/PVP77	26.37	2.568	0.097
Hec0/PVP100	2.26	0.351	0.155
Hec0/PVP100	4.50	0.792	0.176

Section S3. Brillouin Light Spectroscopy

Brillouin Light Spectroscopy (BLS) measures the phonon dispersion, *i.e.*, the wave vector, q, dependent sound velocity, $v_i(q)$, by detecting the Doppler frequency shift, f, in laser light inelastically scattered by sound waves ("phonons"). Since the phonon modes in question are thermally populated, the Bragg condition for light scattering is satisfied independent of the scattering angle, in contrast to the kindred time-domain ("picosecond ultrasonic") techniques that require external phonon injection via special sample preparation. Since the latter typically involves deposition of non-transparent metallic transducer films, they also do not readily allow for transmission and backscattering measurements, further limiting the potential of these techniques for probing anisotropic materials.

Assuming a planar sample, BLS can be conducted in three scattering geometries: transmission, reflection, and backscattering. For angle-dependent measurements in the transmission and reflection geometries, the laser source (λ = 532 nm) was mounted on a goniometer and rotated around the sample, similar to a wide-angle X-ray (WAXS) setup. For the transmission geometry (top-right inset to Figure 3b), the propagation vector, q, of the sound wave lies in the plane of the sample and its modulus, $|q|$, is independent of the refractive index according to $|q|_{\parallel} = (4\pi/\lambda)\sin\beta$, with β being the light incident angle. For the reflection geometry, the Bragg condition is fulfilled for sound waves with q along the normal to the sample plane, so that $|q|_{\perp} = (4\pi/\lambda)\sqrt{n^2 - \sin^2\beta}$, with n being the refractive index of the sample.[8] In order to find n, several points at different β were acquired, and then fit linearly; n was determined under the constraint that the fit has to pass through the origin (Figure S14a), and the obtained values are reported in Table S4. In contrast to the transmission geometry, the range of the dispersion relationship that can be scanned by varying $|q|_{\perp}$ is more restricted due to refraction of the laser beam at the air-sample boundary. Finally, backscattering measurements can be conducted, where the incident and scattered light traverse the same path, and the sample is

mounted on a rotating stage with angular gradation marks. Only a single dispersion point, corresponding to q directed opposite to k_i in the film and of a magnitude, $|q| = 4\pi n/\lambda$, is accessible in the backscattering geometry, but all possible $q/|q|$ directions can be probed. Because backscattering measurements use the same lens for focusing the incident and collimating scattered light, the alignment of the setup is generally much easier, so that all the backscattering spectra were acquired with microscope objectives (typically 10x) to reduce the spectrum accumulation time.

From the given formulas, it is easy to see that the Brillouin frequency shift does not exceed $2\pi v/\lambda$, where v is sound velocity. These frequencies render viscoelasticity effects negligible and are detected using a high-resolution six-pass Tandem Fabry Perot (TFP) interferometer (JRS Instruments, Switzerland) optimized for the 1-50 GHz range. Values still further out on the dispersion relationship can be accessed using, for example, picosecond ultrasonic interferometry (PUI), but at the expense of great effort and without any gain in information for the problem at hand.[9] Finally, BLS also offers direct access to the shear moduli, simply by analyzing scattered light in different polarizations: VV (*i.e.*, vertical incident and vertical scattered light) corresponds to quasi-longitudinal and quasi-transverse phonon modes, and VH (*i.e.*, vertical incident and horizontal scattered light) to the pure-transverse phonon mode (for transversely isotropic samples, HV does not show a transverse peak). Before the BLS measurements, the samples were dried at 100 °C in a vacuum chamber for one week to remove any residual water content.

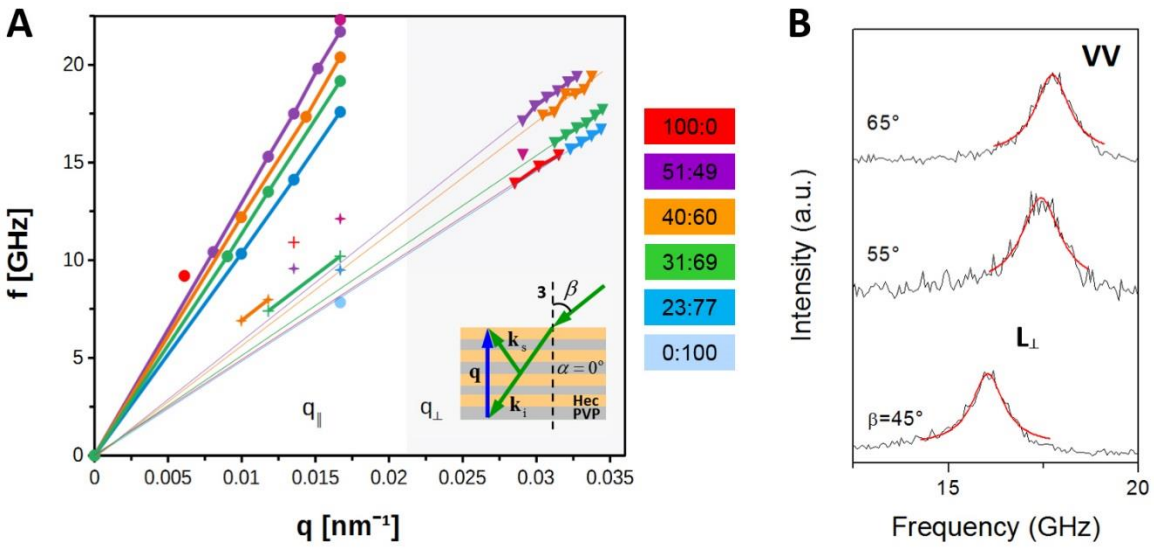

Figure S14. BLS experiments in the reflection geometry. a) Dispersion (frequency *vs*. wave vector) of the longitudinal (L) and transverse (T) phonons in the hybrid stacks and the two constituent components (see the color code) obtained from the polarized (VV) and depolarized (VH) BLS spectra recorded in the reflection geometry (inset). b) Typical VV spectra of the Hec31/PVP69 hybrid film at three laser incident angles.

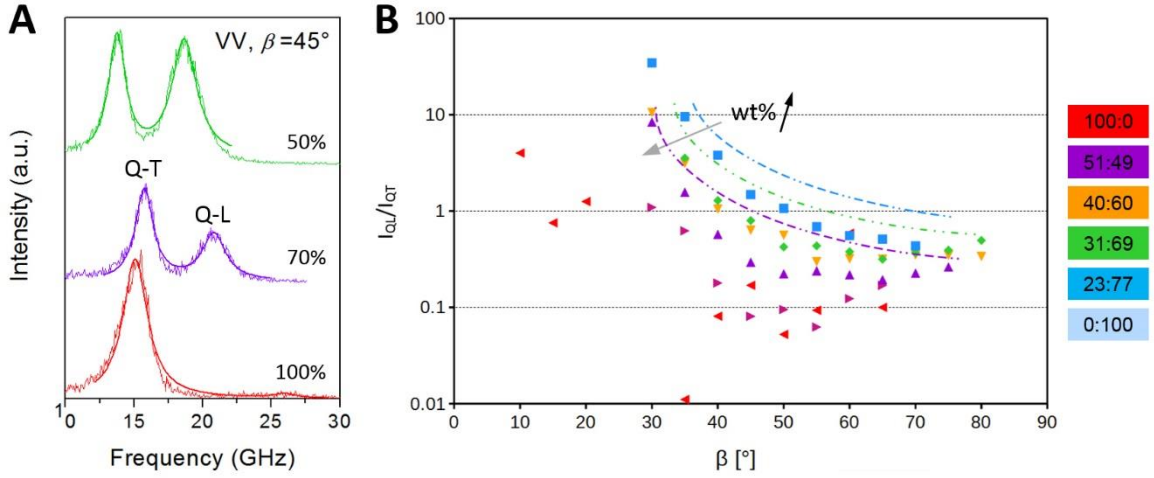

Figure S15. BLS spectra and peak intensity. a) Polarized (VV) BLS spectra recorded in the backscattering geometry (inset to Figure 3a) for two hybrid stacks and the pure Hec film at an incidence angle of 45°. b) The intensity ratio of the Q-L to Q-T peaks in a) *vs.* the laser incident angle.

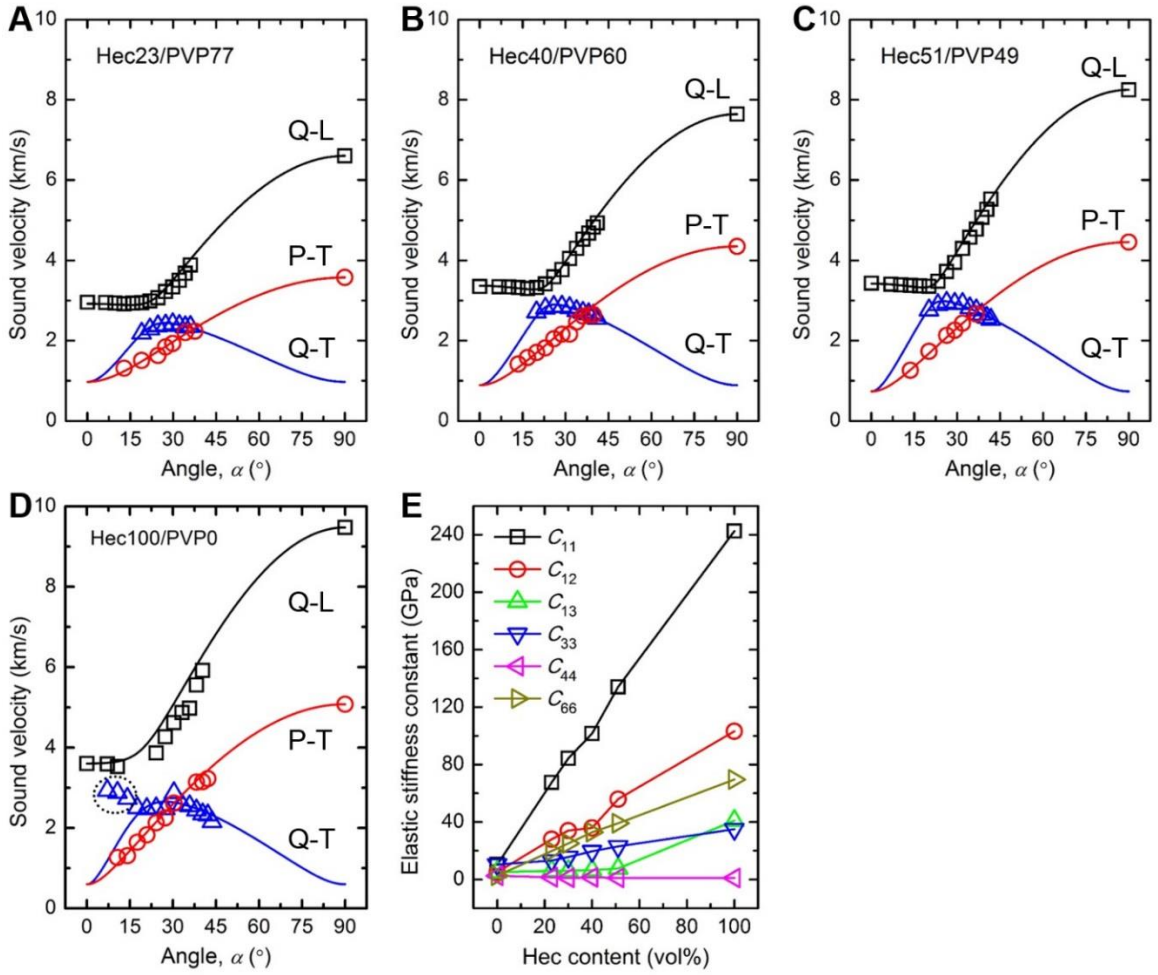

Figure S16. Direction-dependent sound velocities of hybrid stack films. a) Hec23/PVP77, b) Hec40/PVP60, c) Hec51/PVP49, and d) Hec100/PVP0 (the data points in the dotted circle were not used in the fitting). Q-L, P-T, and Q-T represent the quasi-longitudinal, pure-transverse, and quasi-transverse phonon modes, respectively. e) Variation of the elastic stiffness constants with the Hec volume fraction.

Based on the BLS-measured direction-dependent sound velocities, we obtained the elastic tensor within the framework of the Christoffel equation.[10]

$$\begin{bmatrix} \Gamma_{11} - \rho v^2 & \Gamma_{12} & \Gamma_{13} \\ \Gamma_{21} & \Gamma_{22} - \rho v^2 & \Gamma_{23} \\ \Gamma_{31} & \Gamma_{32} & \Gamma_{33} - \rho v^2 \end{bmatrix} \begin{bmatrix} u_1 \\ u_2 \\ u_3 \end{bmatrix} = \begin{bmatrix} 0 \\ 0 \\ 0 \end{bmatrix} \quad \text{(S3)}$$

where ρ is the density of the sample, v is the sound velocity, $u = [u_1, u_2, u_3]^{\mathrm{T}}$ is the displacement vector, and Γ_{ik} (i, k = 1, 2, 3) is the Christoffel stress, which is defined as

$$\Gamma_{\mathrm{ik}} = \sum_{j=1}^{3}\sum_{l=1}^{3} C_{\mathrm{ijkl}} n_{\mathrm{j}} n_l. \tag{S4}$$

Here, C_{ijkl} denotes an element of the 4th rank elastic tensor, and $n = [n_1,\ n_2, n_3]^{\mathrm{T}}$ represents the phonon propagation direction.

For a transversely isotropic material, the elastic tensor, in the Voigt notation, has the following form.[11]

$$\mathrm{C} = \begin{bmatrix} C_{11} & C_{12} & C_{13} & & & \\ C_{12} & C_{11} & C_{13} & & & \\ C_{13} & C_{13} & C_{33} & & & \\ & & & C_{44} & & \\ & & & & C_{44} & \\ & & & & & C_{66} = \dfrac{C_{11} - C_{12}}{2} \end{bmatrix}. \tag{S5}$$

and contains five independent stiffness constants. After some algebra, the sound velocities of the Q-L, Q-T, and P-T modes along a direction defined by α can be represented as follows,

$$v_{\mathrm{Q-L}}(\alpha) = \sqrt{\frac{-A_1\sqrt{A_1^2 - 4A_2}}{2\rho}} \tag{S6}$$

$$v_{\mathrm{Q-T}}(\alpha) = \sqrt{\frac{-A_1\sqrt{A_1^2 - 4A_2}}{2\rho}} \tag{S7}$$

$$v_{\mathrm{P-T}}(\alpha) = \sqrt{\frac{A_3}{\rho}} \tag{S8}$$

where,

$$A_1 = -(\sin^2\alpha C_{11} + \cos^2\alpha C_{33} + C_4 \tag{S9}$$

$$A_2 = \sin^4\alpha C_{11}C_{44} + \sin^2\alpha\cos^2\alpha(C_{11}C_{33} - C_{13}^2 - 2C_{13}C_{44}) + \cos^4\alpha C_{33}C_{44} \tag{S10}$$

$$A_3 = \sin^2\alpha C_{66} + \cos^2\alpha C_{44} \tag{S11}$$

Through nonlinear χ^2 fitting of the BLS-measured sound velocities (*i.e.*, *v vs.* α) with Equations (S6)-(S8), we obtained the elastic stiffness constants as well as their uncertainties.[12] The χ^2 is defined as

$$\chi^2 = \sum_i \frac{\left[\nu_{\mathrm{i,fit}}(C_{11}, C_{12}, C_{13}, C_{33}, C_{44}, \alpha) - \nu_{\mathrm{i,exp}}(\alpha)\right]^2}{\left(\Delta\nu_{\mathrm{i,exp}}\right)^2} \quad \text{(S12)}$$

where $\nu_{\mathrm{i,fit}}$ and $\nu_{\mathrm{i,exp}}$ are the fitted and experimental sound velocities, respectively, $\Delta\nu_{\mathrm{i,exp}}$ is the uncertainty of the measured sound velocity, and the summation is over all experimental sound velocities. By considering the uncertainties of the measured angles, refractive indices, and phonon frequencies, we estimated $\Delta\nu_{\mathrm{i,exp}}$ to be 0.02 $\nu_{\mathrm{i,exp}}$. We imposed the following constraints for the elastic stiffness constants[13]: (1) $C_{11} > |C_{12}|$, (2) $C_{44} > 0$, and (3) $C_{33}(C_{11} + C_{12}) > 2C_{13}^2$, which ensure positive Young's and shear moduli. The availability of experimental data for all the Q-L, Q-T, and P-T modes allows unique determination of C_{11}, C_{12}, C_{13}, C_{33}, and C_{44}.

After that, we calculated the engineering mechanical properties,[11] which include the in-plane Young's modulus ($E_{\parallel}$), cross-plane Young's modulus ($E_{\perp}$), sliding shear modulus (G_{13}), torsional shear modulus (G_{12}), and two characteristic Poisson's ratios (ν_{13} and ν_{12}). Note that only five of the engineering mechanical properties are independent (typically, $E_{\parallel}$, $E_{\perp}$, G_{13}, G_{12}, and one of ν_{13} and ν_{12} are chosen). Also note that to be consistent with the direction-dependent thermal conductivity results, we used subscripts, "$\parallel$" and "$\perp$", to represent directions parallel and perpendicular to the sample film, respectively, rather than directions parallel and perpendicular to the "3"-axis (*i.e.*, the symmetry axis), as seen in typical analysis of transversely isotropic materials. The relevant mechanical properties are summarized in Tables S4 and S5.

Table S4. Summary of elastic stiffness constants. Composition (Hec vol%, Hec wt%), density (ρ), refractive index (n), and elastic stiffness constants (C_{11}, C_{12}, C_{13}, C_{33}, C_{44}, and C_{66}) of the Hec/PVP hybrid Bragg stack films.

Sample ID	Hec vol%	Hec wt%	ρ [gcm^{-3}]	n	C_{11} [GPa]	C_{12} [GPa]	C_{13} [GPa]	C_{33} [GPa]	C_{44} [GPa]	C_{66} [GPa]
Hec0/PVP100	0	0	1.20	1.53*	10.4	5.2	5.2	10.4	2.6	2.6
Hec23/PVP77	23	40	1.55	1.54	67.6 ±1.7	28.0 ±1.9	6.0 ±1.2	13.2 ±0.3	1.5 ±0.1	19.8 ±0.5
Hec31/PVP69	31	50	1.62	1.50	84.3 ±1.5	34.0 ±1.8	6.1 ±1.5	15.7 ±0.3	1.2 ±0.2	25.1 ±0.5
Hec40/PVP60	40	60	1.74	1.47	101.6 ±1.8	35.9 ±2.2	6.5 ±1.8	19.7 ±0.4	1.4 ±0.1	32.9 ±0.6
Hec51/PVP49	51	70	1.97	1.45	134.1 ±2.2	55.9 ±2.9	7.7 ±2.3	23.0 ±0.5	1.1 ±0.1	39.1 ±0.9
Hec100/PVP0	100	100	2.70	1.40	242.5 ±6.2	103.2 ±6.7	40.9 ±5.2	35.0 ±0.9	1.0 ±0.1	69.6 ±1.2

*Source: https://refractiveindex.info/?shelf=organic&book=polyvinylpyrrolidone&page=Konig.

Table S5. Summary of engineering mechanical properties. Composition (Hec vol%, Hec wt%) and engineering mechanical properties of the Hec/PVP hybrid Bragg stack films. $E_{\parallel}$: in-plane Young's modulus; $E_{\perp}$: cross-plane Young's modulus; G_{13}, G_{23}: sliding shear moduli; G_{12}: torsional shear modulus; ν_{13}, ν_{23}, ν_{12}: Poisson's ratios (ν_{13} represents the strain response in the j-direction due to a stress in the i-direction).

Sample ID	Hec vol%	Hec wt%	$E_{\parallel}$ [GPa]	$E_{\perp}$ [GPa]	$\frac{E_{\parallel}}{E_{\perp}}$	$G_{13} = G_{23}$ [GPa]	G_{12} [GPa]	$\nu_{13} = \nu_{23}$	ν_{12}
Hec0/PVP100	0	0	7.0	7.0	1	2.6	2.6	0.33 (assumed)	0.33 (assumed)
Hec23/PVP77	23	40	55.0 ±2.5	12.5 ±0.4	4.4	1.5 ±0.1	19.8 ±0.5	0.06 ±0.01	0.39 ±0.03
Hec31/PVP69	31	50	69.7 ±2.3	15.1 ±0.4	4.6	1.2 ±0.2	25.1 ±0.5	0.05 ±0.01	0.39 ±0.02
Hec40/PVP60	40	60	88.1 ±2.6	19.1 ±0.5	4.6	1.4 ±0.1	32.9 ±0.6	0.05 ±0.01	0.34 ±0.02
Hec51/PVP49	51	70	109.9 ±3.5	22.4 ±0.6	4.9	1.1 ±0.1	39.1 ±0.9	0.04 ±0.01	0.41 ±0.02
Hec100/PVP0	100	100	178.9 ±9.9	25.4 ±2.6	7.0	1.0 ±0.1	69.6 ±1.2	0.12 ±0.02	0.29 ±0.06

Section S4. Evaluation of Interfacial Thermal Conductance

The series resistance model (SRM) shown in Figure 4f illustrates a hybrid stack unit cell consisting of one Hec layer and one PVP layer. We describe the corrugation of the Hec nanosheet (Figure 1b) by a thermal interface conductance, $G_{Hec/PVP}$. For the unit cell in Figure 4f, the total thermal resistance can be calculated as $\frac{d_{XRD}}{k_{\perp}} = \frac{d_{Hec}}{k_{Hec}} + \frac{d_{PVP}}{k_{PVP}} + \frac{2}{G_{Hec/PCP}}$, where d_{XRD} is the basal spacing as determined by XRD (Table S1), is the effective cross-plane thermal conductivity, d_{Hec} = 10 Å, and $d_{PVP} = d_{XRD} - d_{Hec}$. For the thermal conductivity of the two components, we used the following values: k_{Hec} = 5.71 $Wm^{-1}K^{-1}$, and k_{PVP} = 0.17 $Wm^{-1}K^{-1}$. The Hec/PVP interfacial conductance, $G_{Hec/PVP}$, is determined by least squares fitting of the experimental data (red solid line in Figure 4c) to be 89 ± 8 $MWm^{-2}K^{-1}$, which falls well into the range of interfacial conductance reported for inorganic/organic interfaces.[14] We also obtained the Hec/Hec interfacial conductance, $G_{Hec/Hec}$ = 219 ± 28 $MWm^{-2}K^{-1}$, by considering a unit cell consisting of one Hec layer and one Hec/Hec interface (*i.e.*, $\frac{d_{XRD}}{k_{\perp}} = \frac{d_{Hec}}{k_{Hec}} + \frac{1}{G_{Hec/Hec}}$).

Section S5. Uncertainty Analysis

The uncertainties (standard deviations) of the data reported in this work were analyzed by taking into account the instrument accuracy, repetitive measurements, and propagation of uncertainties. The sound velocities were estimated to have an error bar of 2%. The uncertainties of the elastic stiffness constants were determined according to Zgonik *et al.*[12] The uncertainties of the engineering mechanical properties were calculated according to principles of uncertainty propagation. For instance,

$$E_{\perp} = C_{13} - \frac{2C_{13}^2}{C_{11} + C_{12}} \tag{S13}$$

$$\Delta E_{\perp} = \sqrt{\sum_{\mathrm{ij}=11,12,13,33} \left(\frac{\partial E_{\perp}}{\partial C_{\mathrm{ij}}}\right)^2 \left(\Delta C_{\mathrm{ij}}\right)^2 + \sum_{\substack{\mathrm{ij,kl}=11,12,13,33 \\ ij<kl}} 2\frac{\partial E_{\perp}}{\partial C_{\mathrm{ij}}}\frac{\partial E_{\perp}}{\partial C_{k\mathrm{l}}}\Delta C_{\mathrm{ij/kl}}} \tag{S14}$$

where $\frac{\partial E_{\perp}}{\partial C_{11}} = \frac{2C_{13}^2}{(C_{11}+C_{12})^2}$, $\frac{\partial E_{\perp}}{\partial C_{12}} = \frac{2C_{13}^2}{(C_{11}+C_{12})^2}$, $\frac{\partial E_{\perp}}{\partial C_{13}} = -\frac{4C_{13}^2}{C_{11}+C_{12}}$, and $\frac{\partial E_{\perp}}{\partial C_{33}} = 1$. Similar expressions can be derived for the other engineering moduli and the Poisson's ratios.

The uncertainties of the thermal measurement results are analyzed in a similar way, *i.e.*, by considering uncertainty propagation. For example,

$$k_{\parallel} = \alpha_{\parallel}\rho C_{\mathrm{P}} \tag{S15}$$

$$\Delta k_{\parallel} = \sqrt{\left(\frac{\partial k_{\parallel}}{\partial \alpha_{\parallel}}\right)^2 (\Delta\alpha_{\parallel})^2 + \left(\frac{\partial k_{\parallel}}{\partial \rho}\right)^2 (\Delta\rho)^2 + \left(\frac{\partial k_{\parallel}}{\partial C_{\mathrm{P}}}\right)^2 (\Delta C_P)^2} \tag{S16}$$

where $\frac{\partial k_{\parallel}}{\partial \alpha_{\parallel}} = \rho C_{\mathrm{P}}$, $\frac{\partial k_{\parallel}}{\partial \rho} = \alpha_{\parallel} C_{\mathrm{P}}$, and $\frac{\partial k_{\parallel}}{\partial C_{\mathrm{P}}} = \alpha_{\parallel}\rho$. Here we assumed negligible covariance terms. Similar expressions can be derived for $k_{\perp}$, $k_{\parallel}/k_{\perp}$, $\overline{\Lambda}$, etc.

The uncertainties of the data are reported as error bars in the figures shown in the main text and Supporting Information. For clarity, error bars smaller than the symbol size are not shown.

References

1. a) J. Breu, W. Seidl, A. J. Stoll, K. G. Lange, T. U. Probst, Chem. Mater. 2001, 13, 4213-4220; b) M. Stöter, D. A. Kunz, M. Schmidt, D. Hirsemann, H. Kalo, B. Putz, J. Senker, J. Breu, Langmuir 2013, 29, 1280-1285.

2. S. Rosenfeldt, M. Stöter, M. Schlenk, T. Martin, R. Q. Albuquerque, S. Förster, J. Breu, Langmuir 2016, 32, 10582-10588.

3. D. M. Moore, R. C. Reynolds, D. M., X-ray diffraction and the identification and analysis of clay minerals, Oxford University Press, Oxford, U.K., 1997.

4. E. S. Tsurko, P. Feicht, F. Nehm, K. Ament, S. Rosenfeldt, I. Pietsch, K. Roschmann, H. Kalo, J. Breu, Macromolecules 2017, 50, 4344-4350.

5. a) A. Salazar, A. Mendioroz, R. Fuente, Appl. Phys. Lett. 2009, 95, 121905; b) A. Mendioroz, R. Fuente-Dacal, E. Apinaniz, A. Salazar, Rev. Sci. Instrum. 2009, 80, 074904.

6. V. Singh, T. L. Bougher, A. Weathers, Y. Cai, K. Bi, M. T. Pettes, S. A. McMenamin, W. Lv, D. P. Resler, T. R. Gattuso, D. H. Altman, K. H. Sandhage, L. Shi, A. Henry, B. A. Cola, Nat. Nanotechnol. 2014, 9, 384-390.

7. H. Hu, X. Wang, X. Xu, J. Appl. Phys. 1999, 86, 3953-3958.

8. T. Still, High Frequency Acoustics in Colloid-based Meso- and Nanostructures by Spontaneous Brillouin Light Scattering, 1 ed., Springer-Verlag Berlin Heidelberg, 2010.

9. C. Klieber, Ultrafast photo-acoustic spectroscopy of super-cooled liquids, Massachusetts Institute of Technology, 2010.

10. a) S. P. Cheadle, R. J. Brown, D. C. Lawton, Geophysics 1991, 56, 1603-1613; b) M. Mah, D. R. Schmitt, Geophysics 2001, 66, 1217-1225.

11. S. Cusack, A. Miller, J. Mol. Biol. 1979, 135, 39-51.

12. M. Zgonik, P. Bernasconi, M. Duelli, R. Schlesser, P. Günter, M. H. Garrett, D. Rytz, Y. Zhu, X. Wu, Phys. Rev. B 1994, 50, 5941-5949.

13. F. Mouhat, F.-X. Coudert, Phys. Rev. B 2014, 90, 4104.

14. a) M. D. Losego, M. E. Grady, N. R. Sottos, D. G. Cahill, P. V. Braun, Nat. Mater. 2012, 11, 502-506; b) W. L. Ong, S. M. Rupich, D. V. Talapin, A. J. McGaughey, J. A. Malen, Nat. Mater. 2013, 12, 410-415.

13. Outlook

In this thesis, the finite element method (FEM) and lock-in thermography (LIT) were developed for the characterization of nanoscale heat transfer.

The FEM was successfully established to study thermal transport through ordered and disordered colloidal assemblies. These studies revealed several important parameters to fabricate a highly insulating material: particle geometry, interparticle bonding strength, assembly geometry, and mixing of differently sized particles. Nevertheless, there are still some influences which have to be clarified. One example is the diameter of the colloidal building blocks. Here, we have already seen that the size of polymer particles determines the interparticle contact area. Furthermore, preliminary FEM studies showed that, as expected, an increase in contact area raises the overall thermal conductivity. However, a wholistic experimental and theoretical study on various particle types is still missing. Furthermore, FEM studies could help to develop colloidal assembly-based thermal diodes by, *e.g.*, finding an appropriate sample geometry.

Besides the FEM, LIT was successfully built-up and used to characterize the in-plane heat transfer properties of single-phase and hybrid Bragg stacks. However, some changes in the home-built LIT set-up would make this method even more powerful. First of all, the replacement of the used infrared camera by a cooled thermal imaging camera would significantly reduce the measuring time and therefore enhance the sample through-put. Second, the implementation of a heatable sample chamber would enable temperature-dependent heat transfer studies in in-plane direction. This would open up new opportunities for nanoscale heat transfer studies. In Chapter 10, we prove that uncoated semitransparent films can also be evaluated using the simple slopes method. This extends the applicability of LIT to in-situ monitoring of the evolution of the in-plane thermal properties of, for example, polymer films or fiber mats under stretching. I have already performed promising experiments on nonwoven fiber mats consisting of

thermoplastic polyurethane fibers. These measurements showed, on the one hand, that an isotropic in-plane thermal diffusivity is obtained for randomly oriented fiber mats. Upon stretching, however, the thermal diffusivity in stretching direction rose, while the thermal diffusivity in perpendicular direction stayed at a low level. On the other hand, fiber mats with parallelly arranged fibers exhibited already in the unstretched state an anisotropic in-plane thermal diffusivity. Here, the anisotropy ratio increased due to the mechanical stretching. In further work, a detailed study of the interplay of thermal transport, mechanical, and structural properties could be conducted.

Overall, this thesis contributed to an improved understanding of nanoscale thermal transport and laid the basis for future studies on nanostructured materials.

Danksagung

Abschließend möchte ich all denjenigen danken, die zur Fertigstellung meiner Doktorarbeit beigetragen haben:

Zuallererst bedanke ich mich ganz herzlich bei meinem Doktorvater Prof. Dr. Markus Retsch für die interessante und vielseitige Themenstellung, das angenehme Betreuungsverhältnis, die stetige Unterstützung bei Schwierigkeiten sowie die Möglichkeit jederzeit an Konferenzen und Fortbildungen teilzunehmen. Weiterhin danke ich Prof. Dr. Markus Retsch für all die gemeinsamen Aktivitäten innerhalb der Retsch-Gruppe, insbesondere die Paper-Partys und die damit verbundene Wertschätzung unserer Arbeit.

Dank gilt außerdem allen Mitgliedern (und ehemaligen Mitliedern) der Retsch-Gruppe. Hier bedanke ich mich besonders bei Pia Ruckdeschel, Fabian Nutz, Bernd Kopera, Patrick Hummel, Nelson Pech-May und Anna Lechner für die sehr gute und erfolgreiche Zusammenarbeit. An dieser Stelle gebührt Bernd Kopera und Nelson Pech-May zusätzlicher Dank für das Korrekturlesen meiner Doktorarbeit.

Weiterer Dank gilt meinen externen Kooperationspartnern, insbesondere Theresa Schilling, Martin Dulle, Jonas Eichinger, Christian Cyron, für die sehr angenehme und erfolgreiche Zusammenarbeit. Ich danke außerdem Sabrina Thomä, Isabell Sommermann, Dominik Skrybeck und Anton Weissbach, die im Rahmen von Praktika oder als studentische Hilfskräfte einen kleinen Beitrag zu dieser Arbeit geleistet haben. In diesem Zusammenhang bedanke ich mich auch bei Flora Bitterlich, die mir im Rahmen ihrer Bachelorarbeit zugearbeitet hat.

Zuletzt danke ich von ganzem Herzen meiner gesamten Familie. ♥

Vielen Dank euch allen!

Eidesstattliche Versicherungen und Erklärungen

(§ 8 Satz 2 Nr. 3 PromO Fakultät) Hiermit versichere ich eidesstattlich, dass ich die Arbeit selbstständig verfasst und keine anderen als die von mir angegebenen Quellen und Hilfsmittel benutzt habe (vgl. Art. 64 Abs. 1 Satz 6 BayHSchG).

(§ 8 Satz 2 Nr. 3 PromO Fakultät) Hiermit erkläre ich, dass ich die Dissertation nicht bereits zur Erlangung eines akademischen Grades eingereicht habe und dass ich nicht bereits diese oder eine gleichartige Doktorprüfung endgültig nicht bestanden habe.

(§ 8 Satz 2 Nr. 4 PromO Fakultät) Hiermit erkläre ich, dass ich Hilfe von gewerblichen Promotionsberatern bzw. –vermittlern oder ähnlichen Dienstleistern weder bisher in Anspruch genommen habe noch künftig in Anspruch nehmen werde.

(§ 8 Satz 2 Nr. 7 PromO Fakultät) Hiermit erkläre ich mein Einverständnis, dass die elektronische Fassung der Dissertation unter Wahrung meiner Urheberrechte und des Datenschutzes einer gesonderten Überprüfung unterzogen werden kann.

(§ 8 Satz 2 Nr. 8 PromO Fakultät) Hiermit erkläre ich mein Einverständnis, dass bei Verdacht wissenschaftlichen Fehlverhaltens Ermittlungen durch universitätsinterne Organe der wissenschaftlichen Selbstkontrolle stattfinden können.

…….

Ort, Datum, Unterschrift